ABSTRACT

Title of dissertation: A Programmable Five Qubit Quantum Computer Using Trapped Atomic Ions

Shantanu Debnath, Doctor of Philosophy, 2016

Dissertation directed by: Professor Christopher Monroe
Joint Quantum Institute,
University of Maryland Department of Physics and
National Institute of Standards and Technology

Quantum computers can solve certain problems more efficiently compared to conventional classical methods. In the endeavor to build a quantum computer, several competing platforms have emerged that can implement certain quantum algorithms using a few qubits. However, the demonstrations so far have been done usually by tailoring the hardware to meet the requirements of a particular algorithm implemented for a limited number of instances. Although such proof of principal implementations are important to verify the working of algorithms on a physical system, they further need to have the potential to serve as a general purpose quantum computer allowing the flexibility required for running multiple algorithms and be scaled up to host more qubits. Here we demonstrate a small programmable quantum computer based on five trapped atomic ions each of which serves as a qubit. By optically resolving each ion we can individually address them in order to perform a complete set of single-qubit and fully connected two-qubit quantum gates and also

perform efficient individual qubit measurements. We implement a computation architecture that accepts an algorithm from a user interface in the form of a standard logic gate sequence and decomposes it into fundamental quantum operations that are native to the hardware using a set of compilation instructions that are defined within the software. These operations are then effected through a pattern of laser pulses that perform coherent rotations on targeted qubits in the chain. The architecture implemented in the experiment therefore gives us unprecedented flexibility in the programming of any quantum algorithm while staying blind to the underlying hardware. As a demonstration we implement the Deutsch-Jozsa and Bernstein-Vazirani algorithms on the five-qubit processor and achieve average success rates of 95 and 90 percent, respectively. We also implement a five-qubit coherent quantum Fourier transform and examine its performance in the period finding and phase estimation protocol. We find fidelities of 84 and 62 percent, respectively. While maintaining the same computation architecture the system can be scaled to more ions using resources that scale favorably ($O(N^2)$) with the number of qubits N.

A Programmable Five Qubit Quantum Computer Using Trapped Atomic Ions

by

Shantanu Debnath

Dissertation submitted to the Faculty of the Graduate School of the
University of Maryland, College Park in partial fulfillment
of the requirements for the degree of
Doctor of Philosophy
2016

Advisory Committee:
Professor Chris Monroe, Chair/Advisor
Professor Steve Rolston
Professor Trey Porto
Professor Eite Tiesinga
Professor Andrew Childs

To my family

Acknowledgments

During my graduate studies I have had the good fortune of working with some brilliant people and having their support during tough times in the lab. First of all, I want to thank my advisor Chris Monroe who has not only given me the opportunity to work on trapped ion experiments but also a solid start in experimental physics by constantly encouraging me to take up new projects even if it meant dividing my time between experiments. Chris is very close to an ideal advisor I could have hoped for who gave me the freedom to pursue various experimental ideas and instilled in me the energy and optimism necessary to implement them.

I would like to thank Wes Campbell, Dzmitry Matsukevich, Qudsia Quraishi, Dave Hayes and Kihwan Kim for guiding me through various preliminary projects; educating about the underlying concepts and experimental techniques. Also folks in the 'ion-photon networks' lab, Dave Hucul, Kenny Lee, Susan Clark, Volkan Inlek and Grahame Vittorini with whom I have enjoyed working closely in the early years.

After moving to the 'quantum gates' project I worked with Andrew Manning and Taeyoung Choi in what became like a roller coaster ride. We changed lasers and ion traps several times, each time hoping to achieve an ideal multi-qubit system where we could perform qubit selective gates. The end result was most rewarding giving us the basic tools that would become instrumental in performing the experiments in this thesis. Thanks to Andrew who taught me a great deal about handling the complexity in experimental controls and Taeyoung for his excellent leadership and for showing the merits of perseverance in such experiments. I also enjoyed

working with Le Luo and Brian Fields who overlapped briefly in the experiment.

What I consider to be the next step in my graduate life has been the construction of yet another experiment as reported in this thesis. I am thankful to Norbert Linke who has helped make this system nearly optimal through his disciplined approach at troubleshooting, which in spite of being an arduous process became quite enjoyable due to his terrific company. I thank my other lab mates Caroline Figgatt and Kevin Landsman for delving into the nitty-gritties of the experiment and have enjoyed working out solutions together with them. Also Ken Wright, Jeoffrey Ji and Kate Collins for their contribution to the experiment.

I would like to extend my thanks our theory collaborators Luming Duan and Zhexuan Gong for developing the pulse shaping code and to Shengtao Wang for useful discussions. I have also had the privilege to engage in discussions with our IARPA-MQCO and LogiQ program collaborators Jungsang Kim, Ken Brown and Peter Maunz. A special thanks to Kurtis Volin for his input on several optics designs. I would also like to thank my thesis committee members for finding the time to read the thesis and improve it by providing valuable suggestions.

Although I have not worked directly with other members of the Monroe lab I certainly have enjoyed their company. Thanks to Phil Richerme, Emily Edwards, Rajibul Islam, Crystal Senko, Jonathan Mizrahi, Jon Sterk, Simcha Korenblit, Brian Neyenhuis, Aaron Lee, Jake Smith, Kale Johnson, Charles Conover, Chenglin Cao, Daniel Brennan, Paul Hess, Jiehang Zhang, David Wong-Campos, Clay Crocker, Guido Pagano, Marty Lichtman, Steven Moses, Kristin Beck, Harvey Kaplan, Antonis Kyprianidis and Ksenia Sosonova.

Graduate life has been difficult for me and I would not have made it without the support of my family. My parents who fostered my scientific curiosity and got me started in this path. My sister Shawon who has always given me the strength and will to take up challenges in all spheres of life. And my loving wife Sayantani to whom I promised that we will figure things out together. I hope the completion of this thesis is one proof of that promise being kept. Without your support I would not have made it so far.

Table of Contents

List of Tables

List of Figures

List of Abbreviations

DC	Direct Current (also implies static or slowly varying)
UV	Ultra-Violet
IR	Infra-Red
rf / RF	radio frequency
c.w.	continuous wave
AOM	Acousto-Optic Modulator
EOM	Electro-Optic Modulator
RWA	Rotating Wave Approximation
CP	controlled phase gate
CNOT	controlled NOT gate
H	Hadamard gate
PMT	Photo-Multiplier Tube
ICCD	Intensified Charge-Coupled Device
DOE	Diffractive-Optic Element
QFT	Quantum Fourier Tramsform
NA	Numerical Aperture
PID	Proportional-Integral-Derivative
ADC	Analog to Digital Converter
DAC	Digital to Analog Conveter
FPGA	Field Programmable Gate Array
UHV	Ultra-High Vacuum
CF	Con-Flat
NEG	Non-Evaporable Getter
AWG	Arbitrary Waveform Generator
AWG	American Wire Gauge
TMP	Turbo Molecular Pump
PSF	Point Spread Function
VVA	Voltage Variable Attenuator

Chapter 1: Introduction

Quantum computers can be used to solve certain problems much more efficiently than conventional computers. The idea of using a quantum system to process information could be dated back to the early 1980's when proposals made by Feynman [1] and Deutsch [2] showed how the quantum mechanical evolution of a system can be used as a powerful tool for performing computations. In his proposal Feynman suggested the use of a small well controlled quantum system to emulate the behavior of a larger poorly understood quantum system. The advantage of this method becomes apparent when calculations of even moderate size quantum systems becomes exponentially harder to solve using classical computing methods. It is relatively easier to address this problem using a quantum simulator which can be programmed to have nearly the same features as the emulated quantum system. The other proposal made by Deutsch, which intends to solve a mathematical problem, is based on evaluating unknown 'oracle' functions in order to learn about the behavior of the function. Due to the availability of *quantum superposition* as an intrinsic feature of any quantum system, it was shown how this could be used for evaluating the function for all possible inputs simultaneously and therefore learn global properties of the unknown function in a single run. At the heart of such ideas

lies the fundamental properties that are unique to quantum systems alone: namely *quantum superposition* and *quantum entanglement*. The first one allows a system to be in many possible states at once. Once a system is initialized to such a superposition, each state can be made to evolve in parallel under the influence of quantum operations (gates). The elegance of solving a physical or mathematical problem lies in mapping such a problem to the quantum operation that effects the evolution of all possible input states therefore leading to an exponential speedup in information processing due to this *quantum parallelism*. Such quantum evolutions can often lead to quantum entanglement. When the final state exhibits such entanglement it can correlate the different physical parts of the quantum system in a fashion that is not possible classically.

In order to process information in a quantum system an analog of a classical bit (0 or 1) is defined in the quantum world as the qubit. The computational power of a quantum computer is given by its capability of hosting large numbers of such qubits and having high degree of precision in the manipulation of each of the qubits in the system. A quantum system of N such qubits spans a Hilbert space of 2^N basis states. Such exponential growth of states is a prime motivation of using a quantum computer since it makes it possible to evolve an exponentially large number of states under a single quantum evolution operator. A large part of the research in quantum information involves finding efficient methods to map interesting problems into such unitary quantum evolutions. In cases where this can be successfully done, the *quantum parallelism* evolves all the basis states together therefore showing how such an evolution effects all the states. The information

describing the outcome therefore ideally consists of a set of 2^N numbers. However, a measurement of the system following the computation can collapse the system probabilistically and irreversibly into one of the basis states. This strange quality is native to quantum systems and does not happen in classical systems. The effect of measurement can therefore result in a complete loss of information about the system evolution. This problem could in principal be circumvented by making an exponential number of measurements to probe all the 2^N values which implies that the computation also needs to be repeated 2^N times. Therefore, at first glance one might feel that the overall efficiency of a quantum computer only matches that of a classical computer since the quantum algorithm will have to be run an exponential number of time which is also how a classical algorithm would solve the problem (by running it for all 2^N possibilities) in the first place. However, this is not entirely true since most of the information about all the 2^N outcomes can be recovered in only a few runs of the quantum computation if the final superposition state of the system before measurement primarily consists of only a few basis states and to which the system collapses on measurement with high probability. In the context of adiabatic quantum computing this can happen when the system starts in a superposition state that follows a quantum evolution to converge into only a few possible outcomes that defines the natural ground states of a physical system [3, 4]. Therefore, it takes only a few measurements to characterize the final quantum state of the system. In the context of evaluating mathematical functions, the set of 2^N numbers that define the outcome could (for certain function types) have a pattern across them that serves as an imprint of the functions property. This pattern can then be efficiently derived

by interfering all the 2^N numbers using the quantum version of a discrete Fourier transform. Due to such interference it is possible to obtain a computation result where the final outcome consists of single or a superposition of a few possible basis states (much smaller than 2^N). Therefore, the computation needs to be run only for a few times to obtain a global property of the function [5].

A device is a quantum computer if it meets a set of criteria originally proposed by DiVincenzo [6]. These conditions can be summarized as follows,

- A scalable physical systems with well characterized qubits
- The ability to initialize the qubits to a simple fiducial state
- Long coherence times compared to the time scale of gate operations
- A universal set of quantum gates
- A qubit-specific measurement capability

Over the years several systems have been developed to serve as a potential quantum computer. They are based on photonic, solid state or molecular and atomic systems. Among these, trapped ions are the oldest and most mature technology and have been shown to satisfy all qualities required to implement a large scale quantum computer. A qubit in this system is defined by the internal electronic states of an atomic ion that can be prepared in an initial state, manipulated using external electromagnetic fields and measured with high precision [7–10]. In this thesis we will show how one of the candidates (among many other ion species): the $^{171}Yb^{+}$ion makes a very high quality qubit by exhibiting long coherence times compared to the

time scales of performing quantum gates. Trapped ions are also inherently scalable. This is given by the fact that the qubit characteristics are defined by the atomic structure which is the same for all ions of the same element. Therefore increasing the system size merely requires adding more ions to the system where the same set of controls for qubit manipulation applies to each one of them. Increasing the system size by hosting chains of several trapped ions is further aided by the improvement in the trapping technologies. Atomic ions being charged can be trapped with strong confinements provided by electromagnetic fields. An ion trap that provides such fields can be miniaturized to micro-scale sizes with capabilities of fast shuttling ions [11] and directing laser beams at them using integrated optics [12, 13], both of which are important for performing computations. Trapped ion systems also come with a repository of techniques to control and manipulate the qubit with electromagnetic fields in the microwave [14] as well as the optical regime [15, 16]. Individual addressibility of qubits can be based on optical resolution, shelving of qubits to auxillary states and spectral resolution of qubits using field gradients across a linear chain of trapped ions [17–19].

Any quantum computation is executed by applying coherent quantum operations on the qubits. The fundamental operations required for implementing any computation could be listed as : a) single qubit rotation, and b) the two-qubit entangling gate [20, 21]. A system of trapped ions can be individually addressed by laser beams where single qubit rotations can be implemented. For two-qubit gates a spin-spin interaction needs to be induced that leads to the entanglement of the two qubits spin states. In order to mediate such interaction a communication line is

required that connects all the qubits to each other. In trapped ions, strong Coulomb forces between the ions behave like a connection between them. This influences the motion of each ion in the chain as the system can now be considered as a set of harmonic oscillators (one for each ion) that are coupled to each other via the electrostatic repulsion. This results in normal modes of motion of the entire ion chain where all of them oscillate in sync. It is this motional mode that can be used as a quantum bus which behaves like an additional degree of freedom outside the spin Hilbert space where each qubit in the chain can interact with it. Since the normal modes are distributed over the entire ion chain it can be used to exchange information between any two qubits in order to effect two-qubit entangling operations [22]. However, there might be a limitation on the number of ions inside a single ion trap that can be entangled reliably using such local Coulomb interactions. This limits the size of a single computation register, often referred to as a module. For systems that are expected to be larger than a single module the computer can in principle be distributed over several computational modules. A photonic bus can then be used to connect these processing units thereby allowing quantum gates to be performed remotely between modules [23–25].

A quantum computer is scalable when the system size can be increased to have more qubits available for computations without an exponential overhead of the cost of doing so. This is only guaranteed when both the multi-qubit system as well as the multi-qubit control are also scalable. Performing quantum computations on a multi-qubit system can follow one of two possible methods:

a) The hardware and software of the system is tailored to meet the requirements

of running a specific quantum algorithm. Early demonstrations of small scale computations have used this method. See for example NMR systems [26–28], photonic systems [29–31], trapped ions [16,32,33], and solid state systems [34]. A system that is designed to run specific algorithms by definition does not provide any flexibility as required for a general purpose machine

b) The execution of a quantum algorithm follows a computation architecture that decomposes any algorithm into fundamental quantum operations that are executed on a fixed hardware. Performing computations using this method is more universal since multiple algorithms can be executed in the same system. However, the scalability in multi-qubit control of such systems strongly depends on the underlying computation architecture. Using trapped ions as the computing platform already gives us an advantage on reducing the control parameters since all qubits in the processor are identical unlike solid state fabricated "artificial atom" like qubits [35,36] where qubit characteristics vary due to inadvertent inconsistencies in the fabrication of the qubits. A versatile quantum computer requires control at the individual qubit level but it should also minimize the overhead that is required for this control. For example while driving a two-qubit entangling operation it is preferable to apply the gate in a modular fashion only on the participating qubit pair using controls that are only specified by the pair and does not depend on other qubits in the system. Although it seems straightforward to carry this out, it is hard to completely satisfy this criteria in a quantum system since there might be inherent interactions of a qubit with other qubits or with the bath that cannot be completely removed from the system. Moreover without proper individual addressing of qubits, quantum

gates applied on targeted qubits might affect spectator qubits due to crosstalk.

The prime objective of the work reported in this thesis is the development of a programmable quantum computing system with a well defined computing architecture that supports the reconfigurability required to run arbitrary quantum algorithms in the system. The computation architecture of our system is represented in figure 1.1 [37]. At the highest level of the computer a user can program a quantum algorithm using sequences of standard logic gates (high-level commands). These gates are then decomposed into single-qubit (R) and two-qubit (XX) rotations that are native to the multi-qubit trapped ion system. This compiler is internal to the software that follows a specific set of instructions in order to calculate such decompositions. In the next step the software calculates optimized pulse shapes that are used to drive the appropriate XX- and R- gates on the qubits (low-level operations). This sequence of gates are then effected on the hardware that contains five trapped $^{171}Yb^{+}$ions as qubits. The hardware is also setup for individual qubit control using an array of Raman laser beams that address respective qubits by optically resolving them in space. This allows us to apply sequences of single- and two-qubit gates that are optically gated and therefore reconfigurable. By using a static Raman beam array to address individual qubits we also achieve a complete set single and two-qubit rotations that are implemented with a dramatically reduced overhead as compared to contemporary techniques of shuttling [38, 39] and spectral addressing [16, 40].

In this thesis we elaborate on the workings of the system. In order to benefit future members of the lab a didactic tone is maintained throughout where the underlying theory of each experiment is stated in order to corroborate the observations.

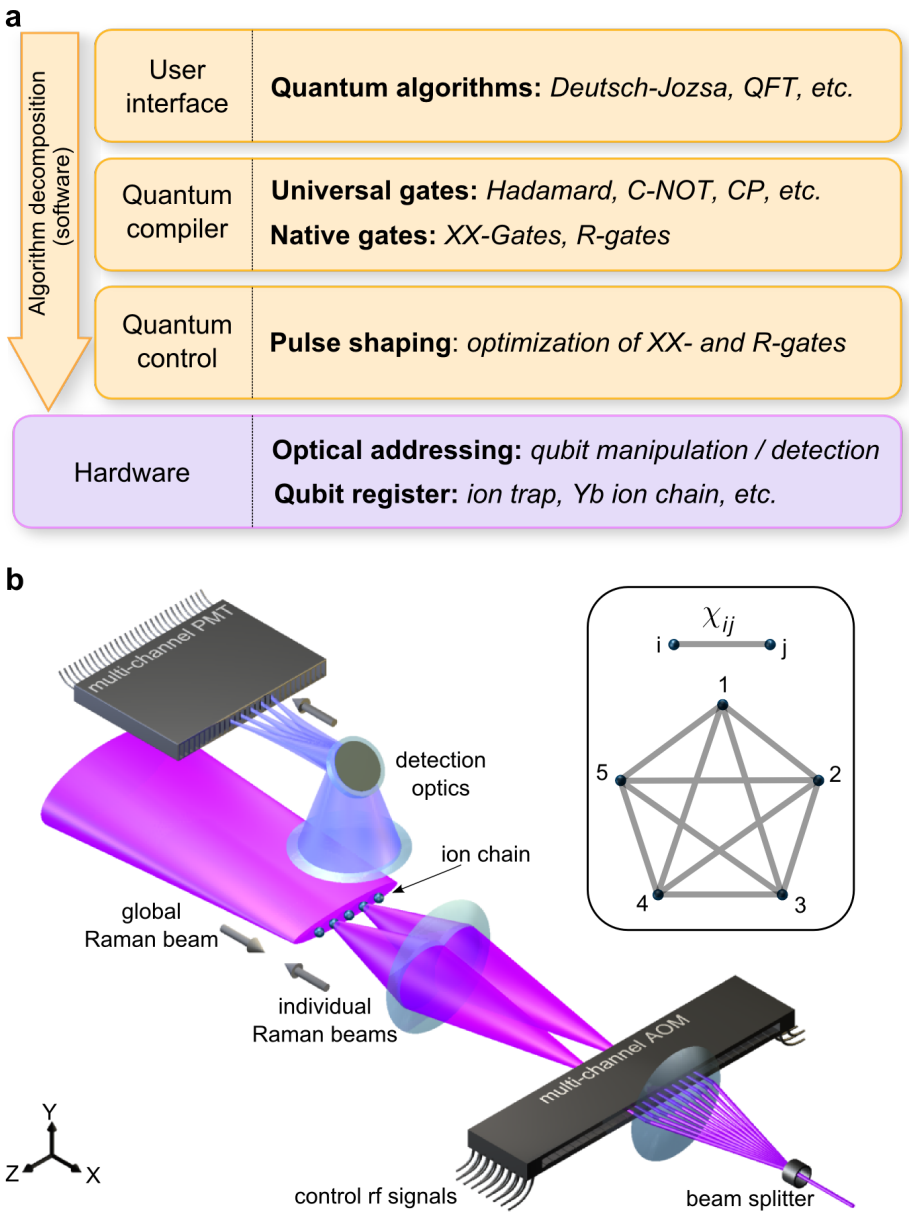

Figure 1.1: **Computation architecture.** a) Hierarchy of operations from software to hardware. b, Hardware setup. A linear chain of trapped ion qubits along the Z axis is shown at the centre of the panel ('Ion chain'). An imaging objective ('Detection optics') collects ion fluorescence along the Y axis and maps each ion onto a multichannel photo-multiplier tube (PMT) for measurement of individual qubits. Counterpropagating Raman beams ('Global' and 'Individual') along the X axis perform qubit operations. A diffractive beam splitter creates an array of static Raman beams that are individually switched using a multi-channel acousto-optic modulator (AOM) driven by radio frequency ('Control radio-frequency signals') to perform qubit-selective gates. By modulating appropriate addressing beams, any single-qubit rotation or two-qubit Ising (XX-) gate can be realized. For the two-qubit gates between qubits i and j, we can continuously tune the nonlinear gate angle χ_{ij}. This represents a system of qubits with fully connected and reconfigurable spin-spin Ising interactions (inset).

The thesis is structured in the following way:

In chapter 2 we discuss the theory behind ion trapping that leads to methods of optimizing the trapping parameters. We describe the ion-trap and give an account of methods used in assembling the one and the construction of the vacuum system around it that allows a high optical access for high resolution individual addressing and detection.

In chapter 3 we discuss the method of qubit manipulation using Raman transitions. We derive general principles of the process and apply it to pulsed laser frequency combs and discuss the unique properties that are important for performing coherent operations.

In chapter 4 we elaborate on the technological side of individual addressing of ions with Raman beams as well as individual detection of ions using custom designed high resolution optics. We further quantify the performance of both these processes.

In chapter 5 we discuss the theory behind single qubit $R-$gates and two qubit $XX-$gates and show how a variety of composite modular logic gates can be constructed from these native rotations. We quantify the performance of both the native and logic gates.

In chapter 6 we report the implementations of various quantum algorithms that are implemented on the 5-qubit processor. The way that these algorithms are based on the quantum Fourier transform is explained. We also report on a fully coherent five-qubit quantum Fourier transform and examine its performance in the protocols of period finding and quantum phase estimation.

Chapter 2: Experimental System

2.1 Introduction

The trapped ion serves as a pristine quantum system since it can be easily isolated from the environment. This is due to the fact that it is trapped in ultra high vacuum (UHV) where the collisions with the background gas are negligible. This can give a considerable advantage over solid state quantum systems where the system is in contact with bulk material that forms a thermal bath and leads to decoherence [36]. Although a trapped atomic ion is free from such a bath, it is nonetheless not immune to background electric and magnetic fields that can perturb the energy levels also causing decoherence. However, the strong interaction of an ion with well controlled electromagnetic fields can give the necessary tools for trapping and manipulation of the ions.

In this chapter we will discuss the theory behind ion-trapping where static and dynamic electric fields are used to trap a linear chain of ions that form a Coulomb crystal due to the joint action of the harmonic trapping potential and the strong repulsion due to the Coulomb forces between the ions. With the correct engineering of the harmonic potential using a segmented linear rf-Paul ion-trap [41] a chain of

many ions can be trapped in a linear configuration with almost uniform spacing between adjacent ions [42]. For such an arrangement of qubits (ions) an obvious method to address and detect each one of them is using linear arrays of optics or optical elements, one assigned to each ion. This will be discussed in detail in chapter 4. Another advantage of such a linear Coulomb crystal is that they have normal modes of motion that are common to the entire chain and excite all ions at once. This is particularly interesting in the context of spin-spin interaction as one can devise methods to turn on interactions between any pair of qubits (ions) of the chain by using these common modes of motion as a medium to propagate perturbations. Since Coulomb interactions are very strong between particles and are long range therefore the spin-spin interaction between qubits in a chain that are also strong and long range (chapter 5). This is essential in performing entangling gate operations between any subsets of qubits in a chain and is one of the prime motivators for developing traps that can hold and manipulate large linear chains of ions [43, 44].

In our experimental setup we hold a chain of five trapped $^{171}Yb^{+}$ions inside an ultra-high vacuum (UHV) chamber using a linear rf-Paul trap. In principal, it should be possible to trap and manipulate a chain that is longer than 5 qubits, however, there are challenges in scaling up the system using a macroscopic (hand assembled) trap. Most of these problems arise from the fact that a macroscopic trap does not provide enough controls to engineer perfect trapping potentials as a micro-trap can [13] and also have imperfections in fabrication that can cause heating of ions in the trap due to the fact that there might be uncompensated electrical noise

that gives rise to excess micromotion [45]. However, a macroscopic trap, as reported here, can provide the easy optical access necessary for high resolution control and measurement of individual qubits and also give deep harmonic trapping potentials that allow long trapping lifetimes. In this chapter we will discuss the construction of the ion trap and the vacuum chamber around it and the usual methods of cooling and trapping of ion crystals. We will also characterize properties of the trap such as heating rates, micromotion and drifts in the trapping strength; all of which are critical for the coherent manipulation of the qubits.

2.2 Ion trapping theory

Intuitively, since an ion carries a charge it should be possible using electric fields that confine it in all three dimensions in space. Implementing this is a bit more tricky since, in practice, it is not possible to have electric field lines point inward to a point without either having a charge at the point or having them leave away from that point in some direction thereby causing anti-trapping. This rule, also known as the Earnshaws theorem [46], can be encapsulated in the equation

$$\bar{\nabla} \cdot \bar{E} = 0 \tag{2.1}$$

for the electric field $barE$ in vacuum much like the kind of ultra high vacuum environment in which we intend to trap an ion.

In order to create trapping for charged particles, oscillating (rf) electric fields

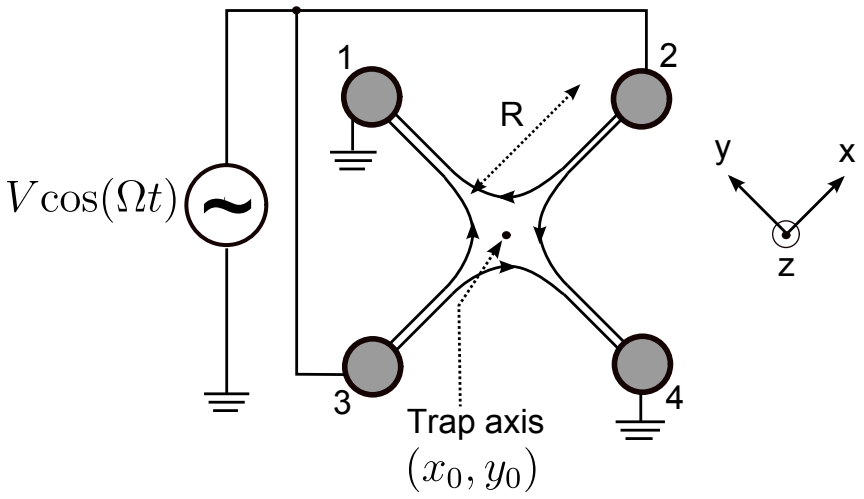

Figure 2.1: **RF quadrupole field for ion trapping.** The RF electric field is generated by four cylindrical rods running parallel to each other along the Z. Electrodes 2 and 3 are driven by a rf source at voltage V and frequency Ω whereas electrodes 1 and 4 are grounded. The figure shows the electric field projection in the X-Y plane. The quadrupole field has zero magnitude at (x_0, y_0). The pseudopotential confinement of an ion happens at this position with a harmonic confinement in the radial direction (XY plane). While trapping multiple ions, the ion chain is aligned along the trapping axis which is parallel to Z and passes through the quadrupole null point (x_0, y_0). Here R is the distance of any of the four trap electrodes from the quadrupole null. We assume that the cylindrical rods have very small diameter compared to R.

are used instead of static ones as proposed by Wolfgang Paul and Hans Dehmelt [41, 47] for which they shared the 1989 Nobel prize. The idea is illustrated in figure 2.1. A quadrupole electric field is created using four electrodes, two of which are driven by an oscillating rf voltage $V\cos(\Omega t)$ at the angular frequency Ω. As a result of this an oscillating potential is created near the trapping zone (x_0, y_0) whose spatial dependence is of the form,

$$\phi(x, y, t) = \frac{V}{2}\cos(\Omega t)\left(1 + \frac{x^2 - y^2}{R^2}\right) \tag{2.2}$$

where R is the distance of (x_0, y_0) from the electrodes and we have limited this treatment to be in the X-Y plane only. This is appropriate in the case of a truly linear ion trap with axial (Z) homogeneity since there will not be any potential gradient (or electric field) along the Z direction. Therefore, the idea behind this derivation is to derive the (radial) confining pseudopotential in the X-Y and hence prove that this scheme works for trapping ions. Here, we assume that the position x and y are measured along the X and the Y axes respectively from the quadropole null (x_0, y_0) which we define to be the origin $(x_0 = 0, y_0 = 0)$. Note that this expression of the potential satisfies the boundary condition at the electrode surfaces ($\phi = V\cos(\Omega t)$ for rf electrodes and $\phi = 0$ for ground electrodes).

In the next step lets write the electric field as a negative divergence of the potential,

$$\bar{E}(x, y, t) = -\bar{\nabla}\phi(x, y, t) = -\frac{V}{R^2}(x\hat{x} - y\hat{y})\cos(\Omega t) = \bar{E}_0(x, y)\cos(\Omega t). \tag{2.3}$$

Note that the electric field agrees with Earnshaws theorem (equation 2.1). In order to understand how this field causes a pseudopotential attracting an ion towards (x_0, y_0) through a harmonic pseudo potential we Taylor expand the electric field about this origin,

$$\bar{E_0}(x, y, t) = \bar{E_0}(x_0, y_0)\cos(\Omega t) + \frac{\partial E}{\partial x}\Big|_{x_0}(x(t) - x_0) + \frac{\partial E}{\partial y}\Big|_{y_0}(y(t) - y_0) \tag{2.4}$$

We can substitute $(x(t) - x_0)$ and $(y(t) - y_0)$ by integrating the force equation obtained from equation 2.3,

$$m\ddot{x} = e\bar{E}_x = -\frac{eV}{R^2}\cos(\Omega t)x \tag{2.5a}$$

$$m\ddot{y} = e\bar{E}_y = +\frac{eV}{R^2}\cos(\Omega t)y \tag{2.5b}$$

where $\ddot{x} = \partial^2 x/\partial t^2$, $\ddot{y} = \partial^2 y/\partial t^2$. $\bar{E}_x$ and $\bar{E}_y$ are the X and Y components of the electric field, respectively. We use the following initial conditions that $x(0) = x_0$ and $\dot{x}(0) = 0$ for integrating equation 2.5 where we assume that the variation of x is small such that the spatial variation of the field $\frac{eVx}{R^2}$ is negligible over the integrated time and can be considered independent of time on the right hand side of the equation. We can also apply this rule while calculating $(y(t) - y_0)$. We then obtain the following solutions,

$$x(t) - x_0 = \frac{eV}{m\Omega^2 R^2}\cos(\Omega t)x \tag{2.6a}$$

$$y(t) - y_0 = -\frac{eV}{m\Omega^2 R^2}\cos(\Omega t)y \tag{2.6b}$$

Now we can use equation 2.6 and equation 2.3 to rewrite equation 2.4. Additionally we can also multiply the electric field $\bar{E}(x, y, t)$ with the charge of the $^{171}Yb^{+}$ion e to obtain the force acting on the ion,

$$\bar{F}(x, y, t) = e\left[\bar{E}_0(x_0, y_0)\cos(\Omega t) - \frac{eV^2}{m\Omega^2 R^4}\cos^2(\Omega t)x\hat{x} - \frac{eV^2}{m\Omega^2 R^4}\cos^2(\Omega t)y\hat{y}\right] \quad (2.7)$$

In order to find the overall effect of the force on the ion over long time scales we can average it over time by integrating equation 2.7 over a time period that is much longer than the oscillation period of the rf-electric field $(1/\Omega)$. Here, the first term averages to 0 and we are left with an average force that acts towards the trap axis (x_0, y_0) and the strength is proportional to the displacement like a harmonic potential,

$$\bar{F}(x, y) = -\frac{e^2V^2}{2m\Omega^2 R^4}x\hat{x} - \frac{e^2V^2}{2m\Omega^2 R^4}y\hat{y} \quad (2.8)$$

Comparing this to the force equation of a harmonic potential $F(r) = -m\omega^2 r$, we obtain the oscillator frequency (or the secular frequency) of the harmonic trap as,

$$\omega = \frac{eV}{2^{1/2}m\Omega R^2} \quad (2.9)$$

2.3 Ion trapping in practice

In the experiment we trap ions using a four blade linear rf-Paul trap. The computer design is shown in figure 2.2. The four blades are analogous to the four cylindrical electrodes shown in figure 2.1 where the diagonally opposite DC elec-

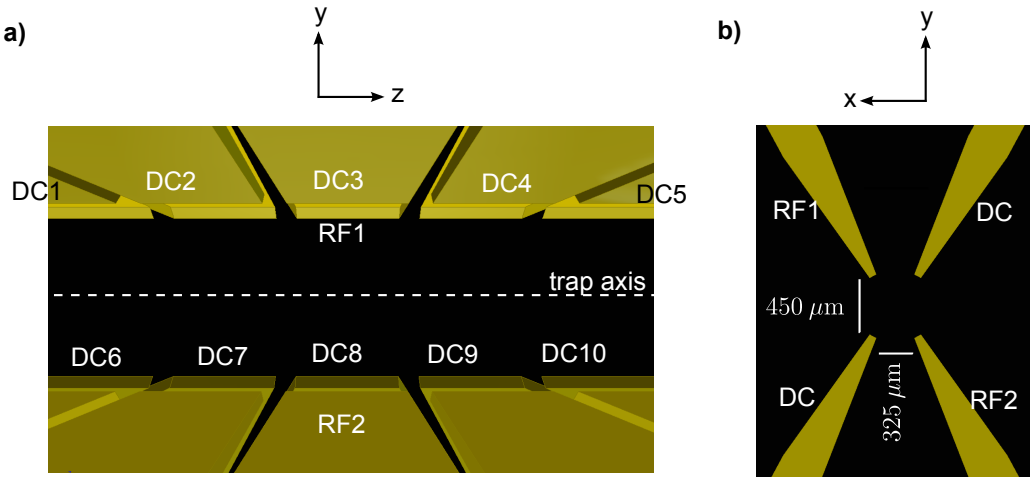

Figure 2.2: **Linear rf-Paul trap using segmented blades.** In practice we use four blades as the electrodes of the linear Paul trap. These blades are segmented along the trap axis Z. a) A view of the segmented blades of each of the four electrodes that form the ion trap. Each of the five segments of each DC electrode (front up and bottom back) are driven by independent DC voltage sources. By applying appropriate voltages in these segments confinement along the trap axis (along Z) can be achieved. b) XY cross section of the four blades that form the radial (XY) quadrupole potential. Opposite blades (RF1 and RF2) are driven at an rf voltage to create the oscillating quadrupole near the trap axis thereby radially confining ions in XY. The DC electrodes are rf-grounded using shunt capacitors (such that they behave as grounded electrodes 1 and 4 as shown figure 2.1). Although rf electrodes are mechanically segmented, they are electrically connected and carry the same applied voltage.

trodes behave as rf ground electrodes as they are connected to ground through a large capacitance ($\sim$ 1nF). Each blade is segmented along the trap axis (Z) direction such that different DC voltages may be applied to individual segments. Each segment is 250 μm in length along Z with a spacing of about 50 μm between adjacent segments. The distance of the trap axis from each electrode (R, see fig 2.1) is about 250 μm.

Both the RF electrodes are driven by the rf voltage $V\cos(\Omega t)$, where $\Omega = 2\pi \times 23.83\,\mathrm{MHz}$. This provides strong radial harmonic confinement in the X and Y direction with a secular frequency that approximately follows equation 2.9. In the experiment we measure the secular frequency to be $\omega_{x,y} \approx 2\pi \times 3\,\mathrm{MHz}$ which gives the approximate value of the rf amplitude $V \approx 400\,\mathrm{V}$.

Although the rf electrodes are segmented, they share a common voltage such that a uniform rf quadrupole potential can be maintained along the trap axis and with no projection of $\bar{E}$ along Z. This is necessary since trapped ions align themselves along the trap axis and they should all see a translationally invariant radial confinement: a property of the linear ion trap. However, in practice it is hard to achieve a truly linear trap unless the electrodes are translationally invariant as well. In our blade-trap the segmentation of the electrodes leaves room for imperfect fabrication which might lead to deviations from the trap behaving linearly.

The segmentation of the electrodes, particularly in the DC electrode, is necessary for confinement of the ions in the axial (Z) direction. The confinement is achieved by applying relatively high potentials at segments that are on either side of the trapping zone compared to the segments in the trapping zone. For example,

in order to trap in the middle zone DC3 and DC8 are kept at a negative potential while a positive potential is applied to electrodes DC2, DC7, DC4 and DC9. This creates a 'direct' harmonic confinement potential due to a DC quadrupole along the Z axis, which is usually an order of magnitude weaker ($\omega_z \approx 0.3$ MHz) than the radial (a bit more 'indirect') harmonic psedopotential confinement.

An ion trap needs to be characterized before use in trapped ion manipulation. One of the things to be checked is whether it behaves as a linear trap and if not whether it might be possible to tune the trapping voltages to create the most stable and close to linear behavior. We perform a series of measurements using a single trapped ion in order to answer these questions. However, in order to corroborate experimental observations (shown in section 2.6) with theory, we need to consider the most general treatment of the motion of an ion in the presence of static and oscillating potentials at the trapping zone of the blade trap [48, 49].

In the presence of the rf and the DC voltages of the segmented blade trap as discussed above the most general form of the potential near the trapping zone is quadrupole in nature and can be written down in the following form [10],

$$\phi_q = \kappa \frac{V}{R^2}\left(\alpha x^2 + \beta y^2 + \gamma z^2\right)\cos(\Omega t) + \kappa' \frac{U}{R^2}\left(\alpha' x^2 + \beta' y^2 + \gamma' z^2\right) + V_0 \cos(\Omega t) + U_0 \tag{2.10}$$

where (x, y, z) is the displacement from the quadrupole null position ($x_0 = 0, y_0 = 0, z_0 = 0$) where the electric field strength is 0. U and V are the applied DC and RF voltages, respectively with values U_0 and V_0 at the quadrupole null position. From Earnshaws theorem (equation 2.1), note that $\alpha + \beta + \gamma = 0 = \alpha' + \beta' + \gamma'$. The

constants κ and κ' are geometric factors that take into account the specific shape and orientation of the RF and DC electrodes of the ion trap, respectively and are fixed values for a given ion trap. In figure 2.1 the null position of the quadrupole is at (x_0, y_0) in the XY plane. In the case of the blade ion-trap the application of the DC voltages on the segments now creates a null position z_0 in the third dimension along the trap axis as well (fig 2.2).

Under ideal conditions $\gamma = 0$ and $\alpha+\beta = 0$. In equation 2.10, we have included a static quadrupole potential proportional to U that arises due to the application of unequal voltage values to the DC segments. For confinement along Z we need to set the voltage values such that $\gamma' > 0$, which as a result creates a static anti-trapping potential in the XY plane as $\alpha' + \beta' = -\gamma' < 0$. However, this DC anti-confinement is weak so that when it is added to the radial pseudopotential the net potential is still confining. Another effect of the DC quadrupole on that radial confinement is that it can break the degeneracy of the radial confinement where $\omega_x = \omega_y = \omega$ (eqn. 2.8 and 2.9) by setting different anti-trapping strengths along X and Y such that $\alpha' \neq \beta'$.

In order to explain the trap behavior, as observed experimentally, we are going to assume that the trap is not linear ($\alpha, \beta, \gamma \neq 0$). Under this condition, the trap in principle will successfully provide confinement in all three directions even if no DC quadrupole is applied ($\alpha', \beta', \gamma' = 0$). Given the geometry of the blade trap we expect γ to be very small thereby only providing a very weak pseudopotential confinement along Z. Hence we find it necessary to apply a DC quadrupole by setting voltages on the DC electrodes such that $\alpha' + \beta' = -\gamma' < 0$ in order to trap along

Z. We could also assume without loss of generality that there is a background static field given by the potential ϕ_b. We can write this background electric field potential as,

$$\phi_b = E_x x + E_y y + E_z z + \phi_0 \tag{2.11}$$

In the absence of this field the ion is most likely to be trapped at this quadrupole null position (x_0, y_0, z_0). However, in practice such stray uniform electric fields are present in the system which then shifts the quadrupole null to a different position [45]. Therefore the total force acting on the ion is now given from equation 2.10 and 2.11 as follows,

$$\bar{F}(x, y, z) = -e\bar{\nabla}(\phi_q + \phi_b) \tag{2.12}$$

We can use this to write down the equation of motion in all the three directions [45],

$$\ddot{u}_i + [a_i + 2q_i \cos(\Omega t + \theta)]\frac{\Omega^2}{4}u_i = \frac{eE_i}{m} \tag{2.13}$$

where u_i is the displacement of the ion from the rf null position along the i-th direction where $i = \{x, y, z\}$. The term a_i is a dimensionless quantity that represent the strength of the DC quadrupole along the i-th direction.

$$a_x = \alpha' \frac{8\kappa' eU}{mR^2\Omega^2},\ a_y = \beta' \frac{8\kappa' eU}{mR^2\Omega^2},\ a_z = \gamma' \frac{8\kappa' eU}{mR^2\Omega^2} \tag{2.14}$$

The term q_i is a dimensionless quantity that represent the strength of the rf quadrupole

along the i-th direction.

$$q_x = \alpha\frac{4\kappa eV}{mR^2\Omega^2},\ q_y = \beta\frac{4\kappa eV}{mR^2\Omega^2},\ q_z = \gamma\frac{4\kappa eV}{mR^2\Omega^2} \tag{2.15}$$

The equations of motion resembles Mathieu equations with a general solution suggested by the Floquet theorem [50]. The solution to the equations of motion, therefore, is of the following form,

$$u_i(t) = [A_i + B_i\cos(\omega_i t)]\left[1 + \frac{q_i}{2}\cos(\Omega t + \theta)\right] \tag{2.16}$$

Note that the displacement has a fast oscillating component at the rf drive frequency Ω. This is referred to as micromotion. The term A_i is the displacement of the ion from rf null due to the background electric field E_i and ω_i is the net secular frequency of the harmonic trap confinement given by the combination of both the static dc potential and the dynamic rf pseudopotential. When the ion is at equilibrium the force due to the harmonic trap is equal and opposite to the force from the background static field. This can be used to evaluate A_i to be,

$$A_i = \frac{eE_i}{m\omega_i^2} \tag{2.17}$$

where,

$$\omega_i = \frac{1}{2}\Omega\left(a_i + \frac{q_i^2}{2}\right)^{\frac{1}{2}} \tag{2.18}$$

We can clearly see that in the absence of a background field $A_i = 0$ the displacement

nearly follows a harmonic oscillation at a slow secular frequency with an amplitude B_i that determines the average energy of the harmonic oscillator. In order to make the trap more harmonic one should reduce the parameter q_i which also can be written as $q_i = 2\sqrt{2}\omega_i/\Omega$ in the limit where $|a_i| \ll q_i^2$ (which is true since the axial confinement is usually much weaker than radial confinement). In any trapped ion experiment it is usually preferable to have a high radial confinement where the secular frequency can be set to have a higher value by increasing the amplitude of the rf voltage V and decreasing Ω. However, in order to keep the micromotion low it is necessary to have the trap secular frequency much smaller than the rf drive frequency Ω.

Figure 2.3a shows a simulation of the ion motion for $A_i = 0$. It is clear that the ion follows a fast micromotion at the frequency Ω with an amplitude that is directly proportional to the displacement of the ion from the rf null. Therefore for trapped ions, such micromotion always exist on top of the slower oscillation from the harmonic pseudo potential confinement. In the presence of the background field, however, there is a finite displacement of the equilibrium ion position from the rf null. In such a scenario the ion motion is mostly dominated by the micromotion. This 'excess micromotion', as shown in figure 2.3b, can be eliminated by compensating for background electric fields by providing appropriate DC voltage bias to the segmented electrodes of the trap. In section 2.6 we will discuss the techniques of measuring such 'excess micromotion' and eliminating the stray background field in order to position the trapped ion at the real rf null of the blade trap.

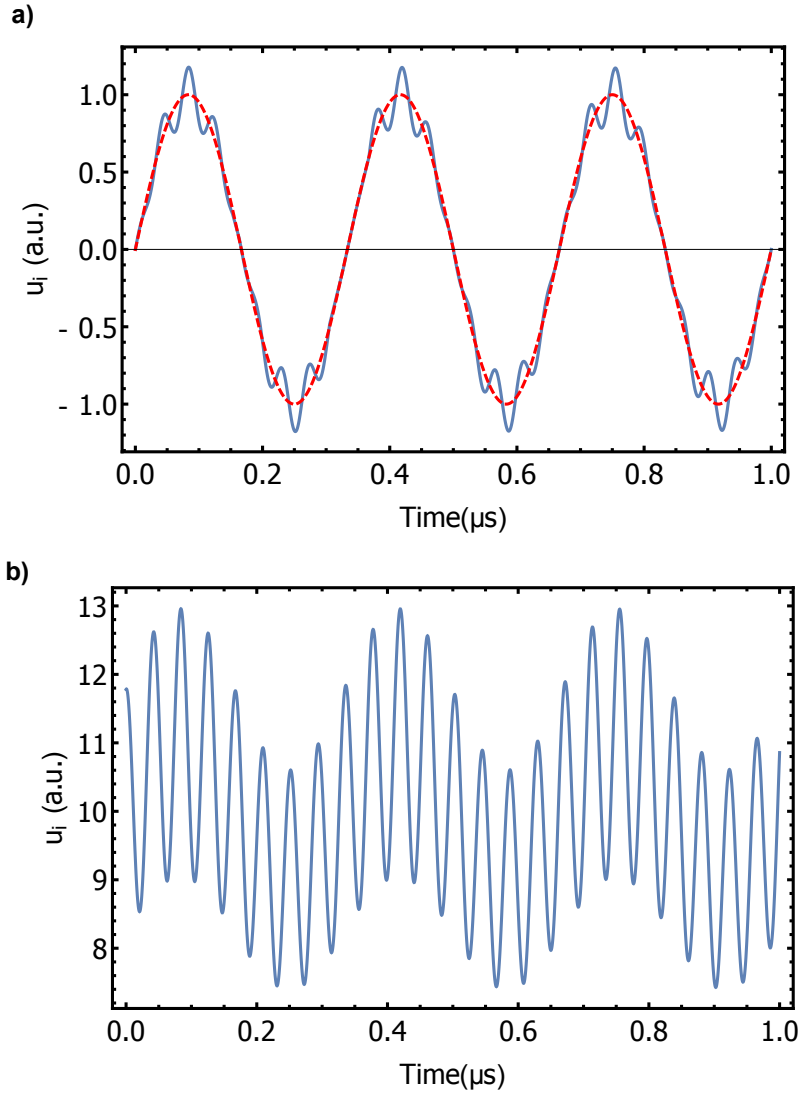

Figure 2.3: **Simulated radial motion of an ion in a linear trap** a) Normal micromotion on top of the secular oscillation is simulated for the radial secular trap frequency of $\omega_r = 2\pi \times 3.0$ MHz and rf drive frequency $\Omega = 2\pi \times 23.83$MHz. The solid blue line shows actual ion motion. The dashed red curve shows oscillation at the same secular frequency for a perfect harmonic confinement. b) Excess micromotion due to background electric field causing a displacement of the ion from rf null that is 10 times the secular oscillation amplitude ($A_i = 10 \times B_i$). This roughly magnifies the micromotion to 10 times that of the normal micromotion.

2.4 The $^{171}\mathrm{Yb}^{+}$qubit

There are many competing trapped ion systems that can be used for quantum information processing such as Ba^{+}, Ca^{+}, Mg^{+}, Hg^{+}, Sr^{+}, Cd^{+}, Yb^{+} etc. [51]. Each system has its own sets of advantages and disadvantages. $^{171}\mathrm{Yb}^{+}$, which is one of the heavier ions is our system of choice. It has a ground state hyperfine manifold, much like a hydrogen atom, that serves as a qubit. More specifically, the $(F = 0, m_F = 0)$ and the $(F = 1, m_F = 0)$ hyperfine levels of the $^2S_{1/2}$ ground state forms the qubit. The relevent level structure of $^{171}\mathrm{Yb}^{+}$is shown in figure 2.4.

There are several advantages of this system that can be deduced from the $^{171}\mathrm{Yb}^{+}$level structure [52]. The hyperfine qubit has an energy splitting of $\omega_{HF} = 2\pi \times 12.6428\,\mathrm{GHz}$ at zero applied magnetic field where the only way state $|1\rangle$ can decay to $|0\rangle$ is through a magnetic dipole transition. At this energy splitting this spontaneous emission rate is virtually zero [53,54]. In the lab frame the $^{171}\mathrm{Yb}^{+}$qubit evolves as

$$|\psi\rangle = \alpha|0\rangle + e^{i(\omega_{HF}+\delta)t}\beta|1\rangle \tag{2.19}$$

where amplitudes α and β are real. Since qubit splitting energy is in the microwave regime, microwave synthesizers and Raman laser beams that coherently manipulate the qubit can all be synchronized by a single microwave synthesizer which is locked to a pristine frequency standard [1]. The hyperfine qubit is also quite stable against dephasing noise that can be caused by fluctuations in the hyperfine splitting. For

[1] Stanford Research Systems FS725 Rubidium Frequency Standard

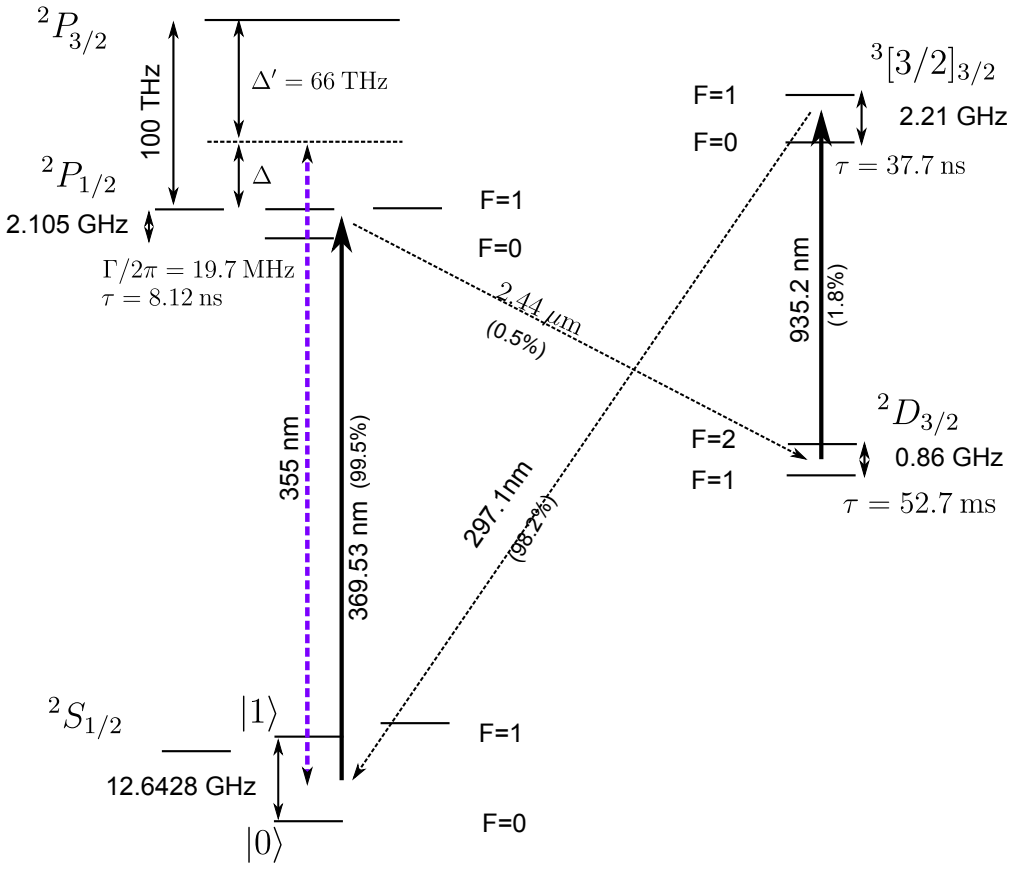

Figure 2.4: **The ^{171}Yb$^+$energy level diagram.** The partial level structure of ^{171}Yb$^+$shows the transitions that are pertinent to the experiment. The solid arrows shows lasers that are used in inducing spontaneous emission in ^{171}Yb$^+$as is necessary for dissipative processes such as doppler cooling of the ion, state preparation and detection of the qubit. The blue (dotted) arrow shows an off-resonant 355 nm mode locked laser that is used to perform coherent manipulations on the qubit using Raman transitions.

example the variation of the qubit splitting δ near zero magnetic field only varies in a quadratic way with the applied field as $\delta = 2\pi \times 310.8B^2$ where the shift is in Hertz and the magnetic field is in Gauss. The smallness of δ makes the qubit not only long lived but also fairly stable with a coherence time usually of the order of a few seconds which can be extended to several thousands of seconds with shielding from magnetic field fluctuations. This is why the qubit levels are often referred to as "clock" states [55]. In our setup we achieve coherence times of the order of 1 second and is typically limited by the coherence of the driving laser field rather than the qubit itself. This coherence time is $\sim 10^3$ times longer than the duration of typical experiments.

The ground $^2S_{1/2}$ and the excited $^2P_{1/2}$ state can be coupled with a UV laser at 369.5 nm that is resonant with this electric dipole transition. Even though there is a small branching ratio to the $^3D_{3/2}$ state this transition is nearly cyclic and allows one to perform dissipative processes like doppler cooling, qubit state preparation and measurement quite efficiently (fig. 2.4) [53, 56]. Another added benefit to this is that the optical addressing techniques (if necessary) for the aforementioned processes is naturally more resolved at this shorter (UV) wavelength. This can help in high fidelity state preparation or measurement of individual qubit within a chain of multiple ions.

2.4.1 Loading $^{171}Yb^{+}$ions

The first step towards trapping $^{171}Yb^{+}$ions is photo-ionization where one of the outer electrons of a neutral atom is stripped using a two photon process to create singly ionized Ytterbium. This involves two transitions, the first being the excitation of the electron from the $^1S_0$ to the $^1P_1$ level in neutral Ytterbium. This is accomplished by applying a continuous-wave (c.w.) laser light at 398.5 nm. Once the electron is excited to the $^1P_1$ level it requires a second photon that has enough energy to excite it to the continuum thereby forming the $^{171}Yb^{+}$ion. Since the second photon is required to have a wavelength less than 394 nm, we can either use c.w. light at 369.5 nm that is already used for the $^2S_{1/2}$ to $^2P_{1/2}$ transition or pulsed laser light at 355 nm (used for Raman transitions).

During the loading of ions an oven containing small fragments of enriched ^{171}Yb (about 95% isotope purity) within a stainless steel tube is resistively heated by passing a current (2.4 A) such that an atomic beam of neutral Ytterbium is created and directed towards the ion trap. About 600μW of 398.5nm light (ionization beam) and 500 μW of 369 nm (or $>$ 1 mW of 355 nm) light are focused to a beam waist of 50 μm and overlapped at the trapping zone during loading. The temperature of the atomic beam is above room temperature and the velocity distribution of neutral Ytterbium is peaked at several hundred meters per second. This gives rise to Doppler shifts of the frequency of the ionizing laser beams as seen by the moving neutral atom. Therefore the frequency of the ionization beam is shifted by $\pm$500 MHz range depending upon the angle of the beam k-vector with the atomic beam.

Additionally, the radial confinement of the trap is also lowered by a factor of 10 in order to trap ions that are at the lower velocity rage of the velocity distribution. This allows the slow moving ions to be cooled easily such that they can form a Coulomb crystal. In the experiment, it is the combination of both reduced trapping rf amplitude and the appropriate shift of the frequency of the ionization beam that optimizes the trapping rate.

2.4.2 Doppler cooling

Once a neutral Ytterbium atom is ionized within the trapping zone it 'sees' the trapping potential. Initially the ion is at a much higher temperature due to its initial velocity and needs to be rapidly cooled down nearer to the ground state of the harmonic well. This is achieved by doppler cooling of the ion using a laser that is detuned from an optical transition between two electronic levels of the atom [53]. The scattering rate in this case is given by,

$$\Gamma_s = \frac{s\frac{\Gamma}{2}}{1 + s + 4\frac{\Delta^2}{\Gamma^2}} \tag{2.20}$$

where the saturation parameter $s = I/I_s$ is the ratio of the beam intensity to the saturation intensity. The saturation intensity $I_s = \pi hc/3\lambda^3\tau$ depends on the wavelength λ of light resonant with the transition and the lifetime of the excited state τ. The parameter Γ is the natural radiative linewidth of the decay from the excited state to the ground state and Δ is the detuning of the excitation laser frequency from resonance.

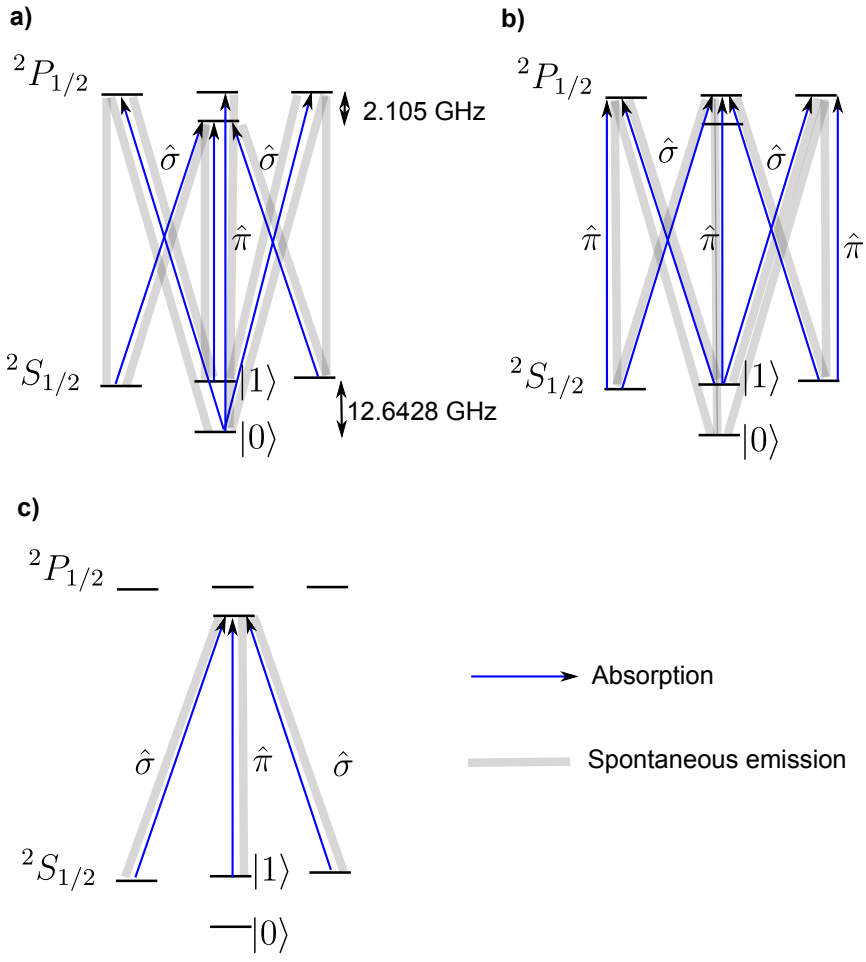

Figure 2.5: $^{171}\mathrm{Yb}^{+}$**Doppler cooling, optical pumping and state detection schemes.** The solid arrows indicate applied frequency and polarization components in the 369.5 nm beams and gray lines show the possible routes for spontaneous emission to the ground state manifold. a) Doppler cooling frequencies and polarization. b) Optical pumping frequencies and polarization required for qubit state preparation in $|0\rangle$, c) Frequency and polarization components for qubit state detection .

In $^{171}Yb^{+}$the $^2S_{1/2}$ and $^2P_{1/2}$ levels form a nearly cyclic two-level system connected by optical transitions, where there is a high probability for the ion to be in these two levels during repeated scattering events of excitation and spontaneous emission (fig. 2.4). The only minor variation from the ideal two-level system is the hyperfine splitting of both levels. This might require additional frequencies to be applied during doppler cooling in order to prevent the population from getting trapped (pumped) to some auxiliary state and prevent any further scattering. Figure 2.5a shows that the light resonant with the $^2S_{1/2}, F = 1$ to $^2P_{1/2}, F = 0$ transition also requires a second frequency that is higher by 14.7 GHz to excite population that might be trapped in the $|0\rangle$ state. This additional frequency of the 369.5 nm cooling beam is obtained from a second-order sideband generated by an electro-optic modulator (EOM) [2] that is resonant at 7GHz and driven with $\sim$ 1W of rf power. In figure 2.4 we also note that there is a 0.5% chance of the $^2P_{1/2}$ state to fall into the $^3D_{3/2}$ manifold. In order to depopulate from this state an IR laser at 935.2 nm is used to excite from the $^3D_{3/2}$ to the bracket state $^3[3/2]_{3/2}$. Due to the nuclear spin $I = 1/2$ of $^{171}Yb^{+}$both these levels also have a hyperfine structures which then requires an additional frequency on the 935.2 nm beam that is higher by 3.07 GHz. This component is given by the first-order sideband created by modulating the beam using a fiber EOM [3] that is resonant at 3.07 GHz and driven by $\sim$ 10 mW of rf power. The polarization of the beams are also critical as seen in figure 2.5a and needs to have both linear along $\hat{\pi}$ and circular $\hat{\sigma}$ components. This can be achieved by adjusting

[2]EOM from New Focus, model 4857 with resonance at 7.37 GHz
[3]EOSpace

the angle between the polarization vector of the beams with the quantization axis for the ion, that is defined by a magnetic field $B = 5.2\,\mathrm{G}$ applied along the X direction of the trap (as shown in fig. 2.2). This magnetic field also removes the degeneracy between the $m_F = \pm 1$ and $m_F = 0$ states of the ground state $^2S_{1/2}, F = 1$ manifold by increasing the Zeeman splitting between the levels. This prevents the ion from getting pumped into a coherent dark state that, depending on the cooling beam polarization, is such a coherent superposition of the Zeeman states that it can have zero net coupling to the excited $^2P_{1/2}, F = 0$ level [57]. The applied magnetic field helps to destabilize this dark state by evolving the phase the constituent Zeeman states at different rates. Nonetheless, due to a presence of this approximate dark state there is a reduction in the overall scattering rate compared to a pure two-level system as suggested in equation 2.20. Additionally the rate also suffers from the branching to and the subsequent depumping from the $^3D_{3/2}$ manifold. This however, might be substantial if either the polarization or the frequency of the 935.2 nm laser is not optimized to efficiently depopulate this state. This is due to the fact that the $^3D_{3/2}$ state has a life time of 52.7 ms which being much longer that the $^2P_{1/2}$ life time of 8.12 ns can temporarily trap the ion in this dark state (see fig. 2.4) [58].

Once the system of lasers are optimally tuned to make an $^{171}\mathrm{Yb}^+$ion to continuously scatter light like a two-level system, we can perform doppler cooling by red-detuning the 369.5 nm cooling laser from resonance (decreasing the laser frequency) [10,59]. The scattering is mostly from the transition between the $\{^2S_{1/2}, F = 1\}$ and $\{^2P_{1/2}, F = 0\}$ levels. At this point we can write the detuning in equation 2.20 as $\Delta = \delta - \bar{k}.\bar{v}$ where $\delta < 0$ is the detuning of the cooling laser from resonance and $\bar{k}.\bar{v}$

gives the first order doppler shift of the ion with velocity $\bar{v}$ scattering a cooling beam photon with k-vector $\bar{k}$. Therefore, while traveling towards the incident photon the ion has a higher rate of scattering a photon since $\bar{k}.\bar{v} < 0$. This process leads to a higher likelihood of absorption of a low energy photon by the atom thereby reducing its momentum by $\hbar k$. In order to find the overall change in the momentum of the ion the recoil momentum from the spontaneous emission of a higher energy photon should also be taken into account. Fortunately the effect from the latter process averages to zero over several scattering events, since the spontaneous emission is isotropic and both $\hat{\pi}$ and $\hat{\sigma}$ photons are emitted with equal likelihood. Therefore, the net effect of this scattering process is the loss of kinetic energy of the ion along the $\bar{k}$ direction of the doppler cooling beam which leads to the eventual cooling of the ion.

During the loading of $^{171}Yb^{+}$ions in the trap the initial kinetic energy of an ion is relatively higher and needs to be reduced by doppler cooling using a beam that is far detuned from resonance (by $\delta = -2\pi \times 300\,\mathrm{MHz}$) compared to the natural line width of the transition $\Gamma = 2\pi \times 19.7$ MHz, such that higher scattering rates are achieved (Δ is small) even for large doppler shifts seen by a fast moving ion. This beam is the same as the one used in the photo-ionization process discussed earlier. Furthermore, the atomic transition is power broadened by increasing the intensity beyond saturation $s \gg 1$. Once the ion has scattered enough photons from this beam and lost sufficient energy, it can now be more efficiently cooled with a weaker cooling beam that is detuned by $\delta = -\Gamma/2 \approx 2\pi \times 10\mathrm{MHz}$ from resonance. With the power set close to saturation the ion is now efficiently cooled down to close to the

motional ground state. We apply $\sim 10\,\mu$W of power to this beam with its $\sim 50\,\mu$m beam waist at the trapping zone.

2.4.3 Qubit state initialization

At the beginning of every experiment the qubit needs to be initialized to a pure state. We choose the state $|0\rangle$ where the qubit is prepared through optical pumping. In any experimental sequence this qubit initialization follows doppler cooling which resulta in the population being spread over all the ground state hyperfine manifold. In order to remove population from the $\{^2S_{1/2}, F = 1\}$ manifold a laser is tuned to resonance on the $\{^2S_{1/2}, F = 1\}$ and $\{^2P_{1/2}, F = 1\}$ transition . This is achieved by modulating the original 369.5nm beam with an EOM[4] that is driven by ~ 0.5W of rf power at 2.1 GHz. As shown in figure 2.5b this leads to spontaneous emission with a high branching ratio to the state $|0\rangle$. Since the laser frequencies are detuned enough not to excite from this state there is near a 100% probability of all the population to accumulate in this state after only a few scattering events. In the experiment the optical pumping takes less than $5\,\mu$s duration to transfer $> 99.7\%$ of the population to the state $|0\rangle$.

2.4.4 Qubit state detection

The state detection of the $^{171}Yb^+$qubit is performed at the end of an experiment and therefore is an important step in determining the fidelity of gate operations preceding it. In other words, the detection fidelity is required to be high in order to

[4]EOM from New Focus, model 4431 with resonance at 2.105 GHz

make a good estimate of the process fidelity of gate operations on the qubits in the chain. The detection scheme of the $^{171}Yb^{+}$qubit is based on state dependent fluorescence. Basically, if the qubit is in the state $|1\rangle$ (bright state) it scatters photons when illuminated by the 'detection' laser beam at 369.5 nm. This is accomplished by tuning the laser to be resonant with the transition from $\{^2S_{1/2}, F = 1, m_F = 0\}$ to $\{^2P_{1/2}, F = 0, m_F = 0\}$. As shown in figure 2.5c this also requires both $\hat{\sigma}$ and $\hat{\pi}$ polarizations due to the eventual participation of all the Zeeman levels of the $\{^2S_{1/2}, F = 1$ ground state manifold. Although the Zeeman splitting between the levels of the $\{^2S_{1/2}, F = 1\}$ manifold is about 7 MHz it is well within the line width of the transition and any population in these states gets excited thereby forming a cyclic process where many photons are scattered. For the state $|0\rangle$ (dark state), however, the frequency of the laser is off resonant by about 14.7 GHz for the dipole allowed transitions to the $\{^2P_{1/2}, F = 1\}$ manifold and therefore does not result in any photon scatter.

In the experiment an imaging objective with a numerical aperture (NA) of 0.37 collects fluorescence from the ions during state detection and images them on single channels of a multi-channel photo-multiplier tube (PMT). We will discuss the optical and electrical design of the imaging system in more detail in chapter 4. The detection beam intensity is maintained close to saturation and is actively stabilized using a digital PID-lock (noise eater) while monitoring the beam intensity using a fast photo diode and feeding back by regulating the power of the rf signal driving the acousto-optic modulator (AOM) that is used to switch the detection beam. We use an FPGA with on board ADC and DAC to readout the intensity from the

photo diode, calculate the PID response and output the analog voltage to a voltage variable attenuator (VVA) that regulated the power of the driving rf signal.

Although the detection scheme has excellent fidelity as transitions from $|0\rangle$are far off resonance and the nearly cyclic nature of the scatter, it is still not a 100% due a several reasons. These are

- Branching from the excited $\{^2P_{1/2}, F = 0\}$ state to the long lived $\{^3D_{3/2}, F = 1\}$ state as shown in figure 2.4 requires the 935.2 nm de-pump laser to be optimally tuned to depopulate efficiently from this manifold and bring it back to the ground state $\{^2S_{1/2}, F = 1\}$ within the detection time. In the experiment we observe that the polarization of the de-pump laser is critical and requires readjusting on a regular basis in order to maximize fluorescence scatter from a 'bright' ion.

- It is important to have a high count of collected photons in a short duration during detection. This is due to the fact that an off resonant excitation to the $\{^2P_{1/2}, F = 1\}$ manifold might inadvertently pump the atom to state $|0\rangle$ on emitting a photon. Hence, even if the qubit originally collapsed to state $|1\rangle$ at the onset of the detection process it could be detected as a dark state $|0\rangle$. The off-resonant excitation that gives rise to this error is only 2.1 GHz (or 100 natural line widths of the transition) away from resonance and has a higher probability of happening for a longer detection duration or due to excess intensity in the detection beam that can cause power broadening of this transition.

- Background scatter of the detection beam from ion-trap features near the trapping zone can give false photon 'clicks' at the PMT and must be removed by using high NA imaging objective along with spatial filters in the optical system in order to selectively collect photons from a very small (real) space containing the trapped ions. This affects the detection fidelity of the dark state $|0\rangle$ since ideally, no photons should be scattered in this case.

During the design of the trap and imaging optics the second and third points can be addressed by making appropriate provisions in the design. For example, the trap assembly must allow short working distance between the ion and the imaging objective that collects fluorescence from the ion. Given that in most traps the objective is placed outside the vacuum chamber this can be achieved by the use of re-entrant windows and an optically open trap such that the Numerical aperture (NA) of light collection can be maximized. This is useful not only in reducing the detection duration but also in achieving shallow depth of focus of the objective that acts like a spatial filter along the optical axis thereby dramatically reducing the collection of background scatter. An optically open trap with sufficient clearence between the detection beam and the trap electrodes also reduces the background scatter.

In the experiment the detection beam is turned on for a duration of 150 μs during which the ion scatters light based on the collapsed state. The probability distribution of detecting a certain number of photons for a typical experimental run is shown in figure 2.6 for both the dark $|0\rangle$ and the bright $|1\rangle$ state. For state $|1\rangle$ on

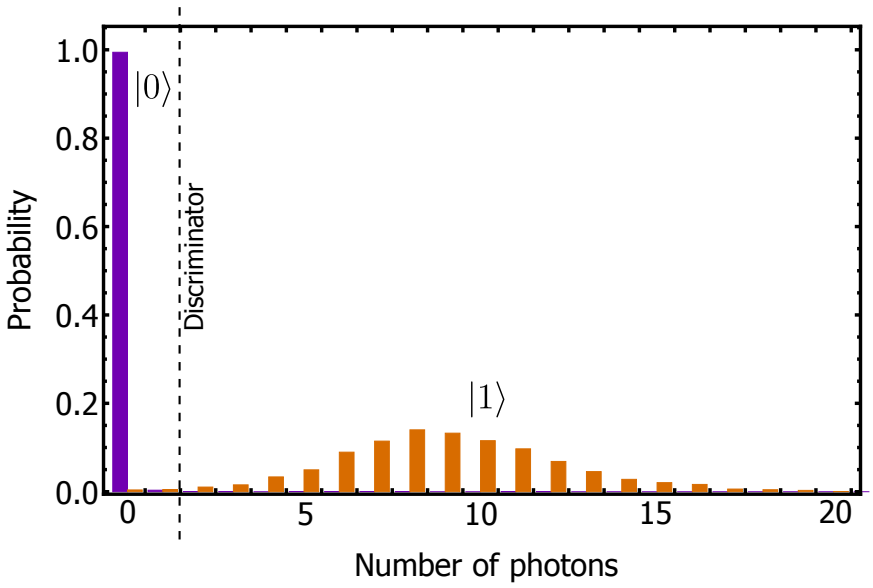

Figure 2.6: **Distribution of collected fluorescence from a single ion.** The probability distribution of collecting a certain number of scattered photons per experimental shot is plotted for the bright $|1\rangle$ and the dark $|0\rangle$ state over a $150\,\mu$s state detection. Each histogram nearly follows a Poisson distribution with an expectation value close to 0 for the dark state and 9 for the bright state. By discriminating events based on > 1 collected photons during the detection cycle, single shot state detection of the qubit can be performed with reasonably high fidelity.

an average 9 photons are scattered while for state $|0\rangle$ no photons are detected. In order to measure the qubit state one can employ a discriminator technique which sets a threshold on the number of detected photons such that if > 1 photons are detected for an experimental run the measured state is assigned to be $|1\rangle$ and $|0\rangle$ otherwise. This single shot detection is critical for several quantum algorithms and protocols where measurement-based quantum gates are performed. In these processes single shot measurements are performed within a sequence of gate operations and therefore need to be of high fidelity such that errors do not accumulate while performing repeated measurements along the sequence. In our system we achieve a fidelity of 99.66(3)% for the preparation and measurement of state $|0\rangle$ and 99.04(5)% for state $|1\rangle$.

In principle, the discrimination technique works for single as well as multiqubit detection by using multiple channels of a PMT array The details will be discussed in chapter 4. We will see that besides the usual error ($< 1\%$) in the single qubit detection, for two or more qubits additional errors arise due to signal cross-talk between neighboring channels of a multi-channel PMT as well as higher rates of background scatter as we bin together more channels of the PMT array for state detection. In order to circumvent these errors a second method can be adopted based on the histogram of scattered photons. Usually this distribution is Poissonian which centers around a value ≈ 0 or 10 or 20 photons for two qubit states in $|00\rangle, (|01\rangle \text{or} |10\rangle)$ and $|11\rangle$, respectively. A state detection in this case can be performed by fitting the measured histogram to known basis histograms. We verified this procedure by detecting two qubit states initialized in $|00\rangle$ after performing an XX-gate entangling

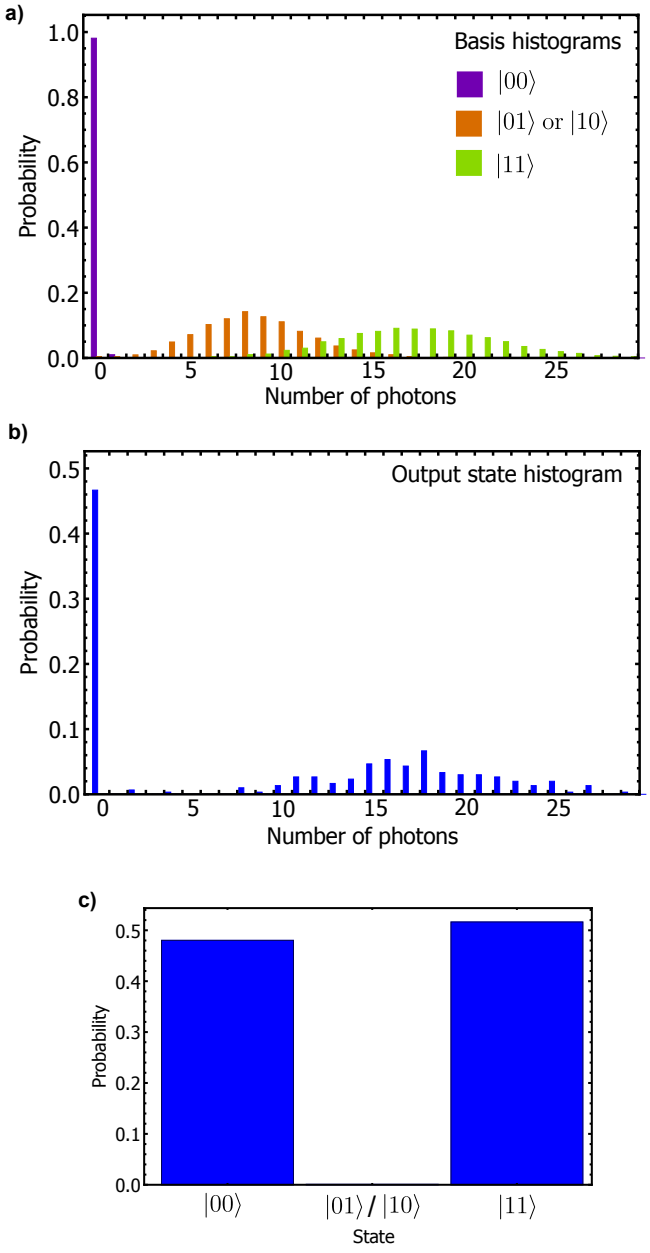

Figure 2.7: **Two-qubit state detection using histogram fitting.** Measurement of a two-qubit state using histogram fitting. a) Basis histograms are obtained by preparing two qubits in one of the four basis states and subsequent measurement of fluorescence. b) Output state histogram is obtained after performing an XX-gate on two qubits initially in $|00\rangle$ and measuring the detection fluorescence. The expected output state is $\frac{1}{\sqrt{2}}(|00\rangle + e^{i\phi}|11\rangle)$. c) The population in the four basis states is obtained from fitting the measured histogram to a linear combination of the basis histograms.

operation [60, 61]. As shown in figure 2.7a, a set of basis histograms are obtained for each of the four basis states, which can be prepared with high fidelity (using microwave Rabi rotations). The basis histograms can be distinguished from one another as they are centered around different values of the average photon number. These basis states can then be used for a two-qubit state detection. Figure 2.7b shows one such example where a histogram obtained from measuring a two-qubit entangled state $\frac{1}{\sqrt{2}}(|00\rangle + e^{i\phi}|11\rangle)$. This histogram can then be fitted to a liner combination of basis distributions,

$$H(n) = P_0 B_0(n) + P_1 B_1(n) + P_2 B_2(n), \tag{2.21}$$

where $H(n)$ is the measured histogram obtained from several experimental repetitions with n as the number of photons detected for single runs of the experiment. The $B_i(n)$ are the basis histograms for i bright ions (in state $|1\rangle$). The fitted parameters P_i correspond to the diagonal elements of the two qubit density matrix ρ as $P_0 = \rho_{00,00}$, $P_1 = \rho_{10,10} + \rho_{01,01}$ and $P_2 = \rho_{11,11}$. Figure 2.7 is one such example illustrating the fitting process where, 2.7c shows the measured population obtained from fitting the output histogram in Fig.2.7b to the basis histograms in Fig.2.7a.

Histogram fitting is a very useful technique that can be used for the calibration of an XX-gate where the variation of populations in the $|00\rangle$ and $|11\rangle$ state is observed as a function of the intensity of the laser that drives the gate. A low population for single bright states (or low value of P_1) suggests a high gate fidelity. In principle this technique provides a better, than might be expected, estimate of

the gate fidelity as the basis histograms already include the state preparation and measurement (SPAM) errors. For example, non zero photon counts due to background scatter or imperfect optical pumping to the dark state $|00\rangle$ is reflected in the basis histograms as photon counts are sampled over thousands of experimental repetitions. This also applies to histograms of single or double bright ions that contain events with zero photon scatter due to a small but non-zero probability of off-resonant pumping to the dark state and due to the fact that the Poisson distribution also gives a small but non-zero probability of events where ≤ 1 photon is detected . Therefore the final measurement of state populations exclude the SPAM errors. The down side to this technique, however, is that the basis histograms can only be used for fitting as long as the system is sufficiently stable to maintain the same rate of fluorescence scatter from the ions. A number of factors such as drifts in laser power/polarization and optical alignment of the imaging system can lead to deviations. A practical approach to tackling this problem is characterizing time scales for systematic drifts and recalibrating the basis histograms accordingly.

2.5 Ion trap assembly and vacuum system

Trapped ion experiments require extreme isolation of the trapped ion from collisions with background gas molecules. Such collisions, when elastic, can cause the heating of the ion thereby reducing its lifetime in the trap. In case of $^{171}Yb^{+}$, collisions can also cause transition to the $^{2}F_{7/2}$ manifold, which has a long lifetime for spontaneous decay to the ground state and therefore requires an additional laser to

depopulate. In addition chemical reactions occur due to inelastic collisions between the ion and a background Hydrogen molecule forming the hydride ion YbH^+ [62]. This is our most likely way of ion loss even at our ultra high vacuum (UHV) conditions. A low pumping rate and residual leakage of Hydrogen through the chamber walls and fused silica windows is to blame. It is therefore desirable to produce a vacuum environment, which is as good as one can reach with efficient pumping for Hydrogen.

2.5.1 Chamber assembly

The vacuum chamber constructed for the experiment is shown in figure 2.8. It is designed to achieve ultra-high vacuum (UHV) pressures of $\sim 10^{-11}$Torr. Achieving such low pressure is non trivial and requires special attention during the assembly of the vacuum chamber. All components (see table 2.5.1) are chosen such that they are UHV compatible, which implies that the rate of outgassing and leakage is very low. We choose ConFlat (CF) flanges for all stainless steel components, which allows all-metal seals with joints formed by stainless steel knife edges pressing into soft copper gaskets permanently deforming it to form a high quality vacuum seal. All windows and electrical feedthroughs have UHV compatible metal to glass seals. It is also necessary to carry out the assembly in a clean room environment to prevent contamination of the vacuum parts from dust particles. Special care is taken to remove and prevent any bodily oils, skin contact, hair etc. from the parts. Each stainless steel component is cleaned in an ultrasound bath of Acetone followed by

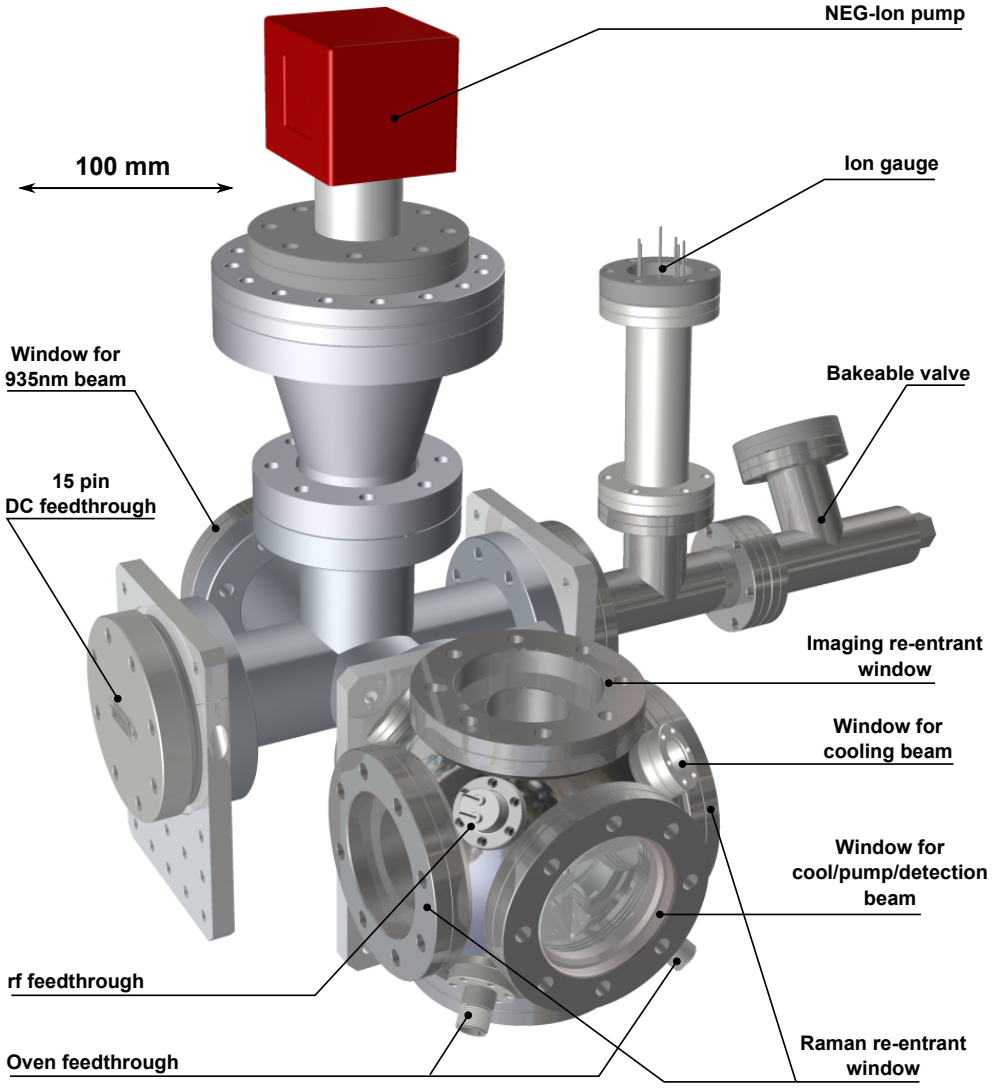

Figure 2.8: **Vaccum system for trapping ions.** A computer design of the vacuum system that contains the ion trap. All components have standard ConFlat (CF) flange connections deigned to operate at ultra-high vacuum (UHV). Once assembled the chamber is baked at 200° C, it is pumped externally through the bakeable valve. The pressure is monitored using an ion gauge. Under normal operation the bakeable valve is closed. Pumping using an internal NEG-Ion pump keeps the chamber pressure at 10^{-11} Torr. The chamber is fitted with fused-silica windows for optical addressing of ions using laser beams. All electrical feedthroughs are UHV compatible and allow electrical connections to the trap as well as the Ytterbium ovens.

wiping with Methanol using cleanroom compatible wipes.

As shown in figure 2.8 the ion trap is hosted inside a 'spherical-cube' chamber with several 4.5" and 1.33" diameter CF flanges. There are two custom designed 40 mm re-entrant windows with a clear aperture of 38 mm that are installed for the delivery of Raman beams [5]. A third 48 mm re-entrant window [6] with a clear aperture of 32 mm is installed to collect ion fluorescence along the vertical (Y) direction using an imaging objective with 0.37 NA. The main chamber hosting the ion-trap is connected to an NEG-Ion pump (internal to the chamber) via a 5-way cross that also has a 15-pin d-sub feedthrough for DC voltage delivery to the trap. The feedthrough is connected to the DC electrodes through 28AWG Kapton coated cables that are about 30 cm in length. The rf feedthrough with two solid copper wires on the other hand is mounted on the main chamber such that relatively short 16AWG Kapton coated cables (of about 7 cm length) can carry the rf voltage to the trap. Each segment of the blades have gold ribbons that are wire bonded to them. The DC ribbons are additionally rf grounded by bonding in-vacuum capacitors to them as shown in 2.9. The cables from the feedthroughs are then connected to the blades by spot welding both the ribbon and the cables to a common constantan foil.

2.5.2 Yb oven

In order to produce an atomic beam of Ytterbium, an oven is constructed using a stainless steel tube that contains a few shards of enriched ^{171}Yb (1 mm in size).

[5] Thickness: 3.5mm. Material: UV-Fused silica (Spectrosil). BBAR coated: 350-700nm. Surface irregularity: $\lambda/8$.

[6] Thickness: 3.0mm. Material: UV-Fused silica (Spectrosil). BBAR coated: 350-700nm. Surface irregularity: $\lambda/8$.

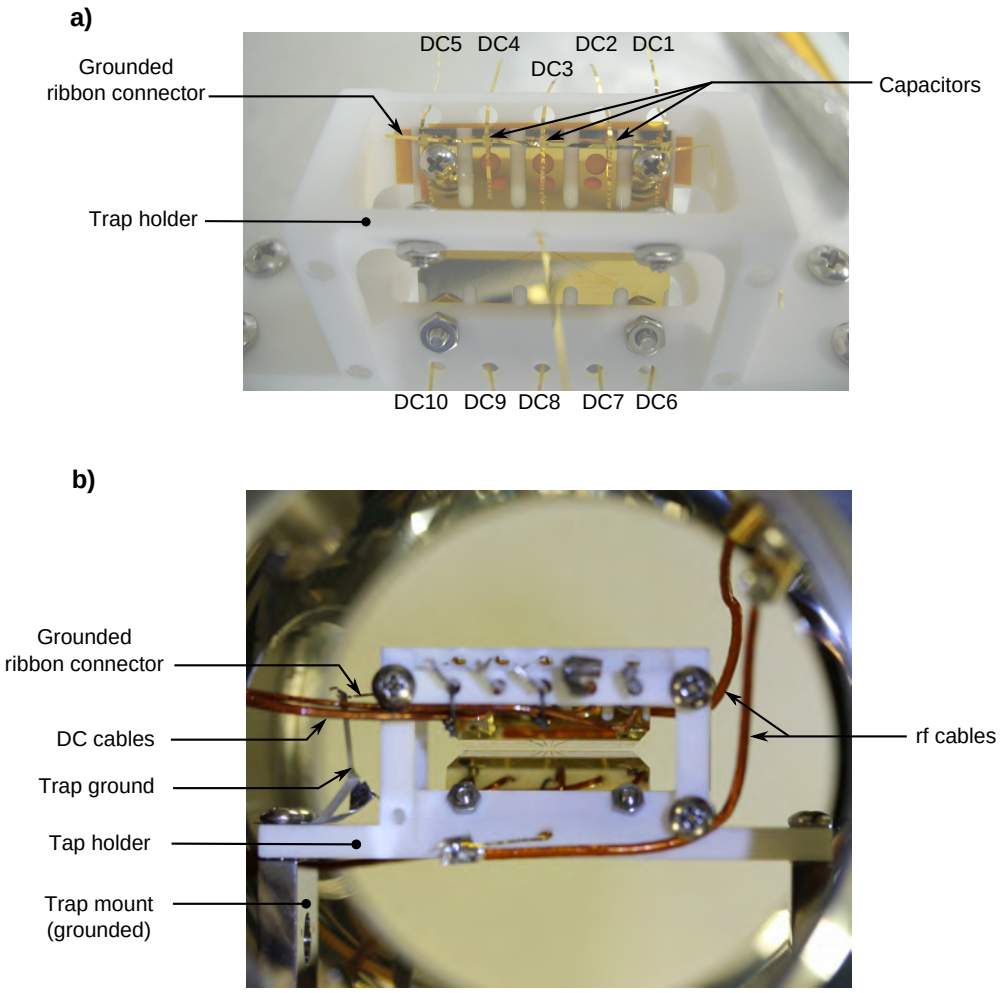

Figure 2.9: **The assembly of the blade trap.** a) Blades are mounted on a Macor trap holder using stainless steel screws. Each blade is pressed against a thin kapton film which prevents it from sliding during alignment. Each DC segment is grounded to the chamber body through a capacitor using gold ribbons. b) The trap holder is mounted on stainless steel adapters that secure it to the vacuum chamber. The adapters also form the ground connection of the trap to the chamber. The figure also shows the routing of the kapton coated RF and DC cables near the trap. .

Part	Quantity	Vendor	Part number
Spherical Cube-4.5”	1	Kimball Physics	MCF450-SphCube-E6A8
Groove grabbers	2	Kimball physics	MCF450-GrvGrb-C02
Trap mount (SS)	2	Maryland machining	N/A
Trap mount adapter (SS)	1	Maryland machining	N/A
Ion trap DC blades	2	Laser micromachining	N/A
Ion trap rf blades	2	Laser micromachining	N/A
Blade holder (Macor)	1	Maryland machining	N/A
In vacuum capacitors	10	ATC	116UL821M100TT
5-Way cross 4.5”	1	MDC	406004
Conical reducer -6” to 4.5”	1	Kurt J. Lesker	CRN600X450
6” to 4.5” reducer flange	1	Kurt J. Lesker	RF600X450
4.5” to 2.75” reducer flange	1	Kurt J. Lesker	RF450X275
Mounting brackets	2	Kimball Physics	MCF450-ExtBrkt-LS
Mounting flange	3	Kimball Physics	MCF450-MtgFlg-E2
Tee-standard 2.75”	1	Kurt J. Lesker	T-0275
Full nipple 2.75”	1	Kurt J. Lesker	FN-0275S
UHV Ion gauge	1	MDC	432004
Bakeable all metal angle valve	1	Kurt J. Lesker	VZCR40R
Zero length viewport	2	Kurt J. Lesker	VPZL-450Q
1.33” Window	2	Kurt J. Lesker	VPZL-133Q
Recessed viewport	1	UKAEA-CCFE	N/A
Reentrant Raman window	2	UKAEA-CCFE	N/A
Reentrant Imaging window	1	UKAEA-CCFE	N/A
rf power feedthrough	1	MDC	9422010
15 D-sub DC feedthrough	1	Accu-Glass	100210
Yb oven feedthrough	2	Accu-Glass	10600
1.33” Blank	2	Kurt J. Lesker	F0133X000N
NEG-Ion pump	1	SAES getters	NEXTorr D-300-5
NEG-ribbon	2’ long	SAES getters	4F0280D
Isotropically enriched ^{171}Yb	few mg	ORNL	N/A

Table 2.1: List of important parts for the vacuum chamber construction. Standard accessories such as copper gaskets, bolts, cables, vented screws etc. are excluded.

During loading of ions a spray of atomic Yb is created when this tube is resistively heated by passing a current. The temperature reached depends on the current and the duration it is turned on. If either of these are too high or long it causes rapid evaporation of Yb thereby forming a spray dense enough to coat surfaces in its way (such as the ion trap electrodes or vacuum windows). In order to prevent this, each oven is tested beforehand by putting them inside a bell-jar under vacuum (10^{-7}Torr) and calibrating the current value for which it forms a mild spot of Yb on the glass surface when it is run for 10 minutes. This sets an upper limit to the current that is allowed to run through the oven. We prepared two ovens with current thresholds of 3.4 A and 4.9 A, respectively. Each oven is mounted such that the atomic beam coming out is directed towards the trapping zone. The ovens are constructed using of a 10 mm long stainless tube. On one side of this tube a Tantalum wire (0.5 mm diameter) is inserted and the tube is crimped to form an electrical contact. The other end of the tube is left open with another Tantalum wire spot welded to it. Each of the Tantalum wires are then connected to copper wires that connect the oven to the feedthrough pins. The choice of these dissimilar materials is made in order to maintain the stainless steel tube at a higher temperature than the copper wires. Both Tantalum and steel have a much lower thermal conductance (and higher electrical resistivity) than copper.

2.5.3 Blade trap assembly

The blade trap as illustrated in figure 2.2 consists of four blades. Each blade is a 50 μm thick Alumina plate that is segmented along the tapered edge with a spacing of 50 μm between segments. In the trapping zone each segment is 250 μm long except the end segments which are ≈ 10 mm long. The blades are coated with gold such that they behave as trap electrodes. The coating on the DC blades is such that each segment is electrically isolated from the other. The rf blades on the other hand have all segments electrically connected. In order to assemble the ion trap each of the blades is mounted on a specially designed holder that is made of Macor as it has low thermal coefficient of expansion. The design of the holder is based on the desired orientation and spacing between the trap electrodes. During assembly, the blades are first mounted on the holder and then adjusted under a microscope such that the segments from all four blades are aligned with each other along the Z-axis where they run parallel to each other and the desired spacing is achieved between the blades. Each blade is then secured to the holder using stainless steel screws. The holder also has provisions for routing gold ribbons that are wire bonded to the blade segments. This prevents them from coming in contact with the electrically grounded re-entrant windows.

As shown in figure 2.9 each DC ribbon is bonded to a in-vacuum 800 pF capacitor. The other terminal of each capacitor is bonded to a common gold ribbon that is electrically grounded to the chamber. Since, Macor has ceramic like qualities it is good for machining but at the same time is quite brittle. Therefore, additional

strain relief rods are used to secure the DC cables (5 cables per blade) which are then spot welded to the DC ribbons. The holder is then mounted on a stainless steel adapter that mechanically attaches it to the rest of the chamber via a pair of groove grabbers at the bottom flange of the spherical-cube chamber.

2.5.4 Chamber bake-out

Once the chamber is assembled it is baked at a high temperature to remove any water from the surface. This also expels Hydrogen that is in the bulk of the stainless steel components. In principle a higher temperature is preferable during the bake as it reduces the duration of the process. However, there is a practical limit to this temperature due to the fragile glass to metal seals of vacuum windows and feedthroughs. Considering all the constraints, we bake the vacuum chamber at 200°C over several days. Since the internal ion pump is not used during most of the bake-out the magnets attached to it [7] are removed to protect them from thermal demagnetization. The bake-out is periodically monitored.

In the beginning the chamber is pumped using a roughing pump and a turbo-molecular pump through a bakeable valve. After initial pumping over a few hours a pressure of 10^{-7} Torr is reached. At this point the Yb ovens are degassed by running current through them (below threshold value). The internal ion gauge is also degassed several times before running it continuously for pressure monitoring. The chamber is then gradually heated at a rate of 0.5°C/min using an industrial oven with a closed loop temperature stabilization. When the chamber temperature

[7] maximum allowed temperature for the ion pump magnets is 150°C

reaches 200°C the NEG element (of the NEG-Ion pump) is 'activated' by heating it to 550°C using a power supply [8] that monitors and controls the NEG temperature. During this process the adsorbed molecules on the the surface of the NEG is dissolved into the bulk thereby renewing the surface. The process also expels a substantial amount of Hydrogen from the bulk of the NEG. The Hydrogen partial pressure then rises and needs to be pumped out efficiently. Figure 2.10 shows the spike in pressure during activation. At other times the NEG element is held at a temperature of 300°C which is slightly higher than that of the chamber (200°C). This 'conditioning' mode of the NEG is maintained in order to prevent pumping of Hydrogen by the NEG thereby saturating it. After activation the chamber is baked for several days under pumping by an external ion pump (500 litres/sec).

Although the NEG is held at 300°C during the bake-out it still pumps by absorbing Hydrogen into its bulk. This is evident from the observation of increased chamber pressure due to the release of this absorbed Hydrogen when the NEG temperature in increased during the bake-out. Due to this residual pumping of Hydrogen it is possible to saturate the NEG[9] during a prolonged bake-out. In this case we need to recover the pumping speed of the NEG which is why it is activated several times during the bake out, each time for a duration of $\sim$ 2 hours. During activation both the TMP and the external ion-pump is used for pumping.

When the bake-out is over, the chamber is cooled down slowly in order to prevent stress from building up due to thermal gradients in the glass to metal

[8] NIOPS-04-Power supply

[9] pumping speed of the NEG falls by 10% when saturated

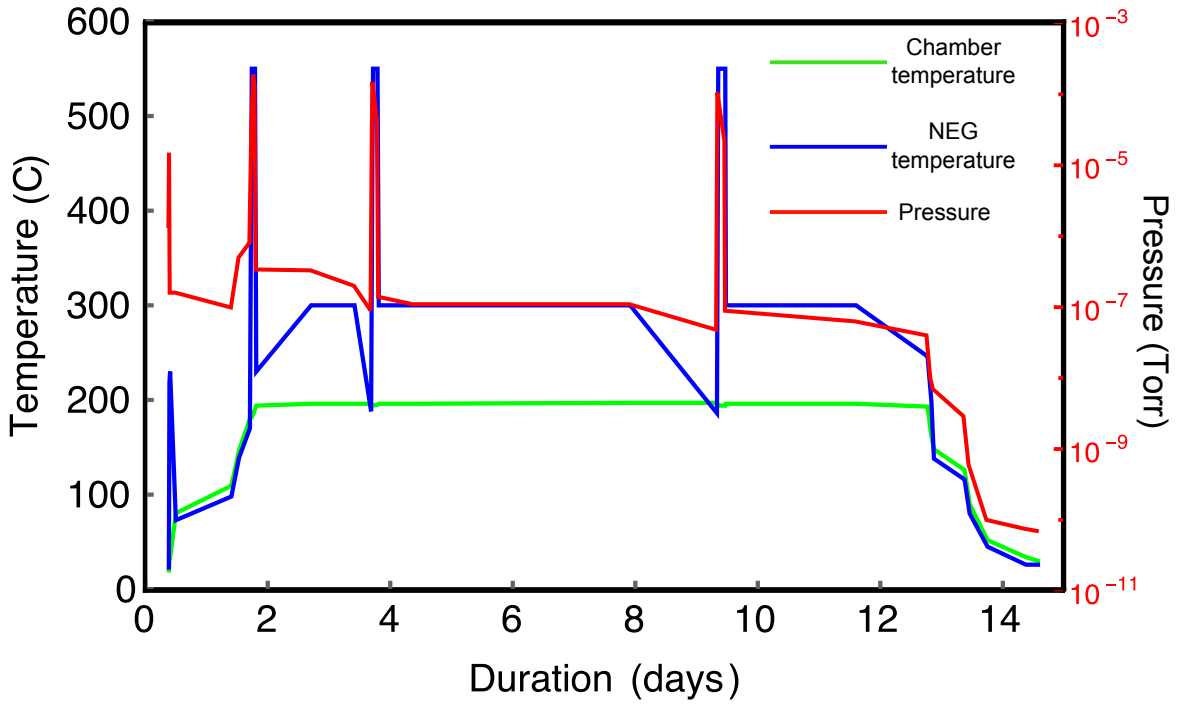

Figure 2.10: **Temperature and pressure plot vs. chamber bake-out time.** The vacuum chamber is baked at ~ 200°C for several days while externally pumping using a turbo molecular pump (TMP) and an ion pump (500 l/sec). The non-evaporable getter (NEG) is constantly maintained at 300°C during the bakeout (conditioning) with occasional activation at 550°C when the surface of the getter is renewed and Hydrogen is expelled from the bulk of the getter and pumped using the external ion-pump and TMP. Here the NEG is activated three times during the bake-out. The pressure displayed in the plot is measured at the ion-gauge inside the vacuum chamber.

seals. At 150°C the magnets for the internal ion pump is mounted and the pump is started. At this point the chamber is pumped using the NEG-ion pump alone as the bakeable valve is closed (hand tightened). At room temperature the chamber reaches a pressure of 7×10^{-11} Torr as read by the ion gauge. However, the pressure at the ion gauge is possibly higher than that at the ion trap. This is due to local heating of the nipple (which is at 60°C) that surrounds the ion gauge and the poor vacuum conductance to the NEG-ion pump. Once the system reaches thermal stability the bakeable valve is closed by applying the appropriate (operating) torque and a pinch-off valve is installed that helps to maintain a pressure of $\sim 10^{-6}$ Torr on the non-UHV side of the valve.

2.6 Micromotion compensation

While trapping an ion in a linear Paul trap, it is important to move it to the rf quadrupole null position (x_0, y_0, z_0) where it does not have excess micromotion. We can apply combinations of DC voltage values that drive individual segments of the DC blades and a DC offset on the RF blades to move the ion in the three orthogonal directions independently and obtain the rf-null position. In order to accomplish this knowledge of the excess micromotion is necessary. According to equation 2.16 excess micromotion in direction i is proportional to the displacement of the ion from the null position in that direction. In the case of trapping using the blade trap we find that it is not an ideal linear rf-Paul trap. This is confirmed by detecting micromotion along the axial Z direction of the trap, which implies $\gamma \neq 0$.

We can therefore apply equation 2.16 in the Z direction to obtain,

$$u_z(t) = [A_z + B_z\cos(\omega_z t)]\left[1 + \frac{q_z}{2}\cos(\Omega t + \theta)\right] \tag{2.22}$$

where $u_z(t)$ is the displacement of the ion along Z and A_z is the displacement of the ion from axial rf null position along Z. In order to set $A_z = 0$ we need to probe $u_z(t)$ and minimize its micromotion. One way to probe $u_z(t)$ is to align a cooling laser beam along the Z direction and scatter light as given by the rate equation 2.20 [45]. Since the detuning of the beam is velocity dependent $\Delta = \delta - \bar{k}.(\partial\bar{u}_z(t)/\partial t)$ this gives rise to a perioding modulation of the scatter rate at frequency Ω. The phase and amplitude of this modulation relative to the trap rf signal is plotted in figure 2.11. Here a single trapped ion is displaced along the Z direction to vary A_z. As the ion position moves through z_0 the displacement A_z changes sign (from positive to negative) which leads to a change in phase (by π) of the correlation signal as well. Near the null position the amplitude of the oscillations also goes to a minima (zero). By tracking the patterns of this micromotion signal we find the null position z_0 to be in the trapping zone nearest to DC segments 4 and 9. The same exercise can be repeated in the X and Y directions to find (x_0, y_0). However, since the quadrupole potential $\{q_x, q_y\}$ is of much higher strength in these directions the micromotion signal is almost an order of magnitude more sensitive to displacements $A_{x/y}$. This implies that it is more important to position the ion chain closer to the radial rf-null (x_0, y_0) in order to have an overall lower value of the micromotion. The axial positioning on the other hand is more forgiving where the axial micromotion

increases at a relatively smaller rate with the ion displacement from axial rf-null position z_0. We take advantage of this fact while trapping a chin of five ions where there is residual axial micromotion of the ions since they spatially separated along the Z direction.

2.7 Secular frequency stabilization

The secular trap frequency in the radial direction is important for performing certain quantum operations where the qubit spin is coupled to the motional mode of the ion defined by the radial or transverse harmonic confinement. One such example is the two qubit entangling $XX-$gate which will be discussed in chapter 5. Therefore, it is essential to stabilize the radial secular frequency in order to achieve a high fidelity of such gate operations. According to equation 2.9 or 2.18, this can be achieved if we stabilize the amplitude of the applied RF voltage V while keeping the rf drive frequency Ω constant [63]. Figure 2.12 shows a schematic of the analog electrical circuit used for this purpose. We use a capacitive divider to pick-off a fraction of the rf voltage $V\cos(\Omega t)$ at the rf feedthough followed by a rectifier in order to obtain a DC signal. This can then be stabilized against a reference voltage V_{ref} as explained in the figure.

The necessity of the secular frequency stabilization stems from the fact that the RF signal that drives the trap has drifts in the amplitude. This can happen due to several reasons. Like any RF circuit, this one has a reactive impedance that depend on the physical dimensions of the distributed circuit which can change

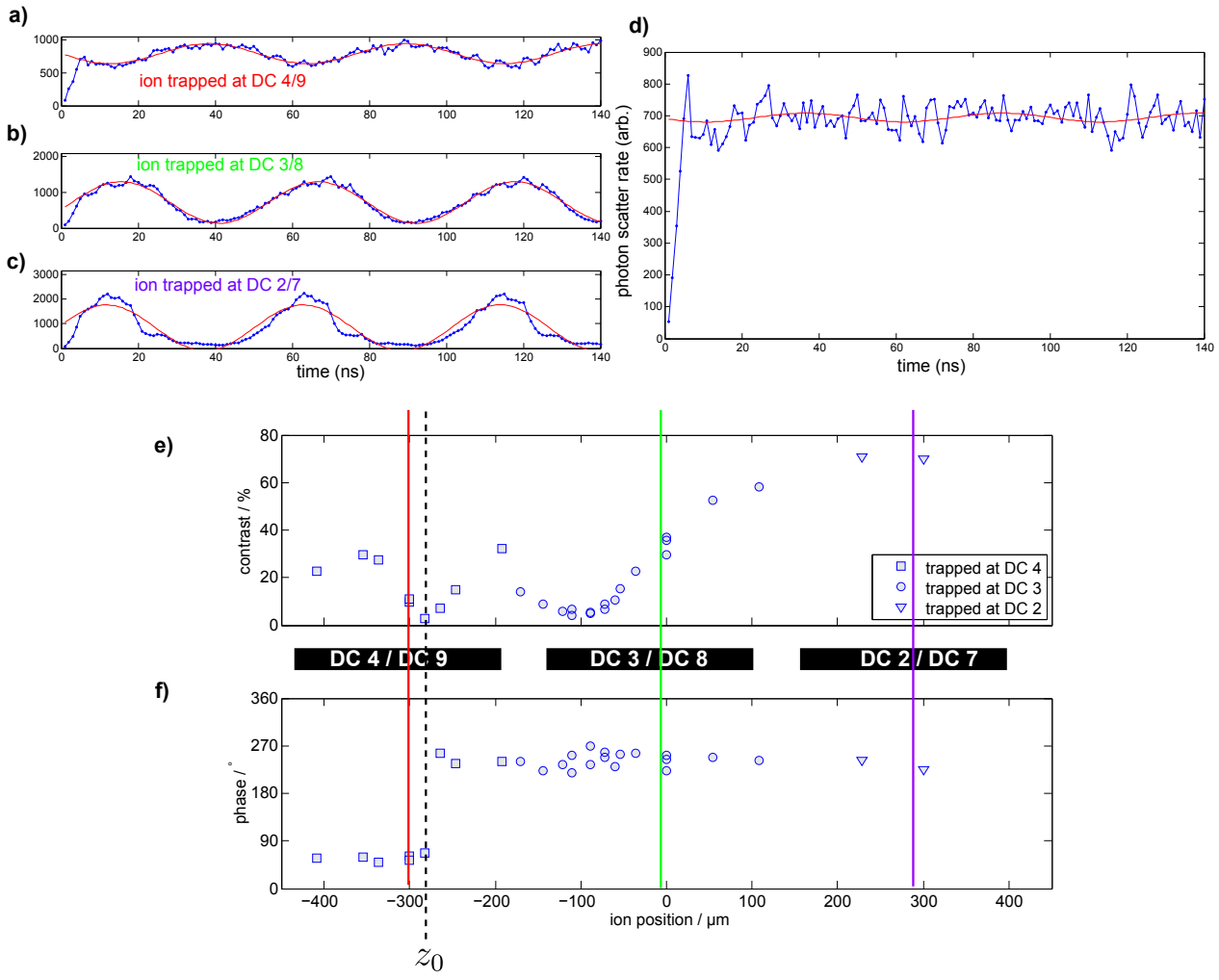

Figure 2.11: **Measurement and compensation of micromotion.** a), b), c), d) Photon scattering rate from a doppler cooling beam along Z. The plots correspond to four ion positions indicated by the (colored) vertical lines in panel (e) and (f). Since the scatter rate is correlated with micromotion the time scan is triggered by the trap rf signal. The amplitude of the oscillating scatter rate shows the magnitude of micromotion and the phase reversal is indication of the ion crossing the rf null position. e) As the ion is moved along the Z-direction of the trap the amplitude of the micromotion signal is measured. The minimum amplitude corresponds to the axial pseudopotential null position z_0. f) The measured phase of the micromotion signal which flips by π across z_0. Panel (d) shows the micromotion signal from the ion at the axial rf-null position.

due to slow temperature changes thereby changing the impedance. One example is the quarter wave resonator [64–66] that is used to amplify and deliver a higher RF voltage to the trap. Other components in the circuit such as rf power amplifiers can have drifts in their gain due to thermal effects as well. It is therefore, necessary to probe the value of the rf voltage at the trap and stabilize it by comparing it to a stable reference.

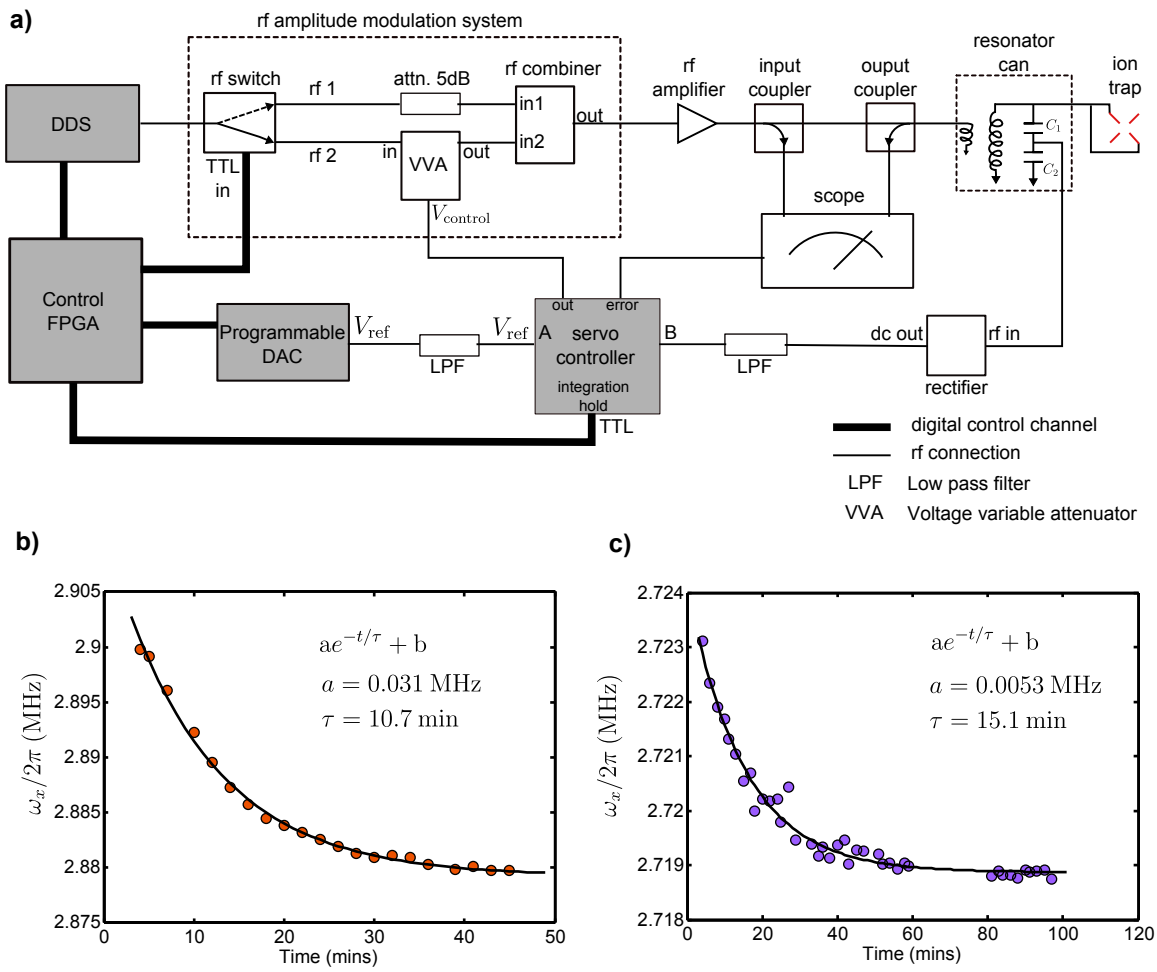

Figure 2.12: **Stabilization of transverse trap frequency.** a) Circuit schematic for amplitude stabilization of trap RF voltage V. A DDS generates the RF signal which is sent to a resonator that amplifies the signal and delivers it to the trap rf-blades. A capacitive divider 'picks-off' a small fraction ($C_2/C_1 = 100$) of this voltage at the rf-feedthrough which is rectified to give a DC signal. The signal is compared to a programmable reference voltage V_{ref} and locked using a PID (servo controller) that sends a feed back to a voltage variable attenuator (VVA). By programming a value of V_{ref} the trap rf potential is stabilized. By programming linear ramps in time the trap confinement can be lowered for ~ 1 sec as is required during the loading of $^{171}\text{Yb}^+$. b) The drift in the secular transverse trap frequency ω_x in the X direction over time without the amplitude lock. The transient drift occurs when the rf is turned off (set to very low value) for 5 mins and then set back to the normal (high) value. The data points show secular frequency measured using a single ion and Raman sideband spectroscopy (section 3.5). c) Same as (b) but with the amplitude lock. The drift is suppressed by a factor of ≈ 6 but still remains due to thermal effects that might be affecting the capacitive divider or the rectifier itself. The long term stability of the trap frequency, however, is within 0.3 kHz. In order to avoid these transient effects the trap rf amplitude is lowered for a short duration of 1 sec during loading which helps in maintaining a thermal equilibrium in spite of large ramps in the rf power.

Chapter 3: Coherent Control of Qubits

Quantum gates are nothing but coherent rotations of qubits. Common techniques of such qubit manipulation involve perturbing the qubit two-level system with electromagnetic radiation that is resonant with the energy splitting of the qubit levels. In $^{171}Yb^{+}$the hyperfine qubit has an energy splitting of 12642.821 MHz and we can implement coherent rotations of the qubit by performing Rabi flopping by directly applying resonant microwave radiation. In practice, the microwave horn that generates such a field is usually situated outside the vacuum chamber several centimeters from the trap. Due to the spread of this microwave field over the entire trap, the microwave Rabi rotations do not provide spatial selectivity of individual qubits in a chain of multiple trapped $^{171}Yb^{+}$ions. Microwaves also do not provide the spin-motion coupling necessary for implementing two-qubit entangling XX-gates due to their relatively long wavelength (2.4 cm at 12.6 GHz). For these reasons the alternative method of stimulated Raman transition is preferred where a pair of laser beams from a 355 nm mode-locked pulsed laser is used to perform coherent rotations of the qubit. By tightly focusing the laser beam on single ions in a chain, individual optical addressing can also be achieved. In this chapter we will discuss the theory behind Raman transitions and provide experimental details of implementing and

characterizing this technique of qubit manipulation using optical fields.

3.1 Raman transitions

A stimulated Raman transition can be described as a two photon process where a two level system is coupled via a third auxiliary state thereby forming a $\Lambda-$ system as shown in figure 3.1 [56]. For this derivation, we can assume that the electric fields are generated from continuous wave (c.w.) laser beams and can be written as

$$\overrightarrow{E_0} = \overrightarrow{\varepsilon_0}\cos(\overrightarrow{k_0}\cdot\overrightarrow{x} - \omega_0^L t + \phi_0), \tag{3.1a}$$

$$\overrightarrow{E_1} = \overrightarrow{\varepsilon_1}\cos(\overrightarrow{k_1}\cdot\overrightarrow{x} - \omega_1^L t + \phi_1), \tag{3.1b}$$

where $\overrightarrow{\varepsilon_0}$ and $\overrightarrow{\varepsilon_1}$ are the field vectors of the two Raman beams, respectively. Also the beams have a wave vectors $\overrightarrow{k_0}$ and $\overrightarrow{k_1}$, respectively that sets spatially-dependent phase offsets. The ion position $\overrightarrow{x}$ is classical and fixed for this treatment. Additional phase offsets ϕ_0 and ϕ_1 can be added to each field using acousto-optic modulators (AOMs). These phases can be varied by simply changing the the RF signal that drives the AOM responsible for switching each of the Raman beams during an experimental sequence.

The first step toward analyzing a Raman process is to recognize the unperturbed Hamiltonian of the system in the absence of any external fields. We can

write this as

$$H_0 = \omega_0|0\rangle\langle 0| + \omega_1|1\rangle\langle 1| + \omega_e|e\rangle\langle e|, \tag{3.2}$$

where the qubit levels $|0\rangle$ and $|1\rangle$ have energies $\hbar\omega_0$ and $\hbar\omega_1$, respectively and the auxiliary sate $|e\rangle$ has energy $\hbar\omega_e$. In this expression and henceforth we set $\hbar = 1$ for simplicity.

We can write down the time varying wave function of this three level system in the following manner

$$\psi(t) = c_0(t)|0\rangle + c_1(t)|1\rangle + c_e(t)|e\rangle \tag{3.3}$$

where the complex amplitudes $c_j(t)$ of the basis states $|j\rangle$ are time varying and $j = \{0, 1, e\}$. Integrating the Schrödinger equation $i\frac{\partial\psi(t)}{\partial t} = H_0\psi(t)$ for the unperturbed Hamiltonian H_0 we obtain

$$c_j = c_j(0)e^{-i\omega_j t} \tag{3.4}$$

where $c_j(0)$ are the respective amplitudes of the basis states $|j\rangle$ at time $t = 0$.

When a perturbation is applied using a pair of Raman beams, the laser fields as expressed in equation 3.1 interact with the atomic dipole. This gives rise to the following interaction Hamiltonian

$$H_I = -\overrightarrow{d} \cdot \overrightarrow{E(t)} \tag{3.5a}$$

$$= -[\bar{d}_{0e}|0\rangle\langle e| + \bar{d}_{1e}|1\rangle\langle e| + \bar{d}_{e0}|e\rangle\langle 0| + \bar{d}_{e1}|e\rangle\langle 1|] \cdot [\overrightarrow{E_0} + \overrightarrow{E_1}]. \tag{3.5b}$$

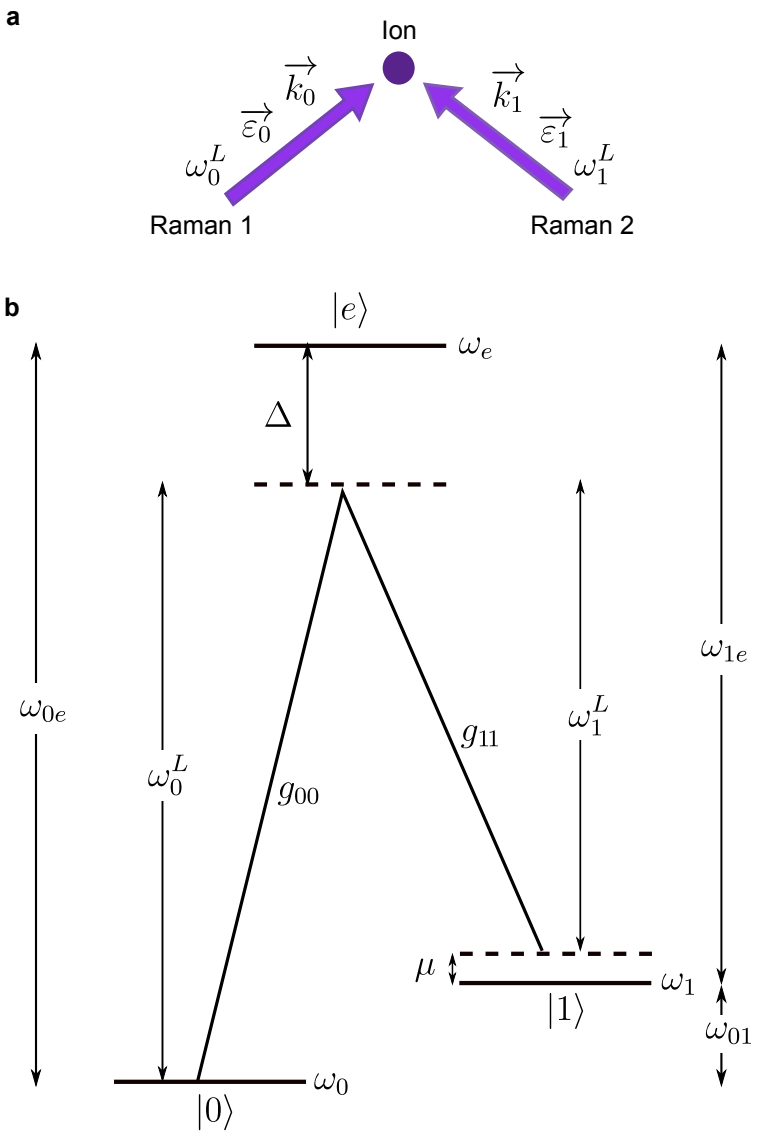

Figure 3.1: **Stimulated Raman transition using c.w. laser beams.** a) Raman beam setup.A pair of Raman laser beams with wave vector $\bar{k}$, electric field vector $\bar{\varepsilon}$ and frequency ω^L. b) Stimulated Raman transition as a two-photon process. Two laser beams with frequencies ω_0^L and ω_1^L couple the qubit levels $|0\rangle$ and $|1\rangle$ to the auxiliary state $|e\rangle$, respectively. The couplings are given by single-photon Rabi frequencies g_{00} and g_{11} for the two Raman beams detuned by Δ from excited state $|e\rangle$ and $\Delta \gg \{g_{00}, g_{11}\}$. Coherent Rabi flopping between state $|0\rangle$ and $|1\rangle$ happens at a Rabi frequency $\Omega = g_{00}g_{11}^*/2\Delta$ when the beat-note between the Raman beams is tuned close the qubit splitting ω_{01}. Here the detuning of the beat-note μ is set according to the requirements of a quantum gate.

Here, $\overrightarrow{d}$ is the electric dipole moment operator that gives the dipole moment vector of the atom and has the following matrix elements:

$$\bar{d}_{0e} = \langle 0|\overrightarrow{d}|e\rangle, \tag{3.6a}$$

$$\bar{d}_{1e} = \langle 1|\overrightarrow{d}|e\rangle, \tag{3.6b}$$

$$\bar{d}_{e0} = \bar{d}^*_{0e} = \langle e|\overrightarrow{d}|0\rangle, \tag{3.6c}$$

$$\bar{d}_{e1} = \bar{d}^*_{1e} = \langle e|\overrightarrow{d}|1\rangle. \tag{3.6d}$$

In order to solve for the system dynamics we can apply the Schrödinger equation for the total Hamiltonian $H = H_0 + H_I$ and find the time dynamics of the coefficients $c_j(t)$ of the wave function.

This gives the following relations:

$$i\dot{c_0}(t) = \omega_0 c_0(t) - \bar{d}_{0e}c_e(t)\cdot[\overrightarrow{\varepsilon_0}\cos(\overrightarrow{k_0}\cdot\overrightarrow{x} - \omega_0^L t + \phi_0) + \overrightarrow{\varepsilon_1}\cos(\overrightarrow{k_1}\cdot\overrightarrow{x} - \omega_1^L t + \phi_1)], \tag{3.7a}$$

$$i\dot{c_1}(t) = \omega_1 c_1(t) - \bar{d}_{1e}c_e(t)\cdot[\overrightarrow{\varepsilon_0}\cos(\overrightarrow{k_0}\cdot\overrightarrow{x} - \omega_0^L t + \phi_0) + \overrightarrow{\varepsilon_1}\cos(\overrightarrow{k_1}\cdot\overrightarrow{x} - \omega_1^L t + \phi_1)], \tag{3.7b}$$

$$i\dot{c_e}(t) = \omega_e c_e(t) - [\bar{d}_{e0}c_0(t) + \bar{d}_{e1}c_1(t)]\cdot[\overrightarrow{\varepsilon_0}\cos(\overrightarrow{k_0}\cdot\overrightarrow{x} - \omega_0^L t + \phi_0) + \overrightarrow{\varepsilon_1}\cos(\overrightarrow{k_1}\cdot\overrightarrow{x} - \omega_1^L t + \phi_1)]. \tag{3.7c}$$

In order to solve the above equations we first transform to a rotating frame with respect to the unperturbed Hamiltonian H_0, as interaction term H_I leads to dynamics that is much slower than those due to H_0. We define slowly varying

amplitudes C_0,C_1 and C_e as,

$$C_0(t) = c_0(t)e^{i\omega_0 t}, \tag{3.8a}$$

$$C_1(t) = c_1(t)e^{i\omega_1 t}, \tag{3.8b}$$

$$C_e(t) = c_e(t)e^{i\omega_e t}. \tag{3.8c}$$

and insert into equation 3.7. We further expand each cosine term of the electric fields as exponentials and obtain

$$\begin{aligned} i\dot{C}_0(t) = &-\frac{1}{2}\bar{d}_{0e}C_e(t)e^{-i\omega_{0e}t}\cdot[\overrightarrow{\varepsilon_0}\left(e^{i(\overrightarrow{k_0}\cdot\overrightarrow{x}-\omega_0^L t+\phi_0)}+e^{-i(\overrightarrow{k_0}\cdot\overrightarrow{x}-\omega_0^L t+\phi_0)}\right) \\ &+\overrightarrow{\varepsilon_1}\left(e^{i(\overrightarrow{k_1}\cdot\overrightarrow{x}-\omega_1^L t+\phi_1)}+e^{-i(\overrightarrow{k_1}\cdot\overrightarrow{x}-\omega_1^L t+\phi_1)}\right)], \end{aligned} \tag{3.9}$$

$$\begin{aligned} i\dot{C}_1(t) = &-\frac{1}{2}\bar{d}_{1e}C_e(t)e^{-i\omega_{1e}t}\cdot[\overrightarrow{\varepsilon_0}\left(e^{i(\overrightarrow{k_0}\cdot\overrightarrow{x}-\omega_0^L t+\phi_0)}+e^{-i(\overrightarrow{k_0}\cdot\overrightarrow{x}-\omega_0^L t+\phi_0)}\right) \\ &+\overrightarrow{\varepsilon_1}\left(e^{i(\overrightarrow{k_1}\cdot\overrightarrow{x}-\omega_1^L t+\phi_1)}+e^{-i(\overrightarrow{k_1}\cdot\overrightarrow{x}-\omega_1^L t+\phi_1)}\right)], \end{aligned} \tag{3.10}$$

$$\begin{aligned} i\dot{C}_e(t) = &-\frac{1}{2}[\bar{d}_{e0}C_0(t)e^{i\omega_{0e}t}+\bar{d}_{e1}C_1(t)e^{i\omega_{1e}t}]\cdot[\overrightarrow{\varepsilon_0}\left(e^{i(\overrightarrow{k_0}\cdot\overrightarrow{x}-\omega_0^L t+\phi_0)}+e^{-i(\overrightarrow{k_0}\cdot\overrightarrow{x}-\omega_0^L t+\phi_0)}\right) \\ &+\overrightarrow{\varepsilon_1}\left(e^{i(\overrightarrow{k_1}\cdot\overrightarrow{x}-\omega_1^L t+\phi_1)}+e^{-i(\overrightarrow{k_1}\cdot\overrightarrow{x}-\omega_1^L t+\phi_1)}\right)]. \end{aligned} \tag{3.11}$$

Then we can apply the Rotating Wave Approximation (RWA) to the above equations, where we ignore terms that oscillate at a much higher rate than others. In order to do this we first note that there are terms on the right-hand side, which oscillate at sums and differences of two large optical frequencies. For a $\Lambda-$system implemented on $^{171}\mathrm{Yb}^{+}$, the qubit energy splitting ω_{01}, the detuning of the Raman laser frequency Δ and the Raman beatnote detuning μ are chosen such that

$\{\omega_{01}, \mu, \Delta\} \ll \{\omega_0^L, \omega_1^L, \omega_{0e}, \omega_{1e}\}$. Keeping terms that oscillate at $\{\omega_{01}, \mu, \Delta\}$ equation 3.9,3.10 and 3.11 can then be written as

$$i\dot{C}_0(t) = \frac{1}{2}C_e(t)\left(g_{00}e^{-i\Delta t} + g_{01}e^{-(\Delta+\mu+\omega_{01})t}\right), \tag{3.12}$$

$$i\dot{C}_1(t) = \frac{1}{2}C_e(t)\left(g_{10}e^{-i(\Delta-\omega_{01})t} + g_{11}e^{-(\Delta+\mu)t}\right), \tag{3.13}$$

$$i\dot{C}_e(t) = \frac{1}{2}C_0(t)\left(g_{00}^* e^{i\Delta t} + g_{01}^* e^{(\Delta+\mu+\omega_{01})t}\right) + \frac{1}{2}C_1(t)\left(g_{10}^* e^{i(\Delta-\omega_{01})t} + g_{11}^* e^{(\Delta+\mu)t}\right). \tag{3.14}$$

Note that the above equations also represent the Schrödinger equation showing the evolution of the system in the rotating frame instead of the lab frame. Each term on the right-hand side corresponds to an off-diagonal coupling term of the Hamiltonian. These terms are proportional to single-photon couplings $g_{\alpha\beta}$, where α represents one of the qubit levels ($|0\rangle, |1\rangle$) coupled to $|e\rangle$ by field $\overrightarrow{\varepsilon_\beta}, (\beta = 0, 1)$. These couplings are position dependent single-photon Rabi frequencies. Assuming that the electric field vector is real valued we can explicitly write down the single photon couplings as

$$g_{00} = \bar{d}_{0e} \cdot \overrightarrow{\varepsilon_0} e^{-i(\overrightarrow{k_0}\cdot\overrightarrow{x}+\phi_0)}, \tag{3.15a}$$

$$g_{01} = \bar{d}_{0e} \cdot \overrightarrow{\varepsilon_1} e^{-i(\overrightarrow{k_1}\cdot\overrightarrow{x}+\phi_1)}, \tag{3.15b}$$

$$g_{10} = \bar{d}_{1e} \cdot \overrightarrow{\varepsilon_0} e^{-i(\overrightarrow{k_0}\cdot\overrightarrow{x}+\phi_0)}, \tag{3.15c}$$

$$g_{11} = \bar{d}_{1e} \cdot \overrightarrow{\varepsilon_1} e^{-i(\overrightarrow{k_1}\cdot\overrightarrow{x}+\phi_1)}. \tag{3.15d}$$

Next, we approximately solve equations 3.12-3.14 by the method of adiabatic elimination. To apply this method we first we consider equation 3.14 under the assumption that coefficients $C_0(t)$ and $C_1(t)$ slower than $C_e(t)$. This is true since the states $|0\rangle$ and $|1\rangle$ are not directly coupled. This allows us the integrate equation 3.14 keeping $C_0(t)$ and $C_1(t)$ constant and find

$$\begin{aligned}
C_e(t) =& -\frac{i}{2}C_0(t)\int_0^t \left(g_{00}^* e^{i\Delta t} + g_{01}^* e^{i(\Delta+\mu+\omega_{01})t}\right) dt \\
& -\frac{i}{2}C_1(t)\int_0^t \left(g_{10}^* e^{i(\Delta-\omega_{01})t} + g_{11}^* e^{i(\Delta+\mu)t}\right) dt \\
=& -\frac{1}{2}C_0(t)\left[g_{00}^*\frac{e^{i\Delta t}-1}{\Delta} + g_{01}^*\frac{e^{i(\Delta+\mu+\omega_{01})t}-1}{\Delta+\mu+\omega_{01}}\right] \\
& -\frac{1}{2}C_1(t)\left[g_{10}^*\frac{e^{i(\Delta-\omega_{01})t}-1}{\Delta-\omega_{01}} + g_{11}^*\frac{e^{i(\Delta+\mu)t}-1}{\Delta+\mu}\right] \\
\approx& -\frac{1}{2\Delta}[C_0(t)\left(g_{00}^* e^{i\Delta t} + g_{01}^* e^{i(\Delta+\mu+\omega_{01})t} - g_{00}^* - g_{01}^*\right) \\
& + C_1(t)\left(g_{10}^* e^{i(\Delta-\omega_{01})t} + g_{11}^* e^{i(\Delta+\mu)t} - g_{10}^* - g_{11}^*\right)].
\end{aligned} \tag{3.16}$$

when $C_e(t=0)=0$. In the last step we use that $\Delta \gg \{\mu, \omega_{01}\}$. We can then use equation 3.12 and 3.16 to obtain

$$\begin{aligned}
\dot{C}_0(t) = \frac{i}{4\Delta}\left(g_{00}e^{-i\Delta t} + g_{01}e^{-(\Delta+\mu+\omega_{01})t}\right)&[C_0(t)\left(g_{00}^* e^{i\Delta t} + g_{01}^* e^{i(\Delta+\mu+\omega_{01})t} - g_{00}^* - g_{01}^*\right)] \\
&+ C_1(t)\left(g_{10}^* e^{i(\Delta-\omega_{01})t} + g_{11}^* e^{i(\Delta+\mu)t} - g_{10}^* - g_{11}^*\right)].
\end{aligned} \tag{3.17}$$

Here, we apply RWA again and ignore terms $e^{i\Delta t}$ and $e^{i(\Delta+\mu+\omega_{01})t}$ that oscillate much

faster and hence average out to zero. Therefore, the expression for $C_0(t)$ is

$$\dot{C}_0(t) = \frac{i}{4\Delta}[C_0(t)\left(|g_{00}|^2 + |g_{01}|^2 + g_{00}g_{01}^* e^{i(\mu+\omega_{01})t} + g_{00}^* g_{01} e^{-i(\mu+\omega_{01})t}\right) + C_1(t)\left(g_{00}g_{11}^* e^{i\mu t} + g_{00}g_{10}^* e^{-i\omega_{01}t} + g_{01}g_{10}^* e^{-i(\mu+2\omega_{01})t} + g_{01}g_{11}^* e^{-i\omega_{01}t}\right)]. \tag{3.18}$$

We can make another RWA to this expression where we assume that the beat-note between the two Raman beams $\omega_{01} + \mu$ is tuned close to qubit resonance such that $\mu \ll \omega_{01}$. This is a valid assumption since $\omega_{01} = \omega_{HF} = 2\pi \times 12.642$ GHz is the qubit splitting energy and in the experiment we usually set the value of the detuning parameter μ in the range $0 \leq |\mu| < 3.1$ MHz while performing coherent gate operations on the qubit. Therefore, equation 3.18 becomes

$$\dot{C}_0(t) = \frac{i}{4\Delta}\left[C_0(t)\left(|g_{00}|^2 + |g_{01}|^2\right) + C_1(t)g_{00}g_{11}^* e^{i\mu t}\right]. \tag{3.19}$$

Similarly, we can calculate the dynamics of coefficient $C_1(t)$ and find

$$\dot{C}_1(t) = -\frac{i}{4\Delta}[C_0(t)\left(g_{10}g_{00}^* e^{i\omega_{01}t} + g_{11}g_{00}^* e^{-i\mu t} + g_{10}g_{01}^* e^{i(\mu+2\omega_{01}t)} + g_{11}g_{01}^* e^{-i\omega_{01}t}\right) + C_1(t)\left(|g_{10}|^2 + |g_{11}|^2 + g_{10}g_{11}^* e^{i(\omega_{01}+\mu)t} + g_{11}g_{10}^* e^{-i(\omega_{01}+\mu)t}\right)], \tag{3.20}$$

which can be simplified using the RWA by removing the fast oscillating terms to give

$$\dot{C}_1(t) = -\frac{i}{4\Delta}\left[C_0(t)g_{00}^* g_{11} e^{-i\mu t} + C_1(t)\left(|g_{10}|^2 + |g_{11}|^2\right)\right]. \tag{3.21}$$

Equations 3.19 and 3.21 can now be used to calculate the evolution of the qubit

in the interaction picture. In fact, the Hamiltonian in this frame can be written as

$$H_{int} = \frac{1}{4\Delta}\begin{bmatrix} (|g_{00}|^2 + |g_{01}|^2) & g_{00}g_{11}^* e^{i\mu t} \\ g_{00}^* g_{11} e^{-i\mu t} & (|g_{10}|^2 + |g_{11}|^2) \end{bmatrix}, \tag{3.22}$$

where the diagonal terms cause rotation of the qubit about the Z-axis of the Bloch sphere (see section 5.1). This is the well known light shift (AC-Stark shift) due to off-resonant electric-dipole coupling of the qubit states to the auxiliary state $|e\rangle$ [56]. We will discuss this in more detail in the following sections. The off-diagonal term in the Hamiltonian, on the other hand, is responsible for rotating the qubit state about an axis on the equator of the Bloch sphere (see section 5.1). This is the more important evolution as it coherently transfers population between the basis states $|0\rangle$ and $|1\rangle$ at a (Rabi-)rate which is proportional to the magnitude of the product of the single photon dipole couplings $g_{00}g_{11}$ and indicate a two photon process.

3.2 355nm pulsed laser for Raman transitions

In order to perform Raman transitions in the $^{171}Yb^{+}$qubit one can choose c.w. lasers with two frequency components as discussed in the previous section. In order to obtain the two laser beams that are (optically) phase locked to each other and have frequencies separated by 12.6 GHz from one another, one could modulate the beams with an AOM or EOM, both of which is difficult to implement at the required frequency due to the limited bandwidth of these devices. We can circumvent this problem by using a train of pulses from a mode-locked laser where

the pulses have a bandwidth in the optical domain [68]. We use a 355nm mode-locked pulsed laser (Nd:YVO4)[1]. With a pulse duration of ~ 10ps its full bandwidth is about $\delta_{BW} = 200$ GHz [69]. This is sufficient for bridging the hyperfine gap between the two levels of the qubit. However, it is not straightforward to implement Raman transitions because a) the central wavelength of the laser (355nm) couples the ground state to both the $^2P_{1/2}$ and $^2P_{3/2}$ state with a detuning of $\Delta = 33$ THz and $\Delta = -66$ THz, respectively as shown in figure 2.4, and b) in the frequency comb regime there are multiple frequency components in the optical spectrum that can potentially drive resonant and off-resonant Raman transitions between the qubit levels.

3.2.1 The frequency-comb picture

As a first step towards understanding Raman transitions caused by a pulsed laser let us assume a setup as in figure 3.2a, where a pair of Raman beams from the same mode-locked laser is split into two beams propagating along different paths, and modulated with AOMs driven at frequencies ω_{AOM1} and ω_{AOM2}. The electric field as seen by the ion from one of the beams (say Raman beam 1) is

$$\bar{E}(t) = \bar{E}_0 \sum_{n=0}^{N} f(t - nT) e^{-i(\omega_c + \omega_{AOM1})t + \phi}, \tag{3.23}$$

where $f(t)$ is the pulse shape in the time domain, T is the time separation between successive pulses, and ω_c is the carrier frequency of the laser (this is at a wavelength

[1]Coherent Palladin. Average power power: 4 Watts

of 355 nm). Here ϕ is the spatially dependent phase of the field. For the next step of this derivation to be valid, we keep the intensity of the laser low enough such that a single pulse only perturbs the qubit by a small amount. This implies that, in order to perform any kind of coherent transition on the qubit, the ion needs to be hit by many pulses ($N \to \infty$). Mathematically, this allows us to describe the electric field in the frequency domain [60], where there are frequency components spaced by the repetition rate of the laser $\omega_r = 2\pi/T$ (see figure 3.2b).

By taking the Fourier transform of equation 3.23 and assume large N we find

$$E = E_0 \sum_{j=-\infty}^{+\infty} \bar{f}(j\omega_r) e^{-i(j\omega_r+\omega_c+\omega_{AOM1})t} e^{i(k_j^0 \cdot x+\phi_0)} \tag{3.24}$$

where $\bar{f}(\omega)$ is the Fourier transform of the pulse envelope $f(t)$ and k_j^0 is the wave vector for the j-th frequency component. ω_{AOM1} and ϕ_0 are the angular frequency and phase respectively, of the rf driving AOM1. We can write down a similar expression for the second Raman beam. The total electric field is then given by

$$\bar{E}_T = \bar{E}_0 \sum_{j=-\infty}^{+\infty} a_j e^{-i(j\omega_r+\omega_c+\omega_{AOM1})t} + \bar{E}_1 \sum_{j=-\infty}^{+\infty} b_j e^{-i(j\omega_r+\omega_c+\omega_{AOM2})t}, \tag{3.25}$$

where $\bar{E}_0$ and $\bar{E}_1$ are the electric field vectors for Raman-1 and Raman-2, respectively. We define variables a_j and b_j as

$$a_j = \bar{f}(j\omega_r) e^{i(k_j^0 \cdot x+\phi_0)}, \tag{3.26a}$$

$$b_j = \bar{f}(j\omega_r) e^{i(k_j^1 \cdot x+\phi_1)}. \tag{3.26b}$$

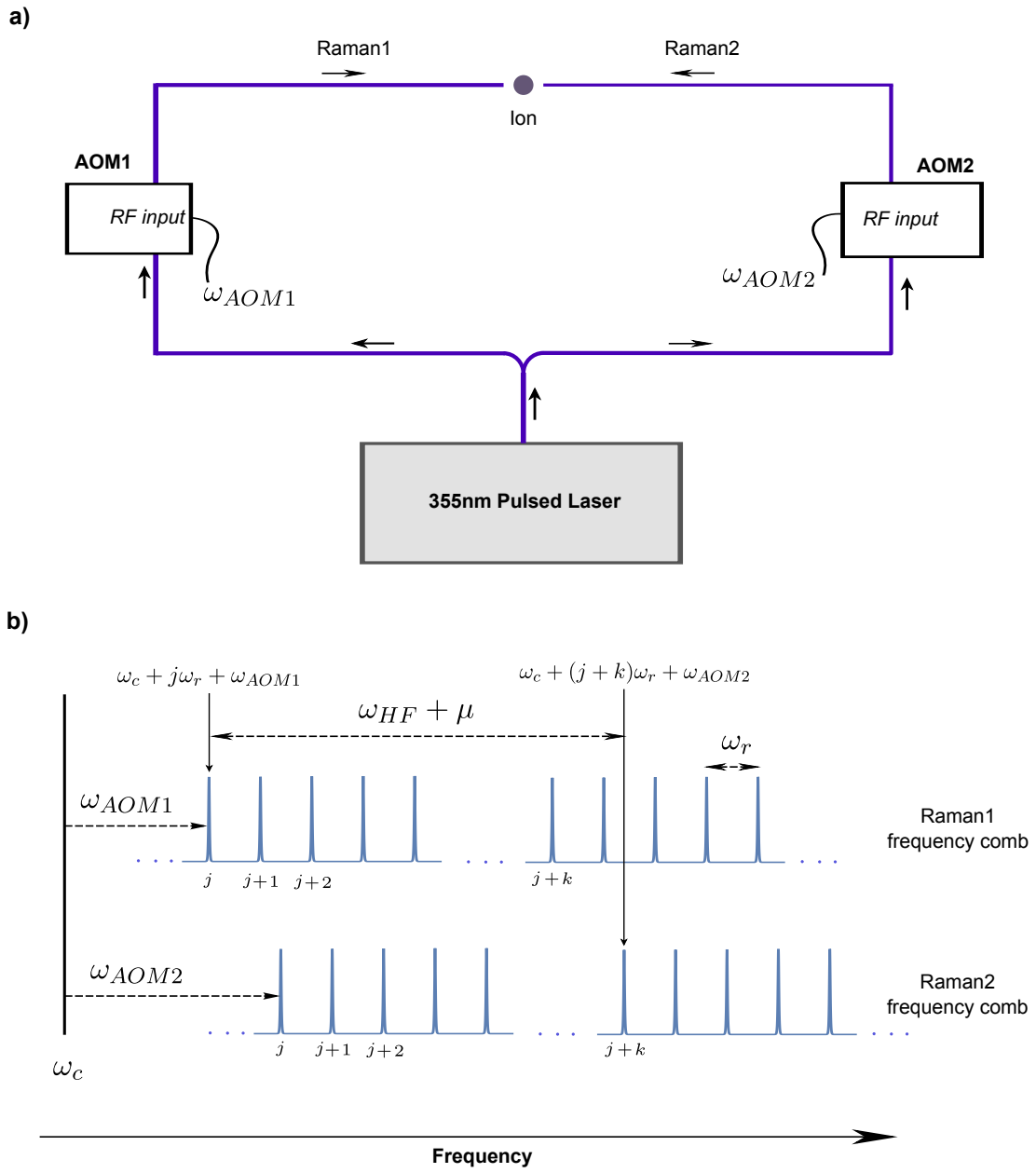

Figure 3.2: **Raman transitions driven by pulsed laser.** a) A 355nm pulsed laser output is split equally into two beams that are modulated using AOMs that are driven at frequencies ω_{AOM1} and ω_{AOM2}, respectively. The beam paths have equal lengths such that pulses are temporally overlapped at the ion position. b) The frequency comb as seen by the ion. Comb-lines are separated by the rep-rate of the laser $\omega_r \approx 119$ MHz. The frequency offset of each comb is adjusted by the AOMs such that a beat-note arising from the interference between the jth combline of Raman1 and $j+k$th combline of Raman 2 is tuned close to qubit resonance where the detuning μ is controlled to drive either a carrier or a motional sideband transition of the qubit.

We need to find out the dynamics of $C_0(t), C_1(t)$ and $C_e(t)$ again for this frequency comb picture. For this derivation we assume a Λ-system like in figure 3.1 and follow the same series of equations as discussed in the c.w. case. However, now we have an electric field that is a sum over the entire set of c.w. components of the frequency comb. In fact instead of separating the frequencies of two c.w. Raman beams by $\omega_{HF} = \omega_{01} = 12.6\,\text{GHz}$ like in figure 3.1 we are going to find many pairs of comb-lines of the total electric field E_T that give 'beat-notes' resonant with the qubit splitting ω_{HF}.

We go to the rotating frame and applying the RWA to obtain a set of equations similar to Eqn. 3.12 -3.14

$$i\dot{C}_0(t) = \frac{1}{2}C_e(t)\,(G_{00} + G_{01})\,e^{-i\Delta t}, \tag{3.27}$$

$$i\dot{C}_1(t) = \frac{1}{2}C_e(t)\,(G_{10} + G_{11})\,e^{-i(\Delta-\omega_{HF})t}, \tag{3.28}$$

$$i\dot{C}_e(t) = \frac{1}{2}C_0(t)\,(G^*_{00} + G^*_{01})\,e^{i\Delta t} + \frac{1}{2}C_1(t)\,(G^*_{10} + G^*_{11})\,e^{i(\Delta-\omega_{HF})t}. \tag{3.29}$$

Here the single photon coupling terms are

$$G_{00} = \bar{d}_{0e}\cdot\bar{E}_0 \sum_{j=-\infty}^{+\infty} a_j e^{-i(j\omega_r+\omega_{AOM1})t}, \tag{3.30a}$$

$$G_{01} = \bar{d}_{0e}\cdot\bar{E}_1 \sum_{j=-\infty}^{+\infty} b_j e^{-i(j\omega_r+\omega_{AOM2})t}, \tag{3.30b}$$

$$G_{10} = \bar{d}_{1e}\cdot\bar{E}_0 \sum_{j=-\infty}^{+\infty} a_j e^{-i(j\omega_r+\omega_{AOM1})t}, \tag{3.30c}$$

$$G_{11} = \bar{d}_{1e}\cdot\bar{E}_1 \sum_{j=-\infty}^{+\infty} b_j e^{-i(j\omega_r+\omega_{AOM2})t}. \tag{3.30d}$$

The difference of these equations of motion from the c.w. case (equation 3.13-3.15) is that the single photon coupling terms G_{ij} are not time independent. Next step we can adiabatically eliminate the excited state. Here, we assume that the coefficients $C_0(t)$ and $C_1(t)$ vary slowly compared to $C_e(t)$. We integrate equation 3.29 with initial condition $C_e(t=0)=0$. We find

$$\begin{aligned} C_e(t) = &-\frac{1}{2}C_0(t)\bar{d}^*_{0e}\cdot(\bar{E}^*_0\sum_j a^*_j\frac{e^{i(\Delta+j\omega_r+\omega_{AOM1})t}-1}{\Delta+j\omega_r+\omega_{AOM1}}+\bar{E}^*_1\sum_j b^*_j\frac{e^{i(\Delta+j\omega_r+\omega_{AOM2})t}-1}{\Delta+j\omega_r+\omega_{AOM2}}) \\ &-\frac{1}{2}C_1(t)\bar{d}^*_{1e}\cdot(\bar{E}^*_0\sum_j a^*_j\frac{e^{i(\Delta-\omega_{HF}+j\omega_r+\omega_{AOM1})t}-1}{\Delta-\omega_{HF}+j\omega_r+\omega_{AOM1}}+\bar{E}^*_1\sum_j b^*_j\frac{e^{i(\Delta-\omega_{HF}+j\omega_r+\omega_{AOM2})t}-1}{\Delta-\omega_{HF}+j\omega_r+\omega_{AOM2}}). \end{aligned} \tag{3.31}$$

Now we substitute C_e in equations 3.27 and 3.28 and get the equations of motion. At this point it is important to expand the G_{ij} in order to apply the RWA and ignore all terms that oscillate too fast. For the sake of cleanliness let us write the equations of motion

$$i\dot{C}_0(t) = \alpha C_0(t) + \beta C_1(t), \tag{3.32}$$

$$i\dot{C}_1(t) = \gamma C_0(t) + \delta C_1(t), \tag{3.33}$$

where the coefficients α and δ correspond to terms that shift the qubit levels $|0\rangle$ and $|1\rangle$, respectively. The coefficients β and γ on the other hand correspond to the coupling strength between the two levels, also known as the Rabi frequency. For the interaction Hamiltonian (as suggested by equations 3.32 and 3.33) to be Hermitian these off-diagonal terms should satisfy the relation $\beta=\gamma^*$.

We can now calculate the coefficients based on the frequency comb picture in figure 3.2b. We assume that the frequencies of the AOMs are such that $\omega_{AOM1} \neq$

ω_{AOM2} and $k\omega_r + \omega_{AOM2} - \omega_{AOM1} = \omega_{HF} + \mu$. Here we assume that the detuning $\mu \ll \omega_r, \omega_{AOM1}, \omega_{AOM2}$ and for all practical purposes are nearly 0. From equation 3.27 we can write down the DC terms in the expression of α as,

$$\alpha = \frac{1}{4}\left(|\bar{d}_{0e}.\bar{E}_0|^2 \sum_j \frac{|a_j|^2}{\Delta + j\omega_r + \omega_{AOM1}} + |\bar{d}_{0e}.\bar{E}_1|^2 \sum_j \frac{|b_j|^2}{\Delta + j\omega_r + \omega_{AOM2}}\right). \quad (3.34)$$

Similarly we find

$$\delta = \frac{1}{4}\left(|\bar{d}_{1e}.\bar{E}_0|^2 \sum_j \frac{|a_j|^2}{\Delta - \omega_{HF} + j\omega_r + \omega_{AOM1}} + |\bar{d}_{1e}.\bar{E}_1|^2 \sum_j \frac{|b_j|^2}{\Delta - \omega_{HF} + j\omega_r + \omega_{AOM2}}\right) \quad (3.35)$$

We note that the main difference between the two light shift terms is in the denominator with the presence of the finite energy splitting of the qubit states (ω_{HF}). Assuming that the qubit energy splitting is much smaller than the bandwidth of the laser we have $|a_j| \approx |a_{j+k}|$. Also the detuning Δ and the AOM drive frequencies are much larger than the laser bandwidth. This allows us to Taylor expand the denominator in equations 3.34 and 3.35 in terms of $\frac{j\omega_r}{\Delta}$ and $\frac{\omega_{HF}+j\omega_r}{\Delta}$, respectively . From equations 3.26 we also note that $|a_j|^2 = |b_j|^2$. Using these relations we obtain approximate light shift terms

$$\alpha = \frac{1}{4}\left(|\bar{d}_{0e}.\bar{E}_0|^2 + |\bar{d}_{0e}.\bar{E}_1|^2\right)\frac{1}{\Delta} \quad (3.36)$$

and

$$\delta = \frac{1}{4}\left(|\bar{d}_{1e}.\bar{E}_0|^2 + |\bar{d}_{1e}.\bar{E}_1|^2\right)\frac{1}{\Delta}\left(1 + \frac{\omega_{HF}}{\Delta}\right), \quad (3.37)$$

as the terms containing $j\omega_r$ add up to zero ($\sum_{j=-\infty}^{\infty} \frac{j\omega_r}{\Delta} = 0$) and $\sum_j |a_j|^2 = 1$.

Next we can calculate the terms β and γ. If we choose to write equation 3.32 and 3.33 in the standard form of the Schrödinger equation $i\hbar\frac{\partial}{\partial t}|\psi\rangle = H_I|\psi\rangle$ then these terms are the off diagonal terms of the interaction Hamiltonian H that couple the qubit levels $|0\rangle$ and $|1\rangle$. This gives rise to coherent rotations of the qubit in a Bloch sphere [53, 56]. Unlike the diagonal terms α and β, which correspond to light shifts, the off-diagonal terms contain products of dipole couplings that have contributions from both Raman beams or more specifically two different frequency components of the frequency combs (Fig. 3.2b). We first expand C_e in equations 3.27 and 3.28 to obtain the expressions

$$\begin{aligned}\beta =& \frac{1}{4}(G_{00} + G_{01})e^{-i\Delta t}\times \\ & \bar{d}_{1e}^* \cdot (\bar{E}_0^* \sum_j a_j^* \frac{e^{i(\Delta-\omega_{HF}+j\omega_r+\omega_{AOM1})t}-1}{\Delta-\omega_{HF}+j\omega_r+\omega_{AOM1}} + \bar{E}_1^* \sum_j\ b_j^* \frac{e^{i(\Delta-\omega_{HF}+j\omega_r+\omega_{AOM2})t}-1}{\Delta-\omega_{HF}+j\omega_r+\omega_{AOM2}})\end{aligned} \tag{3.38}$$

$$\begin{aligned}\gamma =& \frac{1}{4}(G_{10} + G_{11})e^{-i(\Delta-\omega_{HF})t}\times \\ & \bar{d}_{0e}^* \cdot (\bar{E}_0^* \sum_j a_j^* \frac{e^{i(\Delta+j\omega_r+\omega_{AOM1})t}-1}{\Delta+j\omega_r+\omega_{AOM1}} + \bar{E}_1^* \sum_j b_j^* \frac{e^{i(\Delta+j\omega_r+\omega_{AOM2})t}-1}{\Delta+j\omega_r+\omega_{AOM2}})\end{aligned} \tag{3.39}$$

In order to expand the single photon coupling terms G_{ij} in β and γ and perform a RWA, we need to consider two scenarios.

Case 1: Coherent rotations with a single Raman beam frequency comb. Let's assume a situation where the qubit levels can be coupled using a single frequency comb. This implies that $k\omega_r = \omega_{HF} + \mu$ where k is an integer and $\mu \ll \omega_r$ is a small detuning from resonance. If we have control over the rep-rate ω_r of the pulsed laser then we might as well set μ to zero in order to drive resonant Rabi-flops

of the qubit. We make another assumption that $\omega_{AOM1} \neq \omega_{AOM2} \neq 0$. Now we can inspect equation 3.38 and apply the RWA and find

$$\begin{aligned}\beta =& \frac{e^{i\mu t}}{4}(\bar{d}^*_{1e}.\bar{E}^*_0)(\bar{d}_{0e}.\bar{E}_0)\sum_j a^*_{j+k}a_j\frac{1}{\Delta + j\omega_r + \omega_{AOM1} + \mu} \\ &+ \frac{e^{i\mu t}}{4}(\bar{d}^*_{1e}.\bar{E}^*_1)(\bar{d}^*_{0e}.\bar{E}_1)\sum_j b^*_{j+k}b_j\frac{1}{\Delta + j\omega_r + \omega_{AOM2} + \mu}.\end{aligned} \tag{3.40}$$

Similarly, for γ we use equation 3.39 and applying the RWA to find

$$\begin{aligned}\gamma =& \frac{e^{-i\mu t}}{4}(\bar{d}^*_{0e}.\bar{E}^*_0)(\bar{d}_{1e}.\bar{E}_0)\sum_j a_{j+k}a^*_j\frac{1}{\Delta + j\omega_r + \omega_{AOM1}} \\ &+ \frac{e^{-i\mu t}}{4}(\bar{d}^*_{0e}.\bar{E}^*_1)(\bar{d}_{1e}.\bar{E}_1)\sum_j b_{j+k}b^*_j\frac{1}{\Delta + j\omega_r + \omega_{AOM2}}.\end{aligned} \tag{3.41}$$

At this point we can ignore μ in the denominator since it is much smaller than Δ and zero when the qubit is resonantly driven.

Case 2: Coherent rotations with two Raman beams. This scenario fits best to our experimental setup since the rep-rate of the pulsed laser is non-adjustible and a single beam cannot drive resonant transitions. This implies $k\omega_r \neq \omega_{HF}$ for any integer k. The frequency comb picture of the two Raman beams in figure 3.2 closely resembles the system in this case, where the frequency of the AOMs ω_{AOM1} and ω_{AOM2} are adjusted to create a beatnote between sets of comb-lines belonging to both Raman beams. This beat-note can then be tuned to be resonant with the hyperfine qubit splitting ω_{HF}. This resonant condition is satisfied when $k\omega_r + \omega_{AOM2} - \omega_{AOM1} = \omega_{HF} + \mu$. We can now keep the 'DC' terms in equation

3.38 and applying the RWA. This leads to

$$\beta = \frac{e^{i\mu t}}{4}(\bar{d}^*_{1e}.\bar{E}^*_1)(\bar{d}_{0e}.\bar{E}_0)\sum_j a_j b^*_{j+k}\frac{1}{\Delta + j\omega_r + \omega_{AOM1} + \mu}. \tag{3.42}$$

Applying the RWA to equation 3.39 gives the following expression

$$\gamma = \frac{e^{-i\mu t}}{4}(\bar{d}^*_{0e}.\bar{E}^*_0)(\bar{d}_{1e}.\bar{E}_1)\sum_j a^*_j b_{j+k}\frac{1}{\Delta + j\omega_r + \omega_{AOM1}}. \tag{3.43}$$

Like in case 1, we can ignore μ in the denominator.

We note that the diagonal terms of H_I that provide the light shift are 'scalar' quantities that depend on the strengths of the coupling between the qubit levels and the excited state and are the same for the two scenarios (case -1 and -2), where the Raman transition is resonantly driven by a single beam or both Raman beams. We also note that the light shifts are controlled by the intensities ($\propto |E_i|^2 = I_i$) of each Raman beam. However, for practical purposes we are interested in the differential light shift, which is the measure of how much the qubit hyperfine splitting changes due to the unequal shift of the levels. To have a rough idea of the magnitude of this shift, lets consider **case-1** where Rabi flopping is performed by each beam and is also $\propto |E_i|^2 = I_i$ of each beam. We can write the Rabi rate of this case as $\Omega_s = \frac{1}{4}(|\bar{d}.\bar{E}_0|^2 + |\bar{d}.\bar{E}_1|^2)\frac{1}{\Delta}$, where we assume $\bar{d}_{0e} = \bar{d}_{1e} = \bar{d}$ and the sum $\sum_j a^*_{j+k}a_j\frac{1}{\Delta+j\omega_r+\omega_{AOM}} \approx \sum_j |a_j|^2\frac{1}{\Delta} = \frac{1}{\Delta}$. Under these assumptions $\alpha = \frac{1}{4}(|\bar{d}.\bar{E}_0|^2 + |\bar{d}.\bar{E}_1|^2)\frac{1}{\Delta}$ and $\delta = \frac{1}{4}(|\bar{d}.\bar{E}_0|^2 + |\bar{d}.\bar{E}_1|^2)\frac{1}{\Delta}(1 + \frac{\omega_{HF}}{\Delta})$. Therefore the

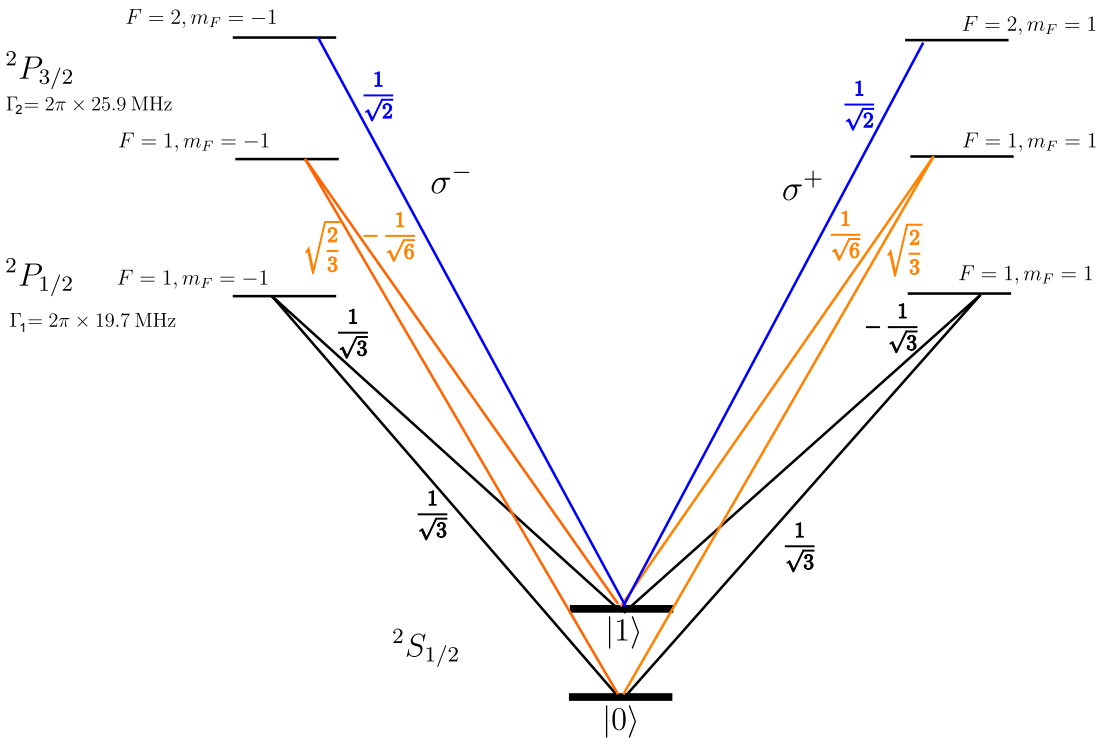

Figure 3.3: **Relevant Clebsch-Gordon coefficients in $^{171}Yb^+$ for Raman transition.** Here we show the relative dipole coupling strengths for the allowed transitions that couple the qubit levels to excited P levels.

differential light shift is

$$\begin{aligned}\Delta_{diff} =& \delta - \alpha = \frac{1}{4}(|\bar{d}.\bar{E}_0|^2 + |\bar{d}.\bar{E}_1|^2)\frac{1}{\Delta}\frac{\omega_{HF}}{\Delta} \\ =& \Omega_s \frac{\omega_{HF}}{\Delta} \approx \Omega_s \times 4 \times 10^{-4}\end{aligned} \tag{3.44}$$

for $\Delta = 2\pi \times 33$ THz. This implies that while performing coherent single qubit rotations using a pair of Raman beams with equal power the Stark shift causes a residual Z-rotation in the Bloch sphere at a rate that is $\sim 10^{-4}$ times slower than the rate the qubit is rotated around an axis on the equator of the sphere.

3.2.2 Raman transitions via multiple excited states

In $^{171}Yb^{+}$, the hyperfine qubit levels are coupled to more than one excited state by the 355 nm Raman laser. The relevent excited states are in the $^2P_{1/2}$ and the $^2P_{3/2}$ manifold as shown in Fig. 2.4 where the detuning of the Raman laser from the virtually excited states are $\Delta = 33$ THz and $\Delta' = -67$ THz, respectively. It is straightforward to extend the results of Raman processes obtained using a single excited state (as discussed in the previous section) to the one having multiple excited states. In order to do so we first need to define the excited states as $|e1\rangle$, $|e2\rangle$, $|e3\rangle$ etc. all of which couple to the qubit levels via single-photon coupling terms G_{00e1}, G_{00e2}, G_{10e1}, G_{10e2} etc. From left to right the indices of these terms depend on the qubit level ($|0\rangle$ or $|1\rangle$), the coupling electric field (E_0 or E_1) and excited state ($|e1\rangle$, $|e2\rangle$ etc.). For example coupling term G_{00e1} can be explicitly written as

$$G_{00e1} = \bar{d}_{0e1}.\bar{E}_0 \sum_{j=-\infty}^{+\infty} a_j e^{-i(j\omega_r + \omega_{AOM1})t}, \tag{3.45}$$

where the dipole matrix element $\bar{d}_{0e1}$ is between $|0\rangle$ and $|e1\rangle$. Using these terms we can modify equation 3.27 and 3.28 which will now contain more terms each corresponding to the amplitude of the excited states $C_{e1}(t)$, $C_{e2}(t)$, $C_{e2}(t)$ etc. Additionally we also get more equations like equation 3.29 for the excited state amplitudes. We can adiabatically eliminate each excited state and substitute their amplitudes in 3.27 and 3.28 to obtain equations of motion for the two level system.

Next we can evaluate the total light shift α and δ and the off diagonal terms β

and γ that give the net coupling between the qubit levels. From the solution of the general set of equations (that are similar to equation 3.27, 3.28 and 3.29) we find that these terms are simply a sum of the contributions of all the $\Lambda-$ systems that are formed from each of the excited states that contribute to the Raman transition. This is shown in figure 3.3 where Clebsch-Gordan coefficients are represented for each dipole coupling term along with the electric field polarizations required for each coupling. Now we can expand the dipole coupling term $\bar{d}_{0e1}.\bar{E}_0$ in the expression of G_{00e1} as $\bar{d}_{0e1}.\bar{E}_0 = -|\bar{E}_0|\langle 0|\mu.\hat{\epsilon_0}|e1\rangle$ where $\hat{\epsilon_0}$ is the unit vector of the electric field and μ is the dipole moment of the atom. We can rewrite the term $\langle 0|\mu.\hat{\epsilon}|e1\rangle$ in terms of the Clebsch-Gordan coefficient to give the following expression [49]

$$\bar{d}_{0e1}.\bar{E}_0 = \sqrt{I_0}C(0,e1)(\hat{\epsilon_0}\cdot\hat{\sigma}_{\pm})\frac{\Gamma}{\sqrt{2I_{sat}}}, \tag{3.46}$$

where $C(0,e1)$ is the Clebsch-Gordan coefficient for angular momentum coupling between $|0\rangle$ and $|e1\rangle$, Γ is the natural radiative linewidth of the transition, and I_{sat} is the saturation intensity. $I_0 = |E_0|^2$ and $\hat{\epsilon_0}$ are the intensity and unit vector of the electric field, respectively. The unit vector $\hat{\sigma}_{\pm}$ defines pure right and left circular polarization, respectively whereas $\hat{\sigma}_{\pi}$ defines (π-)polarization along the quantization axis.

Using equations 3.45 and 3.46 we evaluate the diagonal terms of the interaction Hamiltonian

$$\alpha = \frac{1}{4\Delta}(\frac{1}{3})(I_0+I_1)\frac{\Gamma_1^2}{2I_{sat1}} + \frac{1}{4\Delta'}(\frac{2}{3})(I_0+I_1)\frac{\Gamma_2^2}{2I_{sat2}}, \tag{3.47}$$

$$\delta = \frac{1}{4\Delta}(1+\frac{\omega_{HF}}{\Delta})(\frac{1}{3})(I_0+I_1)\frac{\Gamma_1^2}{2I_{sat1}} + \frac{1}{4\Delta'}(1+\frac{\omega_{HF}}{\Delta'})(\frac{2}{3})(I_0+I_1)\frac{\Gamma_2^2}{2I_{sat2}}, \quad (3.48)$$

where I_{sat1} and I_{sat2} and Γ_1 and Γ_2 are the saturation intensities and natural line widths of the ${}^2S_{1/2}$ to ${}^2P_{1/2}$ and ${}^2S_{1/2}$ to ${}^2P_{3/2}$ transitions, respectively.

Next we can calculate off diagonal terms β and γ. However, for the sake of completeness we will consider the two cases as discussed before:

Case 1: Coherent rotation with single Raman beam frequency comb. We can calculate β from equation 3.40 by substituting the terms that contain the dipole interaction with the electric field using expressions that are of the form as shown in equation 3.46. The expression is

$$\begin{aligned}\beta =& \frac{I_0 e^{i\mu t}}{12}\left(\frac{\Gamma_1^2 A_{k,\Delta}}{I_{sat1}} - \frac{\Gamma_2^2 A_{k,\Delta'}}{I_{sat2}}\right)(-|\sigma_{0+}|^2 + |\sigma_{0-}|^2) \\ &+ \frac{I_1 e^{i\mu t}}{12}\left(\frac{\Gamma_1^2 B_{k,\Delta}}{I_{sat1}} - \frac{\Gamma_2^2 B_{k,\Delta'}}{I_{sat2}}\right)(-|\sigma_{1+}|^2 + |\sigma_{1-}|^2)\end{aligned} \quad (3.49)$$

where we have defined the electric field in terms of angular momentum-1 polarization vectors which consists of components of circular $\sigma-$ and $\pi-$ polarizations with respect to the quantization axis (defined by the magnetic field B). We define the component of electric field $\bar{E}_0$ that is right circularly polarized as $\sigma_{0+} = \hat{\epsilon}_0.\hat{\sigma}_+$ and similarly the component that is left circularly polarized $\sigma_{0-} = \hat{\epsilon}_0.\hat{\sigma}_-$. The electric field in these coordinates can be expressed as

$$E_0 = \sqrt{I_0}\left(\sigma_{0+}\hat{\sigma}_+ + \sigma_{0-}\hat{\sigma}_- + \pi_0\hat{\pi}\right), \quad (3.50a)$$

$$E_1 = \sqrt{I_1}\left(\sigma_{1+}\hat{\sigma}_+ + \sigma_{1-}\hat{\sigma}_- + \pi_1\hat{\pi}\right) \quad (3.50b)$$

and terms A_k and B_k are defined as

$$A_{k,\Delta} = \sum_j \frac{a_j a^*_{j+k}}{\Delta + j\omega_r + \omega_{AOM1}}, \tag{3.51a}$$

$$B_{k,\Delta} = \sum_j \frac{b_j b^*_{j+k}}{\Delta + j\omega_r + \omega_{AOM2}}, \tag{3.51b}$$

where we have removed the detuning μ from the denominator. Since we already showed in equation 3.41 that $\gamma = \beta^*$ we do not need to explicitly write down its expression. At this point we also can expand the terms a_j and b_j as in equation 3.26 and extract the phase offsets to write down β as

$$\beta = \frac{\Omega}{2} e^{i\mu t} e^{i(\Delta\bar{k}.x + \Delta\phi)}, \tag{3.52}$$

where $\Delta\bar{k} = \bar{k}_j - \bar{k}_{j+k}$ which is independent of j and $\Delta\phi = 0$. Here Ω is defined as the Rabi frequency.

Case 2: Coherent rotation with two Raman beams. From equation 3.42 we can obtain the off diagonal term β in the case where coherent Raman transition is performed by tuning frequency combs of two Raman beams. We find

$$\beta = \frac{\sqrt{I_0 I_1} e^{i\mu t}}{12} \left(\frac{\Gamma_1^2 D_{k,\Delta}}{I_{sat1}} - \frac{\Gamma_2^2 D_{k,\Delta'}}{I_{sat2}} \right) (-\sigma_{0+}\sigma^*_{1+} + \sigma_{0-}\sigma^*_{1-}), \tag{3.53}$$

where

$$D_{k,\Delta} = \sum_j \frac{a_j b^*_{j+k}}{\Delta + j\omega_r + \omega_{AOM1}} \tag{3.54}$$

and we use $\gamma = \beta^*$. At this point we also can expand the terms a_j and b_j as in

equation 3.26 and extract the phase offsets to write down β as

$$\beta = \frac{\Omega}{2} e^{i\mu t} e^{i(\Delta\bar{k}.x + \Delta\phi)}, \tag{3.55}$$

where $\Delta\bar{k} = \bar{k}_j^0 - \bar{k}_{j+k}^1$ is the same for all pairs of comblines separated by $k \times \omega_r$. Assuming that the pulse shape envelope in the frequency domain is real ($\bar{f}(j\omega_r)$) the Rabi frequency Ω is real. The phase offset $\Delta\phi = \phi_0 - \phi_1$ is set by the phase of the rf that drives the two Raman beam AOMs. Here Ω is defined as the Rabi frequency and contains terms that are static in time and independent of the ion position.

Now that we have obtained the values of α, β, γ and δ for the $^{171}Yb^{+}$qubit we can obtain the interaction Hamiltonian. By inspecting equations 3.32 and 3.33 and comparing it to the Schrödinger equation $i\frac{\partial\psi(t)}{\partial t} = H\psi(t)$ we can write down the Hamiltonian as,

$$H = \begin{bmatrix} \alpha & \beta \\ \beta^* & \delta \end{bmatrix} = \Delta_c \mathbb{I} + \Delta_{s2}\sigma_z + \frac{\Omega}{2} e^{i\mu t} e^{i(\Delta\bar{k}.x + \Delta\phi)}\sigma^+ + \frac{\Omega^*}{2} e^{-i\mu t} e^{i(\Delta\bar{k}.x + \Delta\phi)}\sigma^- \tag{3.56}$$

where $\Delta_c = (\alpha + \delta)/2$, $\Delta_{s2} = (\alpha - \delta)/2$ and σ^+ and σ^- are the spin raising and lowering operators. Here Δ_c is a shift common to both qubit levels and therefore adds an overall phase during the evolution of the state which can then be ignored. We need to keep the remaining three terms to calculate the evolution of the qubit state. We define the state $\psi(t)$ as,

$$\psi(t) = \sum_n \left(C_{0,n}(t)|0\rangle|n\rangle + C_{1,n}(t)|1\rangle|n\rangle\right) \tag{3.57}$$

where $|n\rangle$ is the motional number (Fock) states of the ion. When the qubit is not entangled with the motion $C_{i,n} = C_i f_n$. In chapter 2 we discussed the harmonic confinement of the $^{171}Yb^{+}$ion in the trap. The motional state of the ion is a result of this confinement. In principal there are three orthogonal axes (two radial and one axial) along which the motional state can be decomposed. However, we will be mostly concerned with the radial mode that is aligned with the $\Delta\bar{k}$ vector of the two Raman beams since it can be coherently excited. Since this mode does not couple to the other radial and axial modes (at least in the regime in which the ion trap operates) we can ignore the state of the other mode.

The dependence of the Rabi frequency Ω, derived above on the two cases of Raman transitions indicates a few properties that are important to keep in mind while setting up the Raman beams in the experiment. For example, if we want to drive coherent rotations using a single Raman beam frequency comb (eq. 3.49, **case 1**) it is important to use circularly polarized light for maximizing Rabi-frequency. We also note that the Rabi frequency depends linearly on the beam intensity. A $\hat{\pi}$ polarization component does not contribute to coupling between the qubit levels. Therefore, it is useful to have the B field parallel to the Raman beam. For **case 2** where we use two frequency combs to drive coherent rotations the Rabi rate can be maximized by choosing a "lin-perp-lin" configuration of the Raman beams and the B field. Here the beams are setup counterpropagating to each other and parallel to the B field. Their linear polarizations are orthogonal to each other and to the field. This is relatively easy to do since the output of the laser is linearly polarized and the AOMs also prefer linear polarization. We also note that the contributions

to the Rabi frequency from the $^2P_{1/2}$ and $^2P_{3/2}$ excited states 'add up' since the detunings from the states are such that $D_{k,\Delta}$ and $D_{k,\Delta'}$ have opposite signs. On the other hand the two-photon differential Stark shift Δ_{s2} have contributions from the two excited levels that partially cancel each other due to opposite signs of the detunings and are weaker by an extra factor of $\frac{\omega_{HF}}{\Delta}$.

3.3 The fourth-order Stark shift

The differential AC-Stark shift Δ_{s2} in the Hamiltonian of equation 3.56 is important in the evolution since it effects a σ_z rotation on the qubits and therefore needs to be taken into account while driving coherent rotations. This light shift simply arises from the fact that the qubit levels are coupled to the excited states through the off resonant Raman beams. A similar shift would occur between the qubit levels themselves if they were to be coupled through a off-resonant microwave field near the qubit frequency ω_{HF}. A single frequency comb from a single pulsed laser beam can also provide a perturbation near the qubit frequency [70]. **Case 1** as defined in the previous section precisely encapsulates this concept, where Equations 3.40 and 3.49 give the expression of the Rabi frequency from the beat note between the $j-$th and the $(j+k)-$th frequency comb line

$$\Omega_k = I_0(-|\sigma_{0+}|^2 + |\sigma_{0-}|^2)\left(\frac{\Gamma_1^2 A_{k,\Delta}}{6I_{sat1}} - \frac{\Gamma_2^2 A_{k,\Delta'}}{6I_{sat2}}\right). \tag{3.58}$$

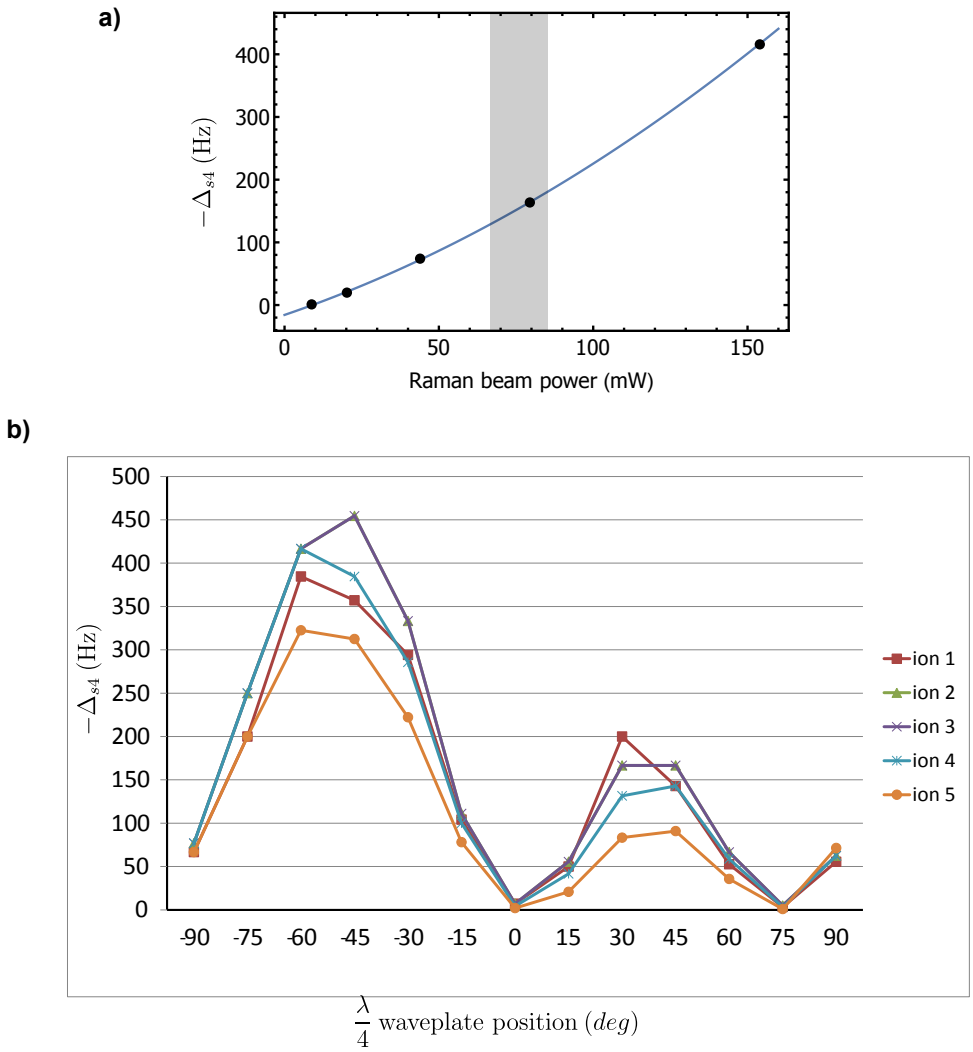

Figure 3.4: **Fourth order stark shift from a single Raman beam.** a) The light shift from a single individual addressing Raman beam is measured using Ramsey spectroscopy. The net shift is negative and its magnitude varies quadratically with the Raman beam intensity verifying it to be the fourth order Stark shift. The shaded area shows the range of power used for performing gate oprations. b) Light shift on five ions are measured for different $\lambda/4$ wave-plate positions. At waveplate positions $+50^0$ or -40^0 the polarization of the beam is mostly circular which results in large shifts (see eqn. 3.58 and 3.59).

This Rabi frequency is zero when the polarization is purely linear. However, if there is an imbalance in the $|\sigma_{0+}|$ and $|\sigma_{0-}|$ component of the Raman beam the Rabi frequency is non zero which off resonantly couples the qubit states. This leads to a fourth order stark shift given by,

$$\Delta_{s4} = -\sum_k \frac{|\Omega_k|^2}{4\mu_k} \tag{3.59}$$

where k defines the the pair of of comb lines that provide the off-resonant beatnote. The detuning in this case is given by $\mu_k = k\omega_r - \omega_{HF}$.

The repetition rate of the pulsed laser used used in the experiment is $\omega_r = 2\pi \times$ 118.314MHz which gives us a set of detunings $\{\mu_k\} = 2\pi \times \{+16.7, -101.5, +135.1, -219.8, \cdots\}$ MHz arranged in increasing order of the detuning magnitude. We observe that the leading contribution to the total shift comes from a beatnote that has a positive detuning which causes the net shift to be negative. We measure this shift using Ramsey spectroscopy as a function of the beam intensity and polarization (figure 3.4). A quarter waveplate is installed in each of the Raman beams to remove any circular component of the polarization as shown in figure 4.5. However, there are some uncompensated fourth order shifts that come from residual circularly polarized light (probably due to mixed polarization) from each Raman beam. In the following sections we will include both the second and fourth order stark shifts in the σ_z terms of the Hamiltonian and denote it as the total light shift seen by a qubit $\Delta_s = \Delta_{s2} + \Delta_{s4}$.

3.4 Locking the Raman beat-note

The 355 nm pulsed laser used is a Coherent Palladin[2] with average power of 4 Watts. It has a repetition rate of $\omega_r = 2\pi \times 118.314\,\text{MHz}$. In order to perform a stimulated Raman transition we choose to use pairs of frequency comb-lines that are separated by nearly $\omega_{HF} = 12.642\,\text{GHz}$. The repetition rate of the laser is chosen to be such that a single frequency comb does not drive any resonant transition. In the experiment this is true as the closest beat note from a single comb is detuned from resonance by $|107 \times \omega_r - \omega_{HF}| \approx 2\pi \times 17\,\text{MHz}$. Therefore in this setup we perform coherent operations using the technique discussed in **case 2** in the previous section. The frequency comb picture in this case is shown in figure 3.2 where we will satisfy the following condition,

$$\omega_{AOM1} + k\omega_r(t) - \omega_{AOM2}(t) = \omega_{HF} + \mu \tag{3.60}$$

In figure 3.2a AOM2 is a speciality multi-channel AOM which has a rf drive frequency at 210 MHz. Therefore, in order to satisfy the resonance condition we choose the parameters: a) $k = 108$ and b) $\omega_{AOM1} = 75\,\text{MHz}$. Note that the repetition rate of the laser is a time varying. This is because the internal cavity of the laser is not actively stabilized and therefore has slow drifts in its length. This causes ω_r to vary in time. This drift is monitored and fed back to the frequency of AOM2 such that the beat-note is stable [71]. We accomplish this by directly probing the term $k\omega_r(t)$

[2]Palladin compact 355-4000; S/N: 99627610188

in equation 3.60 using an ultra fast photo-diode[3] where we measure the frequency of the 108th comb-line and implement a phase-locked feed back loop that modulates the frequency of ω_{AOM2} to compensate for the drift. The schematic of the lock is shown in figure 3.5.

While performing coherent rotations on the qubit AOM1 is driven by an arbitrary waveform generator (AWG) that can be programmed to produce sinusoidal waveforms with a time step resolution of 1 ns and an a 12-bit resolution of the amplitude. By varying the AWG frequency (ω_{AOM1}) we can also change the beatnote detuning μ from qubit resonance.

In figure 3.5 a large bandwidth photo detector is used to directly measure the rf frequency comb of the pulsed laser. The 108th comb-line can be isolated from the others using band pass filters. It is then referenced to a stable synthesized RF signal (at 12.567 GHz). This is done by mixing them together to extract the difference frequency between the two, which is then isolated using filters. Ideally this is the frequency at which AOM2 should be driven in order to produce a stable beatnote between the two Raman beams at the ion (Eq. 3.60). However, due to spectral noise on the signal it is important to filter it further. To achieve this we drive AOM2 with a separate signal generator (HP8640B) and phase lock its frequency to that signal generated from the laser comb line. This is accomplished using a phase-locked loop which modulates the frequency produced by the generator. However, in this case a "tunable low pass filter" sets the modulation bandwidth. By setting this to a lower threshold ω_{AOM2} can be made to have a spectral linewidth narrow enough while it

[3]UPD-30-VSG-P; rise time < 30 ps; band-width > 10 GHz

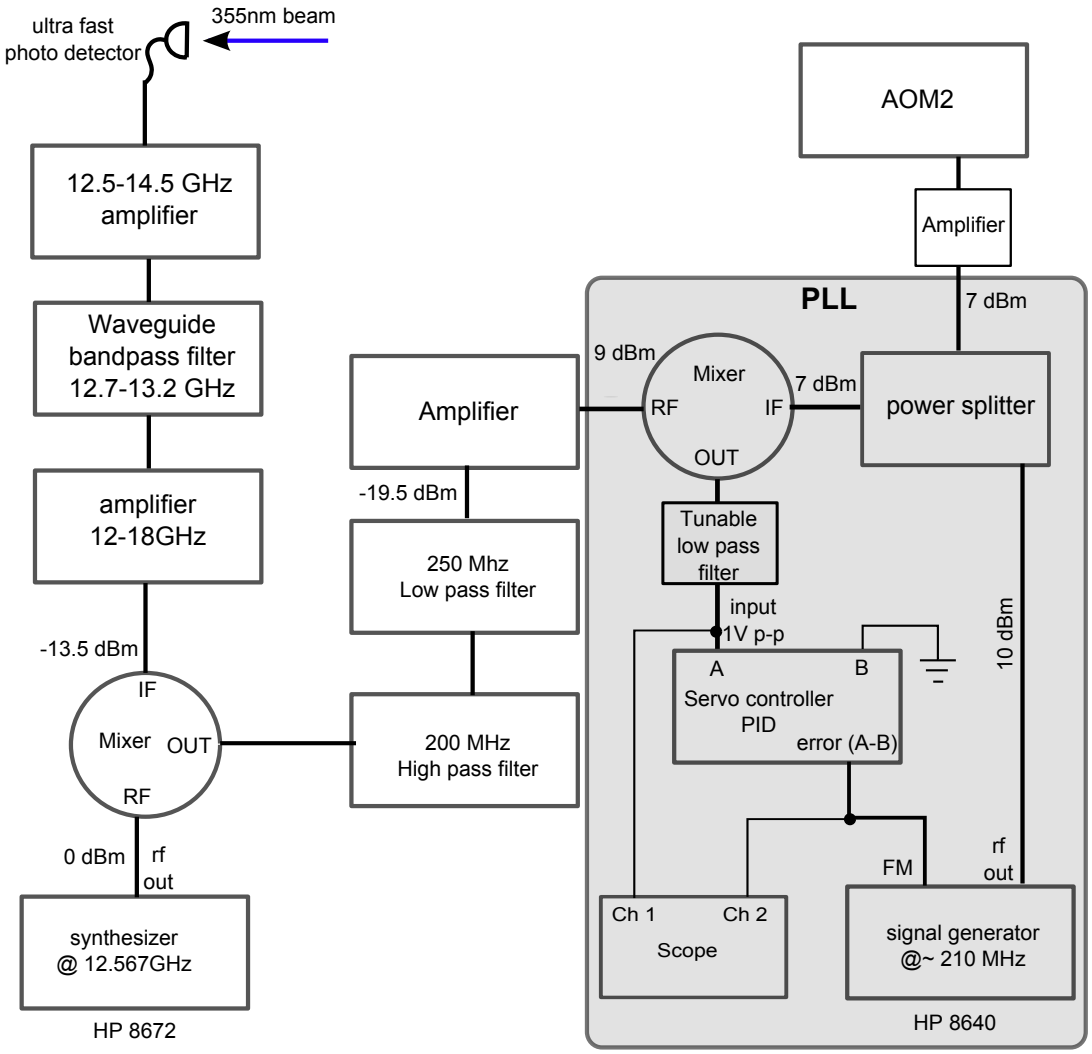

Figure 3.5: **Beat note lock setup.** An ultra fast photo detector is used to measure the frequency components of the pulsed laser out of which the 108th comb line is filtered and mixed with a standard synthesizer. The output corresponds to the time varying frequency ω_{AMO2}. A frequency modulated rf signal from a signal generator is phase locked to this signal using a phase-locked loop (PLL) as showed in the shaded region. Part of this phase locked RF signal is then sent to the AOM2 for shifting Raman beam 2 frequency comb-line. The relevent powers of rf signals are shown in dBm.

slowly changes its value to keep up with the drift in the frequency comb line. In the end it works out such that the optical beatnote that drives the qubit is phase locked to the reference provided by the synthesizer which in turn is referenced to a stable Rubidium signal.

3.5 Single qubit Rabi flopping

The interaction Hamiltonian in equation 3.56 can be transformed to another rotating frame where the qubit splitting is additionally shifted by the stark shift which is $\omega_1 - \omega_0 + \Delta_S$. The interaction Hamiltonian in this frame is then given by $H_I = e^{iH_0 t} H e^{-iH_0 t}$ where $H_0 = \Delta_S \sigma_z$. We can write it as

$$H_I = \begin{bmatrix} 0 & \frac{\Omega}{2} e^{i(\mu-\Delta_s)t} e^{i(\Delta k.x+\Delta\phi)} \\ \frac{\Omega}{2} e^{-i(\mu-\Delta_s)t} e^{-i(\Delta k.x+\Delta\phi)} & 0 \end{bmatrix}. \tag{3.61}$$

This interaction coherently transfers population between the $|0\rangle|n\rangle$ and $|1\rangle|n'\rangle$ states and can be strongly dependent on the motional state of the ion. This comes from the fact that the ion may seem a modulation of the beatnote phase based on its position. The equations of motion of the state amplitudes in this case are given by

$$\dot{C}_{0,n} = -\frac{i}{2} e^{i(\mu-\Delta_s)t} e^{i\Delta\phi} \Omega_{n,n'} C_{1,n'}, \tag{3.62a}$$

$$\dot{C}_{1,n'} = -\frac{i}{2} e^{-i(\mu-\Delta_s)t} e^{-i\Delta\phi} \Omega^*_{n,n'} C_{0,n}, \tag{3.62b}$$

where the Rabi frequency is

$$\Omega_{n,n'} = \Omega\langle n'|e^{i\eta(a+a^\dagger)}|n\rangle = D_{n,n'}\Omega. \tag{3.63}$$

We expand the term $\Delta\bar{k}.x = \eta(a + a^\dagger)$ where η is the Lamb-Dicke parameter and a is the motional mode lowering operator. The Debye-Waller factor $D_{n,n'}$ gives the strength of the coupling based on the motional states involved [10, 72]. Here we can tune the detuning such that $\mu - \Delta_S = 0$ such that there are no time varying terms in the off diagonal terms. This gives rise to resonant Rabi flopping between the states $|0\rangle|n\rangle$ and $|1\rangle|n\rangle$ that coherently transfers the population between the states. This is usually referred to as a carrier transition as it does not change the motional state of the ion and only changes the qubit spin. In this case the Debye-Waller factor can be derived to be

$$D_{n,n} = e^{-\frac{\eta^2}{2}} L_n^0(\eta^2), \tag{3.64}$$

where $L_n^0(\eta^2)$ is the generalized Laguerre polynomial. For the ion near the motional ground state and $\eta^2 \ll 1$ we get $D_{n,n} \approx 1$.

In figure 3.6a we perform rabi flopping using co-propagating beams where $\eta \ll 1$ and therefore the Rabi frequency is practically insensitive to the ion motion. However, since the polarization of the beams is mostly linear hence the Rabi frequency is much smaller compared to the counterpropagating geometry (fig. 3.6b). For this Raman beam geometry $\eta \approx 0.12$ and therefore the the Rabi frequency has a strong dependence on the motional state of the ion. As shown in the figure the

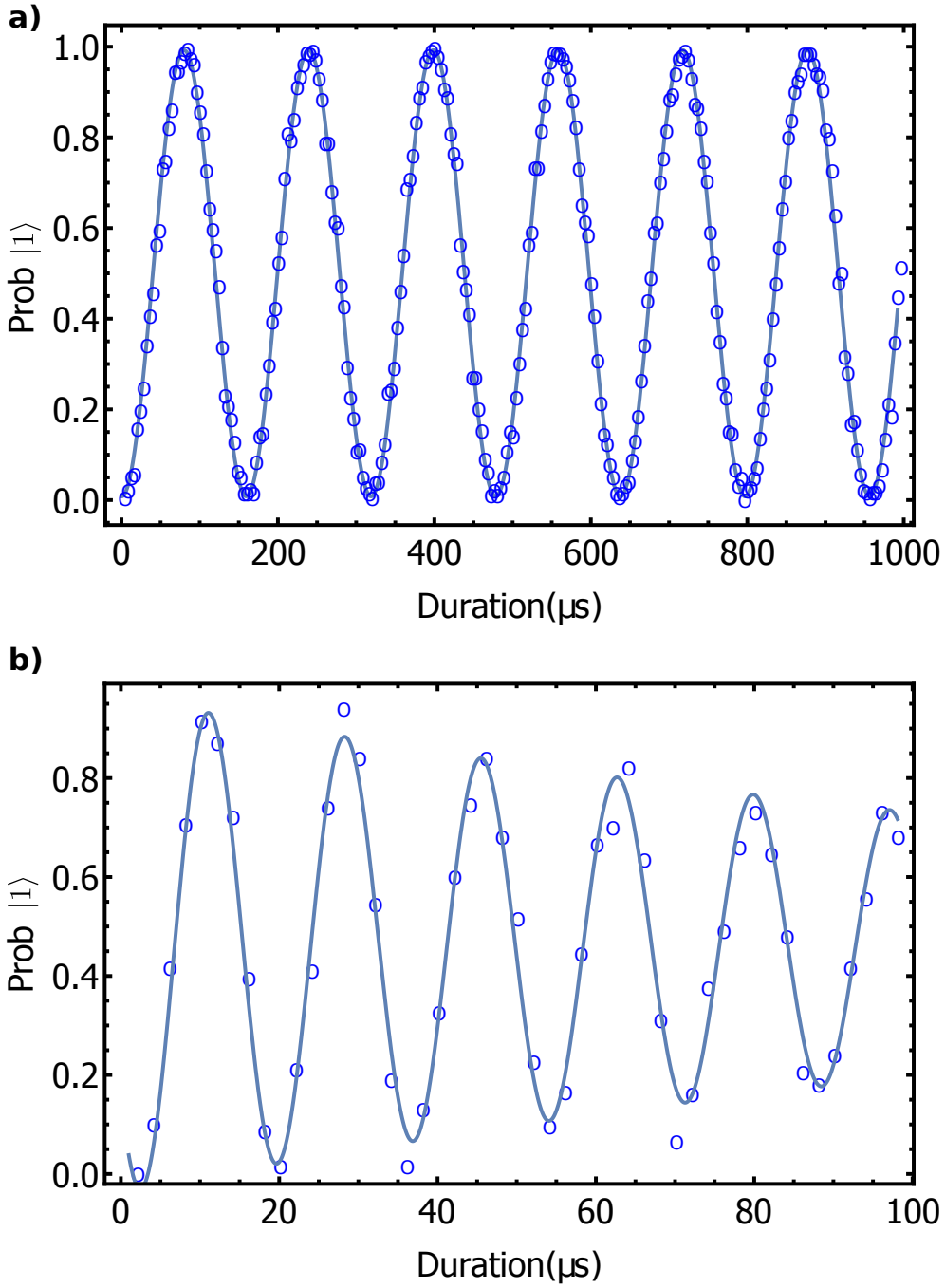

Figure 3.6: **Carrier Rabi flopping.** a) Rabi flopping using co-propagating Raman beam geometry. Due to relatively small $\Delta\bar{k}$ the Rabi frequency Ω has no dependence on the motional state of the ion which leads to the high contrast. b) Rabi flopping using counter propagating Raman beams. Here $\Delta\bar{k}$ is relatively large such that Ω has n dependence. The fit shows a carrier Rabi-flop when the ion is in a thermal state with $\bar{n} \approx 2$

rabi flopping is not as clean since the ion is in a thermal state with average phonon number $\bar{n} = 2$ which varies the Rabi frequency over the different Fock state components of the qubit. This causes a decay in the Rabi flopping due to interference of the different Rabi rates.

In order to couple spin to the motion of the ion we can change the detuning μ such that $\mu - \Delta_s = \pm\omega_x$, where ω_x is the secular frequency of the radial mode of motion along the Δk vector of the Raman beams. This coherently transfers population between the $|0\rangle|n\rangle$ and the $|1\rangle|n \pm 1\rangle$ state. This is commonly referred to as the sideband Rabi flop where that is 'blue' when the motional phonon number is increased by 1 and 'red' when the phonons number is decresed by 1 while flipping the qubit spin from $|0\rangle$ to $|1\rangle$. As discussed earlier the secular trap frequency is $\approx$ 3 MHz which gives a Lamb-Dicke parameter $\eta = 0.12$ for counterpropagating Raman beams. Rabi rate in this case is given by $\Omega_{n,n\pm1} = D_{n,n\pm1}\Omega$ where the Debye-Waller factor is

$$D_{n,n+1} = e^{-\frac{\eta^2}{2}} \frac{\eta\Omega}{\sqrt{n+1}} L_n^1 \eta^2 \approx \frac{\eta\Omega}{\sqrt{n+1}}, \tag{3.65a}$$

$$D_{n,n-1} = e^{-\frac{\eta^2}{2}} \frac{\eta\Omega}{\sqrt{n}} L_n^1 \eta^2 \approx \frac{\eta\Omega}{\sqrt{n}}. \tag{3.65b}$$

Here we have considered $\eta^2 = 0.014 \ll 1$ which gives an approximate Rabi frequency that depends on the motional Fock state $|n\rangle$. In figure 3.7 we plot theoretical Rabi flops for various thermal states of the ion ($\bar{n} = 0.1$ and $\bar{n} = 2$). The carrier rabi frequency is faster than the sideband by the factor η. We also find out that when the ion is not cooled near to the motional ground state there is significant loss

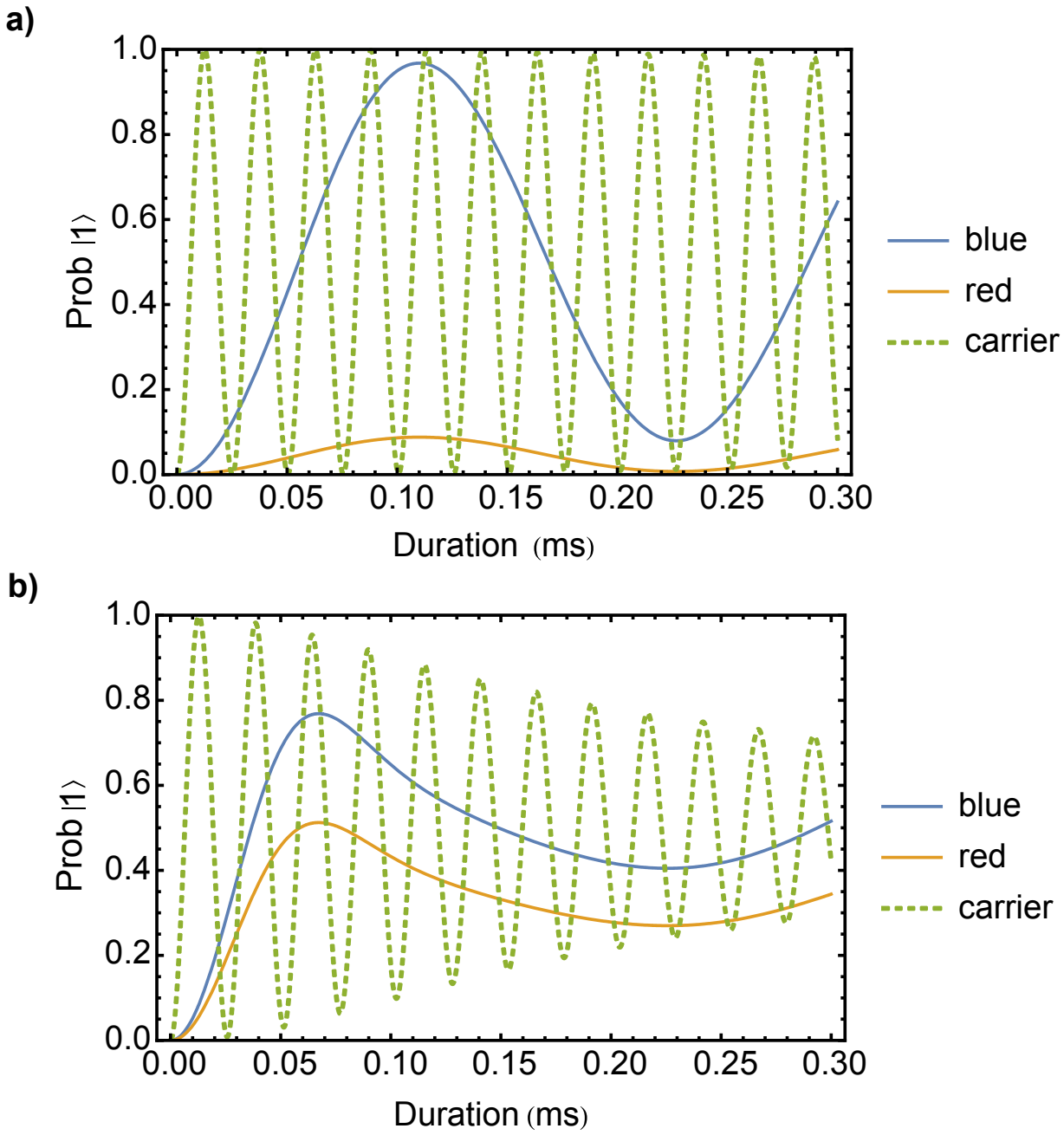

Figure 3.7: **Carrier and sideband Rabi flopping for thermal states** a) Simulation of a carrier Rabi flopping at two photon Rabi frequency $\Omega = 40$ kHz at $\bar{n} = 0.1$. The red and blue sideband rabi-rates are weaker by a factor of $\eta \approx 0.12$ which is the Lamb-Dicke parameter for a radial trap frequency of $\omega_x = 3.0$ MHz. The red sideband transition is suppressed when the ion is initialized to the state $|0\rangle|n\rangle$ where motional phonon number $n \to 0$. b) Simulated Rabi flopping for the ion in thermal state with $\bar{n} = 2$. The decay in the carrier Rabi flopping is due to the $n-$dependence of Ω which leads to the interference of slightly different Rabi rates over the thermal distribution of n.

of contrast in the Rabi flops due to the variation of $\Omega_{n,n'}$. Therefore, we choose to perform Raman sideband cooling to initialize the qubit close to the motional ground state before performing any coherent rotations on it.

For a counter propagating beam geometry as shown in figure 3.2a the wave vector difference between the Raman beams is of the order $\Delta\bar{k} = 2\pi(\frac{1}{\lambda_j}\hat{x} - \frac{-1}{\lambda_{j+k}}\hat{x}) \approx \frac{4\pi}{355}\hat{x}\ \mathrm{nm}^{-1}$. Since the two Raman beams propagate along separate beam paths it is possible to have differential optical path lengths δx in the two arms causing the phase of the beatnote to change by $\delta x\frac{2\pi}{355}$ where δx is expressed in nm. This can be caused by air currents that give rise to local changes in the refractive index or can occur due to vibrations in optical elements (mirrors) in each path. A good way to quantify this 'phase jitter' is by performing a Ramsey interferometry experiment as shown in figure 3.8. Any phase jitter due to the interferometric instability of the two Raman beams can reduce contrast of Ramsey fringes when the qubit and the beatnote are allowed to evolve with respect to each other for sufficient amounts of time such that the relative phase coherence between the two is lost due to either 'phase jitter' or fluctuation is the qubit energy splitting (due to magnetic field noise etc.). The measured coherence in the counter propagating geometry is quantified as the coherence time which is measured to be $T_c = 400\,\mathrm{ms}$. In order to achieve this we put an enclosure around the Raman beams in order to reduce air currents on the optics table. By using stable configurations of mounting mirrors beam pointing errors can be reduced as well.

It is important to note that a co-propagating geometry is less sensitive to interferometric instability due to two reasons:

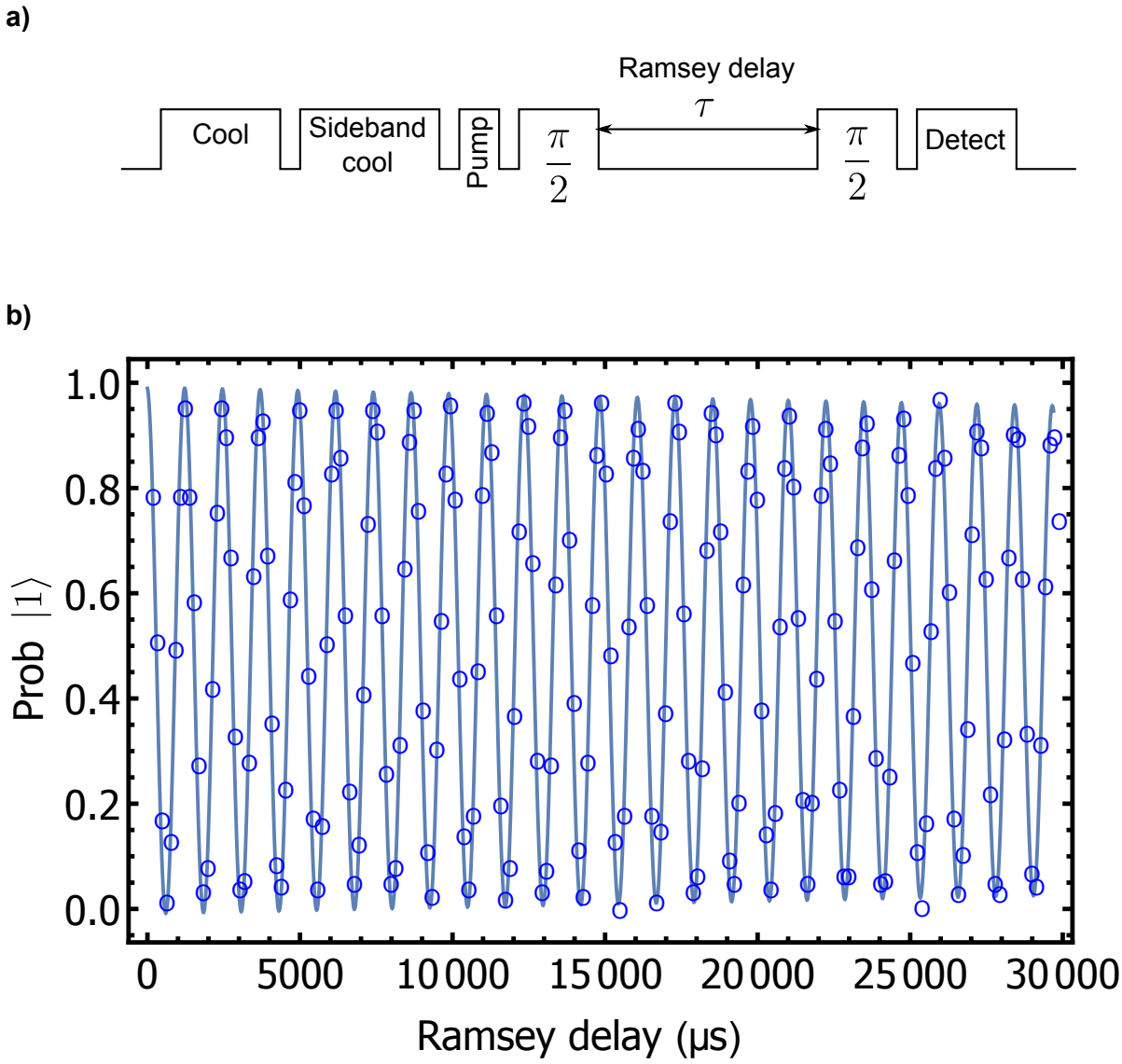

Figure 3.8: **Coherence measurement.** a) A Ramsey interferometry sequence for coherence measurement. The qubit is initialized to state $|0\rangle$ and near the motional ground state. Counterpropagating Raman beams drive Rabi flop between the qubit levels. A $\frac{\pi}{2}$ pulse drives the qubit to the equator of the Bloch sphere where it evolves during the delay time τ at the difference frequency between the beatnote and the qubit splitting ω_{HF}. A $\frac{\pi}{2}$ pulse at the end maps this evolution to the bright state probability Prob $|1\rangle$. b) Ramsey fringes observed as an oscillation of Prob $|1\rangle$. The fringe contrast indicates a high degree of coherence between the freely evolving qubit and the driving beatnote. The contrast should exponentially decay when the driving beatnote (or qubit splitting) has noise that destroys the coherence. The time constant for the decay is exterpolated to be $T_c = 400$ ms where T_c is the coherence time at which the contrast goes to $1/e$.

a) Both the Raman beams share the same optical path due to which any variation in the optical paths of the two presents itself as a 'common mode' noise that affects both the beams equally therefore canceling the effects. This implies that $\delta x \to 0$.
b) The difference in the $\bar{k}$ vectors of copropagating beams is given by $\Delta\bar{k} = 2\pi(\frac{1}{\lambda_j}\hat{x} - \frac{1}{\lambda_{j+k}}\hat{x}) \approx \frac{2\pi \times 12.6\,\mathrm{GHz}}{c}\hat{x}$ which is the inverse of a 12.6GHz microwave wavelength which in free space is 2.4 cm. Usually variations in the optical path lengths of the Raman beams are much smaller than this length scale.

Despite the obvious advantages of interferometric stability of copropagating beams we will use the counterpropagating geometry due to the large value of $\Delta\bar{k}$ achieved in this case. This allows us to excite the motional modes of the ions with a force that is proportional to $\eta\Omega$ by increasing the value of η. Using the counter propagating geometry we can probe the motional state of the ion in the radial direction. By tuning the Raman beatnote at the blue and red sideband frequencies we can rabi flop between $|0\rangle|n\rangle$ and $|0\rangle|n \pm 1\rangle$ accordingly. By fitting this to a thermal state we can extract the average phonon number of the mode. We use this technique in order to find the motional heating rate ($\dot{\bar{n}}$) of the ion in the trap which is an important figure of merit for the ion trap and also sets a limit on the duration of coherent operations that can be performed before re-cooling it to the ground state. Figure 3.9 shows an experimental sequence that initializes a single ion close to the motional ground state and probes its temperature at different times by performing sideband Rabi flopping.

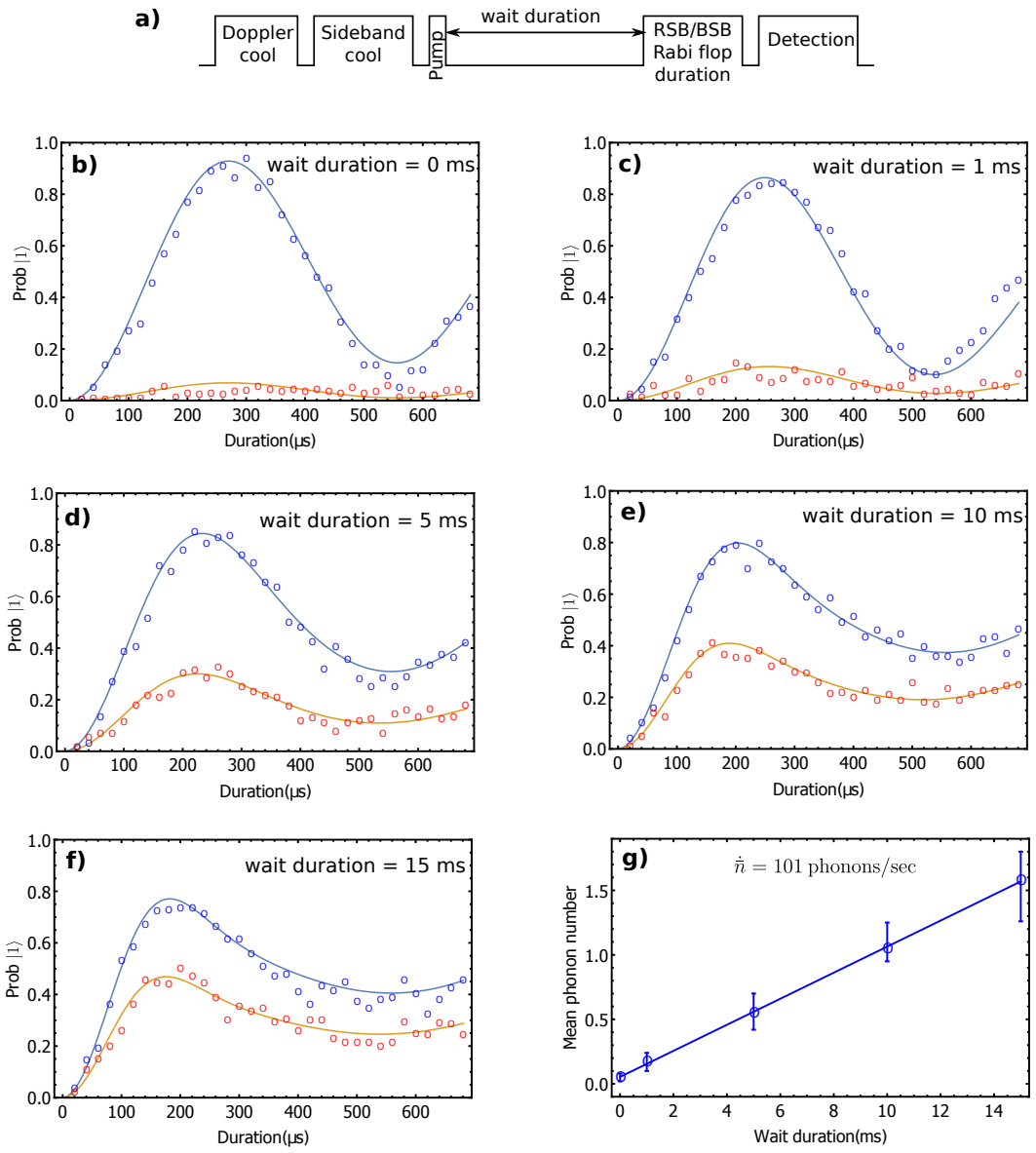

Figure 3.9: **Measurement of trap heating rate using sideband spectroscopy** a) Experimental sequence. The ion is prepared in the $|0\rangle|n=0\rangle$ ground state. A red or blue sideband rabi flop is implemented by spectrally addressing the $|0\rangle|n\rangle \rightarrow |0\rangle|n-1\rangle$ or $|0\rangle|n\rangle \rightarrow |0\rangle|n+1\rangle$ transition respectively. b)-f) Red and blue side band Rabi flopping after different wait times after side band cooling. Due to a finite heating rate of the trap the ion heats up to a thermal state with $\bar{n} \neq 0$. By fitting the Rabi flopping the average phonon number n can be determined as a function of time. g) Linear fit to phonon number vs. time plot. This gives a heating rate $\dot{\bar{n}} = 101$ phonons/s.

Chapter 4: Individual Qubit Addressing

The implementation of quantum algorithms require control and readout of individual qubits. In order to do so, naively one might consider placing qubits far from each other such that they can be manipulated separately with high isolation. However, this also prevents them from interacting with each other specially when such interactions occur though local couplings when they are physically placed close to each other. Using trapped ions a multi-qubit system is often prepared by trapping several ions (each representing a qubit) in a single harmonic trap such that they can strongly interact with each other through electrostatic Coulomb repulsion. By taking advantage of these interactions we can implement two qubit quantum gates between any pairs of ions. By setting trap parameters one might arrange the ions as a linear chain Coulmb crystal. With the ion separation usually of the order of a few microns in this configuration it is challenging to address each one of them.

A few techniques well known for individual addressing are based on spectral resolving of qubits using field gradients [17–19], shelving of qubit states to other electronic levels [16] and spatially resolving individual ions through optical resolution [73]. In our experiment we use the technique of optically (spatially) resolving individual ions for control as well as readout. Unlike spectral resolution, using spa-

tial resolution is not limited by a frequency bandwidth and spectral crowding for more qubits. It also does not interfere with the qubit levels as in shelving techniques. Also, since no two ions can be at the same position, optical resolution techniques are inherently scalable for larger ion chains.

In this experiment we use five $^{171}Yb^{+}$ions that are trapped in a linear chain configuration with approximately 5 μm spacing between adjacent ions. We implement readout using state dependent fluorescence that is collected by a 0.37 numerical aperture (NA) objective. The state detection is an incoherent process where the fidelity of the measurement is determined by the amount of collected fluorescence. Using a high NA objective not only ensures this but also improves the resolution of imaging individual ions which in turn minimizes errors due to the optical crosstalk between the light collected from different ions in the chain. The coherent qubit control on the other hand is implemented by tightly focussing individual Raman beams on each ion in the chain. Since qubit manipulation is a coherent process therefore there is a trade off between maintaining high optical resolution during addressing while maintaining a high phase and intensity stability of the Raman beams. In the following sections we will discuss how we implement high optical resolution in both individual qubit control and measurement.

4.1 Individual qubit state detection

In order to improve state detection we improve the numerical aperture from 0.23 [1] to 0.37 by designing a custom objective lens. The lens design is shown in figure 4.1 with the design parameters shown in table 4.1. Due to high NA the light collection is increased almost by a factor of 3. The lens is designed at 369.5 nm which is the wavelength for the $^2S_{1/2}$ to $^2P_{1/2}$ transition in $^{171}Yb^+$. Therefore, the expected resolution for the imaging of a single ion is 0.5 μm.

The design of the objective is based on the constraints given by the vacuum chamber and the trap(see section 2.5.1). In order to have high NA access in both the detection and Raman beams directions re-entrant windows are used to reduce the working distance of the lens from the trap. However, due to the dimensions of the ion trap and the re-entrant windows the shortest working distance available for imaging is ~ 20 mm. We use a 32 mm clear aperture on the light collection window which allows a window thickness of about 3 mm. The lens assembly is chosen to be composed of standard 1" singlets with a lens holder that attaches to standard SM-1 lens tubes [2].

The objective lens assembly is designed and optimized in OSLO. In this approach we start by setting the NA of the system to be low and simulate spherical aberrations. As the NA is gradually increased aberrations also increase which can then be reduced by adding more singlets to the assembly [74]. The lens assembly

[1] CVI objective used in previous version of the experiment
[2] Thorlabs

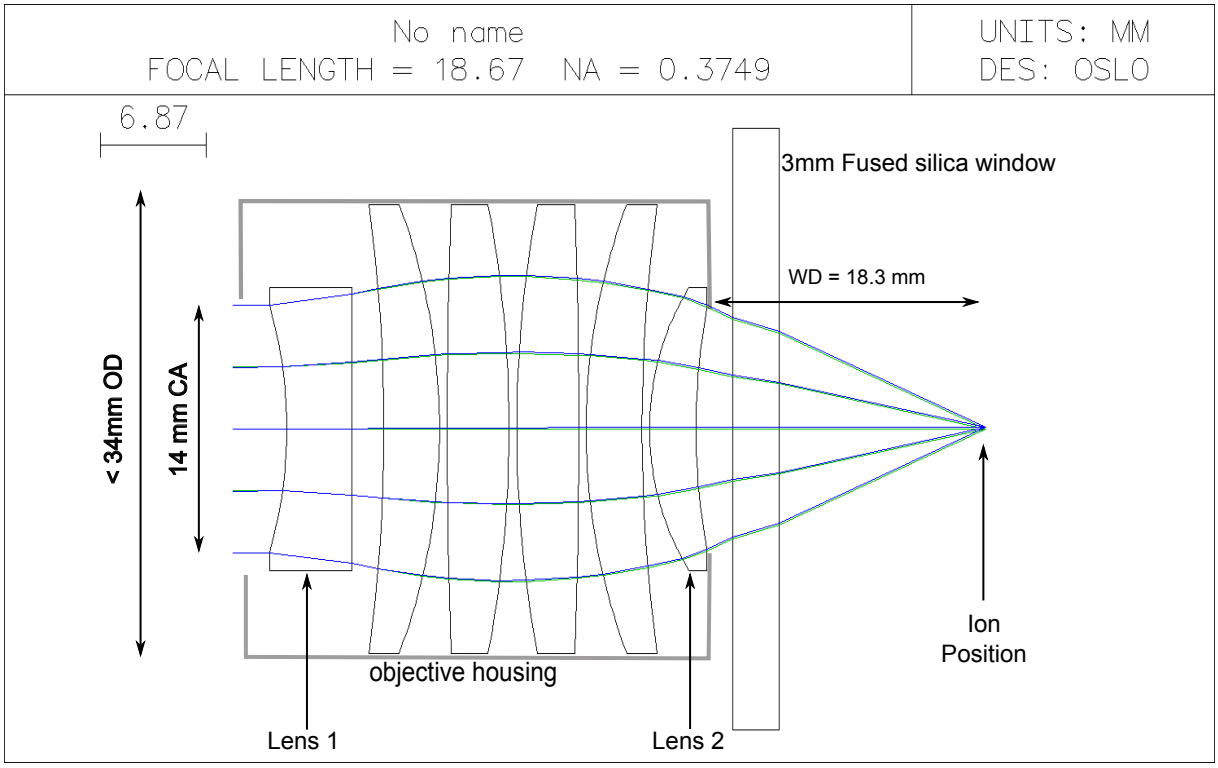

Figure 4.1: **Lens design for light collection.** A 6-element lens design for a 0.38 NA light collection from a trapped ion. The design is adapted for a 3mm thick fused silica vacuum widow. The outer diameter of the lens tube agrees with a 1"-SM1 (Thorlabs) lens tube system and is fitted in a re-entrant viewport with 38mm inner diameter. Lens-1 and Lens-2 are custom designed elements. The remaining singlet lenses in the assembly are commercially available. The design can be optimized to be near diffraction limited for a different window thickness by adjusting the position of Lens 1.

SRF	Radius (mm)	Thickness (mm)	Aperture radius (mm)	Glass	Description
OBJ	–	∞	–	AIR	x
AST	–	0	6.800	AIR	x
2	-22.299 V	4.230 V	7.000	HK9L	Custom Lens-1
3	∞	2.055 V	8.000	AIR	**
4	-82.200	3.600	12.700	HK9L	Thorlabs
5	-32.100	0.500	12.700	AIR	LE1234-A
6	353.300	4.000	12.700	HK9L	Thorlabs
7	-60.020	0.500	12.700	AIR	LBF254-100-A
8	60.020	4.000	12.700	HK9L	Thorlabs
9	-353.300	0.500	12.700	AIR	LBF254-100-A
10	32.100	3.600	12.700	HK9L	Thorlabs
11	82.200	0.500	12.700	AIR	LE1234-A
12	13.782 V	3.000	8.000	HK9L	Custom Lens-2
13	33.693 V	1.500	6.575	AIR	x
14	∞	3	17.000	UVFS	Vacuum
15	∞	0	17.000	VACUUM	window
IMS	–	14.276	–	–	x

** This spacing can be adjusted to correct for variable vacuum window thickness.
SRF- Surface
OBJ- Object
AST-Aperture stop
IMS- Image stop
V- Variable parameter for optimizing the design for minimal aberration
S- Aperture radius calculated from ray tracing
HK9L - Also knows as N-BK7 Borosilicate crown glass is manufactured by CDGM. It has internal transmittace of 0.993 at 370 nm for 10 mm glass thickness.

Table 4.1: Lens design for a 0.38NA objective lens assembly for collecting fluorescence from ions for imaging and detection. It is designed to compensate for aberrations introduces by a 3mm fised silica vacuum window. Each surface is spherical and is characterized by its radius of curvature, aperture size and the thickness of glass following it.

is divided in three parts: a) positive meniscus lens close to the window (Lens-2) , b) a symmetric arrangement of 4 singlets (positive) and c) a negative lens (Lens-1). This design has the following properties:

- Due to several components the peripheral rays are gradually bent over several surfaces thereby keeping the spherical aberration to the lowest order.
- Each singlet with a positive focal length adds a positive aberration component where as Lens 1 and the vacuum chamber window adds a negative aberration component.
- The four singlets in the middle are symmetrically arranged such and the rays bend symmetrically as well across the elements. This minimizes the aberration from this section of the assembly.
- The two lenses in the center of the assembly are chosen to be best form lenses which are optimal since the rays bend around them in an infinite conjugate fashion. The two lenses next to these on either side are positive meniscus lenses that are used to further bend the rays that are already converging on either side of this section.
- Since the spherical aberration contribution from each singlet is in the lowest order therefore we can nearly cancel the positive against the negative aberrations. In order to do so we simply vary the thickness and surface curvatures of Lens-1 and Lens-2 in the design to reach an aberration minima.
- Any excess aberration due to a different vacuum window thickness can be

reduced simply by changing the position of Lens-1.

In this design we use BK-7 glass which is of higher refractive index than UV-grade fused silica. This helps in reducing spherical aberrations. Singlets in the middle section are commercially available[3] whereas Lens-1 and Lens-2 are custom designed. One advantage of this design is that it can be adapted for a thicker window using the same lens stack. Due to a infinite conjugate performance the objective forms an image at infinity. This gives flexibility in setting a variable first stage magnification of the imaging system using a singlet 'tube lens' that allows for easy alignment of the system. Before mounting the objective it is experimentally verified to operate near the diffraction limit (see Appendix A for theoretical simulation and experimental verification of lens performance).

Figure 4.2 shows the setup used for the imaging of ions. Fluorescence from each ion is collected using the objective lens. Collimated output is focussed using a 200 mm focal length best form lens[4] to form an intermediate image with roughly $\times 10$ magnification. Figure 4.2a shows the first stage with an aperture at the image plane. This is used to spatially filter out any background scattered light outside the desired field of view of the objective. Figure 4.2b shows the second stage where a doublet [5] with effective focal length of $\sim$ 22 mm is used to form an image on an intensified charged couple device (ICCD) camera. The doublet is mounted such that its position can be varied in order to image the aperture onto the camera.

Although the objective is designed to be near diffraction limited there can still

[3]Thorlabs best-form and positive meniscus lenses
[4]Thorlabs LBF254-200-A
[5]2 Thorlabs LA4765-UV singlets

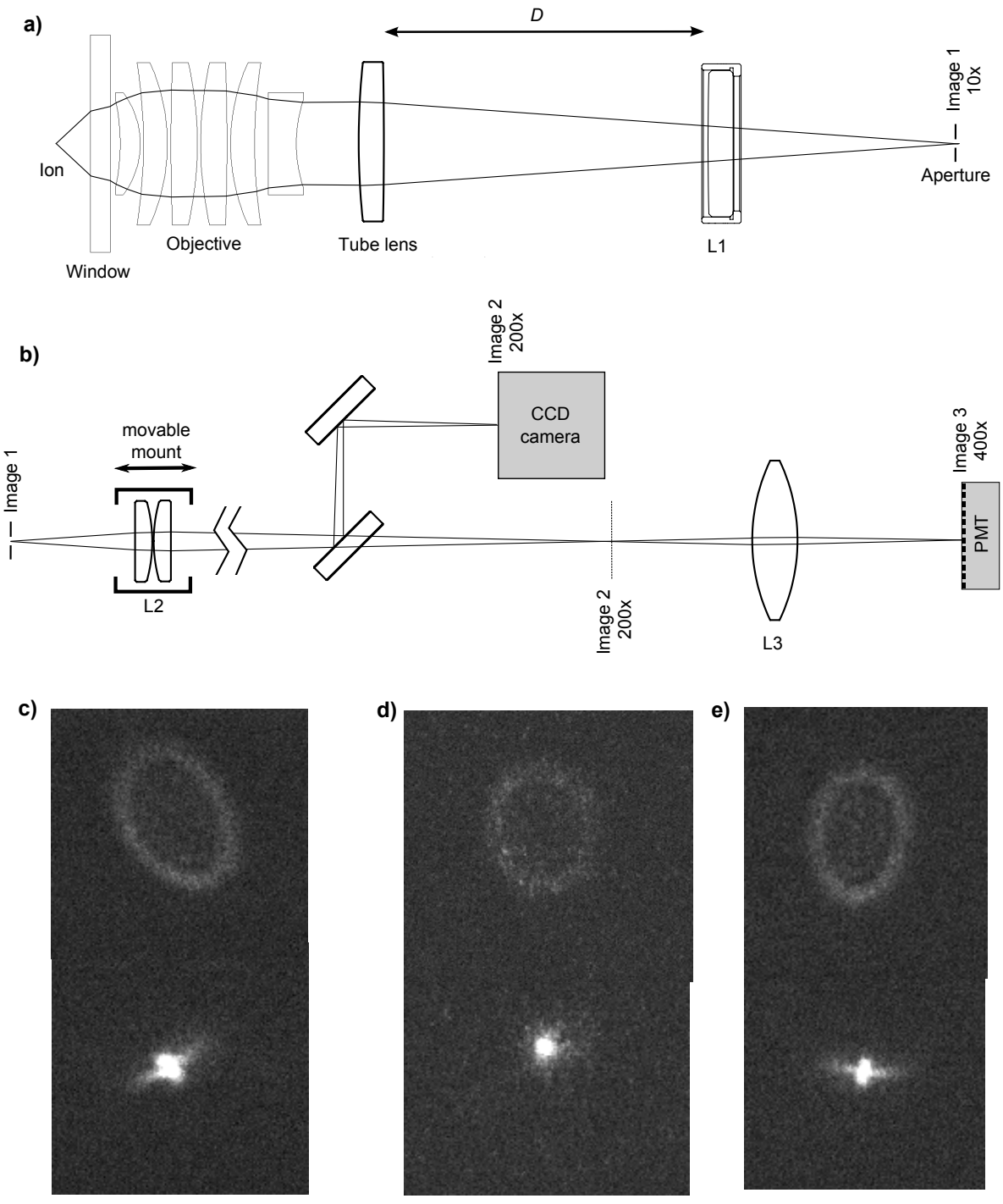

Figure 4.2: **Imaging system for individual detection.** a) First stage imaging using a +200 mm tube lens. A 200 μm $\times$1000 μm aperture is placed at the image plane as a spatial filter. The field of view is set to be $20\times100\mu$m at the ion. b) Second stage imaging used to image the aperture to a camera or a PMT. c) Defocussed (top) and focussed (bottom) image of an ion when astigmatism is undercompensated (D=164 mm). d) Image of the ion when astigmatism is perfectly compensated (D=167mm). e) Image when astigmatism is overcompensated (D=169 mm).

be aberrations introduced from imperfections of the vacuum window and other optical elements in the imaging system. However, since the beam is weakly converging (or diverging) after the tube lens it has a relatively much lower NA and therefore aberrations introduced by the subsequent lens elements are negligible. Therefore, the main contribution of aberration comes from the vacuum window which is situated between the ion and the objective. Due to an NA of 0.37 of the beam at this place very slight misalignments or deviation of the window glass from being perfectly flat can introduce considerable aberrations. We expect to see spherical aberrations due to bending of the window glass in a away that is cylindrically symmetric about the principal axis of the optics. We expect to see 'coma' if the ion is placed off axis and finally 'astigmatism' if the window is not perfectly perpendicular (tilt) to the axis or has a bend that is not cylindrically symmetric. Out of these three aberrations we rule out 'coma' because the ion has to be very close to the principal axis in order to form an image at the aperture (which it does) and the aperture is very well aligned to the principal axis of the objective by mounting them both to a common lens tube.

Since the vacuum window is mounted independently it is more likely to have a tilt which introduces astigmatism in the ion image. This is shown in figure 4.2 c)-e) where we place a slowly focussing cylindrical lens [6] between the tube lens and the aperture and vary its position to perfectly compensate astigmatism. In this figure we show defocussed images of the ion that gives a elliptical or circular halo that is more prominently indicative of uncompensated and compensated astigmatism,

[6]Thorlabs LJ4530RM-A

respectively. After correcting for aberrations the ion image is resolved to 0.55 μm.

For implementing individual state detection of ions we use an array of photo-multiplier tubes [7] which has a quantum efficiency of $\sim 40\%$ at UV. Each channel of the PMT is 0.8 mm wide with a 0.2 mm deadzone between adjacent channels. Due to non trivial electronic signal crosstalk between adjacent channels of the PMT array we map adjacent ions on alternate channels of the PMT. In order to regulate this mapping we implement a third magnification stage for imaging of the ion to the PMT. By changing the position of lens L3 we adjust the magnification to optimize photon counts from each of the five ions on their respective PMT channel.

Figure 4.3 a shows the imaging of individual ions on the channels of a PMT. In this case alternate channels with relatively high photon counts are are the ones that are assigned for state detection for each ion. When a photon is incident on a given channel it generates a photo-electric current which produces a $\sim 10\,\mathrm{mV}$ signal with about 1 ns rise time across a $50\,\Omega$ load. This signal is amplified by a factor of 100 and discriminated against a reference of ~ -1 V which produces a digital TTL signal. This circuit is shown in figure 4.3 b. We use a two stage amplifier that is capacitively coupled to remove any DC signal. The reference voltage on the discriminator is adjusted to remove background noise from a) secondary pulses from internal reflection in the cable b) dark counts that has lower signal strength. Additionally each TTL is stretched to a 40 ns pulse using an FPGA to prevent double counting.

Next we consider the possible sources of measurement cross talk. The cross

[7] Hamamatsu: H7260-200

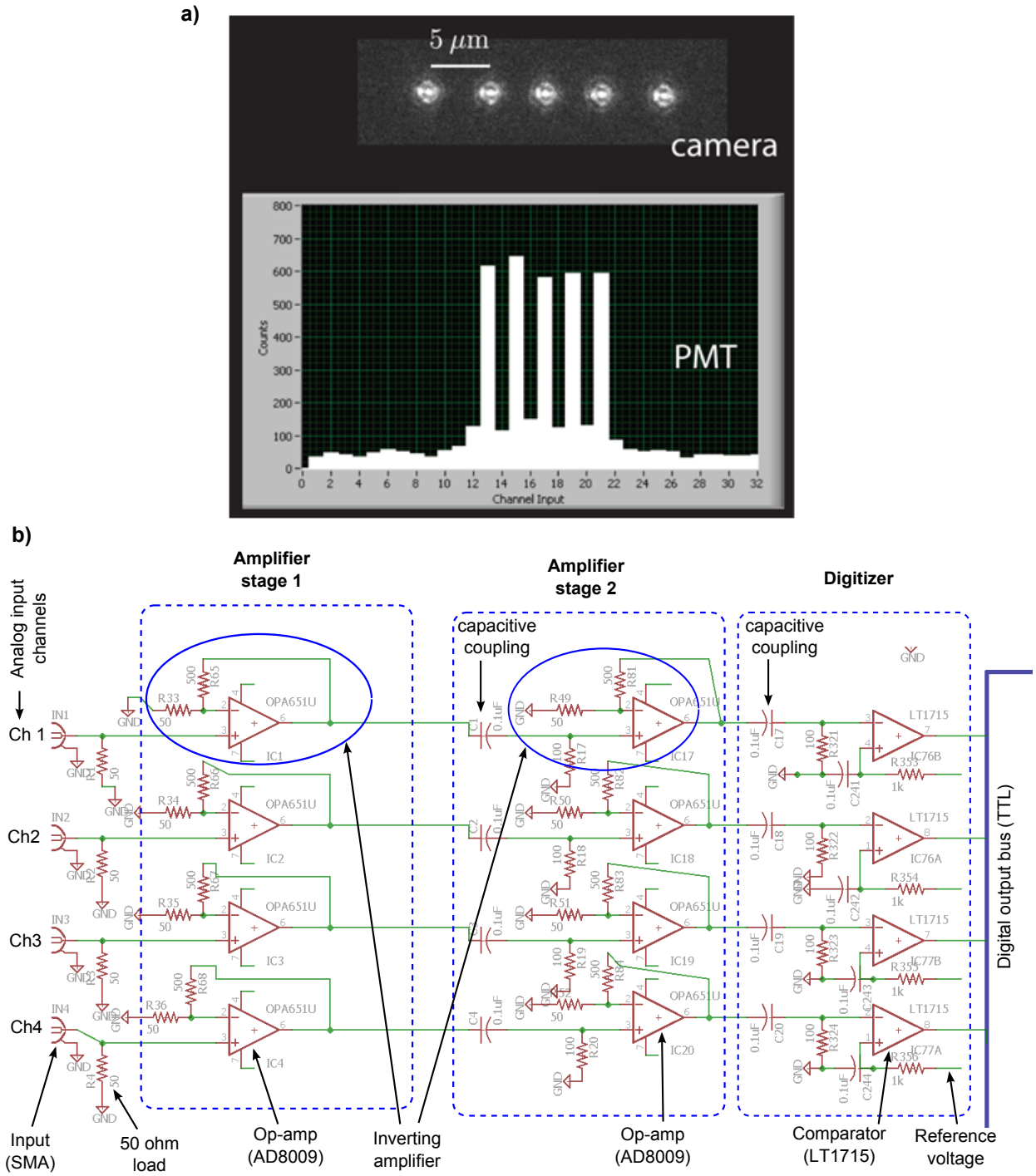

Figure 4.3: **Individual detection using 32-channel PMT array.** a) A linear chain of 5 trapped $^{171}Yb^{+}$ions imaged on a camera and a PMT. The PMT signal is in terms of photon counts for each channel. The optical imaging maps adjacent ion images to alternate channels of a 1D PMT array. b) An analog circuit for amplifying signal from each PMT channel followed by a discriminator that generates a TTL pulses for each incident photon signal. The circuit for one (out of eight) of the amplifier modules is shown that is used for channel-1 through -4 of the PMT array.

talk between photon counts of adjacent ions are dominated by intrinsic signal cross talk between PMT channels where the nearest neighbor cross talk is about 3% where as the to the next to nearest neighbor is about 0.5 %. The second contribution to crosstalk comes from the resolution of the optical imaging system. It is important to remove aberrations that can cause such spillover. After removing all aberrations we achieve a near diffraction limited image with a ratio of the resolution to the inter ion distance being $\frac{0.55\,\mu\mathrm{m}}{5\,\mu\mathrm{m}}$. Although this is within a reasonable limit it is important to note that there is always some residual error due to the outer rings of the point spread function (PSF) which describes the intensity spread of the ion image. This is shown in appendix 1. By choosing alternate PMT channels for mapping the ions we measure a $\sim 1\%$ total spill over in photon counts between nearest ion channels.

In order to experimentally determine the single qubit state detection fidelity and effect of cross on the state detection we look at three relevant scenarios. **a)** Spillover to neighboring ion channels when an ion is prepared in the $|0\rangle$ state (figure 4.4a). We apply the discriminator method to measure the probability of detecting a bright state ($|1\rangle$) state in all three channels and the 0.26 % is the state preparation and measurement (SPAM) error for dark state $|0\rangle$. Since the ion does not scatter many photons in this state the spillover does not affect the nearest channels. **b)** Spillover to neighboring ion channels when an ion is prepared in the bright state $|1\rangle$ (figure 4.4b). Here we see that the SPAM error for the bright state $|1\rangle$ is 0.91 %. Since the bright ion scatters an average of 10 photon during the detection cycle there is higher spillover to neighboring channels. We find that measuring the neighboring ion channels gives a false positive for a bright state with a probability of 0.3 % and

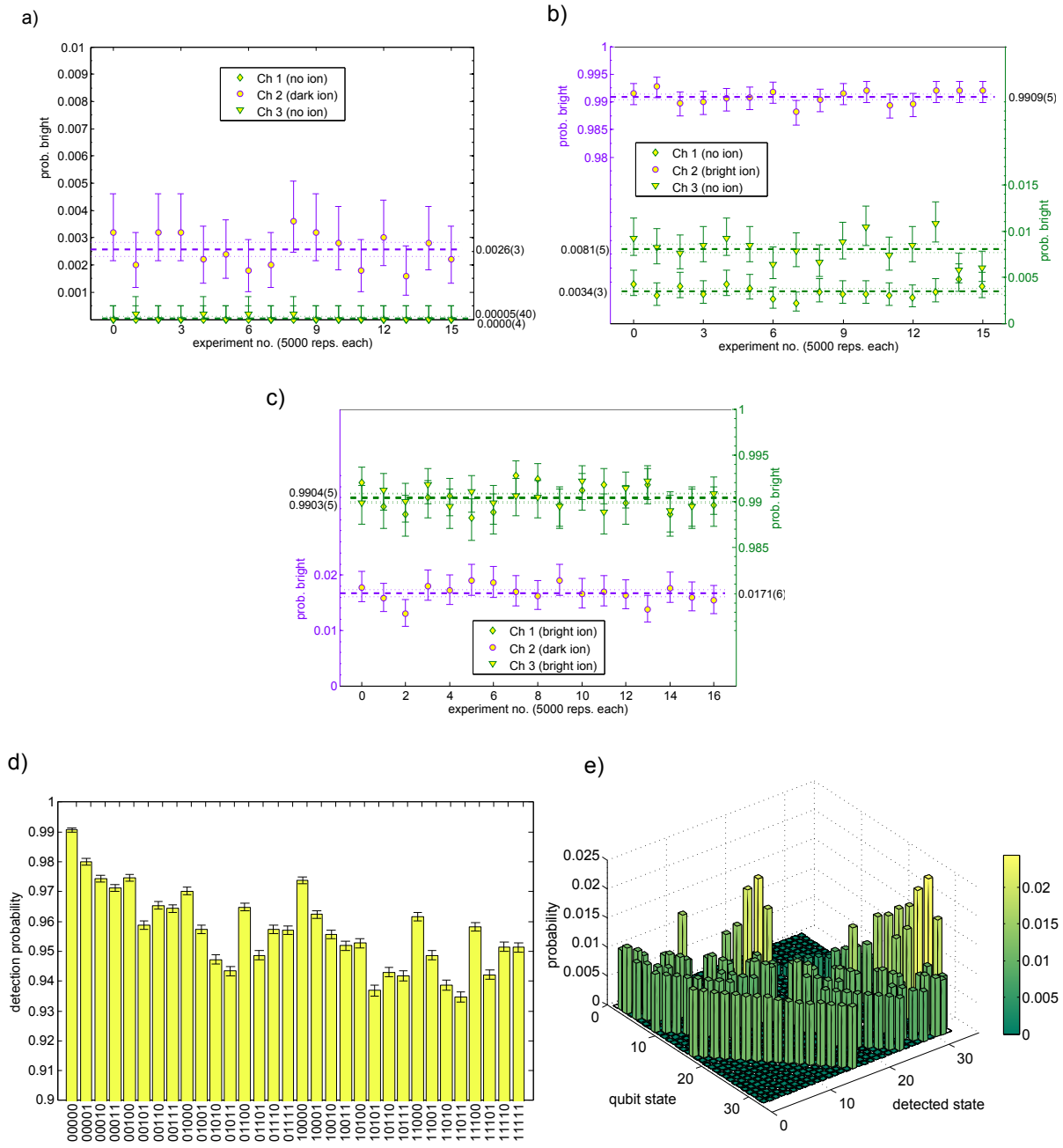

Figure 4.4: **Detection fidelity with crosstalk between PMT channels.** a) Single shot probability (using discriminator method) of detecting bright state $|1\rangle$ in three adjacent PMT channels with a dark ion in the middle channel (prepared in state $|0\rangle$). b) Probability of detecting a bright state with a bright ion in the middle channel. Probability of detecting bright state with the middle ion dark and outer ions bright in a three ion chain. d) State preparation and measurement (SPAM) fidelity for 5-qubit states. e) SPAM cross talk matrix with only off diagonal terms for 5-qubit states.

0.8 %, where the asymmetry comes from the inherent asymmetry of the signal cross talk between neighboring channels of the PMT array itself. **c)** Spillover from two adjacent bright ions when the middle one is in the dark state (figure 4.4c). This gives rise to maximum error due to spillover from bright ions on both side. By comparison with fig. 4.4a we see an additional error of 1.4 % in the dark state detection of the middle ion on top of the SPAM error.

Now we can go ahead and measure the SPAM error matrix for five ions by measuring photon counts from each of the five corresponding PMT channels and applying a discriminator to perform single shot 5-qubit state detection. Figure 4.4 d) and e) shows the SPAM fidelity for each of the 32 states and the probability of measuring the wrong state for each prepared state, respectively. By observation we can deduce that the high SPAM fidelity of state $|00000\rangle$ is due to high single qubit SPAM fidelity of the state $|0\rangle$ and due to to the fact the ideally no photon is scattered by the ions which removes any cross talk issues. On the other hand the SPAM fidelity of state $|11111\rangle$ is 95 % is much lower and is dominated by the single qubit SPAM fidelity (99 %) of state $|1\rangle$ ($0.95 \approx 0.99^5$). The signal cross talk does not play a major part in the SPAM since all the ions are in the bright state. The lowest SPAM fidelity is for the state $|10101\rangle$ where both the single qubit (bright state) SPAM and maximal spillover crosstalk (as in fig. 4.4c) plays a part.

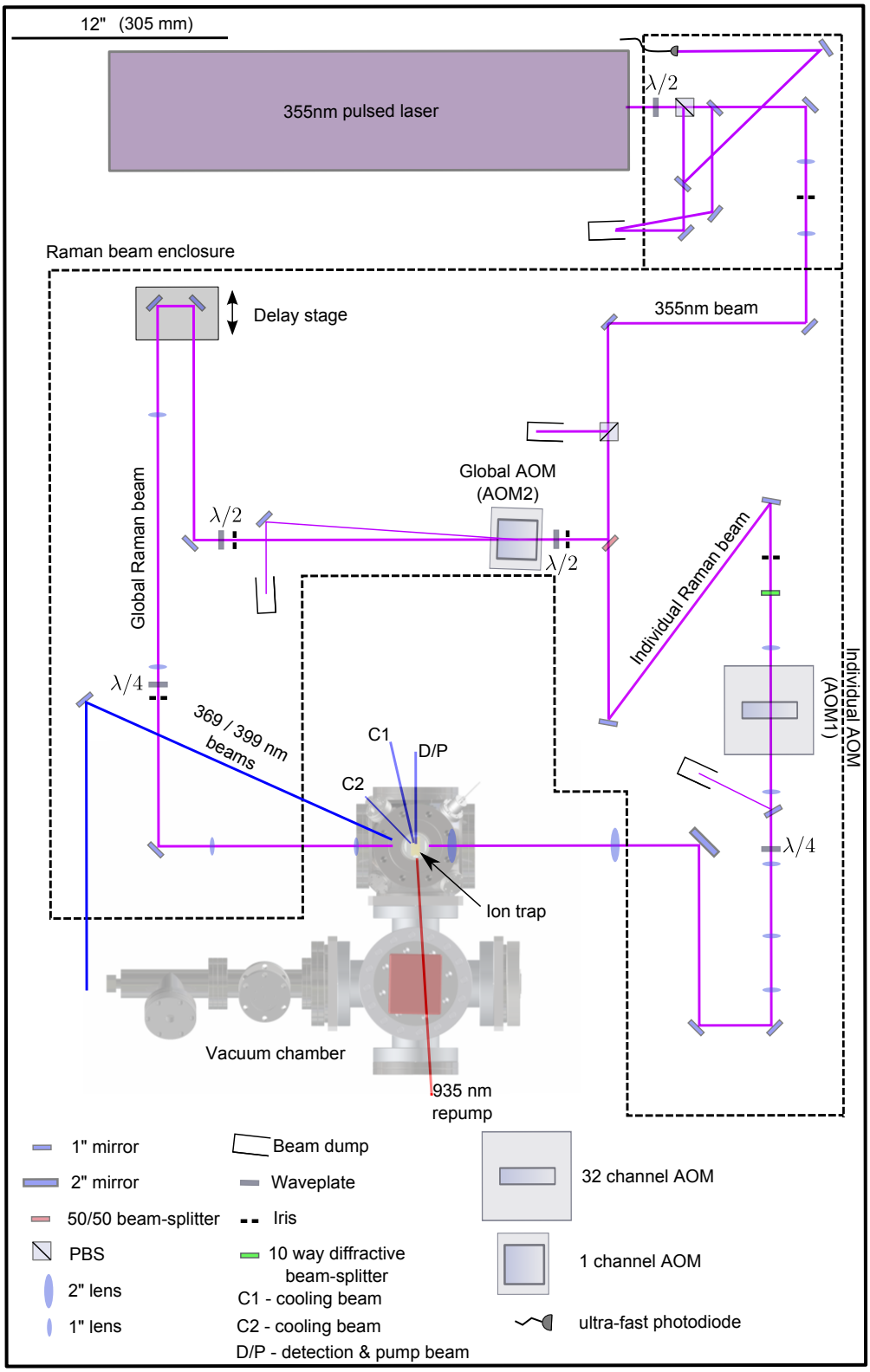

Figure 4.5: **Optics layout for Raman beams.**

4.2 Individual qubit manipulation

Individual addressing of qubits is necessary for implementing quantum algorithms. We use counterpropagating Raman beams for qubit manipulation. Individual qubit addressing is achieved by focussing independent Raman beams on single ions in a chain. The layout of the optical path of the Raman beams is shown in figure 4.5 where a single beam from a 355nm pulsed laser is split using a 50/50 beam splitter. One of these beams is shaped to globally address all five qubits uniformly. This is modulated using a single channel AOM which is driven by an arbitrary waveform generator. The second beam is used for individual addressing where it is split into ten beams using a diffractive optic element (DOE) which acts as a 10-way beam splitter. Each beam is focussed onto individual channels of a 32-channel AOM [8]. By driving each AOM channels with rf signal we can selectively switch on individual Raman beams and drive Raman transitions on corresponding qubits.

In order to optically resolve single ions in the chain for in individual addressing Raman beam is tightly focussed to a 2 μm bean diameter at the ion position. This requires the beam to be of relatively high NA (0.15-0.2 NA) compared to the global Raman beam which is shaped to have gaussian width of 75 μm and 10 μm in the Z- and Y-direction, respectively. Figure 4.6a shows the gaussian picture [75] of beam shaping of a single individual Raman addressing beam where the gaussian beam width is shown at various beam positions. In order to minimize crosstalk between adjacent channels of the 32-channel AOM each beam is focussed to $< 100\mu$m

[8]Harris- Model H-601 Series 32-Channel UV Acousto-Optic Modulator, PN: 66948-226460-G01

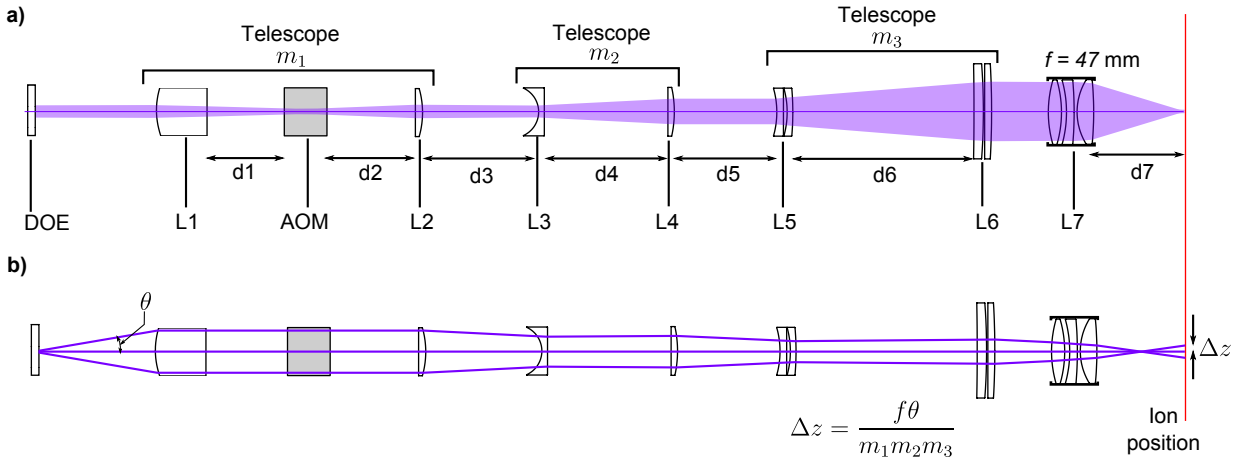

Figure 4.6: **Raman beam individual optical addressing.** a) The Gaussian picture of a single Raman beam. The beam forms a focus at AOM crystal and at the ion position. The beam is magnified by a factor of $m = m_1 m_2 m_3 \approx 40$ using a three stage telescope and forms a ~ 0.15NA after the final focussing triplet. b) Three adjacent rays from the diffractive optic element (DOE) are traced as they go through the optics. The three stage telescope reduce the angular separation between the rays by a factor of m before they hit the final focussing triplet. The spacing of the focussed beam spots at the ion chain is decided by this angle and the effective focal length of the triplet. The distances between optics are $d1 = 65.7; d2 = 81.5; d3 = 67; d4 = 87.5; d5 = 62.2; d6 = 417$ mm. $d7 \sim 40$ mm is the working distance that is adjusted to focus the beam at the ion position.

diameter inside the AOM crystal. This is followed by successive telescopic expansion of the beam by a factor of ≈ 40 which is then focussed to a tight spot using a focusing triplet with a working distance of ~ 40 mm.

Figure 4.6b shows three adjacent rays out of the ten from the DOE. The angular separation between adjacent rays is $\theta = 4.3$ mrad which sets the focal length of lens L1 ($f_1 \approx 91$ mm) such that each of the rays are mapped to adjacent channels of the AOM which are spaced by $\approx 400\,\mu$m. Once the rays travel through the succesive telescopes with magnification $m \approx 40$ the angular separation between the rays is decreased by a factor of m. Therefore at the focal point of the final focussing lens (which is also the ion chain position) the spacing between adjacent focussed spots is given by,

$$\Delta z = \frac{f\theta}{m} \tag{4.1}$$

where f is the focal length of the final focussing triplet L7.

Since the individual addressing beam has an NA of 0.15-0.2 slight optical misalignment can introduce aberrations in the beam. This gives rise to higher intensity and phase noise on the Raman beat-note that drives coherent qubit rotations. Ideally one can improve beam alignment by profiling it on a camera which is particularly hard for small spot sizes due to a resolution limit ($2.2 \times 2.2\,\mu$m) set by the pixels. Therefore, it is preferable to use the ion for this purpose as it not only useful in profiling the intensity but also the phase of the beam.

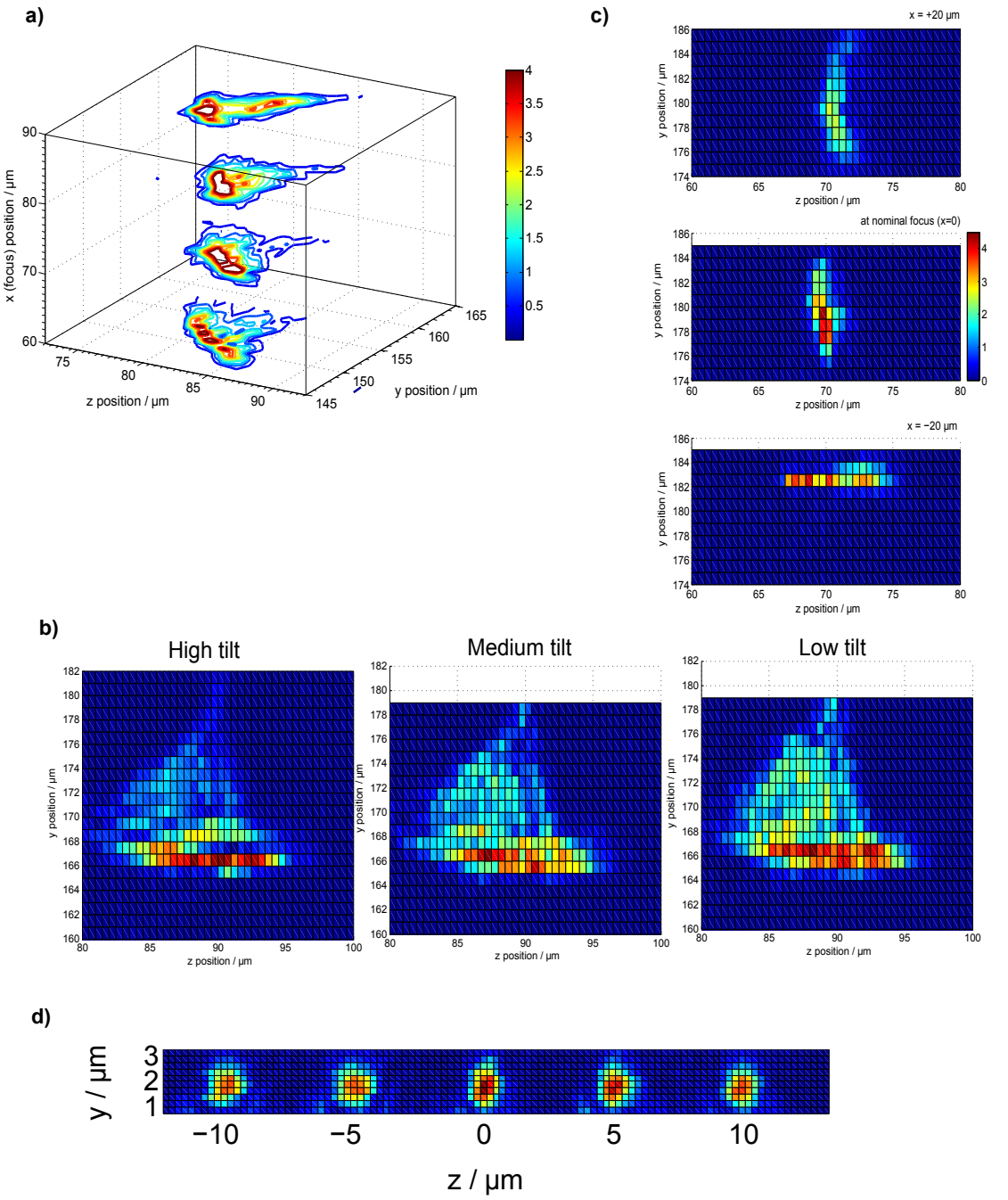

Figure 4.7: **Raman individual addressing beam amplitude profiling.** a) A Z-Y beam profile for the individual Raman beam is made by rotating a single qubit form dark state $|0\rangle$ to bright state $|1\rangle$ and measuring the average number of scattered photons. As the X (focus) direction is scanned the profile shows 'coma' and 'astigmatism'. b) Beam profiles with 'coma' as the tilt between the wave-vector of the beam and the optical axis is reduced thereby reducing 'coma'. c) Beam profiles with 'astigmatism' showing focus in the Z- and Y-direction that occur at two different focal points along the beam direction X. d) Amplitude profiles of 5 individual addressing beams after reducing aberrations and measured by scanning all the beams with a single stationary ion.

Since the Rabi frequency if single qubit rotations is dependent on the Raman beam intensities as $\Omega \propto \sqrt{I_0 I_1} = |E_0||E_1|$ we can use this to measure the electric field amplitude of the individual Raman beam. A single beam is translated in the Z and Y direction in steps as small as 20 nm while rotating a single qubit prepared in state $|0\rangle$. The relative amount of rotation is given by the probability of the qubit in state $|1\rangle$ which in turn is proportional to the field amplitude of the individual Raman beam. Figure 4.7 a-c shows beam profiles for a single beam with aberrations: mainly 'coma' and 'astigmatism'. We expect 'coma' because the wave vector of the beam is not parallel to the optical axis. We expect 'astigmatism' due to a tilt in the vacuum window with respect to the high NA beam after the focussing triplet L7. Both this aberrations are eventually corrected by aligning the optical axis of the lens system to that of the vacuum window and subsequently aligning the beam wave-vector to this axis. It is important to note that the optical path from L3 to L7 (fig. 4.6) has the beam expanding along a path that is not a straight line (fig. 4.5) which leaves room for aberrations that can be introduced from mirror curvatures and decentration of lenses (specially lenses L5 and L6 in telescope m_3).

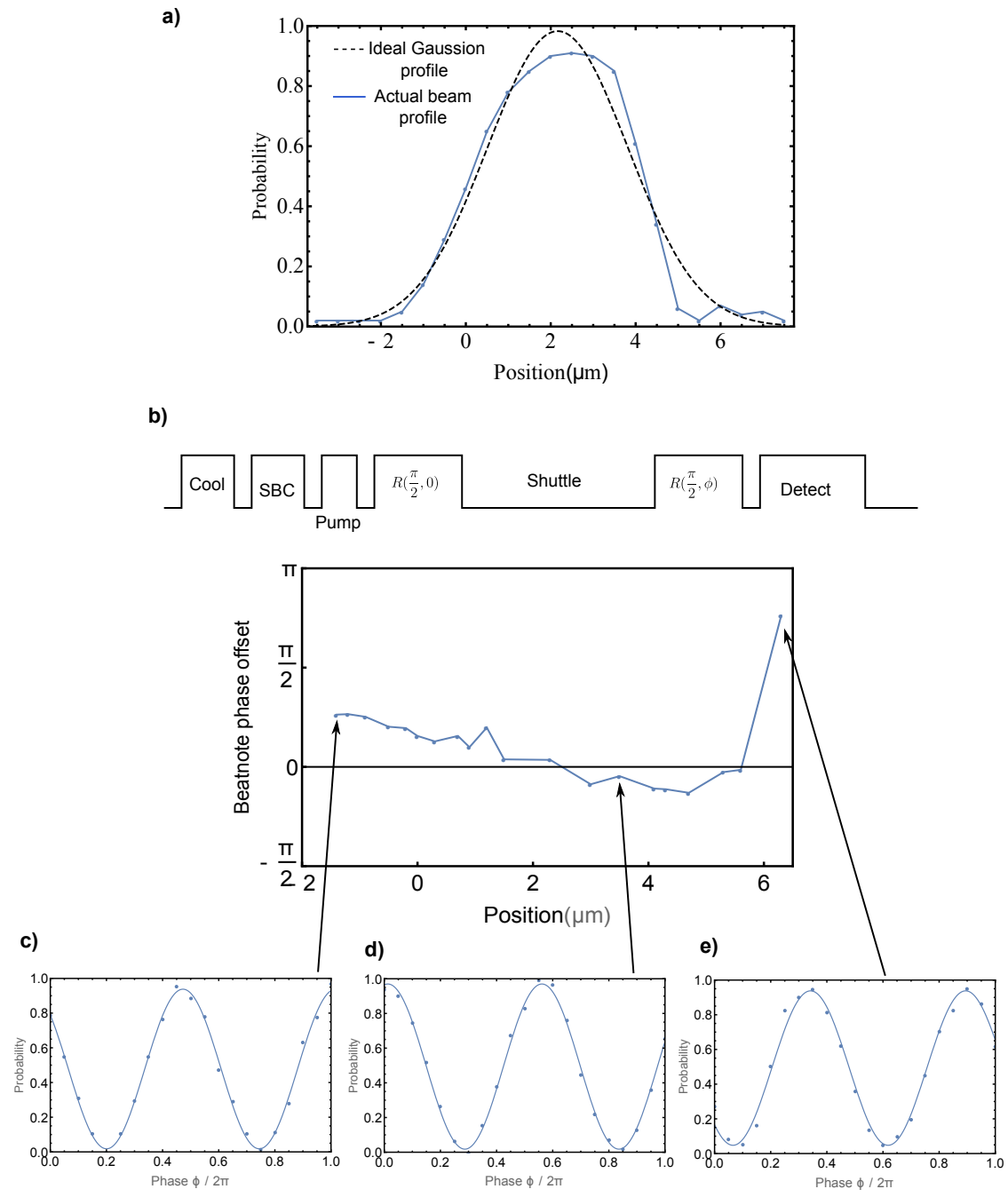

Figure 4.8: **Amplitude and phase profiling of an individual addressing Raman beam.** a) The relative field amplitude across the width of an individual addressing Raman beam given by position dependent Rabi frequency $\Omega(z)$. b) A Ramsey sequence with two $\frac{\pi}{2}$ pulses applied at two beam positions. The phase difference of Raman beat-note as a function of beam position is indicative of a Δk vector projection along Z (linear gradient) and also wavefront distortion due to partial beam clipping (non-linear gradient at the beam edge). This creates distortion is both phase(b) and amplitude(a). c),d),e) Measured Ramsey fringes at different shuttled ion positions showing different phase offsets.

Besides amplitude, a single ion can also be used to profile the phase of the Raman beat-note. In this case we need to shuttle the ion across the Raman beam to sample the position dependent beat-note phase. For this we first tune the beat note to drive 'carrier' Rabi flops as discussed in section 3.4. We note that the off diagonal terms of the interaction Hamiltonian (equation 3.60) has a phase that is given by $\Delta\bar{k} \cdot x + \Delta\phi$ where $\Delta\bar{k} \cdot x$ is the position dependent phase and $\Delta\phi$ is a static phase set by the AOM. In a counterpropagating Raman beam geometry the value of $\Delta\bar{k}$ is $\frac{2\pi}{355}\text{nm}^{-1}$ in the radial direction (X) and should ideally be zero along the axial direction Z. However, a small projection of $\Delta\bar{k}$ along Z or optical aberration (wavefront distortion of individual Raman beam) can give rise to weak phase gradients in Z.

In figure 4.8 a we first look at an amplitude profile of a Raman beam by measuring the position dependent Rabi rate $\Omega(z)$. In order to measure the Z-dependent phase profile we perform a Ramsey interferometry where we fist apply a $\frac{\pi}{2}$ rotation at the center of the beam and then shuttle the ion to a different Z-position to perform a second $\frac{\pi}{2}$ rotation. The position dependent beat-note phase in this case changes the axis of the second $\frac{\pi}{2}$ rotation with respect to the first one in the Bloch sphere picture (chapter 5) which fails to rotate the qubit from $|0\rangle$ to state $|1\rangle$ in two successive $\frac{\pi}{2}$ pulses. However, we can figure out the the difference in these two phases by scanning $\Delta\phi$ of the second $\frac{\pi}{2}$ pulse (using AOM1) and obtain Ramsey interferometric fringes of the probability of preparing state $|1\rangle$ as a function of $\Delta\phi$. Figure 4.8b shows this sequence and the relative phase difference across the beam which are calculated at each position using Ramsey fringes (fig. 4.8c-e).

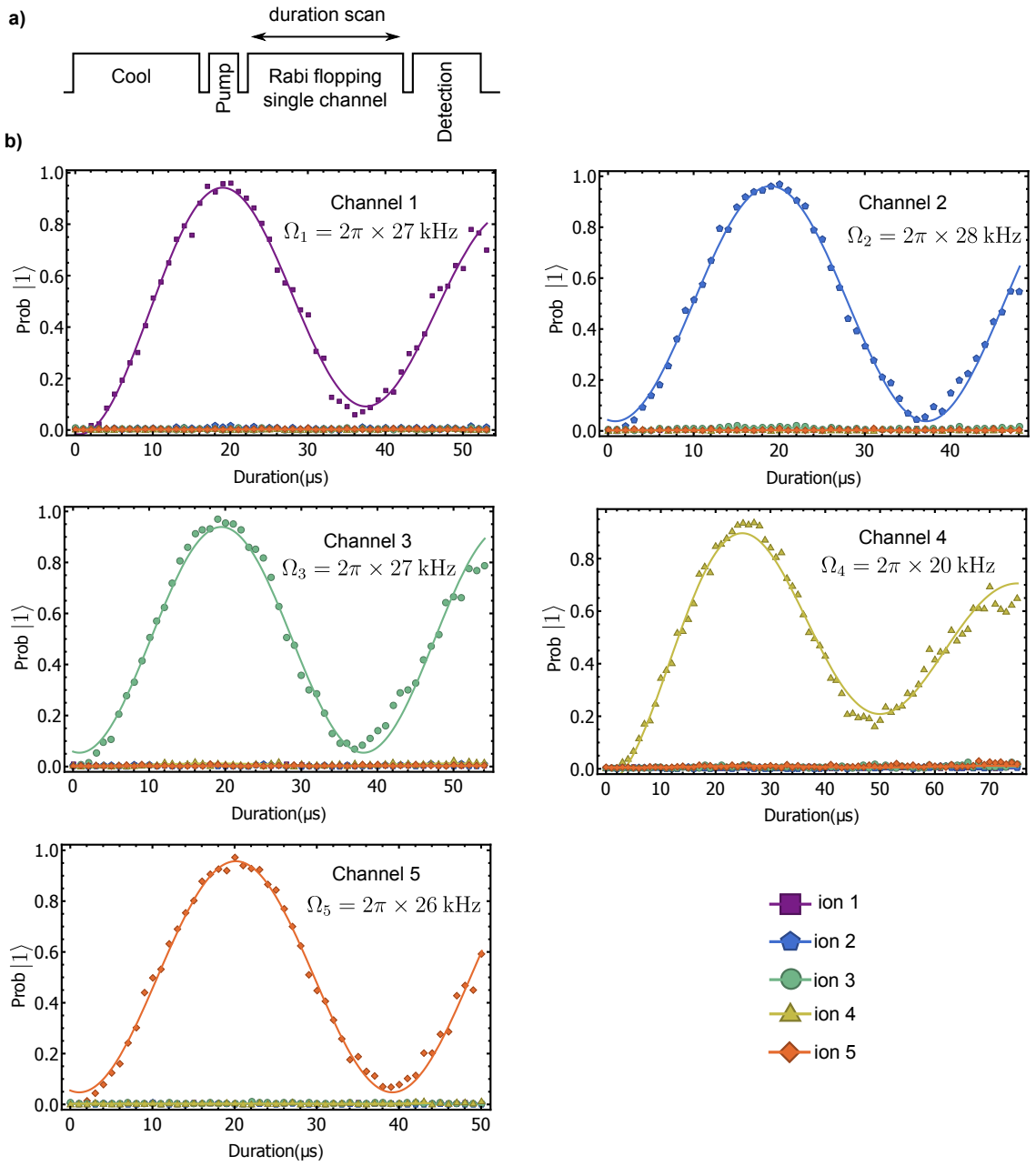

Figure 4.9: **Rabi flopping on individual ions using individual channels.** a) Experimental sequence where we perform carrier Rabi flopping on each ion without side band cooling. b) If the crosstalk die to Raman beam spillover is low enough then all the qubits except for the one addressed stays in state $|0\rangle$. The addressed qubit performs Rabi flopping. The decay is due to Rabi rates interfering due to the ions being in a thermal state with $\bar{n} > 0$. See figure 3.6. The fit is an exponentially decaying sine function that is used to extract the qubit specific Rabi rate Ω_i

In order to individually address ions, each individual addressing Raman beams are focussed to a 2 μm gaussian beam diameter as shown in figure 4.7 d. We choose five (out of ten) beams from the DOE that are modulated by five adjacent channels of the multi channel AWG. The individual channels are driven by rf signal that is generated from the beat-note lock setup (it drives AOM 2 as in figure 3.4). The global beam is switched by the global AOM (AOM1 as in figure 3.2) which is driven by an arbitrary waveform generator (AWG) that is used to tune the beat-note detuning from carrier resonance μ (as in equation 3.60) and the phase in the off-diagonal terms of the interaction hamiltonian $\Delta\phi = \phi_0 - \phi_1$. Here, ϕ_1 is static where as ϕ_0 can be varied by changing the phase of the rf that drives the global AOM (AOM1). For any given ion i in a the chain, the beat-note offset phase $\Delta k_i \cdot x_i + \Delta\phi$ is set to 0 at $\phi_0 = 0$. This defines rotation of the qubit about the $X-$axis in the Bloch sphere (to be discussed in the next chapter). By simply changing $\phi_0 = \frac{\pi}{2}$ the rotation axis can be change to Y. However, it is important to note that since it is most likely that the beat-note wave vector Δk_i varies slightly across ions along with their positions x_i, the $X-$axis of rotation is not the same across the ions in the absolute frame (lab frame) but relative to their fixed positions and the time t_0 at which coherent rotations start, the X-axis of rotation X_i for each qubit is well defined. As far as the magnitude of the Rabi frequency on a single ion is concerned, it can be expressed as,

$$\Omega = KP\sqrt{\frac{p(1-p)\eta_G\eta_I\eta_{DOE}}{2bA_IA_G}} \tag{4.2}$$

where P is the average power from the pulsed laser, p is the fraction of power that goes to the global Raman beam, η_G and η_I are the diffraction efficiencies of the global and individual AOMs respectively, η_{DOE} is the diffraction efficiency of the beamsplitter (see figure 4.5) and b is the number of beams it splits into. The effective area of the spot size of the individual and global beams at the ion are given by A_I and A_G, respectively where $\frac{A_G}{A_I} \approx 200$. K is a proportionality constant that depends on the single photon coupling terms in the Raman transition and the pulsed laser characteristics, both of which are constants in the experiment (as shown in equation 3.54). It also depends on the polarization of the Raman beams which although may slightly vary across the individual Raman beams are nonetheless static as long as the optics is not modified. Figure 4.9 shows Rabi flopping on individual ions in a five ion chain performed by switching individual channels of the AOM.

In order to measure the crosstalk due to optical spillover we turn on one of the AOM channels to drive carrier Rabi flopping on one of the ions in the chain. Any residual optical spillover can cause neighboring (non addressed) ions to undergo much slower Rabi flopping. By measuring the ratio of the Rabi frequency of unaddressed ions to that of the one addressed we obtain the crosstalk matrix for individual Raman addressing. This data is shown in figure 4.10.

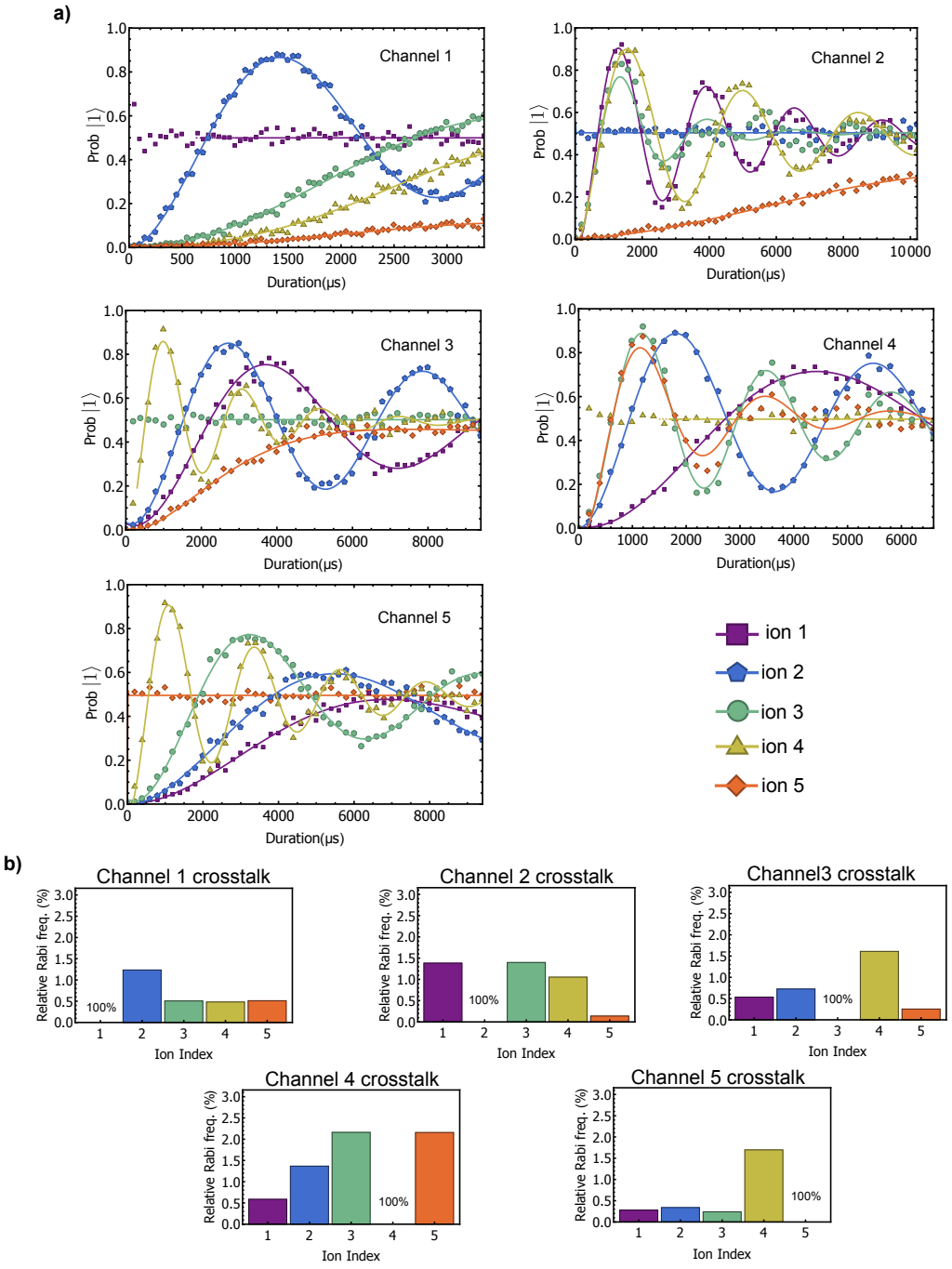

Figure 4.10: **Crosstalk in Rabi frequency due to individual Raman beam spillover.** a) Rabi flopping duration scans on all five qubits. The addressed ion flops quicker and damps to 50% bright state over a long duration scan. The flopping on other ions indicate that this damping is related to the ion temperature and not the qubit coherence. b) Ratio of Rabi rates that give the Raman spillover matrix elements for five addressing beams (switched by five AOM channels) over five qubits.

Chapter 5: Quantum Gates

In order to implement a quantum algorithm the first step is to express it as a sequence of gate operations. Usually algorithms are constructed out of sequences of logic gates that have roots in classical computing. For example, the controlled not gate which is analogous to a two bit addition (modulo 2) or an XOR operation is frequently used as a two-qubit gate. In a physical quantum computing platform such as trapped ions, these standard gates are not available by default. However, one could in principal construct them using a collection of more fundamental unitary operations that are native to the system. In trapped ion chains single qubit Rabi-rotations and two qubit entangling gates forms the basis of constructing any modular logic gate such as the controlled-NOT, conditional-phase, Hadamard etc. In this chapter we will discuss the implementation of these native operations and the subsequent construction of standard logic gates using them.

5.1 Native single qubit R-gate

It is usually quite useful to represent a single qubit wave function as a Bloch vector. In this picture this is the vector position of a point on the surface of the

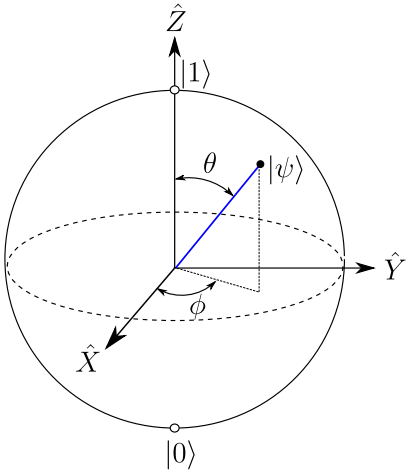

Figure 5.1: **Single qubit representation on a Bloch sphere** A single qubit can be in a superposition of $|0\rangle$ and $|1\rangle$ which being the eigen states of σ_z and are situated at the poles of the Bloch sphere. The angle θ gives the relative amplitude of the coefficients where $|C_0| = \sin(\theta/2)$, $|C_1| = \cos(\theta/2)$. The angle ϕ gives the relative phase between C_0 and C_1.

Bloch sphere (figure 5.1) with the center of the sphere as the origin. Here we can conveniently describe the qubit using the angles θ and ϕ as,

$$|\psi\rangle = \sin(\theta/2)|0\rangle + e^{i\phi}\cos(\theta/2)|1\rangle \tag{5.1}$$

In this picture single qubit gates are nothing but rotation of this vector $|\psi\rangle$ about an axis that passes through the origin of the Bloch sphere. In order to implement this we can apply the single-qubit rabi flopping Hamiltonian as discussed in section 3.4 (equation 3.60) such that it resonantly drives the carrier Rabi flopping by setting $\mu - \Delta_s = 0$. In this case the Bloch vector rotates about an axis that is on the equator of the Bloch sphere. The relative position of this axis with respect to the

$\hat{X}$ axis is then given by the off-diagonal phase of the Hamiltonian,

$$H_I = \begin{bmatrix} 0 & \frac{\Omega}{2}e^{i\phi} \\ \frac{\Omega}{2}e^{-i\phi} & 0 \end{bmatrix} = \frac{\Omega}{2}\sigma_\phi \tag{5.2}$$

Here $\phi = \Delta\bar{k} \cdot x + \Delta\phi$ defines the Pauli spin operator $\sigma_\phi = \cos(\phi)\sigma_x + \sin(\phi)\sigma_y$, where σ_x and σ_y are the Pauli matrices. In order to define an axis of rotation we assign $\phi = 0$ for the fixed ion position x and for $\phi_0 - \phi_1 = \Delta\phi = 0$ (where we have individually set $\phi_0 = 0$ and $\phi_1 = 0$). The Hamiltonian in this case is given by $H_I = \Omega\sigma_x$. By simply setting $\phi_0 = \pi/2$ we can rotate about the Y axis in which case the Hamiltonian is $H_I = \Omega\sigma_y$. This is implemented by shifting the phase of the rf that drives the global AOM.

In the general form the rotation about an arbitrary axis along the equator can be expressed as the unitary evolution $U(t) = e^{-iH_I t} = e^{-i\frac{\Omega}{2}t\sigma_\phi} = e^{-i\frac{\theta}{2}\sigma_\phi}$. This gives us the single qubti native R-gate that is defined as,

$$R_\phi(\theta) = \begin{bmatrix} \cos\left(\frac{\theta}{2}\right) & -i\sin\left(\frac{\theta}{2}\right)e^{-i\phi} \\ -i\sin\left(\frac{\theta}{2}\right)e^{i\phi} & \cos\left(\frac{\theta}{2}\right) \end{bmatrix} \tag{5.3}$$

where a rotation of the qubit about X axis by an amount θ is denoted by $R_{\phi=0}(\theta) = R_x(\theta)$. Similarly we can also define $R_y(\theta)$ where $\theta = \Omega t$. The rotation angle in this case is decided by the duration t of the carrier pulse and the Rabi frequency Ω which is pre-calibrated for each of the five qubits in the trap (figure 5.2).

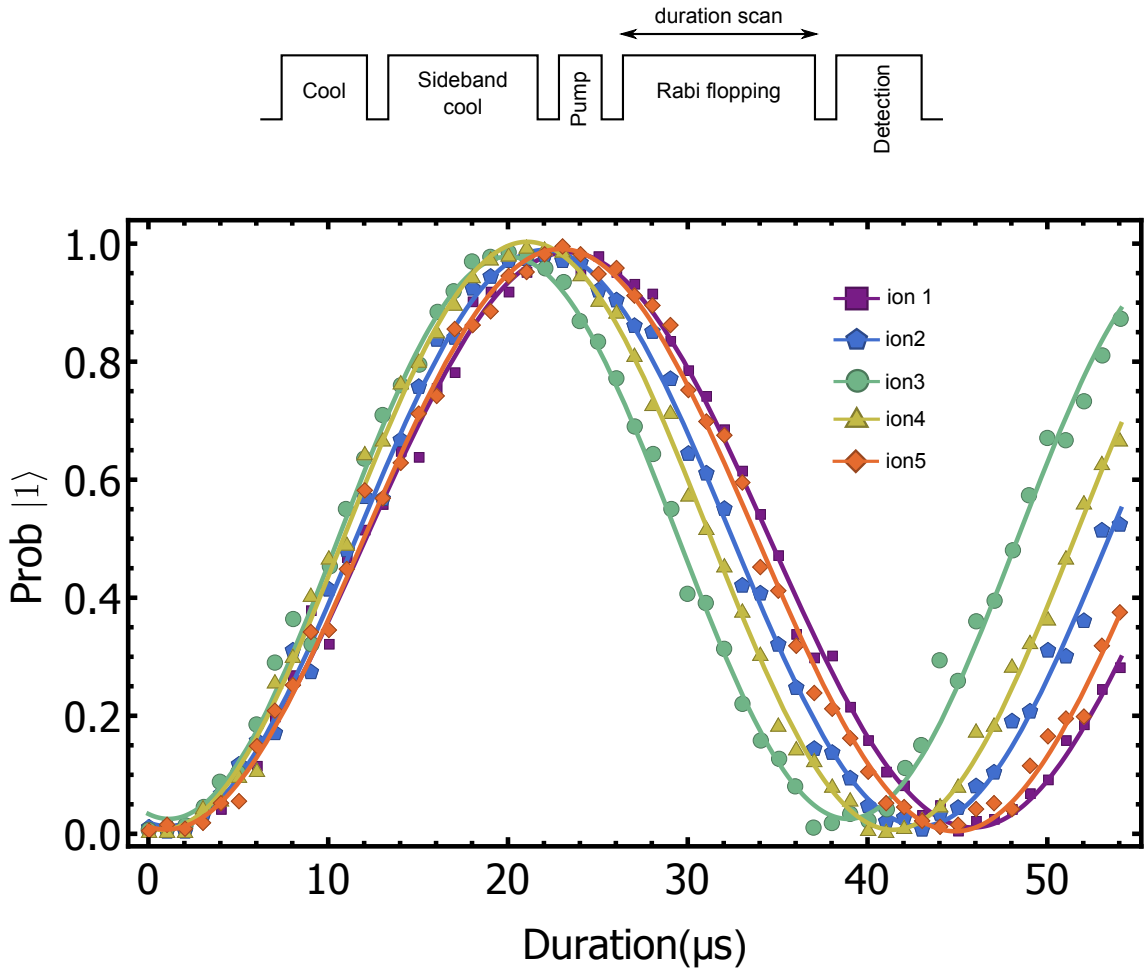

Figure 5.2: **Calibration of Single qubit Rabi-frequencies for 5 ions.** A chain of five ions are cooled to near the motional ground state in the radial trap direction using Raman sideband cooling. The Raman beatnote is tuned to the resonance of the carrier transition and all ions are driven simultaneously. The Rabi frequencies are obtained by fitting the oscillation in the probability of the bright state for each ion ($P_{|1\rangle} = \sin^2(\frac{\Omega}{2}t)$).

5.2 Native two qubit XX-gate

Besides single qubit gates, a quantum algorithm also requires two qubit gates. These gates can be considered as a conditional R-gate where a rotation is performed on one of the qubits based on the state of the second one. As a result of this operation they tend to entangle the two qubits. In a chain of trapped atomic ions a conditional gate can only be performed if the state of one qubit affects another one through a spin-spin interaction [76, 77]. $^{171}Yb^{+}$'clock' qubits are naturally isolated from the environment and from other qubits in a linear chain which makes them good quantum memories. Therefore, invoking the interaction between the spins of any two qubits in a chain is a complicated problem.

In order to address this problem it was proposed that the qubit information could be transferred to the motional mode of the trapped ion chain [22, 40]. The motional modes being distributed through the entire length of the chain serves as a quantum information bus that can now be used to mediate the spin-spin interaction between any two ions in the chain [78, 79]. We can understand how this works by first looking at the spatial and spectral structure of the normal modes of motion of an ion chain [43].

5.2.1 Normal modes of motion

As discussed in chapter 2 an ion is trapped using a harmonic confinement in all the three directions. With multiple ions in the trap we can make a liner

chain configuration by making the axial trap frequency ω_z much smaller than the transverse trap frequencies ω_x and ω_y. The ions form a liner chain due to the combined effect of the trap confinement and the Coulomb repulsion between the ions. The equilibrium positions of the ions are then given by the minimum energy configuration of the system where the attractive potential of the harmonic trap balances the Coulomb repulsion between the ions [43]. Now, if we displace the ions from their equilibrium positions then they not only experience a restoring force from the harmonic trap ($-m\omega^2\Delta x$) but also from the strong Coulomb force from other ions in the trap due to a slight change in the distance between them. In the regime where this displacement is small this can be imagined as a system of coupled harmonic oscillators [80]. This gives rise to a set of normal modes of motion of the entire ion chain where each mode oscillates at a unique frequency and has a displacement vector that defines the relative movement of each ion of the chain. By treating each of the orthogonal trapping directions (x,y,z) independently we can obtain a set of normal modes for each direction of the harmonic trap. Here the modes along the ion chain direction z are the axial modes whereas those along the x and y are referred to as the radial (transverse) modes. For N ions in the trap there are N normal modes along each direction. In the experiment we have $N = 5$ ions where we use the transverse modes along x as the quantum bus. On order to find the normal modes it is sufficient to know the positions of each ion (z_i) along the axial direction and the trap frequencies ω_x and ω_z which can be experimentally measured by driving axial and radial motional sideband transition using a single trapped ion. The transverse mode eigen frequencies $\omega_k = \sqrt{\lambda_k}\omega_z$ and the normal

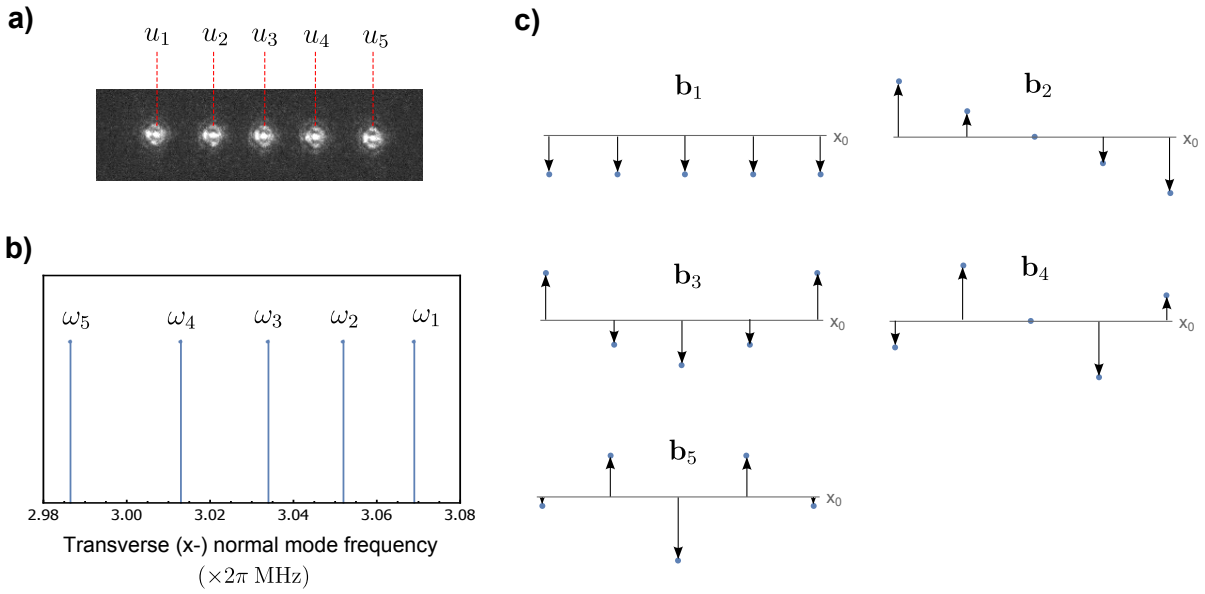

Figure 5.3: **Transverse normal modes of motion for 5 ions.** a) A linear chain of 5 trapped ions. The normalized axial positions $\{u_i\}$ are measured using the camera image to be $\{-1.80738, -0.840048, 0., 0.857019, 1.79889\}$ where the axial trapping frequency is $\omega_z/2\pi = 0.270$ MHz. b) Experimentally measured frequencies of the transverse normal modes along the $X-$direction using Raman sideband spectroscopy. Here $\{\omega_i\}/2\pi = \{3.0692(2), 3.0522(2), 3.0344(2), 3.0127(2), 2.9867(2)\}$ MHz. c) The normal mode vectors $\mathbf{b}_k$ showing the collective displacements of ions (shown in magnitude and direction by arrows) from their equilibrium position x_0.

mode eigen vectors $\mathbf{b}_k$ can be obtained by the diagonalization of the matrix A with $A\mathbf{b}_k = \lambda_k \mathbf{b}_k$. Here, the matrix A is given by [78],

$$A_{m,n} = \begin{cases} (\frac{\omega_x}{\omega_z})^2 - \sum_{p=1, p\neq j}^{N} \frac{1}{|u_n - u_p|^3} & \text{if } n = m \\ \frac{1}{|u_n - u_m|^3} & \text{if } n \neq m \end{cases} \tag{5.4}$$

Here we use the normalized ion positions $u_i = z_i/l_0$ where the length scale $l_0 = (e^2/4\pi\epsilon_0 M\omega_z^2)^{1/3}$. The eigen vector $\mathbf{b}_k$ corresponds to the transverse mode k with a relative displacement of the $j-$th ion given by the $j-$th component of the

vector $\mathbf{b}_k^j$. Figure 5.3 shows the experimentally measured normal mode frequencies for 5 trapped ions. The normal mode vector $\mathbf{b}_1$ is the common mode of motion where all the ions have the same amplitude. This is equivalent to the case of a single trapped ion which is why the common mode frequency is the same as the trap frequency ($\omega_1 = \omega_x$).

5.2.2 The spin-spin interaction

In a chain of trapped ions a two qubit spin-spin interaction is mediated by the normal modes of motion of the ion chain. In this scheme a qubit spin is coupled to a normal mode of motion of the chain (using a sideband transition) which leads to an entanglement of the spin state to the motional state. Since the motional mode is common to the entire chain we can now apply another set of sideband rotations that imprints the motional state back to the spin state of a second qubit leaving the motional mode in its original state and the two spins entangled. This method was originally proposed in reference [22] which used discrete rotations at the sideband transitions in order to implement the entangling gate operation. However, this requires the motional state to be initialized to the ground state (n=0) with high fidelity which is a challenging task when there are many modes of motion with non zero heating rates. Therefore, for practical reasons it is convenient to choose a second scheme, originally proposed in reference [76, 81, 82] where the spins of two qubits are continuously coupled and decoupled from the motional mode by simultaneously driving an off resonant red and blue sideband transition on each of the qubits. To

show how this works we can start with the generic Hamiltonian of the single spin Rabi flopping as derived in chapter 3 (equation 3.62) and apply it to the $i-$th ion in the chain. If we shift the detuning μ by the same amount as the stark shift Δ_s we can set $(\mu - \Delta_s) \rightarrow \mu$ where μ is now the detuning from the Stark shifter carrier transition. We rewrite the Hamiltonian as,

$$H_I = \Omega_i e^{i\mu t} e^{i(\Delta\bar{k}.x_i + \Delta\phi_i)} \sigma_i^+ + H.c. \tag{5.5}$$

where we are interested in expanding the term $\Delta\bar{k}.x_i$. First we recall that $\Delta\bar{k} = \bar{k}_j^0 - \bar{k}_{j+l}^1$ is the difference in wave vectors of the $j-$th combline of Raman beam-1 and $(j+l)-$th combline of Raman beam-2 which is considered a constant for all pairs of comb lines separated by a frequency of $l \times \omega_r$. Since the $\Delta\bar{k}$ is directed along X we express the position operator x_i in terms of the X transverse normal modes (fig 5.3) as $x_i = \sum_p^N X_{i,p}^0 (a_p + a_p^\dagger)$ where a_p and $a_p^\dagger$ are the lowering and raising operator of the $p-$th normal mode and $X_{i,p}^0 = \mathbf{b}_p^i \sqrt{\frac{\hbar}{2M\omega_p}}$ is the zero point spread of the ion. Now we can write the term $\Delta\bar{k}.x_i$ as,

$$\Delta\bar{k}.x_i = \sum_{p=1}^{N} \eta_p^i \left(a_p + a_p^\dagger\right) \tag{5.6}$$

where the Lamb-Dicke parameter $\eta_p^i = |\Delta\bar{k}| X_{i,p}^0$. In the so called Lamb-Dicke limit the spatial extent of the ion motion in vibrational level n does not see much variation of the driving beatnote phase which is aptly described by the relation $(\eta_p^i)^2(n+1) \ll 1$. This allows us to expand the term $e^{i\Delta\bar{k}.x}$ only upto the first order and give an

approximate expression $e^{i\Delta\bar{k}.x} \approx 1 + i\Delta\bar{k}.x$. By substituting this in the Hamiltonian in equation 5.5 and going to the motional rotating frame with respect to $H_0 = \sum_{p=1}^{N} \omega_p a_p^\dagger a_p$ we get.

$$H_I = \left[\Omega_i \sigma_i^+ + i \sum_{p=1}^{N} \eta_p^i \Omega_i (a_p e^{-i\omega_p t} + a_p^\dagger e^{i\omega_p t}) \sigma_i^+\right] e^{-i(\mu t + \Delta\phi_i)} + H.c. \tag{5.7}$$

In order to achieve spin-spin interaction we need to drive the red and blue sidebands off-resonantly. To implement this we can tune the beatnote close to the blue sideband such that $\mu = \omega_p + \delta_p$ where δ_p is a small detuning from the $p-$th mode. The resulting Hamiltonian drives an off-resonant blue sideband transition. For the red sideband we can apply a beatnote with an equal and opposite detuning $-\mu$. When both the beat notes are applied simultaneously the resulting Hamiltonian is of the form,

$$\begin{aligned}
H_{MS} =& \frac{\Omega_i}{2}\left[1 + i\sum_{p=1}^{N} \eta_p^i (a_p e^{-i\omega_p t} + a_p^\dagger e^{i\omega_p t})\right]\left(e^{-i(\mu t + \Delta\phi_i^b)} + e^{-i(-\mu t + \Delta\phi_i^r)}\right)\sigma_i^+ + H.c. \\
=& \Omega_i \left[1 + i\sum_{p=1}^{N} \eta_p^i (a_p e^{-i\omega_p t} + a_p^\dagger e^{i\omega_p t})\right]\cos(\mu t - \phi_i^m)\sigma_i^+ e^{-i\phi_i^s} + H.c. \\
=& \Omega_i \cos(\mu t - \phi_i^m)\sigma_{\phi_i^s}^i + \Omega_i \sum_{p=1}^{N} \eta_p^i \cos(\mu t - \phi_i^m)(a_p e^{-i\omega_p t} + a_p^\dagger e^{i\omega_p t})\sigma_{\phi_i^s - \pi/2}^i
\end{aligned} \tag{5.8}$$

where we define $\phi_s^i = (\Delta\phi_i^r + \Delta\phi_i^b)/2$ and $\phi_m^i = (\Delta\phi_i^r - \Delta\phi_i^b)/2$. The first term of the Hamiltonian shows the off resonant carrier transition where the spin operator $\sigma_{\phi_i^s}^i = \cos(\phi_i^s)\sigma_x^i + \sin(\phi_i^s)\sigma_y^i$. Here ϕ_s^i defines the axis of rotation in the Bloch sphere(see equation 5.2). The second term in the Hamiltonian defines a spin dependent force on the ion. The spin operator in this term is defined by $\sigma_{\phi_i^s - \pi/2}^i = \cos(\phi_i^s - \pi/2)\sigma_x^i +$

$\sin(\phi_i^s - \pi/2)\sigma_y^i$. It is important to note that the spin phase ϕ_s^i is simply defined by the phases (ϕ_0 and ϕ_1) of the rf frequencies that drives the Raman beam AOMs [83]. By setting the phase of the global AOM $\phi_0 = \pi/2$ we get $\phi_i^s = \Delta\phi_i^r = \Delta\phi_i^b = \pi/2$ and $\phi_i^m = 0$, which results in the following Hamiltonian,

$$H_{MS} = \sum_i \Omega_i \cos(\mu t - \phi_i^m)\sigma_y^i + \sum_i \sum_{p=1}^{N} \Omega_i \eta_p^i \cos(\mu t - \phi_i^m)(a_p e^{-i\omega_p t} + a_p^\dagger e^{i\omega_p t})\sigma_x^i \quad (5.9)$$

where the summation over i indicates multiple qubits driven with the strength Ω_i. In the limit where $\Omega_i \ll \mu$ the off resonant carrier transition is weak and hence can be neglected [84, 85]. The resulting Hamiltonian that is responsible for the qubit evolution is,

$$H_{MS}(t) = \sum_i \sum_{p=1}^{N} \Omega_i \eta_p^i \cos(\mu t - \phi_i^m)(a_p e^{-i\omega_p t} + a_p^\dagger e^{i\omega_p t})\sigma_x^i \quad (5.10)$$

which can be exponentiated using the Magnus formula to obtain the evolution operator,

$$U(\tau) = exp\left[-i\int_0^\tau dt H_{MS}(t) - \frac{1}{2}\int_0^\tau dt_2 \int_0^{t_2} dt_1 [H_{MS}(t_2), H_{MS}(t_1)]\right] \quad (5.11)$$

The higher order terms of the expansion essentially go to zero due to the commutation relations of a_p and $a_p^\dagger$. From the above expression we observe that the first term has a single-spin operator σ_x^i where as the second term contains two-spin operators of the form $\sigma_x^i\sigma_x^i = \mathbb{I}$ (which adds an unimportant global phase) and $\sigma_x^i\sigma_x^j$ (which is the spin-spin interaction term between two qubits i and j). On evaluating the

integrals we get,

$$U(\tau) = exp\left[\sum_{i}\sum_{p=1}^{N}\left(\alpha_{i,p}(\tau)a_p^{\dagger} + \alpha_{i,p}^{*}(\tau)a_p\right)\sigma_x^i + i\sum_{i,j}\chi_{i,j}(\tau)\sigma_x^i\sigma_x^j\right] \tag{5.12}$$

The motional part of the first term has the exact form of the displacement operator $\hat{D}(\alpha) = exp(\alpha a^{\dagger} - \alpha^{*}a)$. This leads to a spin-motion entanglement of $i-$th qubit due to a spin (σ_x^i) dependent displacement $\alpha_{i,p}(\tau)$ of the ion. For a more generalized time dependent Rabi frequency $\Omega_i(t)$ the displacement of the $p-$th mode is given by,

$$\alpha_{i,p} = -\int_0^{\tau}\eta_p^i\Omega_i(t)\cos(\mu t - \phi_i^m)e^{i\omega_p t}dt \tag{5.13}$$

The spin-spin interaction term $\chi_{i,j}(\tau)$ is given by,

$$\chi_{i,j}(\tau) = \sum_{p=1}^{N}\eta_p^i\eta_p^j\int_0^{\tau}\int_0^{t_2}dt_2dt_1[\Omega_i(t_2)\Omega_j(t_1)\sin(\omega_p(t_2-t_1))\cos(\mu t_2-\phi_i^m)\cos(\mu t_1-\phi_j^m)] \tag{5.14}$$

In order to achieve a pure spin-spin coupling the spin-motion coupling term of equation 5.12 must be zero. This implies that $\alpha_{i,p}(\tau) = 0$ at the end of the Molmer-Sorensen interaction thereby decoupling the motion from the spin at the end of the gate. For a constant pulse where $\Omega_i(t) = \Omega$ the displacement of the $p-$th normal motional mode is approximately given by,

$$\alpha_{i,p}(\tau) \approx \frac{\Omega\eta_p^i}{2}\left(\frac{1 - e^{-i\delta_p\tau}}{\delta_p}\right)e^{-i\phi_i^m} \tag{5.15}$$

where $\delta_p = \mu - \omega_p$ is the detuning of the beatnote from the motional mode. It

is apparent from this expression that $\alpha_{i,p}(\tau) = 0$ when $\delta_p \tau = 2n\pi$ (n being an integer). Note that this spin motion decoupling is solely decided by the motional mode frequency ω_p which in the single sideband resolved limit [68, 79] is the only mode that the spin couples primarily to. In this case the gate duration τ can be tuned such that this condition is satisfied for the given mode. However, for multiple ions there are several modes (fig. 5.3) of motion that can be simultaneously excited. This happens as a result of reduced gate duration and higher spin dependent force $\Omega_i \eta_p^i$. This implies that equation 5.15 needs to be satisfied for all values of $p = \{1, 2, 3, 4, 5\}$ where we have five sets of detunings $\{\delta_p\}$. It is highly unlikely that there is a solution for τ that can decouple all motional modes.

In order to circumvent this problem we implement a pulse shaping technique [86, 87] where the spin dependent force is modulated in time as a piecewise constant segmented pulse defined by,

$$\Omega_i(t) = \Omega(t) = \begin{cases} \Omega_1 & 0 < t \leq \tau/P \\ \Omega_2 & \tau/P < t \leq 2\tau/P \\ \vdots & \\ \Omega_P & (P-1)\tau/P < t \leq \tau \end{cases} \tag{5.16}$$

where the indices on the right hand side of the equation refers to the pulse segment (and not the ion) with a total of P segments in the pulse shape. While inducing spin-spin coupling among multiple ions all of them are subjected to the same pulse shape. The displacement of the motional modes can be recalculated for a given

pulse shape vector $\mathbf{\Omega} = \{\Omega_1, \Omega_2, \cdots, \Omega_P\}$ as,

$$\begin{aligned}\alpha_{i,p}(\tau) =& -\eta_p^i \sum_{j=0}^{P} \Omega_j \int_{(j-1)\tau/P}^{j\tau/P} \cos(\mu t) e^{i\omega_p t} dt \\ =& \sum_{j=1}^{P} C_{p,j}^i \Omega_j = (C^i \mathbf{\Omega})_p\end{aligned} \tag{5.17}$$

where we have ignored phase ϕ_i^m since it only adds a global phase to the motion (eqn. 5.15). Here, C^i is a rank-2 tensor whose elements are pre-calculated for the $i-$th ion in the chain. For different ions i and j excited simultaneously in the chain the relationship between the rows of the two tensors is given by $C_p^i/C_p^j = \eta_p^i/\eta_p^j = \mathbf{b}_p^i/\mathbf{b}_p^j$. The spin-spin interaction phase can also be calculated to be,

$$\chi_{i,j}(\tau) = \sum_{k,k'=1}^{P} \Omega_k \Omega_{k'} D_{k,k'}^{i,j} = \mathbf{\Omega}^T D^{i,j} \mathbf{\Omega} \tag{5.18}$$

where $D_{i,j}$ is a rank-2 tensor defined by,

$$D_{k,k'}^{i,j} = \sum_{p=1}^{N} \eta_p^i \eta_p^j \int_{(k-1)\tau/P}^{k\tau/P} dt_2 \int_{(k'-1)\tau/P}^{k'\tau/P} dt_1 \sin(\omega_p(t_2 - t_1)) \cos(\mu t_2 - \phi_i^m) \cos(\mu t_1 - \phi_j^m) \tag{5.19}$$

In order to implement a pure spin-spin interaction of the ion pair $\{i, j\}$ we have to satisfy the following conditions,

- All motional modes should be decoupled from the spin at the end of the gate. This implies $C^i\mathbf{\Omega} = 0$, which gives a set of N linear equations with complex coefficients $C_{a,b}^i$. One can separate the real and imaginary parts of the equations to give a set of $2N$ equations instead, which implies $2N$ constraints

that have to be satisfied by the pulse solution $\mathbf{\Omega}$. The trivial solution $\mathbf{\Omega} = 0$ must be ignored. It is important to note that the solution $\mathbf{\Omega}$ for C^i also works for the tensor C^j (for ion j) due to the relation between the corresponding rows of the two tensors as mentioned before.

- The resultant spin-spin interaction phase between the ions $\chi_{i,j}(\tau) = \mathbf{\Omega}^T D^{i,j} \mathbf{\Omega} \neq 0$, which is why $\mathbf{\Omega} = 0$ is not a valid solution.

Taking a simple look at the constraints we find that for a total number of partitions $P = 2N+1$ of the pulse shape $\mathbf{\Omega}$ all constraints should ideally be satisfied giving a unique solution. However, it is important to note two properties of the constraint equations: a) The linear equations (equation 5.17) does not give $2N$ entirely independent set of equations on separating the real and imaginary parts of $C^i_{p,j}$ since $\Re(C^i_{p,j})$ and $\Im(C^i_{p,j})$ are related. b) Equation 5.18 expressing $\chi_{i,j}(\tau)$ is a non linear equation which can be satisfied to be of non-zero value automatically if $\mathbf{\Omega} \neq 0$. Therefore, this constriant does not change the pulse shape but only magnifies it by a constant factor $0 < s < s_{max}$ in order to set $\chi_{i,j}(\tau) = \theta_{i,j}$. Here $\theta_{i,j}$ is a finite two qubit rotation angle which is usually set to $\pm\frac{\pi}{4}$ in order to generate a maximally entangled two qubit GHZ state $(|00\rangle + e^{i\phi}|11\rangle)/\sqrt{2}$ from an initial state $|00\rangle$. In order to clarify this point, lets assume that $\mathbf{\Omega}$ is a solution to $C^i\mathbf{\Omega} = 0$ as well as $C^j\mathbf{\Omega} = 0$. This means that the normalized vector $\Omega_{Norm} = \frac{\mathbf{\Omega}}{|\mathbf{\Omega}|}$ is also a solution. Now lets assume that the driving Rabi-frequency of ion i and j are Ω_i and

Ω_j, respectively then,

$$\chi_{i,j} = \Omega_i \Omega_j \left[(\Omega_{Norm})^T D^{i,j} \Omega_{Norm} \right] = \Omega_i \Omega_j \chi^0_{i,j} \tag{5.20}$$

Since $\chi^0_{i,j} \neq 0$ we can tune Ω_i and Ω_j to achieve the desired two qubit phase $\chi_{i,j}$. Therefore, although we might start with $P = 2N + 1$ segments to solve for $\mathbf{\Omega}$ the number of independent parameters in the pulse shape is truly N. Hence, a pulse shape with fewer segments could also give an exact solution.

The pulse shapes for the two-qubit interaction could be as simple as solving the $2N$ set of linear equations which then gives you a solution set of $2N$ vectors. However, the gate the fidelity for these different solutions might differ especially when the Rabi-frequencies Ω_i and Ω_j are adjusted to satisfy $\chi_{i,j} = \pi/4$ (lets say). therefore, an optimization needs to be done in order to maximize the gate fidelity for the minimum amount of laser power (lower values of Ω_i and Ω_j) which results in one of the solutions to be optimal. The details of this method is described in reference [61].

The implementation of pulse shaped Molmer-Sorensen interaction [81, 82] is shown in figure 5.4. The modulation of Rabi frequency is achieved using an AWG that drives the global beam which illuminates both the participating ions in the chain selected by switching the appropriate individual addressing Raman beams. For each value of detuning μ, an optimal pulse shape can be calculated (Appendix B) for the chosen gate duration of $\tau = 235\,\mu$s. In the figure we have shown a pulse shape that drives a two-qubit gate between ions 1 and 5. From the trajectory of all

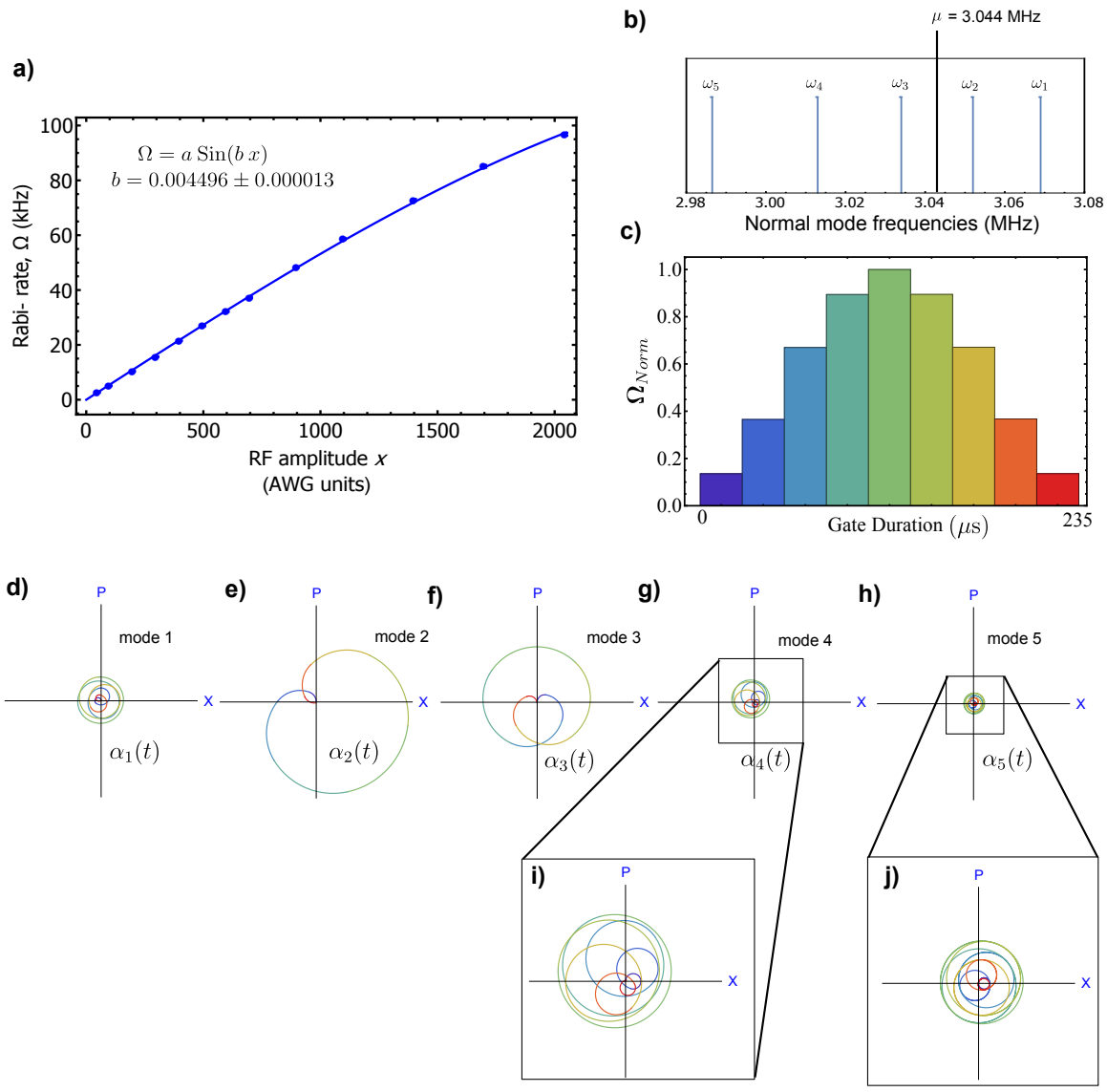

Figure 5.4: **XX-gate pulse shaping.** a) Calibration of the Rabi frequency as a function of the applied AWG amplitude of rf driving the global Raman beam. The Rabi frequency is obtained for various (11-bit) amplitude values by Rabi flopping at the carrier transition of a single ion. During a Molmer-Sorensen interaction each of the two beatnotes (detuned by μ and $-\mu$ from the carrier) is driven upto a maximum amplitude of 1023 (10-bit).b) The detuning μ chosen for a two-qubit gate on ions $\{1, 5\}$. c) The pulse solution for $\tau = 235\ \mu$s at this detuning. d)-h) The spin-dependent force on each qubit displaces the motional wavepacket for each of the normal modes of motion 1-5, respectively. $\alpha_p(t)$ is the time dependent displacement in phase space where the color coded paths correspond to the pulse segments in (c). Modes 2 and 3 are excited more since the beatnote is tuned closer to these modes. All trajectories are plotted in the same scale. i) Mode-4 trajectory magnified 3×. j) Mode-5 trajectory magnified 5×.

the five transverse modes it is clear that all modes are excited during the gate and have to be decoupled at the end. Even with 9 segments ($N < 9 < 2N + 1$) this is possible where the symmetry of the pulse solution hints at the fact that the number of independent variables describing the the pulse shape is less than 9. The pulse shape solution are discussed in appendix 2 which shows that the symmetry of the solution holds for almost the entire range μ that span the spectral bandwidth of all the five modes.

When the optimal pulse is applied that decouples all motional modes the unitary evolution operator (equation 5.12) takes the form of the spin-spin ($\sigma_x^i \sigma_x^j$) coupling between the two qubits. This operation, also dubbed as the XX-gate, can be expressed as,

$$XX(\chi_{i,j}) = exp[i\chi_{i,j}\sigma_x^i\sigma_x^j] = \begin{bmatrix} \cos(\chi_{ij}) & 0 & 0 & -i\sin(\chi_{ij}) \\ 0 & \cos(\chi_{ij}) & -i\sin(\chi_{ij}) & 0 \\ 0 & -i\sin(\chi_{ij}) & \cos(\chi_{ij}) & 0 \\ -i\sin(\chi_{ij}) & 0 & 0 & \cos(\chi_{ij}) \end{bmatrix} \tag{5.21}$$

In figure 5.5 we show the action of $XX(\pm\frac{\pi}{4})$ on an initial state that creates a maximally entangled state $(|00\rangle \mp i|11\rangle)/\sqrt{2}$, respectively. Here, the sign of $\chi_{i,j}$ depends on the participating ions due to its dependency on the product of the Lamb-Dicke parameters $\eta_p^i \eta_p^j$ (equation 5.14), which in turn depends on the normal mode vectors $\mathbf{b}_p$. The final set of solutions of XX-gates for all 10 possible qubit pairs in the 5 ion chain therefore has an additional parameter $\alpha_{i,j} = \text{sgn}(\chi_{i,j})$ which

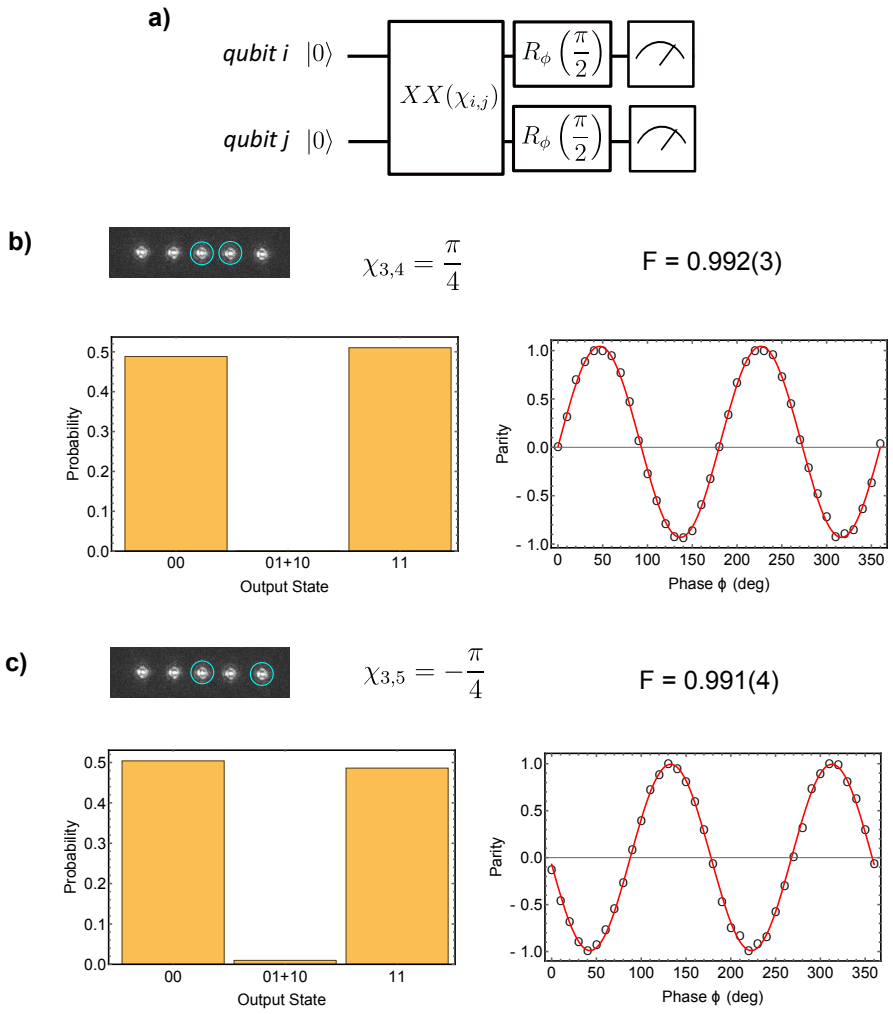

Figure 5.5: **XX-gate characterization.** The fidelity of an XX-gate is measured for an entangling operation where $|\chi_{i,j}| = \frac{\pi}{4}$. The ideal output state is expected to be $|\psi_{id}\rangle = (|00\rangle - ie^{i\phi'}|11\rangle)/\sqrt{2}$. **a)** Shows the gate operation followed by single qubit $\pi/2$ rotations about variable axis ϕ followed by measurement.**b)** An XX-gate on qubits $\{3, 4\}$ is performed leading to population distributed nearly equally in output states $|00\rangle$ and $|11\rangle$. A sequence as in (a) is also implemented where the two qubit parity is measured for various values of $0 \leq \phi \leq 2\pi$. The parity sinusoidally oscillates with a periodicity of 2 and a phase offset of $\phi'/2$. Here $\phi'/2 = 0$ which indicates that $\alpha_{3,4} = +1$. The gate fidelity is given by the measured probabilities P_{00} and P_{11} of states $|00\rangle$ and $|01\rangle$, respectively and the contrast Π_c of the parity curve. The fidelity expression is $F = (P_{00} + P_{11} + \Pi_c)/2$ [77]. **c)** Same as (b) where the XX-gate is performed on qubits $\{3, 5\}$. The offset phase of the parity curve is $\phi'/2 = \pi/2$ which gives $\alpha_{3,5} = -1$. For calculating gate fidelity the populations are measured using basis histogram fitting (see section 2.4.4) and hence SPAM errors are excluded. However, the sine function obtained from the least squares fit slightly overestimates the parity contrast Π_c and hence the measured value for F is an upper bound (but close) to the actual fidelity. The error in the last significant digit is statistical.

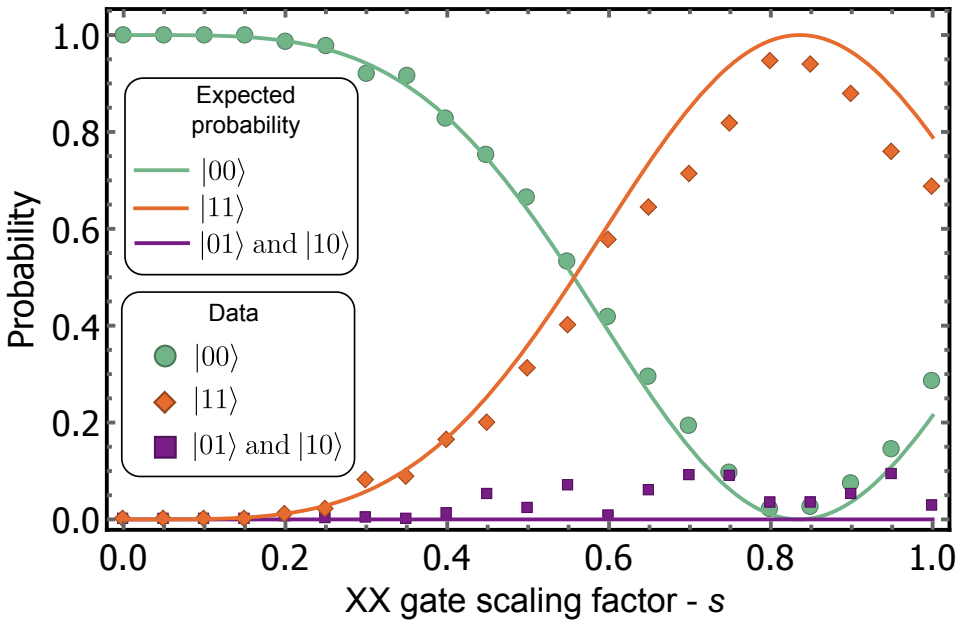

Figure 5.6: **Calibration of two-qubit XX gate.** Two-qubit population variation with the scale parameter s where the XX-gate pulse shape on on qubits i and j are $s\Omega_i\mathbf{\Omega}_{Norm}$ and $s\Omega_j\mathbf{\Omega}_{Norm}$, respectively. Here the gate is between qubits 1 and 5 and a rotation of $\chi_{1,5} = -\pi/4$ is achieved for $s = 0.56$. The theory curves, based on the relation $\chi_{i,j} = R_{i,j}s^2$, are fitted to the data to obtain $R_{i,j}$ for each ion pair $\{i, j\}$.

is important to take into account while constructing modular two-qubit composite gates. It can be probed using a parity scan as shown in figure 5.5 b) and c).

Just like a single qubit rotation a two-qubit XX-gate on an initial state $|00\rangle$ can also be visualized as a rotation on a Bloch sphere. In this case the poles represent $|00\rangle$ and $|11\rangle$. However, unlike the single qubit rotation angle θ the two qubit rotation angle $\chi_{i,j}$ does not linearly grow with time. In fact the duration of the XX-gate is fixed to be $\tau = 235\ \mu$s for all qubit pairs. The value of $|\chi_{i,j}|$ is varied using the relationship in equation 5.20. In order to implement this we scale both the Rabi frequencies Ω_i and Ω_j by a factor s $(0 \leq s \leq 1)$ by changing the AWG amplitude according to the calibration shown in figure 5.4a. This leads to a

quadratic variation of $|\chi_{i,j}|$ with s. The effect of this continuous tuning of the two qubit rotation is shown in figure 5.6.

5.3 Composite gates

A quantum algorithm is usually written as a sequence of standard logic gates [88, 89]. These gates are by definition modular which allows them to be simply programmed in a reconfigurable sequence irrespective of the underlying hardware. In order to understand what this means in the context of the five qubit trapped ion quantum processor, lets take an example of an elementary (native) two qubit XX-gate that we have discussed in the previous section. We observe that the native form of the quantum gate as shown in equation 5.21 has real and imaginary parts usually not seen in a standard two qubit logic gate such as the CNOT gate. Also it is dependent of the qubit pair $\{i, j\}$ that define the calibration constant $R_{i,j}$ (fig5.6) and the sign of the spin-spin interaction $\alpha_{i,j}$ (fig. 5.5).Programming algorithms directly in the form of native $R-$ and $XX-$ is challenging due to the difficulty in the 'book keeping' of many qubit dependent paramaters. Therefore, it is most useful to construct a compiler that translates standard logic gates (Hadamard, CNOT, controlled-phase etc.) into native rotations. We refer these standard logic gates as composite gates as they are comprised of several $R-$ and $XX-$ gates in order to **a)** execute the desired operation of the standard logic gate and **b)** remove qubit specific parameters allowing them to be invoked in a 'modular' fashion in an algorithm sequence.

5.3.1 Single qubit composite gates

The single qubit composite gates that we are required to implement in the experiment are the R_z gate and the Hadamard gate (H).

Single qubit Z-rotation: The single qubit Z-rotation can be easily implemented through controlled Stark shifts that changes the qubit energy splitting which causes rotation of the qubit around the Z axis of the Bloch sphere. This is a bit difficult in our experimental setup since it requires the use of additional $\Pi-$ polarization of the 355nm Raman beam that can cause a light shift to effect the Z-rotation [70]. One could also perform a $Z-$ rotation by simple advancing the phase of the Raman beatnote that drives all the coherent operations on the qubits. This is only possible if beat notes driving individual qubits can be phase shifted independently. IN our setup the beat note phase and only be set using the global Raman which implies that individual qubit selectivity is not possible. As a result, it is necessary to effect the R_z rotation using sequence of three single qubit $R-$rotations

$$R_z(\theta) = R_{-y}(\frac{\pi}{2})R_x(\theta)R_y(\frac{\pi}{2}). \tag{5.22}$$

Hadamard gate (H): The Hadamard gate is similar to a $R_y(\pi/2)$ gate and sometimes can even be replaced by it. However, unlike the $R_y(\pi/2)$ rotation, a Hadamard applied twice is equivalent to an identity operation ($H \cdot H = \mathbb{I}$) which could be a necessary property required by some algorithms thereby prohibiting the substitution of the Hadamard with a $R_y(\pi/2)$ rotation. Hence we implement the

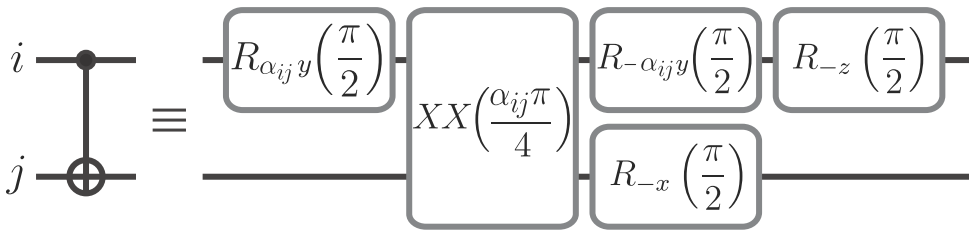

Figure 5.7: **CNOT gate circuit.** A controled not operation is implemented between control qubit i and target qubit j. The sign of the two-qubit rotation $\alpha = \text{sgn}(\chi_{i,j)} = \pm 1$ for $\chi_{i,j} > 0$ and $\chi_{i,j} < 0$, respectively. The value of $|\chi_{i,j}| = \pi/4$. We define $R_{\alpha_{ij}y(\theta)} = R_{\pm y}(\theta)$ for $\alpha_{ij} = \pm 1$, respectively.

Hadanard gate as

$$H = R_{-x}(\pi)R_y(\frac{\pi}{2}). \tag{5.23}$$

5.3.2 Two qubit composite gates

Two qubit logic standard logic gates such as the controlled-NOT (CNOT) and the controlled-phase (CP) gates both require a single $XX-$gate along with several $R-$gates. The optimal decomposition of each logic gate is obtained such that the number of $R-$gates can be minimized. The inherent sign $\alpha_{i,j}$ of the two qubit rotation $\chi_{i,j}$ is taken into account in the decomposition by adjusting the axis of the single qubit $R-$gates such that the final gate operation is independent of the ion pair $\{i, j\}$ thus making them modular. The details circuits and gate properties are discussed below.

CNOT gate: The circuit for the CNOT gate is shown in figure 5.7. The two qubit rotation is set to $|\chi_{i,j}| = \pi/4$. The single qubit R_y rotations that sandwich the $XX-$gate are executed about an axis defined by $\alpha_{i,j}$ which leads to the final

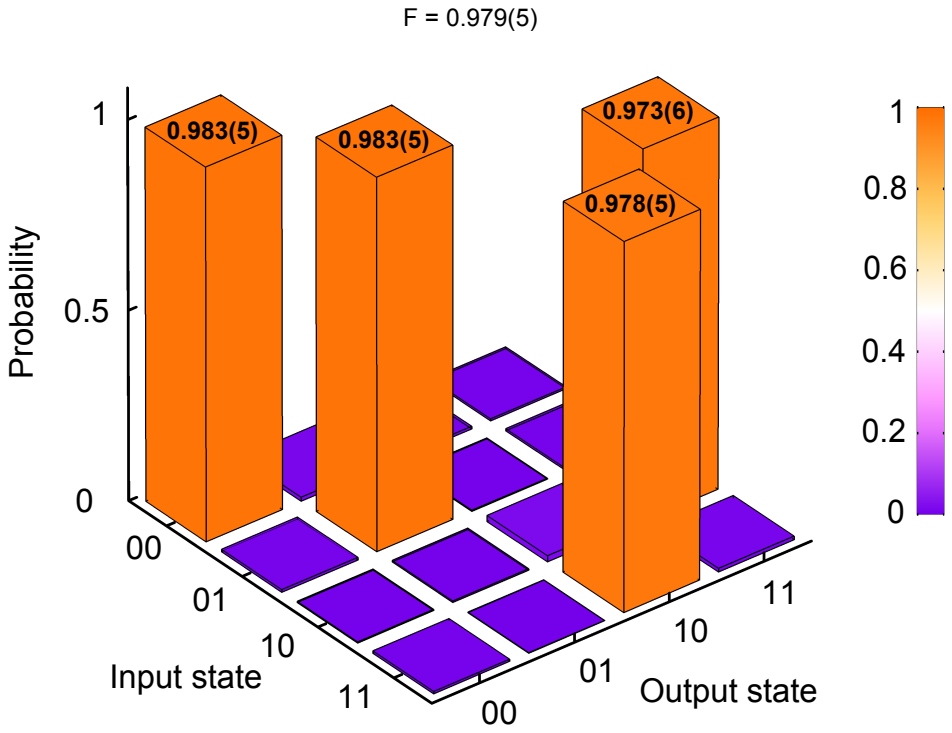

Figure 5.8: **CNOT-15 gate fidelity.** A CNOT gate is applied between qubits 1 and 5 for each of the four input states and the corresponding output populations are measured. The fidelity in each case is give by the probability of expected output state (as shown in bold on top of bars). The overall gate fidelity is F=0.979(5) where the error is a statistical estimate.

operation independent of the sign as,

$$CNij = \begin{bmatrix} 1 & 0 & 0 & 0 \\ 0 & 1 & 0 & 0 \\ 0 & 0 & 0 & 1 \\ 0 & 0 & 1 & 0 \end{bmatrix} \tag{5.24}$$

where i is the control qubit and j is the target qubit. The circuit for contructing a CNOT gate is shown in figure 5.11. Figure 5.8 shows a CNOT gate between qubits 1 and 5 and the associated fidelity of the gate. We implement the CNOT gate on all ten pairs of qubits and obtain the mean fidelity for each as shown in table 5.3.2.

Ion pair	Fidelity (%)	Ion pair	Fidelity(%)
1,2	96.4(6)	2,4	98.5(7)
1,3	97.6(7)	2,5	96.8(7)
1,4	95.9(7)	3,4	96.6(5)
1,5	97.9(5)	3,5	97.6(6)
2,3	95.6(6)	4,5	97.2(5)

Table 5.1: CNOT gate fidelity for various ion pairs.

In section 3.2.2 and 3.5 we discussed about the second and fourth order Stark shifts that change the qubit energy splitting when it is illuminated by the 355nm pulsed laser during Raman transitions. The measurement of the CNOT gate fidelity (as shown in figure 5.8 for CN15) is based on the output populations and discounts the phase in front of the states which ideally is supposed to be zero. However, in the presence of a Stark shift which is small compared to the gate duration (say $\epsilon \gg 1/\tau_{CN}$) the CNOT operation is modified to $CNijR_z^i(\epsilon.\tau_{CN})R_z^j(\epsilon.\tau_{CN})$ where $R_z^j(\epsilon.\tau_{CN})$ is a Z rotation on qubit j and τ_{CN} is the CNOT gate duration. In order

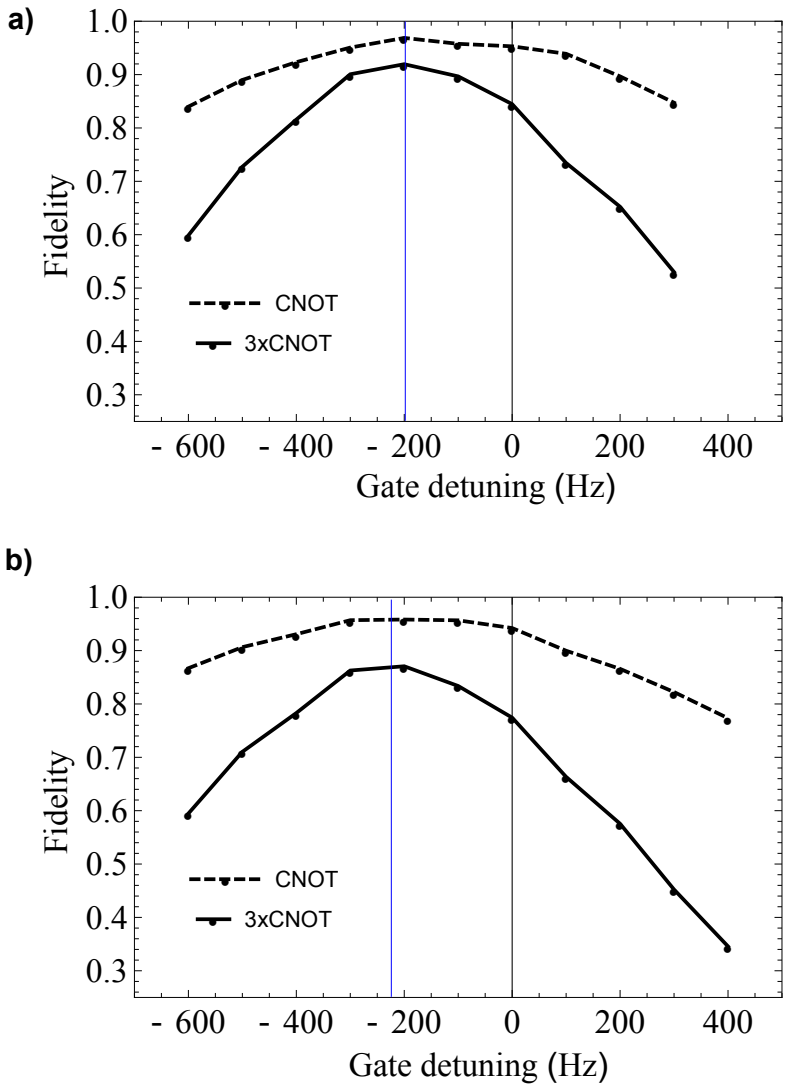

Figure 5.9: **CNOT gate fidelity variation with gate detuning.** CN15 is implemented on the initial state $|10\rangle$. The fidelity is measured from the probability of the expected output state $|11\rangle$ after 1×CNOT or 3×CNOT. The fidelity has a higher sensitivity with the beat-note detuning in the latter case due to the relatively more number of gates that accumulate effects of the Stark shift. As the detuning is scanned the fidelity peaks at a value where the beatnotes of the constituting $R-$ and $XX-$gates correspond to the qubit splitting that is Stark shifted by $\approx -200\,\text{Hz}$ as shown by the blue lines. **a)** Shows the variation of fidelity of the CNOT gate where the $XX-$gate used has a pulse shape at a detuning μ (fig 5.4b) that requires low laser power. **b)** Same as (a) but using an $XX-$gate at a different detuning μ' that uses higher laser power. This results in a slightly higher magnitude of the Stark shift (peak position of fidelity). The measured value of Stark shift in either case (a) and (b) is $|\Delta_s| \approx 200\,\text{Hz}$ which is small enough ($\frac{1}{|\Delta_s|} = 5\,\text{ms} \gg \tau_{CN} \approx 300\,\mu\text{s}$) to accumulate a substantial error only when multiple CNOT gates are executed in an algorithm sequence.

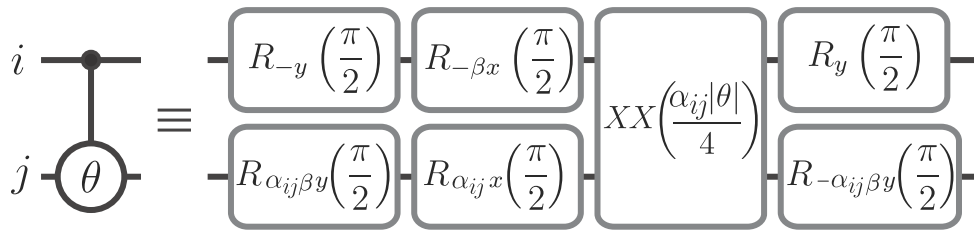

Figure 5.10: **Controlled-phase gate circuit.** A controlled phase (CP) gate with i as the control and j as the target qubit. The CP gate has two parameters in its decomposition. $\beta = \text{sgn}(\theta) = \pm 1$ when $\theta > 0$ and $\theta < 0$ respectively. Similarly the sign of the two qubit rotation is given by $\alpha_{ij} = \text{sgn}(\chi_{ij})$. The value of χ_{ij} is determined by θ as $|\chi_{ij}| = |\theta|/4$.

to circumvent this problem it is important to shift the frequency of all the beatnotes involved in driving the constituting $R-$ and $XX-$gates by the same amount as the Stark shift experienced by the qubit. The workings of this is illustrated in figure 5.9 where we apply a CNOT gate on qubits 1 and 5 with beatnotes shifted by various amounts from the 'zero point' (non-Stark shifted qubit). The peak of the fidelity at one such detuning indicates the magnitude and sign of the Stark shift experienced by the qubit. Since Stark shift is much smaller than the $R-$ and $XX-$gate durations it is particularly useful to use composite gates (and sometime many of them) in a sequence to amplify this effect and therefore calibrate the driving beatnotes in order to follow the shifted qubit while the Raman lasers are on.

CP gate: The two qubit controlled-phase gate is constructed as a composite gate as shown in figure 5.10. It is important to point out that in this case the controlled phase θ decides the value of the two qubit $XX-$gate rotation $|\chi_{ij}| = |\theta|/4$. This implies that in order to span $-\pi \leq \theta \leq +\pi$ we require a maximum laser power that allows $|\chi_{ij}| = \pi/4$. For example, according to figure 5.6 the scaling parameter

for the $XX-$gate pulse has to be varied in the range $0 \leq s \leq 0.56$ for implementing any value of the controlled phase θ between ions 1 and 5. The controlled phase gate has the following form,

$$CNij = \begin{bmatrix} 1 & 0 & 0 & 0 \\ 0 & 1 & 0 & 0 \\ 0 & 0 & 1 & 0 \\ 0 & 0 & 0 & e^{i\theta} \end{bmatrix} \tag{5.25}$$

where i is the control qubit and j is the target qubit.

In order to characterize the gate we need to perform a series of measurements as shown in figure 5.11 and 5.12. Here we perform a CP gate between ion 1 and 3 that have been initialized to the state $(|0\rangle + |1\rangle)|0\rangle/\sqrt{2}$ (fig. 5.11a and 5.12a). A final $R_y(\pi/2)$ rotation on qubit 1 takes it to the state $|1\rangle$ leaving qubit 3 in the initial $|0\rangle$ state. This outcome holds true for all values of θ thereby validating the first three rows of the CN gate (equation 5.25). For probing the controlled phase θ a CP gate is applied on the initial state $(|0\rangle + |1\rangle)|1\rangle/\sqrt{2}$ (fig. 5.11b,c and 5.12b,c). The resulting state is of the form $(|0\rangle + e^{i\theta}|1\rangle)|1\rangle/\sqrt{2}$ where we can apply a $R_y(\pi/2)$ gate on the first qubit to make an $X-$basis measurement of the first qubit (fig. 5.11b and 5.12b) or we can apply a $R_x(\pi/2)$ gate on it to make a $Y-$basis measurement (fig. 5.11c and 5.12c). By doing this tomography on the first qubit for both cases where the control and the target is flipped (fig. 5.11 is for CP13 and fig. 5.12 is for CP31) we prove that the operation is symmetric under qubit swap and that the desired phase ϕ is achieved.

The sequence as shown in figure 5.12c is implemented an all 10 pairs of qubits

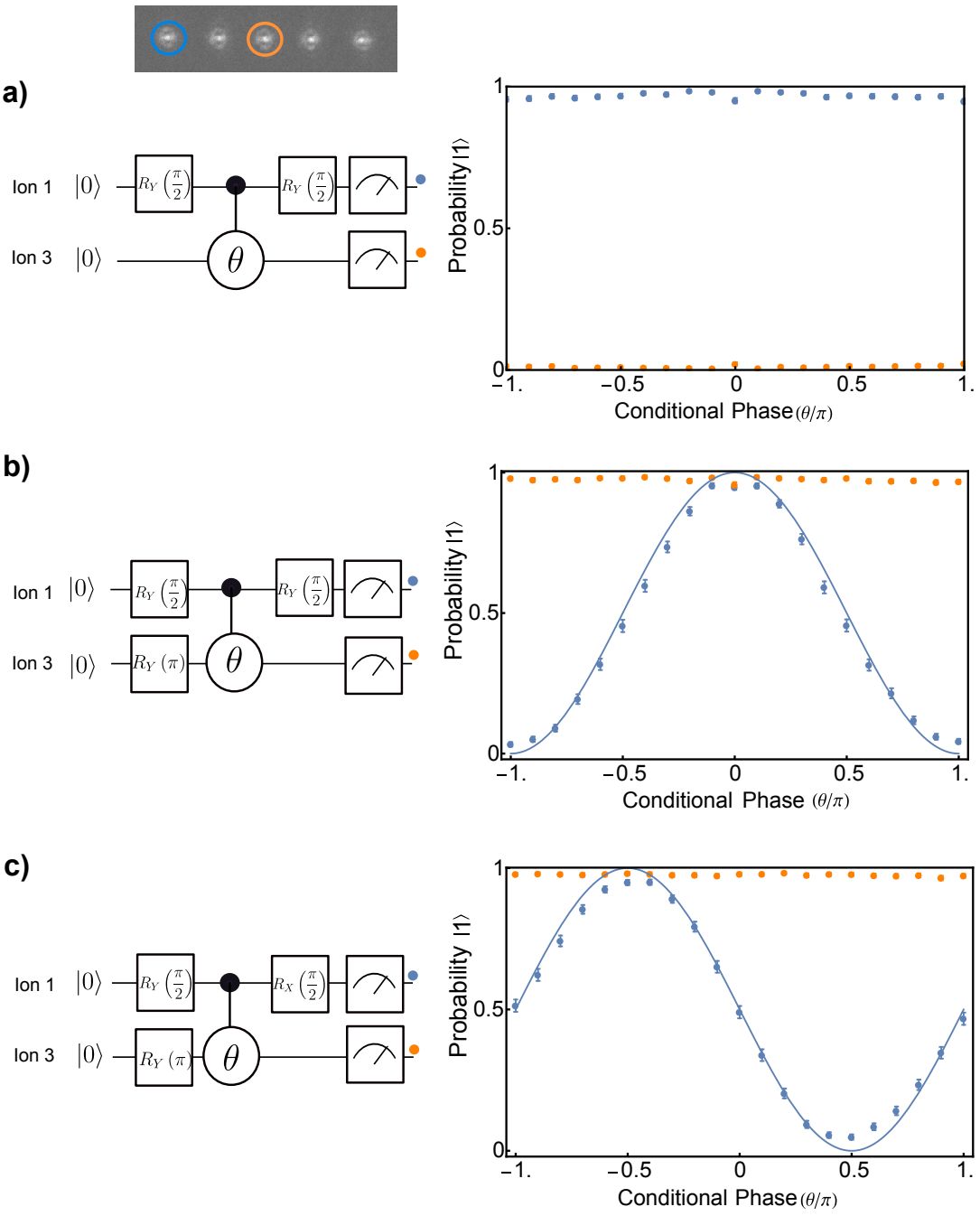

Figure 5.11: **Two qubit partial tomography after CP13 gate. a)** A CP gate is performed for a range of $-\pi \leq \theta \leq \pi$ between 1 and 3 (color coded) after preparing them in the state $(|0\rangle + |1\rangle)|0\rangle/\sqrt{2}$ with qubit 1 as control. Since the state is left unchanged by the gate an analysis $R_y(\pi/2)$ takes the first qubit to $|1\rangle$. **b)** A CP is performed on the initial state $(|0\rangle + |1\rangle)|1\rangle/\sqrt{2}$ which changes it to $(|0\rangle + e^{i\theta}|1\rangle)|0\rangle/\sqrt{2}$. The $R_y(\pi/2)$ measures the first qubit in $X-$basis. The blue line shows the ideal value. **c)** Same as (b) with the first qubit being measured in the $Y-$basis. Blue curve shows ideal value.

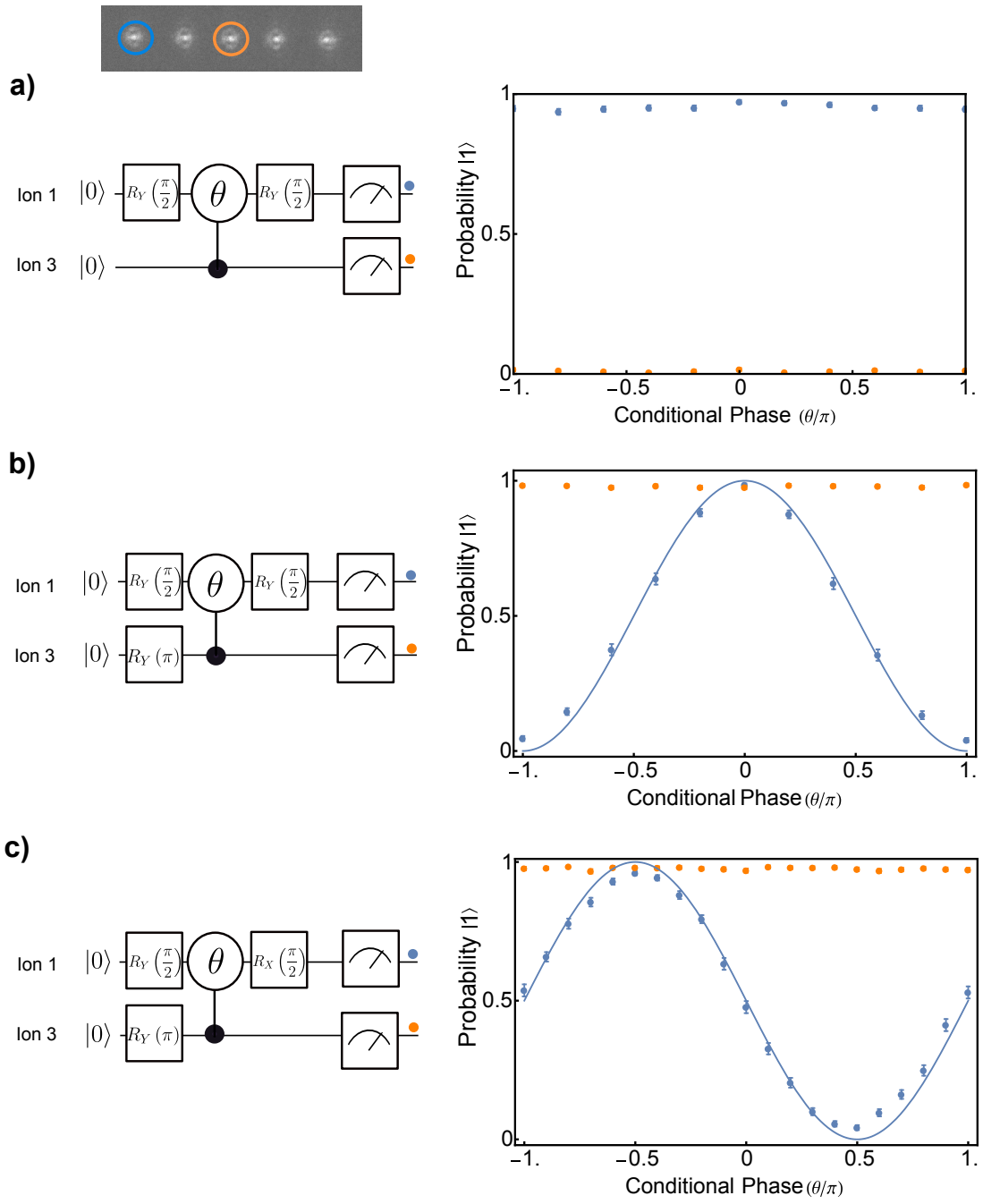

Figure 5.12: **Two qubit partial tomography after CP31 gate. a)** A CP gate is performed for a range of $-\pi \leq \theta \leq \pi$ between 1 and 3 (color coded) after preparing them in the state $(|0\rangle + |1\rangle)|0\rangle/\sqrt{2}$ with qubit 3 as control. Since the state is left unchanged by the gate an analysis $R_y(\pi/2)$ takes the first qubit to $|1\rangle$. **b)** A CP is performed on the initial state $(|0\rangle + |1\rangle)|1\rangle/\sqrt{2}$ which changes it to $(|0\rangle + e^{i\theta}|1\rangle)|0\rangle/\sqrt{2}$. The $R_y(\pi/2)$ measures the first qubit in $X-$basis. The blue line shows the ideal value. **c)** Same as (b) with the first qubit being measured in the $Y-$basis. Blue curve shows ideal value.

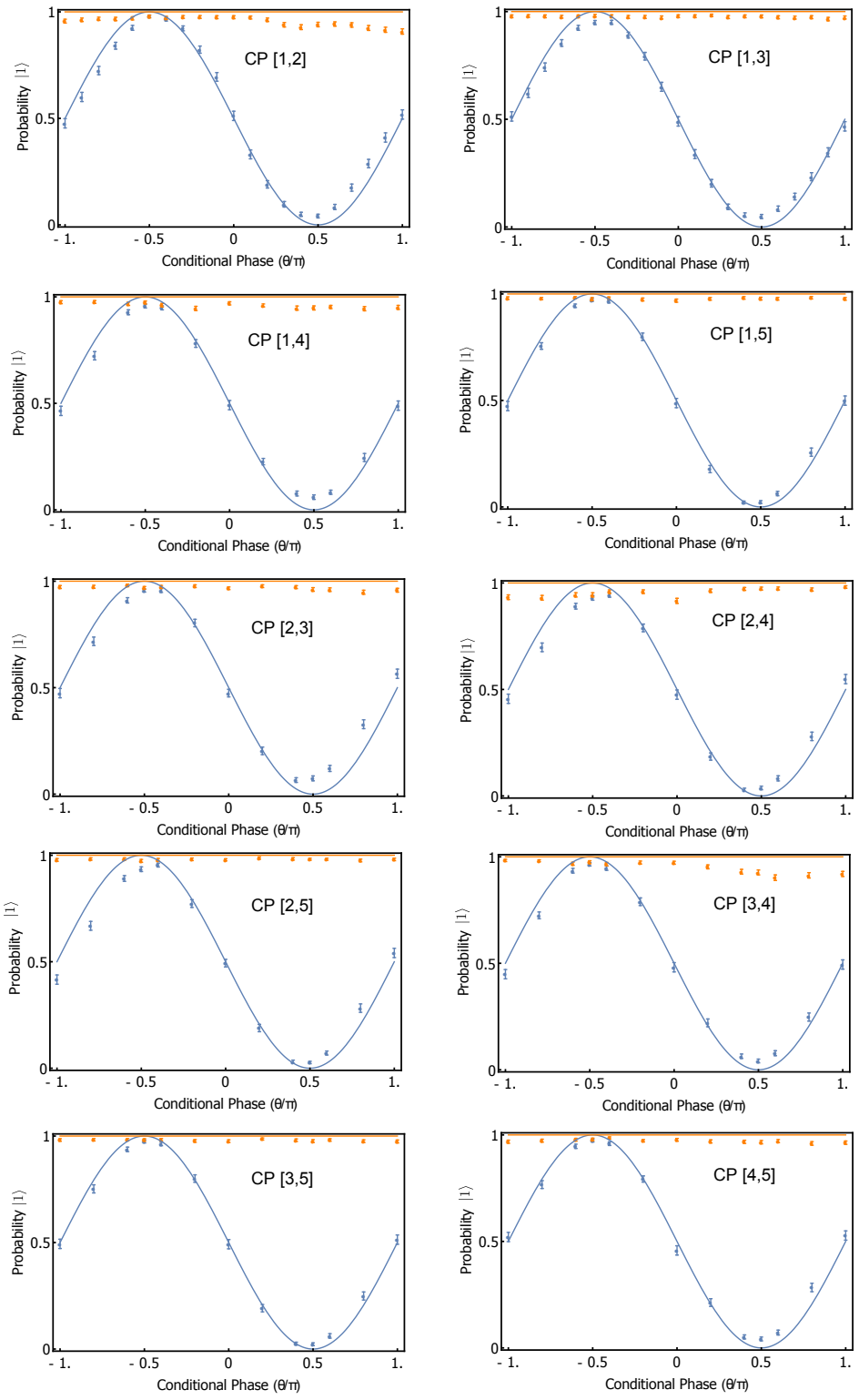

Figure 5.13: **Controlled-phase gates for 5 ions.** The sequence in fig.5.12c is implemented for all ion pairs. The theory curves in red and blue show the ideal value of the probability $P(|1\rangle)$ for the control and target qubit, respectively. The data points have statistical error bars for a 95% confidence interval.

in the 5 ion chain (figure 5.13). The final $R_y(\pi/2)$ rotation on the first qubit projects the conditional phase θ to the population of the target qubit 1 as $P(|1\rangle) = (1 - \sin(\theta)/2))$, where $P(|1\rangle)$ is the probability of the qubit state being $|1\rangle$. We measure the fidelity of the CP gates at the conditional phases $\theta = \pm\pi/2$, which correspond to the geometric phase $\chi_{ij} = \pm\pi/8$. It is particularly simple to measure the fidelity at these points since the ideal output state is $|01\rangle$ and $|11\rangle$, respectively. It will also be shown in the next chapter that while performing a QFT or QFT^{-1} the conditional phase lies within the range $-\pi/2 \leq \theta \leq \pi/2$. Within this range, the maximum deviation of the measured state probability from the ideal occurs at the extremes $\theta = \pm\pi/2$ (see fig. 5.13). Therefore, the fidelity measure at these points is probably the lower bound for the gate fidelity for all the values of θ within this range. Table 5.2 shows the CP gate fidelites for all ion pairs as measured for $\theta = \pm\pi/2$.

Ion pair	Fidelity at $\theta = \frac{\pi}{2}$ (%)	Fidelity at $\theta = -\frac{\pi}{2}$ (%)
1,2	91.1(6)	96.1(4)
1,3	93.6(5)	93.3(6)
1,4	91.6(6)	93.3(6)
1,5	95.9(4)	95.3(3)
2,3	90.7(6)	93.2(5)
2,4	94.2(5)	90.8(6)
2,5	95.8(4)	91.7(6)
3,4	91.0(6)	94.7(5)
3,5	96.0(4)	96.0(4)
4,5	93.5(6)	95.8(4)

Table 5.2: Controlled-phase gate fidelity for various ion pairs. The errors in the last significant digit is statististical showing a cofidence interval of 95%.

Chapter 6: Quantum Algorithms

The quantum algorithms that we choose to implement on the five qubit system are based on the quantum version of the discrete Fourier transform [88]. These algorithms illustrate how speedup is achieved when investigating global properties of mathematical functions using *quantum parallelism* where parallel function evaluations for all possible classical input states is carried out. In order to understand the way this works we can first portray this class of algorithms as the more generic quantum phase estimation problem as represented in figure 6.1 [5]. Here we start with a measurement register that has $N = 5$ measurement qubits all initialized to the state $|0\rangle$. By applying a Hadamard gate on each qubit we prepare a state that has a uniform superposition of all possible $5-$bit classical inputs $0 \leq x \leq 31$ represented as

$$|\psi_{in}\rangle = \frac{1}{\sqrt{32}} \sum_{x=0}^{31} |x\rangle, \tag{6.1}$$

where x is the decimal representation of the binary 5-qubit state. For example, $|5\rangle = |00101\rangle$.

The next step in the algorithm is to apply a controlled unitary U to an ancilla register that has been initialized to the state $|\psi_a\rangle$. This implies that U has a

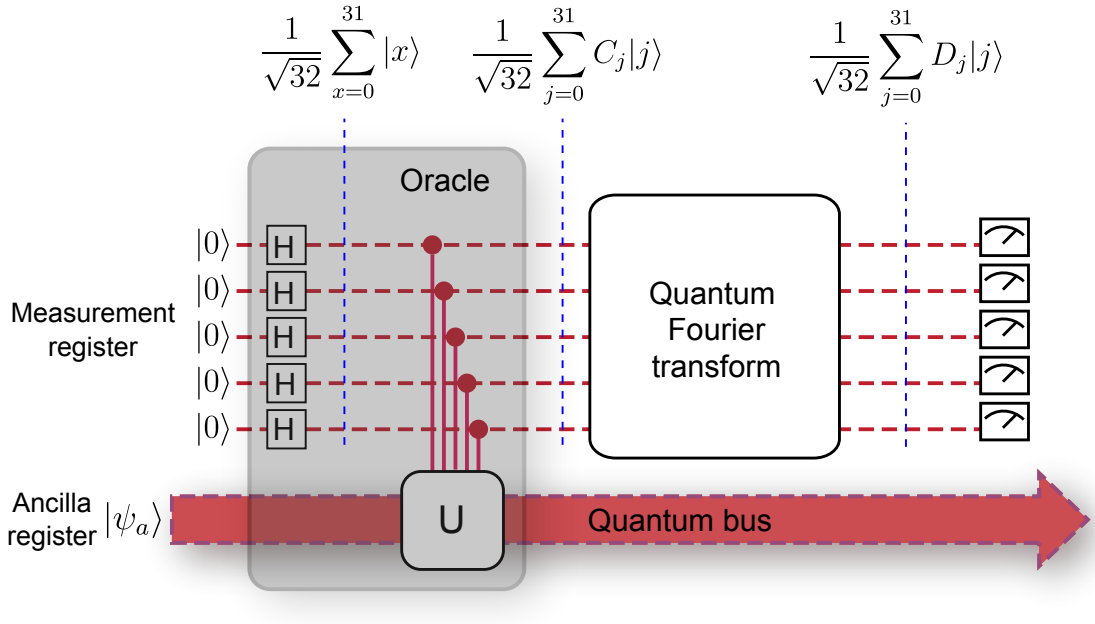

Figure 6.1: **Algorithm circuit for a generic quantum phase estimation**

different effect on the ancilla for each of value of $x = \{X_1, X_2, X_3, X_4, X_5\}$ where $X_1 - X_5$ represent each of the bits in the measurement register. The reason this step is important is because we can solve some mathematical problems by judiciously choosing the unitary U and the ancilla state $|\psi_a\rangle$. In order to see how this works lets say that we have a mathematical function $f(x)$ that takes a 5-bit input $x = \{X_1, X_2, X_3, X_4, X_5\}$ and gives a real valued output. This can formally be represented as $f : \{0, 1, 2 \ldots 31\} \rightarrow \mathbb{R}$. Lets say that the explicit form of the function is unknown (black box or an 'oracle') and the only way to understand some of its global properties is by evaluating it for each of the $2^5 = 32$ input values of x. Now it might be possible to choose the unitary U and the ancilla state $|\psi_a\rangle$ in such a way that the controlled-U results in a 'phase-kickback' to each of the basis states $|x\rangle$. That is the transformation of $|x\rangle \rightarrow e^{i\pi f(x)}|x\rangle$. This means that for the input state

$|\psi_{in}\rangle$ the controlled-U produces the output state

$$|\psi_1\rangle = \frac{1}{\sqrt{32}} \sum_{j=0}^{31} e^{\pi i f(j)} |j\rangle = \frac{1}{\sqrt{32}} \sum_{j=0}^{31} C_j |j\rangle. \tag{6.2}$$

This is equivalent to a parallel evaluation of the function for all values of j ($0 \leq j \leq 31$). Now that we have the function evaluated we need to probe for its properties. A simple measurement of each of the coefficients is impossible to carry out in a single step since any attempt at measuring this would collapse the wavefunction to any of the basis states $|x\rangle$ thereby erasing the phase information [67], whereas in the superposition form the information about $f(x)$ is still preserved in the coefficients of the state. Therefore, one of the smart things one can do is to apply a quantum Fourier transform (QFT) to the state that might reveal the periodicities of the function $f(x)$.

In this context we first need to define the QFT [90]. A quantum Fourier transform (QFT) is the quantum version of the discrete Fourier transform which is the following unitary transformation for a $N-$qubit state

$$|x\rangle \xrightarrow{QFT} \frac{1}{\sqrt{2^N}} \sum_{y=0}^{2^N-1} e^{2\pi i x y/2^N} |y\rangle. \tag{6.3}$$

For a single qubit this operation is none other than the Hadamard gate

$$\begin{aligned} |0\rangle &\xrightarrow{QFT \text{ or } H} \frac{1}{\sqrt{2}} \sum_{y=0}^{1} e^{i2\pi 0.y/2} |y\rangle = \frac{1}{\sqrt{2}} (|0\rangle + |1\rangle) \\ |1\rangle &\xrightarrow{QFT \text{ or } H} \frac{1}{\sqrt{2}} \sum_{y=0}^{1} e^{i2\pi 1.y/2} |y\rangle = \frac{1}{\sqrt{2}} (|0\rangle - |1\rangle). \end{aligned} \tag{6.4}$$

In practice we use the $R_y(\pi/2)$ single qubit rotation instead of the Hadamard (H) gate, as it is easier to implement and also because it follows a unitary evolution that closely resembles that shown in eqn. 6.3 and is of the form

$$\begin{aligned} |0\rangle &\xrightarrow{R_y(\pi/2)} \frac{1}{\sqrt{2}} \sum_{y=0}^{1} e^{i2\pi 0.\bar{y}/2} |y\rangle = \frac{1}{\sqrt{2}}(|1\rangle + |0\rangle) \\ |1\rangle &\xrightarrow{R_y(\pi/2)} \frac{1}{\sqrt{2}} \sum_{y=0}^{1} e^{i2\pi 1.\bar{y}/2} |y\rangle = \frac{1}{\sqrt{2}}(|1\rangle - |0\rangle), \end{aligned} \tag{6.5}$$

where $\bar{y}$ is the bit wise inversion of y.

Now we can express the resulting state after applying a QFT on the input state $|\psi_1\rangle$

$$|\psi_1\rangle \xrightarrow{QFT} \sum_{j=0}^{31} D_j |j\rangle, \tag{6.6}$$

where the coefficient D_j could be expressed as,

$$D_j = \frac{1}{32} \sum_{k=0}^{31} e^{2\pi i j.k/32} C_k = \frac{1}{32} \sum_{k=0}^{31} e^{2\pi i (jk/32 + f(k)/2)}. \tag{6.7}$$

In the final step of the algorithm we measure the state of the register. Here, the probability of measuring any of the basis states $|j\rangle$ is given by $|D_j|^2$, which depends on $f(x)$. It might be possible that $f(x)$ is periodic with period y. In that case $|D_y|^2 = 1$ for state $|y\rangle$ and zero otherwise. This means that upon measurement we would observe the state $|y\rangle$ with unit probability thereby confirming that the function is periodic. This leads to a single shot determination of this property of the function [91]. Other properties of $f(x)$ can also be measured if it can reduced to a periodic phase modulation in the superposition state of the measurement register.

In the following sections we will describe the implementation of a few algorithms all of which follow the rules of the quantum phase estimation protocol. We will define function $f(x)$ and their respective properties that we will probe using this protocol. Although the size of the mesurement and ancilla register will be redefined in order to fit the algorithms into the five qubit system, the underlying circuit structure shown in figure 6.1 will stay the same. For the Deutsch-Jozsa and Bernstein-Vazirani algorithms will use single qubit QFTs on the measurement register whereas for the phase estimation algorithm we will employ a fully-coherent five qubit QFT.

6.1 Deutsch-Jozsa algorithm

The Deutsch-Jozsa algorithm is used to determine whether a function $f(x)$ (the 'oracle') is constant or balanced [91]. A function with a $N-$bit input and a 1-bit output ($f : \{0, 1, 2, \ldots, 2^N - 1\} \rightarrow \{0, 1\}$) is balanced when exactly half of its inputs result in the output 0 and the other half in the output 1, while a constant function returns a single value (0 or 1) irrespective of the input. Figure 6.2a shows the implementation of the algorithm for a balanced function. The function has a three bit input $x = \{X_1, X_2, X_3\}$ and its value is stored in the function register X_4. Here we program 7 out of 70 possible oracles of three-qubit balanced functions by using seven different sequences of CNOT gates between each of the qubits in the control register and the function register initialized to the state $|0\rangle$ (see Fig 6.2a). This leads to implementing balanced functions that are the sum (modulo 2) of one

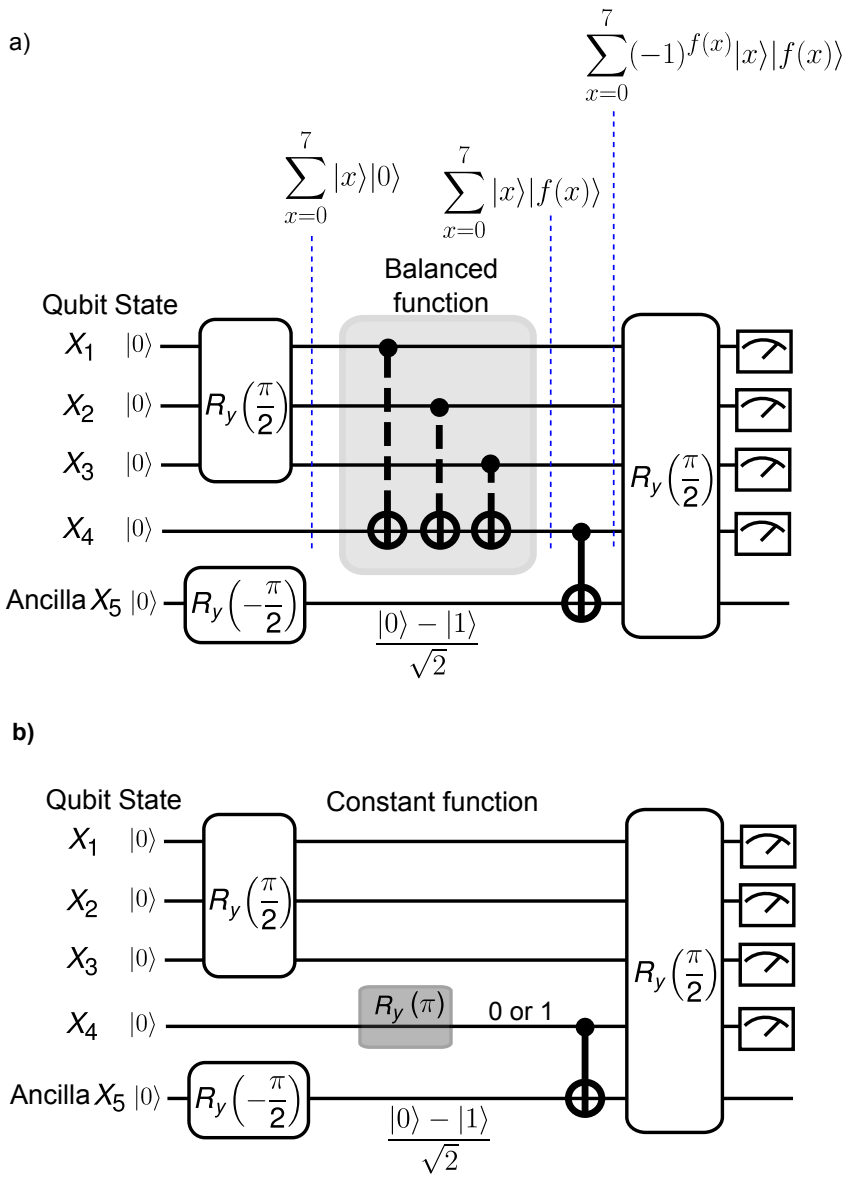

Figure 6.2: **Algorithm circuit for implementing Deutsch-Jozsa algorithm.** a) The oracle for balanced function is implemented through CNOT gates shown in the shaded regions of the circuit. For balanced function oracles we apply each of the seven possible CNOT combinations, indicated in light grey. The $R_y(\pi/2)$ rotations are applied to qubits X_1, X_2, X_3 at the beginning and to all the qubits before measurement. b) The constant function oracle is implemented by simply initializing X_4 to 0 or 1 by applying a $R_y(\pi)$ pulse on it. $R_y(\pi/2)$ rotations are applied on each qubit of the control register X_1, X_2, X_3 and the ancilla X_5 in the beginning. Also $R_y(\pi/2)$ gates are applied on all qubits in the end to implement single qubit QFT on them. The ancilla only provides a phase kick-back but is not entangled to the first four qubits which is why it is discarded while measuring the outcome of the algorithm.

or more control bits.

For the implementation of the algorithm we prepare all five qubits to state $|0\rangle$. This is followed by a $R_y(\pi/2)$ rotations on the qubits in register $x = X_1X_2X_3$ in order to create a superposition of all possible inputs to the function. The ancilla register is defined by single qubit X_5 that is initalized using a $R_{-y}(\pi/2)$. The resulting five qubit state is given by

$$|\psi\rangle_0 = \frac{1}{\sqrt{8}} \sum_{x=0}^{7} |x\rangle_{123} \otimes |0\rangle \otimes \frac{|0\rangle_5 - |1\rangle_5}{\sqrt{2}}. \tag{6.8}$$

The function evaluating oracle is then applied in the form of a set of CNOT gates between $X_1X_2X_3$ and the function register X_4 which write the corresponding balanced function value to X_4. In order to program constant functions we do not apply CNOT gates. Instead, we set X_4 to either 0 or 1 as shown in figure 6.2b. The resulting state of all the qubits is given by,

$$|\psi\rangle_1 = \frac{1}{\sqrt{8}} \sum_{x=0}^{7} |x\rangle_{123} |f(x)\rangle_4 \otimes \frac{|0\rangle_5 - |1\rangle_5}{\sqrt{2}} \tag{6.9}$$

A controlled unitary is now applied on the ancilla qubit. In this algorithm it is between X_4 and the ancilla X_5 which flips the ancilla qubit based on the function value $f(x)$. This results in 'phase kick-back' to produce the state,

$$|\psi\rangle_2 = \frac{1}{\sqrt{8}} \sum_{x=0}^{7} (-1)^{f(x)} |x\rangle_{123} |f(x)\rangle_4 \otimes \frac{|0\rangle_5 - |1\rangle_5}{\sqrt{2}} \tag{6.10}$$

After the 'phase kick-back' is achieved the final step of the algorithm is to

perform a single qubit QFT on all qubits. Then we measure the state of the first four and can ignore the ancilla qubit, since it is not entangled with the other qubits. The state of qubits $X_1X_2X_3X_4$ before measurement can be written as

$$\begin{aligned}|\psi\rangle_3 &= \frac{1}{8}\sum_{y=0}^{7}\sum_{x=0}^{7}(-1)^{f(x)}(-1)^{\bar{y}\cdot x}|y\rangle_{123}\otimes\frac{|1\rangle_4+(-1)^{f(x)}|0\rangle_4}{\sqrt{2}}\\ &= D_{0000}|0000\rangle + D_{0001}|0001\rangle + \ldots\\ &\ldots + D_{1110}|1110\rangle + D_{1111}|1111\rangle,\end{aligned} \tag{6.11}$$

where $\bar{y}$ is the bit-wise inversion of y.

If $f(x) = a$ is a constant function (with $a = \{0, 1\}$), the coefficients of the basis states $|1110\rangle$ and $|1111\rangle$ are

$$D_{1110} = \frac{1}{8\sqrt{2}}(-1)^a\sum_{x=0}^{7}(-1)^{000\cdot x} = \frac{(-1)^a}{\sqrt{2}} \tag{6.12}$$

$$D_{1111} = \frac{1}{8\sqrt{2}}\sum_{x=0}^{7}(-1)^{000\cdot x} = \frac{1}{\sqrt{2}}. \tag{6.13}$$

If $f(x)$ is a balanced function, then the coefficients are

$$D_{1110} = \frac{1}{8\sqrt{2}}\sum_{x=0}^{7}(-1)^{000\cdot x}(-1)^{f(x)}(-1)^{f(x)} = \frac{1}{\sqrt{2}} \tag{6.14}$$

$$D_{1111} = \frac{1}{8\sqrt{2}}\sum_{x=0}^{7}(-1)^{000\cdot x}(-1)^{f(x)} = 0. \tag{6.15}$$

Here we use the property that $f(x) = 0$ for exactly half of the values of x and 1 for the rest. Conditioned upon $X_4 = 1$, there is unit probability of measuring $X_1, X_2, X_3 = 111$ for a constant function and 0 probability of measuring the same

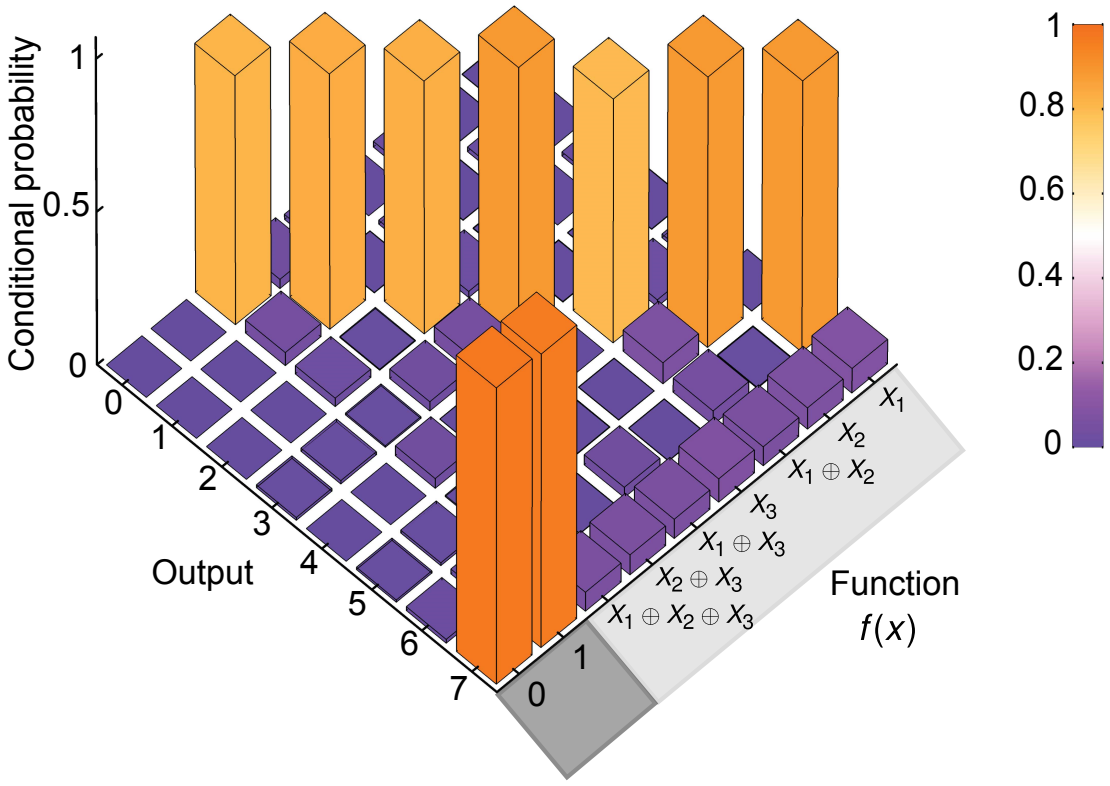

Figure 6.3: **Results of Deutsch-Jozsa algorithm.** Measured populations of the output state for various functions, conditioned upon measuring $X_4 = 1$. The two constant functions $f = 0$ and $f = 1$ are indicated in dark grey, and the seven balanced functions given by particular CNOT gate combinations are indicated in light grey. Measurement of the output $\{X_1X_2X_3\} = 111 = 7$ indicates a constant function, while any other value $(0 - 6)$ indicates a balanced function.

outcome when the function is balanced (Eqn. 6.13 and 6.15). In equation 6.11, note that the probability of measuring $X_4 = 1$ is 0.5 irrespective of the number of qubits in the input (control) register of the function. The data shown in figure 6.3 shows the algorithm outcome for different instances of balanced and constant functions. For these specific set of function implementations the average success probability of detecting a constant function in a single shot correctly is 0.967(2) and that of detecting a balanced function is 0.932(3).

6.2 Bernstein-Vazirani algorithm

The Bernstein-Vazirani algorithm is a variant of the Deutsch-Jozsa algorithm [92, 93]. The black-box (oracle) function in this algorithm is known to perform the inner product of two $N-$bit strings. The function can be written as

$$f_c(x) = c \cdot x = c_1 \cdot x_1 \oplus c_2 \cdot x_2 \oplus \ldots \oplus c_N \cdot x_N, \tag{6.16}$$

which is a modulo-2 dot product of the bit strings c and x. The aim of this algorithm is to find the bit string $c = \{c_1 c_2 \ldots c_N\}$ in a single trial.

In order to implement this algorithm in the five qubit system we define the function to take a four bit input $x = \{X_1 X_2 X_3 X_4\}$ and therefore can be defined as $f : \{0, 1, \ldots, 15\} \rightarrow \{0, 1\}$. The bit string c that defines the function therefore is also a four bit number. The circuit for the algorithm is shown in figure 6.4 where an input superposition of all possible four bit classical states in created by applying

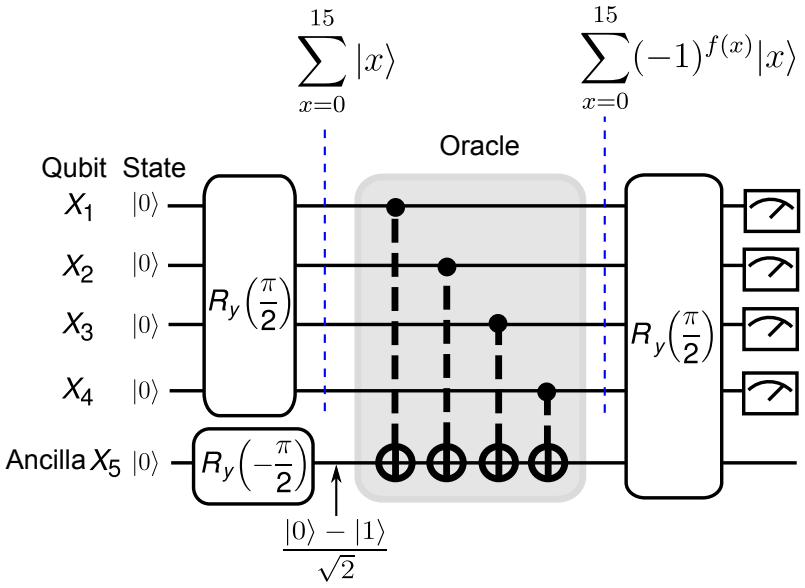

Figure 6.4: **Algorithm circuit for implementing Bernstein-Vazirani algorithm.** The circuit consists of $R_y(\pi/2)$ rotations in the beginning to prepare the superposition of the measurement register and are also applied in the end to effect a single qubit QFT on each of the qubits. The shaded region (oracle) contains programmed CNOT gate combinations used to implement different oracle states c that define the function $f_c(x) = c \cdot x$.

a $R_y(\pi/2)$ rotation on $X_1X_2X_3X_4$ and preparing the ancilla X_5 using a $R_{-y}(\pi/2)$. The state of all the qubits after initialization is given by

$$|\psi\rangle_0 = \frac{1}{\sqrt{32}} \sum_{x=0}^{15} |x\rangle_{1234} \otimes (|0\rangle_5 - |1\rangle_5). \tag{6.17}$$

The action of the oracle is then to evaluate $f_c(x)$ and add it to the ancilla qubit. This is achieved by applying a particular pattern of CNOT gates, determined by c, between the qubits $x = \{X_1X_2X_3X_4\}$ and the ancilla $X_5 = \frac{|0\rangle - |1\rangle}{\sqrt{2}}$. For example if $c = \{1010\}$ then CNOT gates are appled between X_1 and X_5 and between X_3 and X_5. The action of the oracle could be considered as a controlled-NOT gate on the ancilla where the control is the function value $f_c(x)$. This leads to the state

$$\begin{aligned} |\psi\rangle_1 =& \frac{1}{\sqrt{16}} \sum_{x=0}^{15} |x\rangle_{1234} \otimes |f_c(x) \oplus X_5\rangle \\ =& \frac{1}{\sqrt{16}} \sum_{x=0}^{15} (-1)^{f_c(x)} |x\rangle_{1234} \otimes \frac{|0\rangle_5 - |1\rangle_5}{\sqrt{2}}. \end{aligned} \tag{6.18}$$

Here we obtain 'phase kick-back' $e^{\pi i f_c(x)}$ in the coefficients since the ancilla is prepared in the state $X_5 = \frac{|0\rangle - |1\rangle}{\sqrt{2}}$. In the final step of the algorithm we perform $R_y(\pi/2)$ rotations on all the qubits in order to apply a single qubit QFT on them which results in the state

$$\begin{aligned} |\psi\rangle_2 =& \frac{1}{16} \sum_{x,y=0}^{15} (-1)^{c.x} (-1)^{\bar{y}.x} |y\rangle_{1234} \otimes |1\rangle_5 \\ =& (D_{0000}|0000\rangle + D_{0001}|0001\rangle + \ldots + D_{1111}|1111\rangle) \otimes |1\rangle_5, \end{aligned} \tag{6.19}$$

where $\bar{y}$ is the bit wise inversion of y and $\bar{y}.x$ is also the modulo-2 dot product of

the bit strings $\bar{y}$ and x. Now if we calculate the coefficient $D_{\bar{c}}$ we get,

$$D_{\bar{c}} = \frac{1}{16}\sum_{x=0}^{15}(-1)^{c.x}(-1)^{\bar{\bar{c}}.x} = \frac{1}{16}\sum_{x=0}^{15}(-1)^{2c.x} = 1 \tag{6.20}$$

Therefore, there is a unit probability of obtaining the state $|\bar{c}\rangle$ when we measure the measurement qubits $X_1X_2X_3X_4$, which is nothing but the bit wise inverted value of c. In the experiment we construct the 'oracle' function for all 16 possible values of c by choosing different CNOT combinations between the measurement qubits and the ancilla. The outcome for each function is shown in figure 6.5. We find an average success probability of 0.903(2) of finding the correct c in a single shot. The error within parenthesis is a statistical estimate for a 1σ confidence interval.

6.3 Quantum phase estimation protocol

The quantum phase estimation protocol has a closer resemblence to the circuit shown in figure 6.1 since it involves the application of a $N-$ qubit QFT where $N > 1$ unlike the algorithms discussed above. The phase estimation algorithm is mainly used in solving the eigen-value problem of the form

$$A|\phi\rangle = e^{-i\phi}|\phi\rangle, \tag{6.21}$$

where A is a unitary operator that operates on an eigen state $|\phi\rangle$ to yield a phase term $e^{-i\phi}$ as the eigen value. In a quantum phase estimation protocol a $N-$qubit measurement register sets the resolution of the phase measurement, and the size

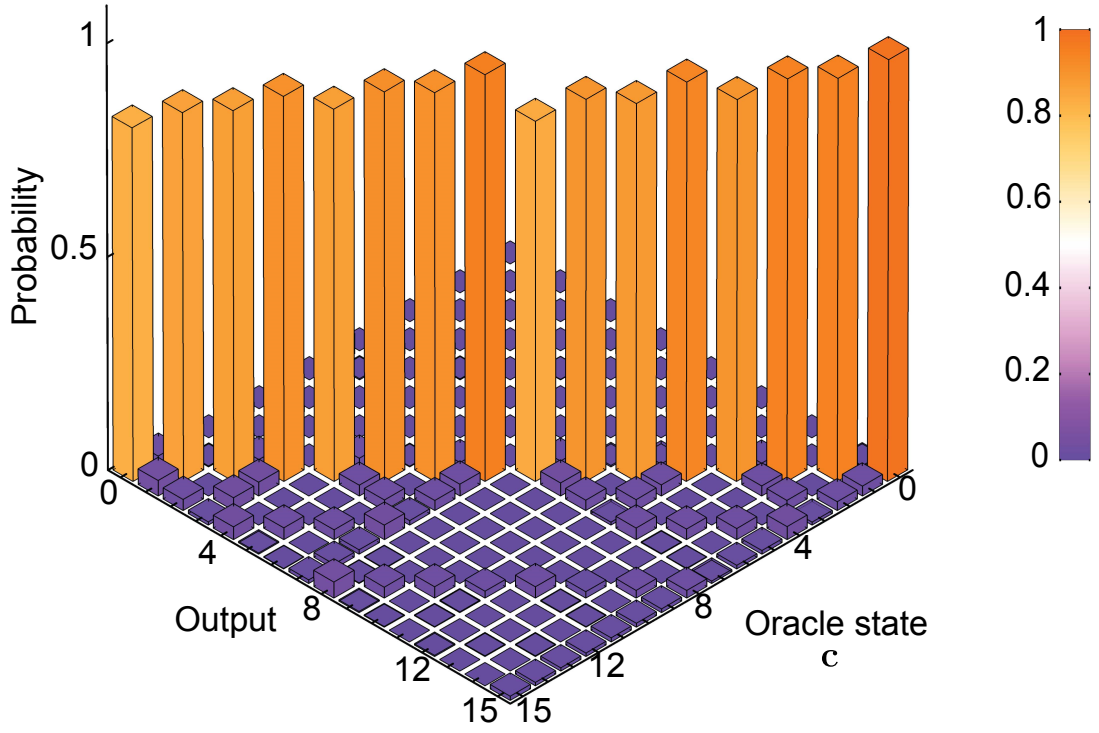

Figure 6.5: **Results of Bernstein-Vazirani algorithm** Measured output population for various oracle states c. The most likely output is ideally the inverted oracle state $\bar{c}$ which is obtained with an averagesuccess probability of 0.903(2). The error is the statistical estimate of 1 s.d. confidence interval and is evaluated for each implementation of the algorithm for a given oracle state.

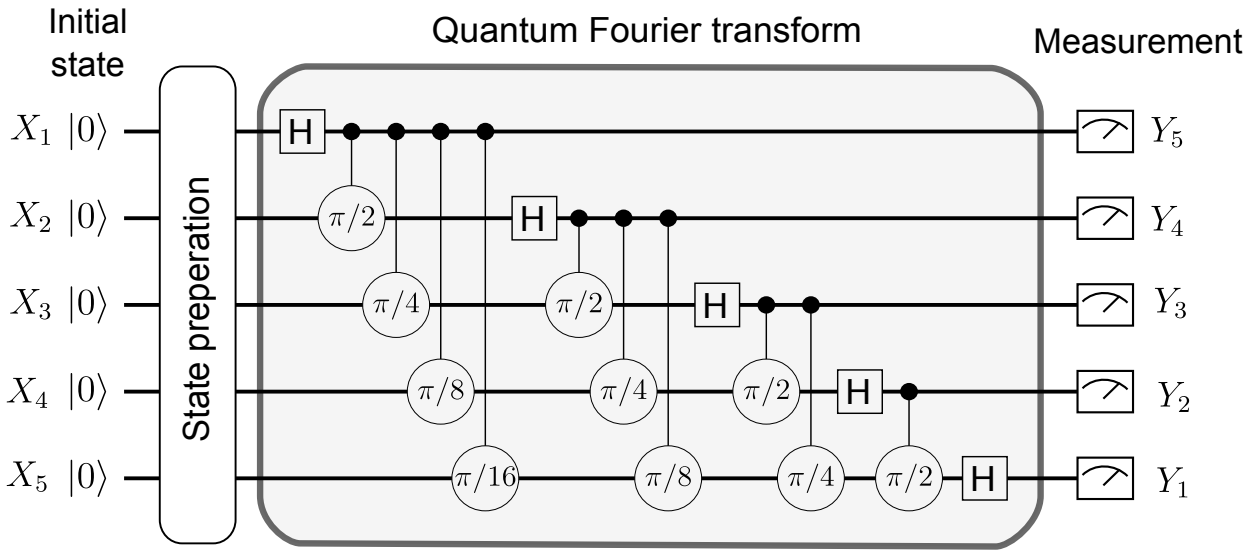

Figure 6.6: **Circuit for the implementation of quantum Fourier transform** A five qubit QFT is tested by applying it to states prepared (denoted by 'state preparation') with predetermined amplitude or phase modulation of the coefficients C_x of the input state $\sum_{x=0}^{31} C_x|x\rangle$. This is followed by applying the fully coherent 5-qubit QFT (shaded grey) followed by a measurement of the output state where the qubits are read out in reverse order.

of ϕ determines the size of the matrix operator A. In order to find the eigenvalue controlled unitary (A) operations are performed on an ancilla register initialized to $|\phi\rangle$. This requires a good guess of the eigen vector $|\phi\rangle$. As a result of the controlled A operation, a 'phase kick-back' is obtained on the state of the measurement register. The final step is the implementation of an $N-$qubit QFT which then can measure the value of ϕ with $N-$bit precision.

Before delving into the math of the phase estimation algorithm we first need to discuss the implementation of the $N-$qubit QFT. Unlike the single qubit version of the QFT which only requires single qubit rotations, the $N = 5$ qubit QFT is relatively more complicated. In the circuit of the multi-qubit QFT as shown in figure 6.6 we note that there are $\binom{N}{2} = 10$ controlled-phase gates that need to be performed along with the composite Hadamard (H) gates in order to implement the fully coherent version of the QFT. Although a semi-classical version of the QFT could also be implemented with single qubit rotations based on measurement and classical feed-forward [38, 94], we implement the coherent version. The main reason for this is to exploit all the two qubit gates in the system and evaluate their combined performance in a relevant algorithm and also due to the fact that being coherent this version of the QFT is truly reversible and can be concatenated in an algorithm sequence. The fully coherent QFT as shown in figure 6.6 is implemented on five qubits using a total of 80 native gates (10 $XX-$gates and 70 $R-$gates).

Following the algorithm circuit in figure 6.1 a controlled unitary operator $A^{\otimes x}$ is applied based on the state of the measurement register x. Therefore, the mea-

surement register state is similar to equation 6.2. More specifically it is of the form

$$|\psi\rangle_1 = \frac{1}{\sqrt{32}} \sum_{k=0}^{31} e^{-ik\phi}|k\rangle. \tag{6.22}$$

This shows a linear phase modulation of the coefficients C_k. We also note that this state is not an entangled state and can be represented as a product state of the five qubits as $|\psi\rangle_1 = \frac{1}{\sqrt{32}} \otimes_{j=1}^{5} (|0\rangle + e^{-i2^{j-1}\phi}|1\rangle)$. Therefore, in the experiment we prepare the phase modulation by simply performing single qubit $R-$gates on each of the qubits about an appropriate axis on the Bloch sphere without reference to the ancilla space. The application of the QFT on this state follows equation 6.6 where the coefficient D_j of the state $|j\rangle$ is now given by

$$D_j = \frac{1}{32} \sum_{k=0}^{31} e^{2\pi ijk/32 - ik\phi}. \tag{6.23}$$

This clearly shows that $D_j = 1$ if $2\pi j/32 = \phi$. In this case the phase ϕ is mapped to the output state $|j\rangle$ which is measured with unit probability. This makes the phase estimation protocol a single-shot measurement protocol.

Figure 6.7 shows the results of applying a QFT in order to estimate ϕ by mapping its value to the population of the output state. This is repeated for several cases of ϕ where it is incremented in steps of $2\pi/64$ over the range of 0 to 2π. Values of ϕ that are integral multiples of $2\pi/32$ result in the output state $|32\phi/2\pi\rangle$ ideally with unit probability. In the experiment this is achieved with a success probability of 0.619(5). For those values of ϕ that are non-integer multiples of $2\pi/32$, the

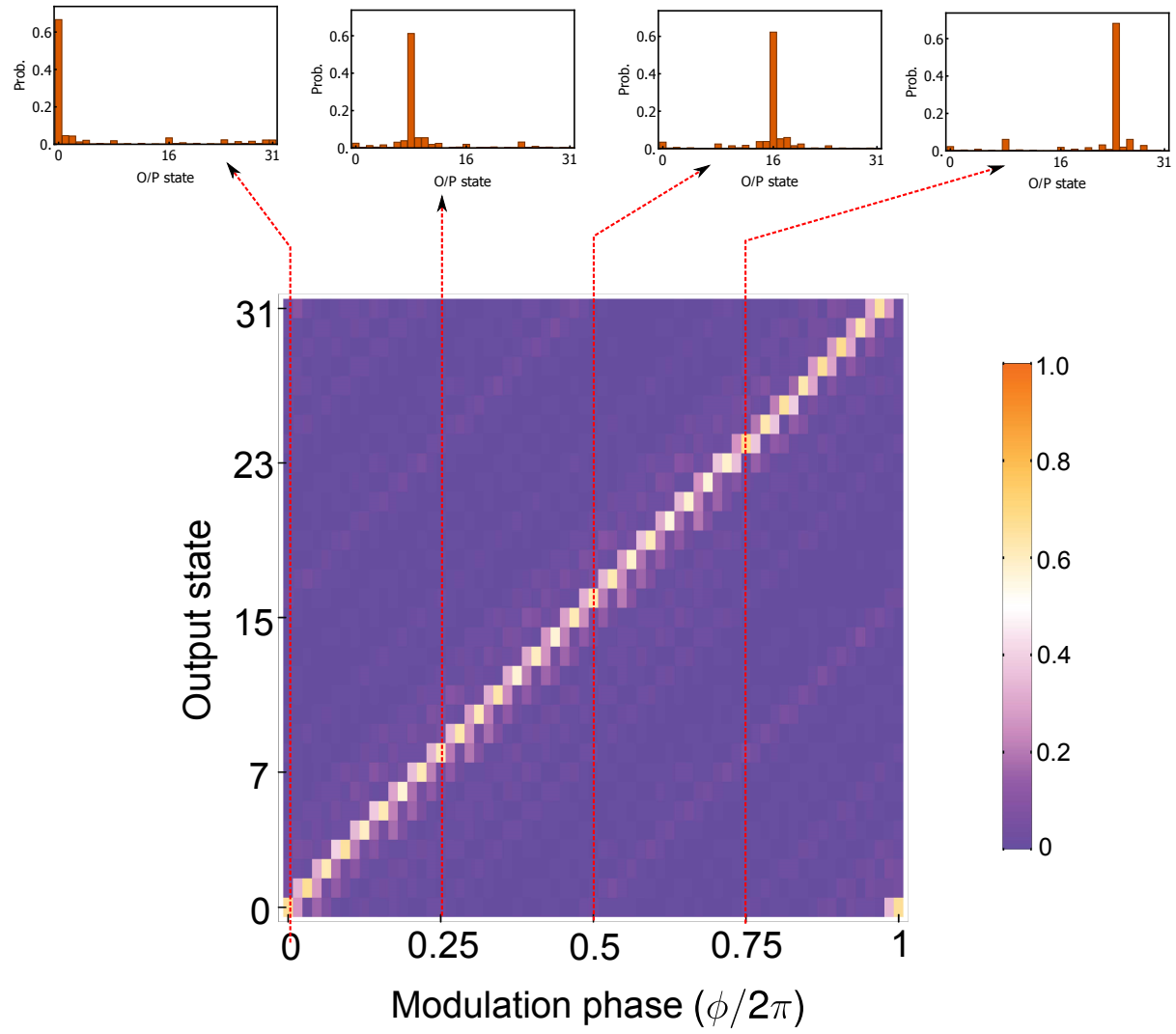

Figure 6.7: **Performance of QFT in phase estimation** Quantum phase estimation using five measurement qubits. The plot shows populations in the output state that estimates the given phase modulation ϕ of the input state amplitudes $\{C_k\}$ of the input state $\sum_{k=0}^{31} C_k|k\rangle$. Probabilities in the output state population are colour coded. We observe the correct value of the phase in each case with a probability > 0.6. The experiment is repeated 8,000 times for each value of ϕ. The insets show explicitly the population in the measured output state for various values of $\phi = \{0, \pi/2, \pi, 3\pi/2\}$. The sharp peaks in probability of the expected output state $|j\rangle$ show that the five qubit QFT truly provides a $5-$bit resolution.

population is distributed mainly between the nearest 5-bit approximate states. For a useful demonstration of the 5-qubit phase estimation problem one might consider an acilla space which is large enough such that solving the eigen value (Eqn. 6.21) problem is classically not feasible. In this case one might also prolong the application of the unitary $A = \exp[-iHt]$ by increasing t such that higher resolution of ϕ might be obtained while keeping the size of measurement register the same.

6.4 Quantum period finding protocol

The quantum period finding algorithm is the application of the five qubit QFT to a superposition state $\sum_{j=0}^{31} C_j|j\rangle$ where the coefficients C_j exhibit a type of periodic modulation of their amplitude. In the previous algorithms discussed so far the coefficients C_j exhibited phase modulations that was picked up by the QFT. The period finding protocol on the other hand serves as an indispensable part of the Shor's [95] factorization algorithm where the periodicity of the amplitude of coefficients leads to efficiently finding the 'order': a critical step that is exponentially harder to implement on a classical computer [88]. In this section we will not elaborate on the Shor's algorithms since we only implement the period finding protocol (a subroutine of the original algorithm) to examine the performance of the QFT.

The circuit for the period finding protocol follows that of figure 6.6 where single qubit rotations prepare the five qubits in a way such that the coefficients mimic the kind of amplitude modulation as would be expected in a Shor's factorization algorithm. Table 6.4 shows the various prepared states with their respective peri-

Input state	**Period**
$\frac{1}{\sqrt{32}}(\|0\rangle + \|1\rangle)(\|0\rangle + \|1\rangle)(\|0\rangle + \|1\rangle)(\|0\rangle + \|1\rangle)(\|0\rangle + \|1\rangle)$	1
$\frac{1}{\sqrt{16}}(\|0\rangle + \|1\rangle)(\|0\rangle + \|1\rangle)(\|0\rangle + \|1\rangle)(\|0\rangle + \|1\rangle)\|1\rangle$	2
$\frac{1}{\sqrt{32}}(\|0\rangle + \|1\rangle)(\|0\rangle + \|1\rangle)(\|0\rangle + \|1\rangle)(\|0\rangle + e^{i6.2\pi/16}\|1\rangle)(\|0\rangle + i\|1\rangle)$	3
$\frac{1}{\sqrt{8}}(\|0\rangle + \|1\rangle)(\|0\rangle + \|1\rangle)(\|0\rangle + \|1\rangle)\|11\rangle$	4
$\frac{1}{2}(\|0\rangle + \|1\rangle)(\|0\rangle + \|1\rangle)\|111\rangle$	8
$\frac{1}{\sqrt{2}}(\|0\rangle + \|1\rangle)\|1111\rangle$	16
$\|11111\rangle$	32

Table 6.1: A list of input states that are prepared in the QFT-period finding protocol. Each input state is theoretically calculated to give a certain periodicity as indicated in the right column.

odicity. We see that the modulation of the amplitudes is such that the input state is of the form,

$$|\psi\rangle_1 = C(|j\rangle + |j + r\rangle + |j + 2r\rangle + \ldots) \tag{6.24}$$

where C is the common coefficient (and normalizing constant) to all the basis states and r is the periodicity. The only exception to this construction is the state prepared for periodicity 3. From table 6.4 we see that this state has both amplitude and phase modulation which was numerically found to give a periodicity of three and therefore used as one of the input state due to the ease of preparation by using $R-$gates only. A purely amplitude modulated period-3 state on the other hand is complicated to contruct using single qubit gates only but can be created by using two qubit entangling gates [38]. The results from the period finding protocol are shown in figure 6.8 where it is compared with the theoretical populations. We evaluate the squared statistical overlap [96] between the experimental and theoretical populations to quantify the fidelity of the protocol.

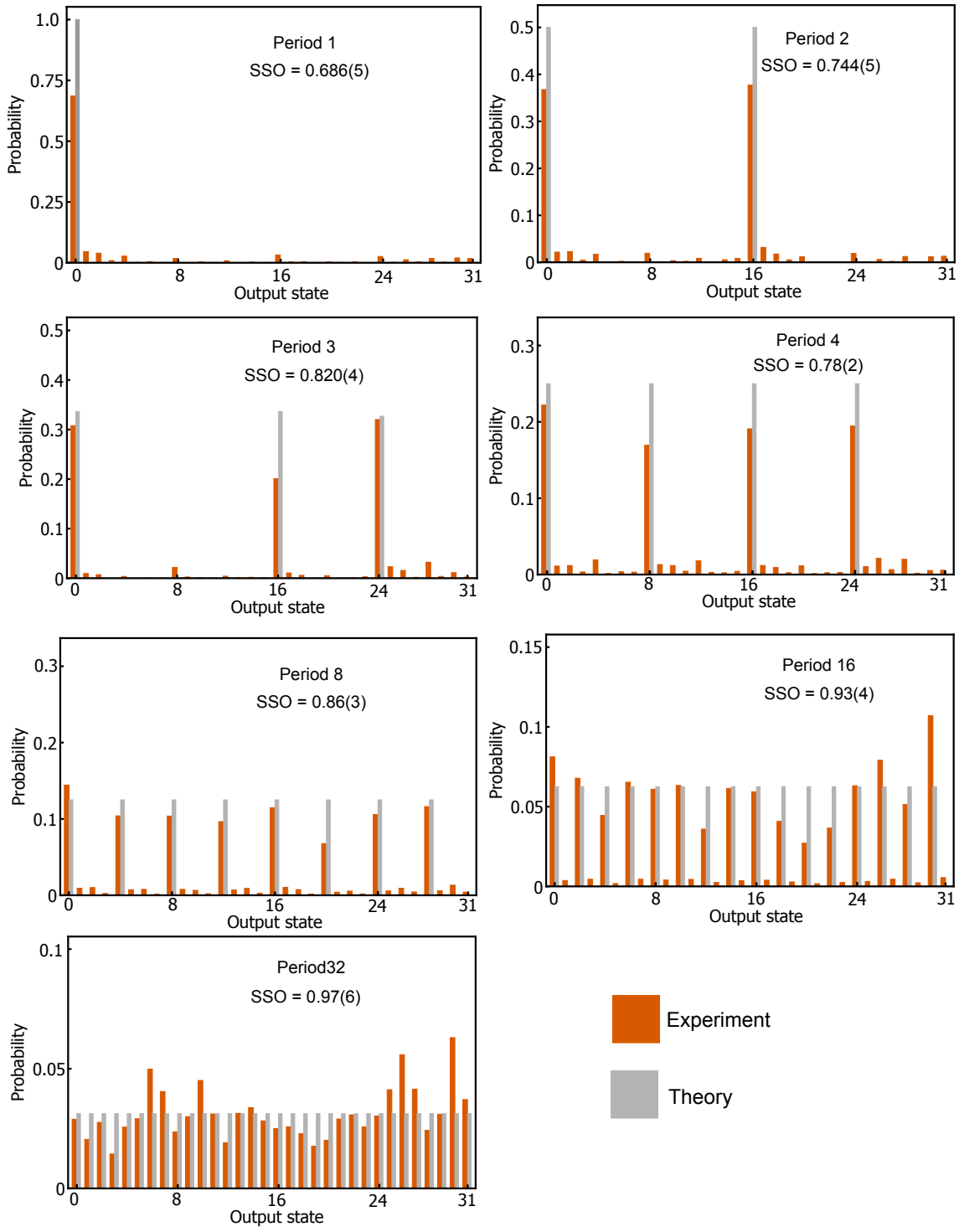

Figure 6.8: **Performance of QFT in period finding.** Input states are prepared using single-qubit rotations to modulate the 32 state amplitudes with periods 1, 3, 4, 8, 16, and 32 (see table6.4). The squared statistical overlap (SSO) [38, 96] signifies the fidelity of the protocol where the error is a statistical estimate over 8,000 experimental repetitions. The grey and red bars represent populations calculated from theory and measured in the experiment, respectively.

Chapter 7: Outlook

7.1 Improving gate fidelity

In the experiments the overall fidelity of any algorithm is limited mainly due to the native gate errors ($< 2\%$) which can then propagate into the composite logic gate errors ($< 5\%$). These errors are dominated by the imperfections in the Raman beams. The individual addressing Raman beam has a high NA which can lead to intensity noise at the qubit since the beam size is small and also due to gradients in the refractive index across the beam that can occur due to air currents. In order to prevent this an active stabilization of the Raman beams can be adopted that prevents beam steering and stabilizes intensity. These techniques have recently been proven to work while implementing high fidelity single and two qubit gates using Raman beams [8, 9]. We can also minimize addressing cross talk by improving the optical resolution by using ever higher NA lenses as has been recently demonstrated for a $^{171}Yb^{+}$system using 355nm Raman lasers [73].

Stark shifts of the second and fourth order also affects the gate fidelity. In this case the applied beat-note during the gate is detuned from the intended frequency by $\Delta_s = \Delta_{s2} + \Delta_{s4}$. Since the stark shift is dependent on the Raman beam intensities it

is usually unequal across the chain. Ideally it can be compensated entirely by shifting the driving beat-note of the gate according to pre-calibrated Stark shifts on each ion. However, this is not possible in the current system since the Raman beatnote frequency is decided by the global Raman beam which is common to all the qubits and cannot compensate for the individual and unequal Stark shifts experienced by the qubits.

7.2 Scaling up the system

The algorithms presented here illustrate the computational flexibility provided by the trapped-ion quantum architecture. Within a single module, this system can be scaled to dozens of qubits by linearly increasing the number of radio-frequency controls and AOM and PMT-channels at the hardware level. In software, the number of $XX-$ and $R-$gate calibrations required to compile any logic gate scale as $O(N^2)$ and $O(N^1)$ since there are N possible single qubit rotations operators and $\binom{N}{2} = N(N-1)/2$ possible $XX-$gates.

As more ions are added to a chain, the ratio of axial-to-transverse confinement must be weakened to maintain a linear crystal ($\omega_z/\omega_x < 0.6N^{-0.86}$) [44]. For constant transverse confinement, this means that the minimum ion spacing remains the same. However, this will slow the gates down. In our setup (for $N = 5$) two-qubit XX-gates for any ion pair $\{i, j\}$ have a duration of $\tau = 235\,\mu$s, which depends on the spectral splitting of the transverse modes ($\tau \sim \omega_x/\omega_z \sim N^{1.7}$). As more ions are added to the chain, the axial confinement must be weakened to maintain a linear

crystal. This will slow down the $XX-$gate duration roughly as $N^{1.7}$ [44], but the crosstalk is not expected to get worse since the inter ion distance is maintained. Finally, implementing this architecture on multi-zone ion traps such as surface traps will provide further control over the connectivity of qubits though fast shuttling for scalable computation [11, 97]. This will also enable selective measurement of qubits that can be fed-forward classically to perform conditional operations in the module [39] as required for fault-tolerant computing [51, 98].

Appendix A: Imaging objective characterization

Figure A.1a shows the simulation of the objective lens assembly in OSLO. The optical path difference is within $\lambda/4$ for a field angle of 0.35^0 which shows that he objective is nearly diffraction limited for a field of view of $\pm 100\mu$m. The point spread function (PSF) indicated the resolution with which a single ion is imaged. The PSF near diffraction limit is given by a Airy function. The theoretical diffraction limit is set by the radius of the first Airy ring which in this case is $0.5\,\mu$m. Figure A.1b shows the fractional energy within a certain radius of the PSF. This corresponds to the number of photons collected from a single ion. Outside a radius of $5\,\mu$m there is a few percent of the total intensity that gives an inherent optical crosstalk between PMT channels of neighboring ions that cannot be completely removed.

Figure A.2 shows an experimental setup for studying the performance of the objective. A $\times 10$ magnified image is formed with an NA of 0.38. The expected resolution in the imaging is obtained from the sharpness of the edges of the test pattern mask.

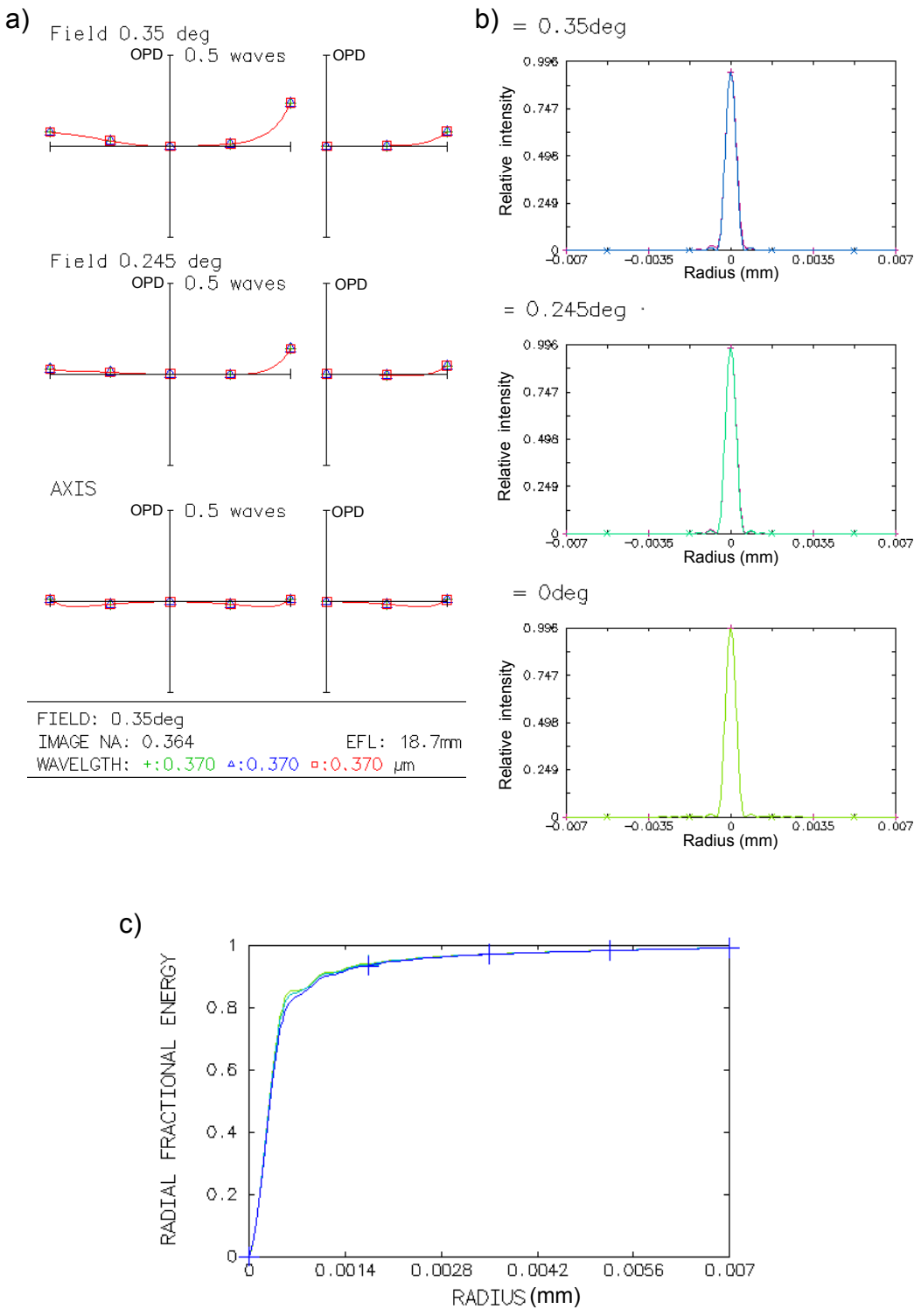

Figure A.1: **Simulated performance of objective lens design.** a) Optical path difference in units of λ for various field angles. b) Point spread function or the impulse response of the optical system. c) Integrated fractional energy (fraction of collected photons) as a function of the radius.

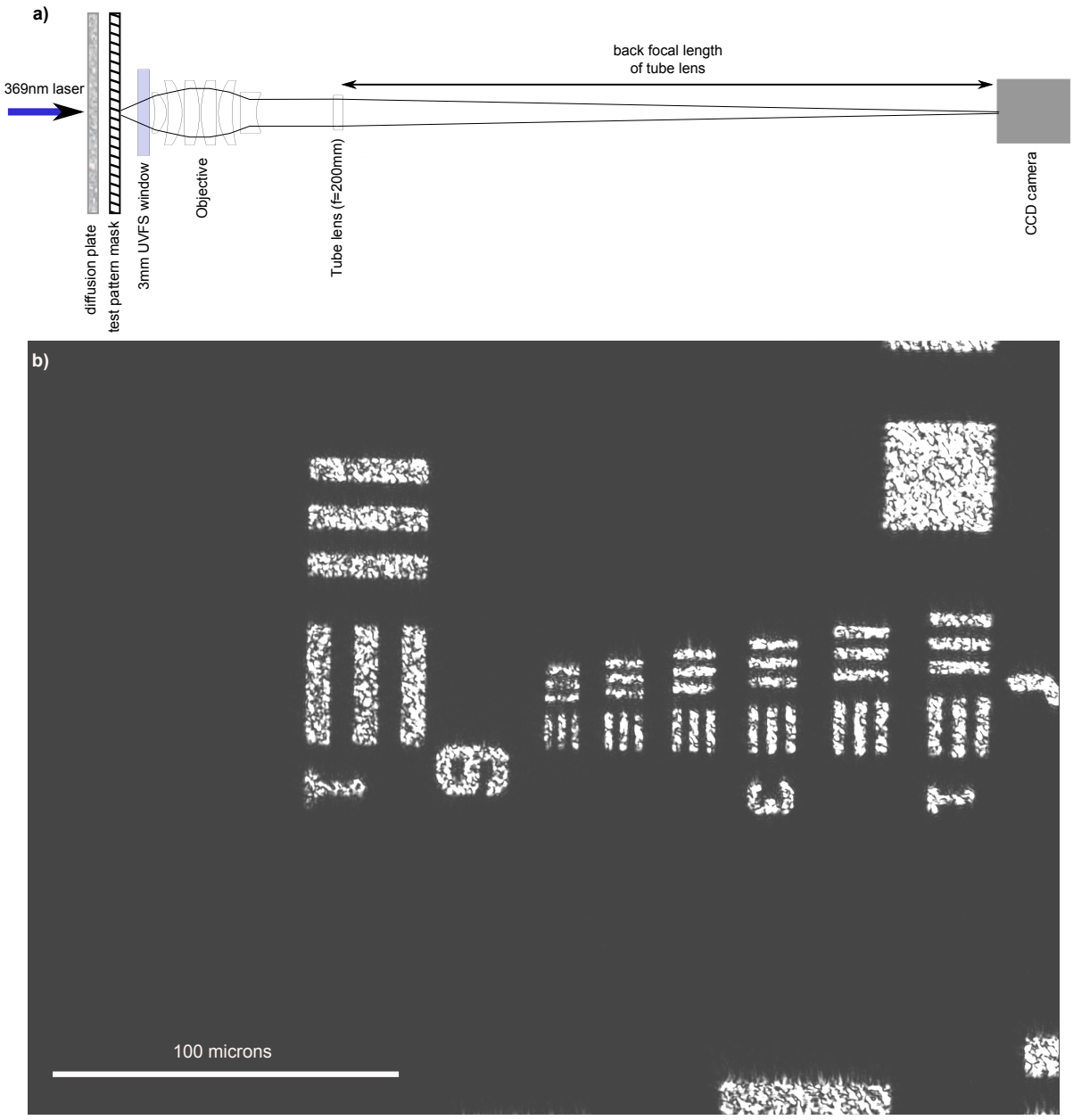

Figure A.2: **Experimental characterization of imaging objective.** a) A setup to image a test pattern using a 0.37 NA objective with a $\approx$ 10x magnification stage. b) Test pattern as imaged on a camera. Features in the center has a 2.2 μm thickness. Resolving the patterns in both horizontal and vertical direction indicates near diffraction limited performance. A slight tilt of the UVFS window along the horizontal axis is hard to eliminate and therefore creates aberration in the vertical direction as seen from the blurring of horizontal edges of the test pattern. The CCD is adjusted such that patterns are overexposed at the brightest spots. This makes the ripples at the edges more prominent. The rapidly decreasing intensity of these ripples as we move away from the edge is a characteristic of the point spread function at near-diffraction limit.

Appendix B: XX-gate pulse shape solution

In order to apply a two-qubit $XX-$gate it is important to choose a pulse shape at a certain gate detuning μ. We try to find an optimal solution for a 9-segmented pulse. The duration of the gate is fixed to 235 μs and pulse shape is obtained for a two-qubit rotation $|\chi_{ij}| = \pi/4$. The solution is obtained for each detuning value as it is scanned across the five transverse modes. The criteria for choosing a pulse shape are: a) the pulse solution requires low power, and b) the pulse solution is relatively insensitive to the detuning over a small range (say ± 1 kHz).

Figure B.1 and B.2 shows pulse shape solution for an $XX-$gate on ions 1 and 5 and on ions 1 and 3, respectively. We observe a symmetry in the pulse shape at almost every value of the detuning μ. There are potentially two values of the detuning where the gate requires lower Rabi frequency and the solutions are 'flat'. Although it is favorable to have such detuning insensitive pulse shapes it is not necessary if the transverse trap frequencies are fairly stable. The fidelity is very close to 1 for almost all detuning values. The phase of the two-qubit rotation χ_{15} and χ_{13} is shown in fig. B.1c and B.2c, respectively as a function of detuning where it takes the value $\pi/4$ at some regions and $-\pi/4$ at other.

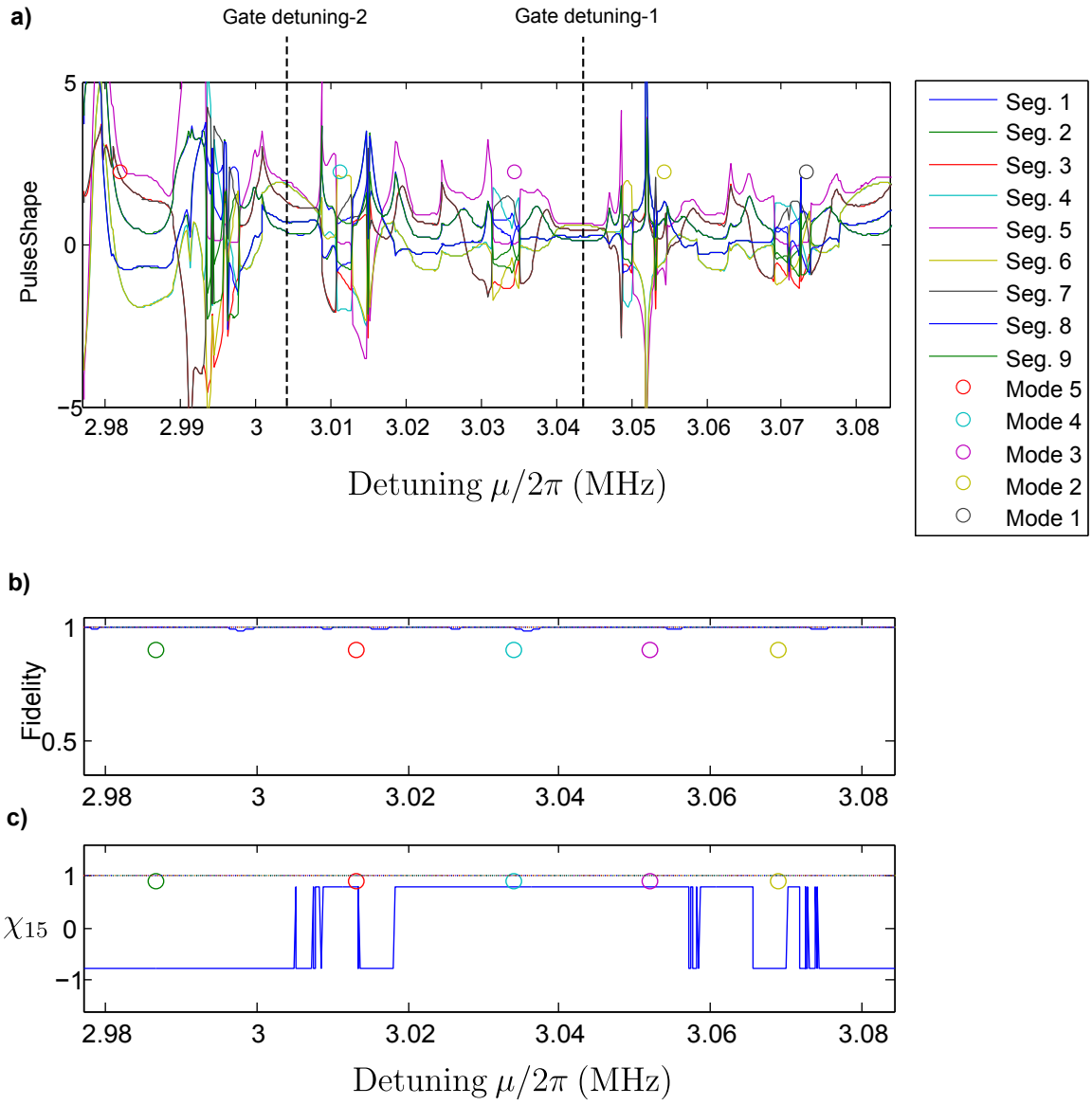

Figure B.1: **Pulse shaping solution for XX15.** a)Solution for a 9-segment pulse for performing a $XX(\pm\pi/4)$ gate on ions 1 and 5. A solution is obtained at every value of the detuning parameter μ. The gate detuning is chosen such that the pulse shape is relatively insensitive to detuning errors that may rise due to fluctuations in mornal mode frequencies of the ion chain. b) The theoretical gate fidelity is neary 1 for all detuning values. c) The sign of the rotation (χ_{ij}) can be positive or negative depending on the detuning value and the ions participating in the XX-gate. (compare with fig. B.2c)

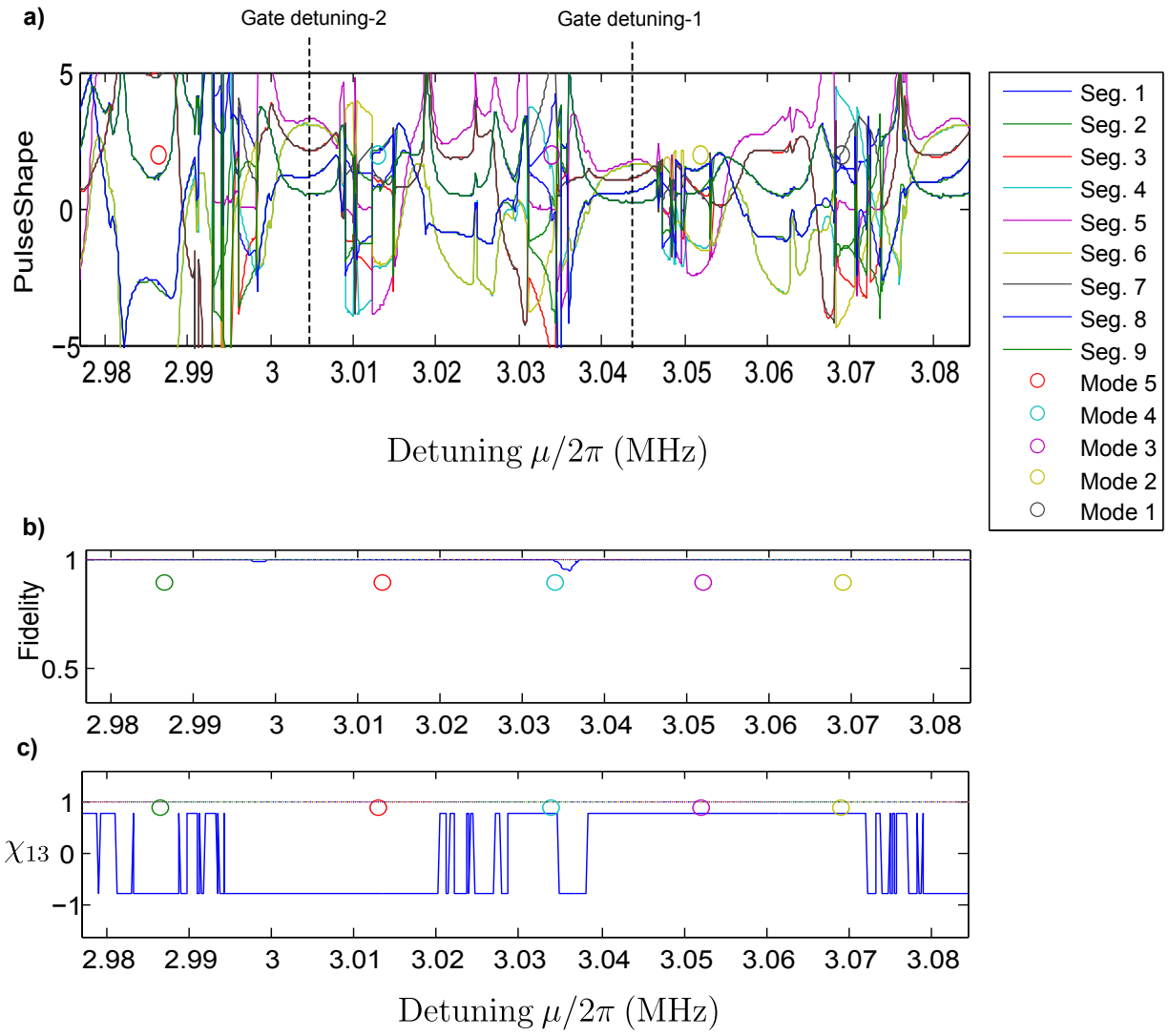

Figure B.2: **Pulse shaping solution for XX13.** a)Solution for a 9-segment pulse for performing a $XX(\pm\pi/4)$ gate on ions 1 and 3. A solution is obtained at every value of the detuning parameter μ. The gate detuning is chosen such that the pulse shape is relatively insensitive to detuning errors that may rise due to fluctuations in mornal mode frequencies of the ion chain. b) The theoretical gate fidelity is neary 1 for all detuning values. c) The sign of the rotation (χ_{ij}) can be positive or negative depending on the detuning value and the ions participating in the XX-gate. (compare with fig. B.1c)

Bibliography

[1] R. P. Feynman, "Simulating physics with computers," *International Journal of Theoretical Physics*, vol. 21, no. 6-7, pp. 467–488, 1982.

[2] D. Deutsch, "Quantum Theory, the Church-Turing Principle and the Universal Quantum Computer," *Proceedings of the Royal Society A: Mathematical, Physical and Engineering Sciences*, vol. 400, pp. 97–117, jul 1985.

[3] K. R. Islam, *Quantum Simulation of Interacting Spin Models with Trapped Ions*. PhD thesis, University of Maryland, 2012.

[4] R. Islam, C. Senko, W. C. Campbell, S. Korenblit, J. Smith, A. Lee, E. E. Edwards, C.-C. J. Wang, J. K. Freericks, and C. Monroe, "Emergence and Frustration of Magnetism with Variable-Range Interactions in a Quantum Simulator," *Science*, vol. 340, pp. 583–587, may 2013.

[5] R. Cleve, A. Ekert, C. Macchiavello, and M. Mosca, "Quantum algorithms revisited," *Proceedings of the Royal Society of London A: Mathematical, Physical and Engineering Sciences*, vol. 454, no. 1969, pp. 339–354, 1998.

[6] D. P. DiVincenzo, "The Physical Implementation of Quantum Computation," *Fortschritte der Physik*, vol. 48, pp. 771–783, sep 2000.

[7] R. Noek, G. Vrijsen, D. Gaultney, E. Mount, T. Kim, P. Maunz, and J. Kim, "High speed, high fidelity detection of an atomic hyperfine qubit," *Optics Letters*, vol. 38, p. 4735, nov 2013.

[8] C. J. Ballance, T. P. Harty, N. M. Linke, M. A. Sepiol, and D. M. Lucas, "High-Fidelity Quantum Logic Gates Using Trapped-Ion Hyperfine Qubits," *Phys. Rev. Lett.*, vol. 117, p. 060504, aug 2016.

[9] J. P. Gaebler, T. R. Tan, Y. Lin, Y. Wan, R. Bowler, A. C. Keith, S. Glancy, K. Coakley, E. Knill, D. Leibfried, and D. J. Wineland, "High-fidelity universal gate set for 9Be+ ion qubits," *Physical Review Letters*, vol. 117, no. 6, p. 060505, 2016.

[10] D. J. Wineland, C. Monroe, W. M. Itano, D. Leibfried, B. E. King, and D. M. Meekhof, "Experimental Issues in Coherent Quantum-State Manipulation of Trapped Atomic Ions," *J. Res. Natl. Inst. Stand. Technol*, vol. 103, no. 103, pp. 1689–1699, 1998.

[11] R. Bowler, J. Gaebler, Y. Lin, T. R. Tan, D. Hanneke, J. D. Jost, J. P. Home, D. Leibfried, and D. J. Wineland, "Coherent diabatic ion transport and separation in a multizone trap array," *Physical Review Letters*, vol. 109, no. 8, pp. 1–4, 2012.

[12] S. Seidelin, J. Chiaverini, R. Reichle, J. Bollinger, D. Leibfried, J. Britton, J. Wesenberg, R. Blakestad, R. Epstein, D. Hume, W. Itano, J. Jost, C. Langer, R. Ozeri, N. Shiga, and D. Wineland, "Microfabricated Surface-Electrode Ion Trap for Scalable Quantum Information Processing," *Physical Review Letters*, vol. 96, p. 253003, jun 2006.

[13] J. True Merrill, C. Volin, D. Landgren, J. M. Amini, K. Wright, S. Charles Doret, C.-S. Pai, H. Hayden, T. Killian, D. Faircloth, K. R. Brown, A. W. Harter, and R. E. Slusher, "Demonstration of integrated microscale optics in surface-electrode ion traps," *New Journal of Physics*, vol. 13, p. 103005, oct 2011.

[14] C. Piltz, T. Sriarunothai, S. S. Ivanov, and S. Wölk, "Versatile microwave - driven trapped ion spin system for quantum information processin g a," *Science Advances*, vol. 1600093, no. 2016, pp. 1–22, 2016.

[15] J. Benhelm, G. Kirchmair, C. F. Roos, and R. Blatt, "Towards fault-tolerant quantum computing with trapped ions," *Nature Physics*, vol. 4, no. 6, pp. 463–466, 2008.

[16] T. Monz, D. Nigg, E. A. Martinez, M. F. Brandl, P. Schindler, R. Rines, S. X. Wang, I. L. Chuang, and R. Blatt, "Realization of a scalable Shor algorithm," *Science*, vol. 351, pp. 1068–1070, mar 2016.

[17] U. Warring, C. Ospelkaus, Y. Colombe, R. Jordens, D. Leibfried, and D. J. Wineland, "Individual-ion addressing with microwave field gradients," *Physical Review Letters*, vol. 110, no. 17, pp. 1–5, 2013.

[18] N. Navon, S. Kotler, N. Akerman, Y. Glickman, I. Almog, and R. Ozeri, "Addressing two-level systems variably coupled to an oscillating field," *Physical Review Letters*, vol. 111, no. 7, pp. 1–5, 2013.

[19] C. Piltz, T. Sriarunothai, a. F. Varón, and C. Wunderlich, "A trapped-ion-based quantum byte with 10(-5) next-neighbour cross-talk.," *Nature communications*, vol. 5, p. 4679, 2014.

[20] D. P. DiVincenzo, "Two-bit gates are universal for quantum computation," *Physical Review A*, vol. 51, no. 2, pp. 1015–1022, 1995.

[21] A. Barenco, C. H. Bennett, R. Cleve, D. P. DiVincenzo, N. Margolus, P. Shor, T. Sleator, J. A. Smolin, and H. Weinfurter, "Elementary gates for quantum computation," *Physical Review A*, vol. 52, pp. 3457–3467, nov 1995.

[22] J. I. Cirac and P. Zoller, "Quantum Computations with Cold Trapped Ions," *Phys. Rev. Lett.*, vol. 74, no. 20, 1994.

[23] C. Monroe and J. Kim, "Scaling the Ion Trap Quantum Processor," *Science*, vol. 339, pp. 1164–1169, mar 2013.

[24] C. Monroe, R. Raussendorf, A. Ruthven, K. R. Brown, P. Maunz, L. M. Duan, and J. Kim, "Large-scale modular quantum-computer architecture with atomic memory and photonic interconnects," *Physical Review A - Atomic, Molecular, and Optical Physics*, vol. 89, no. 2, pp. 1–16, 2014.

[25] D. Hucul, I. V. Inlek, G. Vittorini, C. Crocker, S. Debnath, S. M. Clark, and C. Monroe, "Modular entanglement of atomic qubits using photons and phonons," *Nature Physics*, vol. 11, pp. 37–42, nov 2014.

[26] I. L. Chuang, L. M. K. Vandersypen, X. L. Zhou, D. W. Leung, and S. Lloyd, "Experimental realization of a quantum algorithm," *Nature*, vol. 393, no. 6681, pp. 143–146, 1998.

[27] N. Linden, H. Barjat, and R. Freeman, "An implementation of the Deutsch-Jozsa algorithm on a three-qubit NMR quantum computer," *Chemical Physics Letters*, vol. 296, no. October, pp. 61–67, 1998.

[28] L. M. Vandersypen, M. Steffen, G. Breyta, C. S. Yannoni, M. H. Sherwood, and I. L. Chuang, "Experimental realization of Shor's quantum factoring algorithm using nuclear magnetic resonance.," *Nature*, vol. 414, no. 6866, pp. 883–887, 2001.

[29] B. L. Higgins, D. W. Berry, S. D. Bartlett, H. M. Wiseman, and G. J. Pryde, "Entanglement-free Heisenberg-limited phase estimation," *Nature*, vol. 450, no. 7168, pp. 393–396, 2007.

[30] E. Brainis, L.-P. Lamoureux, N. Cerf, P. Emplit, M. Haelterman, and S. Massar, "Fiber-Optics Implementation of the Deutsch-Jozsa and Bernstein-Vazirani Quantum Algorithms with Three Qubits," *Physical Review Letters*, vol. 90, no. 15, p. 157902, 2003.

[31] E. Martín-López, A. Laing, T. Lawson, R. Alvarez, X.-Q. Zhou, and J. L. O'Brien, "Experimental realization of Shor's quantum factoring algorithm using qubit recycling," *Nature Photonics*, vol. 6, pp. 773–776, oct 2012.

[32] S. Gulde, M. Riebe, G. P. T. Lancaster, C. Becher, J. Eschner, H. Häffner, F. Schmidt-Kaler, I. L. Chuang, and R. Blatt, "Implementation of the Deutsch-Jozsa algorithm on an ion-trap quantum computer.," *Nature*, vol. 421, no. 6918, pp. 48–50, 2003.

[33] K.-A. Brickman, P. C. Haljan, P. J. Lee, M. Acton, L. Deslauriers, and C. Monroe, "Implementation of Grover's quantum search algorithm in a scalable system," *Physical Review A*, vol. 72, p. 050306, nov 2005.

[34] F. Shi, X. Rong, N. Xu, Y. Wang, J. Wu, B. Chong, X. Peng, J. Kniepert, R. S. Schoenfeld, W. Harneit, M. Feng, and J. Du, "Room-temperature implementation of the deutsch-jozsa algorithm with a single electronic spin in diamond," *Physical Review Letters*, vol. 105, no. 4, pp. 2–5, 2010.

[35] C. R. Monroe, R. J. Schoelkopf, and M. D. Lukin, "Quantum Connections," *Scientific American*, vol. 314, no. 5, pp. 50–57, 2016.

[36] M. H. Devoret and R. J. Schoelkopf, "Superconducting Circuits for Quantum Information: An Outlook," *Science*, vol. 339, pp. 1169–1174, mar 2013.

[37] S. Debnath, N. M. Linke, C. Figgatt, K. A. Landsman, K. Wright, and C. Monroe, "Demonstration of a small programmable quantum computer with atomic qubits," *Nature*, vol. 536, pp. 63–66, aug 2016.

[38] J. Chiaverini, J. Britton, D. Leibfried, E. Knill, M. D. Barrett, R. B. Blakestad, W. M. Itano, J. D. Jost, C. Langer, R. Ozeri, T. Schaetz, and D. J. Wineland, "Implementation of the Semiclassical Quantum Fourier Transform in a Scalable System," *Science*, vol. 308, no. 5724, pp. 997–1000, 2005.

[39] J. Chiaverini, D. Leibfried, T. Schaetz, M. D. Barrett, R. B. Blakestad, J. Britton, W. M. Itano, J. D. Jost, E. Knill, C. Langer, R. Ozeri, and D. J. Wineland, "Realization of quantum error correction.," *Nature*, vol. 432, no. 7017, pp. 602–605, 2004.

[40] T. Monz, K. Kim, W. Hänsel, M. Riebe, A. S. Villar, P. Schindler, M. Chwalla, M. Hennrich, and R. Blatt, "Realization of the quantum Toffoli gate with trapped ions," *Physical Review Letters*, vol. 102, no. 4, pp. 1–4, 2009.

[41] W. Paul, "Paul-electromagnetic-traps-for-charged-and-neutral-particles.pdf," *Reviews of Modern Physics*, vol. 62, no. 3, p. 531, 1990.

[42] G. D. Lin, S. L. Zhu, R. Islam, K. Kim, M. S. Chang, S. Korenblit, C. Monroe, and L. M. Duan, "Large Scale Quantum Computation in an Anharmonic Linear Ion Trap," *EPL (Europhysics Letters)*, vol. 86, p. 60004, jan 2009.

[43] D. F. V. James, "Quantum dynamics of cold trapped ions with application to quantum computation," *Applied Physics B: Lasers and Optics*, vol. 66, no. 2, p. 20, 1997.

[44] J. P. Schiffer, "Phase transitions in anisotropically confined ionic crystals," *Physical Review Letters*, vol. 70, pp. 818–821, feb 1993.

[45] D. J. Berkeland, J. D. Miller, J. C. Bergquist, W. M. Itano, and D. J. Wineland, "Minimization of ion micromotion in a Paul trap," *Journal of Applied Physics*, vol. 83, no. 10, pp. 5025–5033, 1998.

[46] J. D. Jackson, *Classical Electrodynamics*. New Delhi: John Wiley and Sons, 3 ed., 2007.

[47] F. G. Major and H. G. Dehmelt, "Major-Exchange-Collision-Technique-for-rf-Spectroscopy-of-Stored-Ions-1968.pdf," *Physical Review*, vol. 170, no. 1, 1968.

[48] S. Olmschenk, *Quantum teleportation between distant matter qubits*. PhD thesis, University of Michigan, 2009.

[49] J. A. Mizrahi, *Ultrafast Control of Spin and Motion in Trapped Ions*. PhD thesis, University of Maryland, 2013.

[50] N. W. McLachlan, *Theory and Application of Mathieu Functions*. Dover Publications, Inc., 1964.

[51] A. Steane, "The ion trap quantum information processor," *Applied Physics B: Lasers and Optics*, vol. 64, pp. 623–643, jun 1997.

[52] S. Olmschenk, K. Younge, D. Moehring, D. Matsukevich, P. Maunz, and C. Monroe, "Manipulation and detection of a trapped Yb^{+} hyperfine qubit," *Physical Review A*, vol. 76, pp. 1–9, nov 2007.

[53] H. J. Metcalf and P. van der Straten, *Laser cooling and trapping*. Springer-Verlag, 1 ed., 1999.

[54] M. O. Scully and M. S. Zubairy, *Quantum Optics*. Cambridge University Press, 1 ed., 1997.

[55] P. Fisk, M. Sellars, M. Lawn, and G. Coles, "Accurate measurement of the 12.6 GHz "clock" transition in trapped 171Yb+ ions," *IEEE Transactions on Ultrasonics, Ferroelectrics and Frequency Control*, vol. 44, pp. 344–354, mar 1997.

[56] D. Budker, D. F. Kimball, and D. P. Demille, *Atomic physics: An exploration through problems and solutions*. Oxford University Press, 2 ed., 2008.

[57] D. J. Berkeland and M. G. Boshier, "Destabilization of dark states and optical spectroscopy in Zeeman-degenerate atomic systems," *Physical Review A*, vol. 65, no. 3, p. 033413, 2002.

[58] S. Olmschenk, D. Hayes, D. N. Matsukevich, P. Maunz, D. L. Moehring, K. C. Younge, and C. Monroe, "Measurement of the lifetime of the 6p 2P1/2 level of Yb+ S.," *Physical Review A*, vol. 80, p. 022502, aug 2009.

[59] W. M. Itano and D. J. Wineland, "Laser cooling of ions stored in harmonic and Penning traps," *Physical Review A*, vol. 25, no. 1, pp. 35–54, 1982.

[60] D. L. Hayes, *Remote and Local Entanglement of Ions using Photons and Phonons*. PhD thesis, University of Maryland, 2012.

[61] T. A. Manning, *Quantum information processing with trapped ion chains*. PhD thesis, University of Maryland, 2014.

[62] K. Sugiyama and J. Yoda, "Production of YbH+ by chemical reaction of Yb+ in excited states with H2 gas," *Physical Review A*, vol. 55, pp. R10–R13, jan 1997.

[63] K. G. Johnson, J. D. Wong-Campos, A. Restelli, K. A. Landsman, B. Neyenhuis, J. Mizrahi, and C. Monroe, "Active stabilization of ion trap radiofrequency potentials," *Review of Scientific Instruments*, vol. 87, no. 5, p. 053110, 2016.

[64] W. W. Macalpine and R. O. Schildknecht, "Coaxial Resonators with Helical Inner Conductor," *Proceedings of the IRE*, 1959.

[65] A. Zverev and H. Blinchikoff, "Realization of a filter with helical components," *Component Parts, IRE Transactions on*, vol. 8, no. 3, pp. 99–110, 2002.

[66] J. D. Siverns, L. R. Simkins, S. Weidt, and W. K. Hensinger, "On the application of radio frequency voltages to ion traps via helical resonators," *Applied Physics B: Lasers and Optics*, vol. 107, no. 4, pp. 921–934, 2012.

[67] J. J. Sakurai, *Modern Quantum Mechanics*. 2009.

[68] D. Hayes, D. N. Matsukevich, P. Maunz, D. Hucul, Q. Quraishi, S. Olmschenk, W. Campbell, J. Mizrahi, C. Senko, and C. Monroe, "Entanglement of atomic qubits using an optical frequency comb," *Physical Review Letters*, vol. 104, no. 14, pp. 1–4, 2010.

[69] J. Mizrahi, B. Neyenhuis, K. G. Johnson, W. C. Campbell, C. Senko, D. Hayes, and C. Monroe, "Quantum control of qubits and atomic motion using ultrafast laser pulses," *Applied Physics B*, vol. 114, no. 1-2, pp. 45–61, 2014.

[70] A. C. Lee, J. Smith, P. Richerme, B. Neyenhuis, P. W. Hess, J. Zhang, and C. Monroe, "Engineering Large Stark Shifts for Control of Individual Clock State Qubits," *arxiv.org/abs/1604.08840*, pp. 1–7, apr 2016.

[71] R. Islam, W. C. Campbell, T. Choi, S. M. Clark, C. W. S. Conover, S. Debnath, E. E. Edwards, B. Fields, D. Hayes, D. Hucul, I. V. Inlek, K. G. Johnson, S. Korenblit, A. Lee, K. W. Lee, T. A. Manning, D. N. Matsukevich, J. Mizrahi, Q. Quraishi, C. Senko, J. Smith, and C. Monroe, "Beat note stabilization of mode-locked lasers for quantum information processing.," *Optics letters*, vol. 39, no. 11, pp. 3238–41, 2014.

[72] D. M. Meekhof, D. Leibfried, C. Monroe, and B. E. King, "Experimental Creation and Measurement of Motional Quantum States of a Trapped Ion," *Brazilian J. Phys.*, vol. 27, no. 2, pp. 178–192, 1997.

[73] S. Crain, E. Mount, S. Baek, and J. Kim, "Individual addressing of trapped 171Yb+ ion qubits using a microelectromechanical systems-based beam steering system," *Applied Physics Letters*, vol. 105, no. 18, pp. 1–5, 2014.

[74] R. E. Fisher, B. Tadic-Galeb, and P. R. Yoder, *Optical System Design*. Mc Graw Hill, 2 ed., 2008.

[75] A. E. Siegman, *Lasers*. University science books, 1 ed., 1986.

[76] G. J. Milburn, S. Schneider, and D. F. V. James, "Ion Trap Quantum Computing with Warm Ions," *Fortschritte der Physik*, vol. 48, no. 9-11, pp. 801–810, 2000.

[77] K. Kim, M. S. Chang, R. Islam, S. Korenblit, L. M. Duan, and C. Monroe, "Entanglement and Tunable Spin-Spin Couplings between Trapped Ions Using Multiple Transverse Modes," *Physical Review Letters*, vol. 103, no. 12, pp. 1–4, 2009.

[78] S. L. Zhu, C. Monroe, and L. M. Duan, "Trapped ion quantum computation with transverse phonon modes," *Physical Review Letters*, vol. 97, no. 5, pp. 1–4, 2006.

[79] D. Hayes, S. M. Clark, S. Debnath, D. Hucul, I. V. Inlek, K. W. Lee, Q. Quraishi, and C. Monroe, "Coherent Error Suppression in Multiqubit Entangling Gates," *Physical Review Letters*, vol. 109, p. 020503, jul 2012.

[80] C. Marquet, F. Schmidt-Kaler, and D. James, "Phonon-phonon interactions due to non-linear effects in a linear ion trap," *Applied Physics B: Lasers and Optics*, vol. 76, no. 3, pp. 199–208, 2003.

[81] K. Mølmer and A. Sørensen, "Multiparticle Entanglement of Hot Trapped Ions," *Physical Review Letters*, vol. 82, no. 9, pp. 1835–1838, 1999.

[82] A. Sørensen and K. Mølmer, "Entanglement and quantum computation with ions in thermal motion," *Physical Review A*, vol. 62, p. 022311, jul 2000.

[83] P. J. Lee, K.-a. Brickman, L. Deslauriers, P. C. Haljan, L.-M. Duan, and C. Monroe, "Phase Control of Trapped Ion Quantum Gates," *J. Opt. B.*, vol. 371, p. 21, 2005.

[84] C. F. Roos, "Ion trap quantum gates with amplitude-modulated laser beams," *New Journal of Physics*, vol. 10, 2008.

[85] G. Kirchmair, J. Benhelm, F. Zähringer, R. Gerritsma, C. F. Roos, and R. Blatt, "Deterministic entanglement of ions in thermal states of motion," *New Journal of Physics*, vol. 11, 2009.

[86] T. Choi, S. Debnath, T. A. Manning, C. Figgatt, Z. X. Gong, L. M. Duan, and C. Monroe, "Optimal quantum control of multimode couplings between trapped ion qubits for scalable entanglement," *Physical Review Letters*, vol. 112, no. 19, pp. 1–5, 2014.

[87] S. L. Zhu, C. Monroe, and L. M. Duan, "Arbitrary-speed quantum gates within large ion crystals through minimum control of laser beams," *Europhysics Letters*, vol. 73, no. 4, pp. 485–491, 2006.

[88] M. A. Nielsen and I. L. Chuang, *Quantum Computation and Quantum Information*. Cambridge University Press, 1 ed., 2002.

[89] M. Nakahara and T. Ohmi, *Quantum Computing*. Boca Raton: CRC Press, 1 ed., 2008.

[90] P. W. Shor, "Algorithms for Quantum Computation: Discrete Logarithms and Factoring," *IEEE*, pp. 124–134, 1994.

[91] D. Deutsch and R. Jozsa, "Rapid solution of problems by quantum computation," *Proceedings of the Royal Society of London A: Mathematical, Physical and Engineering Sciences*, vol. 439, pp. 553–558, 1992.

[92] E. Bernstein and U. Vazirani, "Quantum Complexity Theory," *SIAM Journal on Computing*, vol. 26, no. 5, pp. 1411–1473, 1997.

[93] C. H. Bennet, E. Bernstein, G. Brassard, and U. Vazirani, "Strengths and weaknesses of quantum computing," *SIAM J. Comput.*, vol. 26, no. 5, pp. 1510–1523, 1997.

[94] R. B. Griffiths and C.-S. Niu, "Semiclassical Fourier transform for quantum computation," *Physical Review Letters*, vol. 76, no. 17, pp. 3228–3231, 1996.

[95] P. Shor, "Polynomial-Time Algorithms for Prime Factorization and Discrete Logarithms on a Quantum Computer," *SIAM Journal on Computing*, vol. 26, no. 5, pp. 1484–1509, 1997.

[96] C. A. Fuchs, "Distinguishability and Accessible Information in Quantum Theory," *arXiv preprint quant-ph/9601020*, no. December, 1996.

[97] D. Kielpinski, C. Monroe, and D. J. Wineland, "Architecture for a large-scale ion-trap quantum computer," *Nature*, vol. 417, no. 6890, pp. 709–711, 2002.

[98] P. Shor, "Fault-tolerant quantum computation," in *Proceedings of 37th Conference on Foundations of Computer Science*, pp. 56–65, IEEE Comput. Soc. Press, 1996.